Investigating dry powder flow within large-scale, counter-rotational, intermeshing Twin-Screw Mixers (TSMs), via Digital Image Processing (DIP) and Positron Emission Particle Tracking (PEPT).

A thesis submitted by

Sean Clifford

For the award of Doctor of Engineering

Biopharmaceutical and Bioprocessing Technology Centre
School of Chemical Engineering and Advanced Materials
Newcastle University

January 2020

Acknowledgements

Firstly, I wish to thank my academic supervisor, Professor Serafim Bakalis, for his guidance and encouragement throughout the course of my studies. I would also like to gratefully acknowledge the input of my industrial supervisors Jerome Castro and Nigel S. Roberts at Procter & Gamble (P&G), for their support and advice whilst carrying out the trials, and for giving key insight into the needs of industry which will no doubt hold me in good stead during my future career.

I would like to give an extra special thank you to my wife Helen, whose continued support and patience throughout my doctorate helped keep things in perspective. A huge debt of gratitude is also given to my mother and father for all the good advice I have received from them over the years, which for better or worse has made me who I am today.

Much appreciation is given to key members of staff and students at the following companies and institutions: The School of Chemical Engineering & Advanced Materials at Newcastle University, The School of Chemical Engineering at Birmingham University, The School of Chemical & Process Engineering at Leeds University, The Centre for Process Innovation (CPI) in Sedgefield, Ajax Equipment, as well as P&G's Newcastle Innovation Centre, who have aided me either through enlightening discussion, and/or through physically helping with data acquisition whilst utilising the large scale equipment.

I would also like to thank the other postgraduate students within both Newcastle and Birmingham's Engineering Doctoral Training Centres. As they provided me with a much needed series of distractions intermittently throughout the endeavour. Finally, I wish to thank the Engineering and Physical Sciences Research Council (EPSRC) for providing me with the funding needed to complete my studies.

Abstract

Solids processing is a common procedure spanning a wide selection of different industries. Fields as diverse as Fast Moving Consumer Goods (FMCG), pharmaceuticals, fine chemicals and even mineral processing will adopt some kind of solids handling technique, at some stage in a products development. Common objectives during solids processing include: (1) ensuring adequate and consistent mixing of multiple ingredients, and/or (2) adjusting the physicochemical properties of the particles, in order to improve bulk handling and metering, or to otherwise customise the product to look and behave in some desirable fashion [1, 2].

Despite its prevalence throughout industry, these procedures are noted for being notoriously inefficient owing to the complex interplay between chemical (and/or physical) rate processes and system geometry. Continuous twin-screw processing however, shows great promise with regard to improving this state of affairs, due to their inherent modularity coupled with a relatively small flow channel diameter. These properties, it is believed, may be exploited to facilitate a precise and homogeneous application of parameters (such as shear) upon the bulk, as it propagates axially through the system, which in turn could reduce deviations from a set-point [3, 4, 5].

This document investigates dry powder transport phenomena within large-scale Twin-Screw Mixers (TSMs), via Positron Emission Particle Tracking (PEPT) and Digital Image Processing (DIP). Changes to flow, as a result of altering: TSM size, internal geometry, screw speed and powder feed rate, has been thoroughly examined, and key underlying mechanisms identified. Due to the vast knowledge gap within literature pertaining to such vessels the work presented is highly novel, and should be of great interest to both industrialists and academics alike.

This document also established a highly novel and robust framework for efficiently characterising powder flow within a TSM. This has been used to good effect whilst investigating two geometrically similar TSMs, of two different sizes, in order to help inform a capital investment decision for purchasing a commercial scale version of the machine.

The PEPT investigation contained within the report has established that the bulk flows within the TSM annular spaces at the same rate as the screw lead rotates. In the TSMs Nip Region however, the average bulk velocity is approximately twice this magnitude.

Contents

Abbreviations & Nomenclature

$\bar{x}(\lambda)$, $\bar{y}(\lambda)$, $\bar{z}(\lambda)$	The 'XYZ' tristimulus values based on the colour matching functions of the standard observer	[%]
β	RSM Constant	[Various]
$\boldsymbol{\tau}$	Mean Residence Time	[s]
ΔE	Empfindung (Sensation) Difference	
Δt	Time Interval	[s]
ρ	Density	[kg/m^3]
τ_i	Time Spent in a Single CSTR in a T-i-S Model.	[s]
θ	Normalised Time	[Dimensionless]
ε	RSM Error	[Various]
C	Concentration of Tracer	[Various Units]
d	Distance	[m]
$E(t)$	Residence Time Function	[Dimensionless]
$F(\theta)$	Cumulative Normalised Residence Time Function	[Dimensionless]
Fr	Froude Number	[Dimensionless]
N	Number of Revolutions	[s^{-1}]
R^2	Coefficient of Determination	[Dimensionless]
s^2	Mass Weighted Composition Variance	[Dimensionless]
t	Time	[s]
API	Active Pharmaceutical Ingredient	
BBTC	Biopharmaceutical Bioprocessing Technology Centre	

CCD Central Composite Design

CIE International Commission on Illumination (Commission Internationale de l'Éclairage)

CoR Co-rotating

CPI Center for Process Innovation

CSTR Continuously Stirred Tank Reactors

CtrR DP Counter-rotating down-pumping

CtrR UP Counter-rotating up-pumping

D	Diameter of the Screw	[m]
d	Dead Zone Volume Fraction	[Dimensionless]
Da	Axial Dispersion Coefficient	[m^2/s]
Da/uL	Dispersion Number	[Dimensionless]

DEM Discrete Element Method

Di	Inner Screw Diameter	[m]
Di:Do	Ratio between Inner and Outer Screw Diameter	[Dimensionless]

DIP Digital Image Processing

Do	Outer Screw Diameter	[m]

DoE Design of Experiments

EM Electromagnetic

EngD Engineering Doctorate

EPSRC Engineering and Physical Sciences Research Council

f Fraction of LoRs used to Calculate PEPT Particle Locations

f_{OPT} Optimised Fraction of LoRs used to Calculate PEPT Particle Locations

FDA Food and Drug Administration

FMCG Fast Moving Consumer Goods

GRG	Generalised Reduced Gradient	
IV	Independent Variables	
L	Length of Vessel/Screw	[m]
L/D	Length over Diameter	[Dimensionless]
L/S	Liquid Binder to Solid Powder Ratio	[%(w/v) or %(w/w)]
LDA	Laser Doppler Anemometry	
LoR	Line of Response	
N	Number of LoRs used to Calculate PEPT Particle Locations	
n	Number of CSTRs	[Dimensionless]
p	Plug Flow Volume Fraction	[Dimensionless]
P&G	Procter & Gamble	
PAT	Process Analytical Technology	
PBM	Population Balance Model	
PEPT	Positron Emission Particle Tracking	
PFR	Plug Flow Reactor	
PSD	Particle Size Distribution	
QA	Quality Assurance	
QbD	Quality by Design	
R&D	Research & Development	
RGB	Red, Green and Blue	
RPM	Revolutions Per Minute	$[min^{-1}]$
RSS	Residual Sum of Squares	$[s^2]$
RTD	Residence Time Distribution	
SE	Standard Error	

SMEs Small and Medium Sized Enterprises

T-i-S Tanks-in-Series

TSE Twin-Screw Extruder

TSM Twin-Screw Mixer

u Fluid Flow Rate [m/s]

VIF Variance Inflation Factors

X, Y, Z Imaginary Primary Colours for the CIE 1931 XYZ Colour Space

y RSM Dependent Variable [Various]

List of Figures

List of Tables

Chapter 1

Introduction

1.1 Research Background

In April 2014, a consortium embarked upon a research venture christened 'Project Chariot'. Bodies comprised within the agreement included: P&G, CPI, AJAX Equipment and the Universities of Leeds, Birmingham, Durham and Cranfield.

The partners were able to secure funding for £8.85 million from the governments 'Advanced Manufacturing Supply Chain Initiative' (AMSCI). A summary of the project's remit was duly defined by the AMSCI as being: 'to open up new markets for particle based products manufactured in existing UK plants'. The consortium itself dedicated £9.05 million into the venture, bringing total investment to £17.89 million.

Through this close collaboration between: UK academics, Small and Medium Sized Enterprises (SMEs) and large industrialists, a template has been constructed in which the synergistic effects have been keenly felt, as each organisation is able to inject their own distinctive strengths and expertise in order to achieve mutual benefit. Furthermore, it is perhaps easy to surmise that should such collaborations thrive and become the normal state of affairs, the nation will become an ever more attractive proposition in regards to locating powder manufacturing operations.

The project presented here was forged through Newcastle University's 'Biopharmaceutical and Bioprocessing Technology Centre's (BBTC's) close ties with the 'Centre for Doctoral Training in Formulation Engineering', at Birmingham University (both being EPSRC Doctoral Training Centres). As the award of Engineering Doctorate (EngD) awarded by such centres is industry focussed in nature, the work was planned in such fashion as to directly fulfil the needs of an industrialist, in this case P&G.

To this end, the document presented here addresses the feasibility of conducting large scale powder processing using TSMs, through a thorough examination of dry powder motion at 2 different scales. As investigations pertaining to such vessels are scarce throughout academic literature [6],

the fundamentals of particle flow phenomena taking place within them is still largely unknown. Therefore, this investigation seeks to directly address this state of affairs through the utilisation of advanced diagnostic tools and algorithms, such as: DIP, PEPT, Design of Experiments (DoE) based regression analysis and Tanks-in-Series (T-i-S) modelling.

Within Chapter 1 Section 1.2, the background theory needed to understand how DIP has been utilised to great affect within the food industry has been summarised. This knowledge was subsequently employed to develop a strategy for measuring the critical Residence Time Distribution (RTD) index; which has been described in full within Section 3.2. Section 1.3 analyses academic literature with regard to TSMs, in order to place this documents importance in context. Finally, each subsequent chapter within the report has been summarised in Section 1.4, with respect to how it fulfils the requirements of the Engineering Doctorate, whilst simultaneously being of relevance to the industrial partner P&G.

1.2 Digital Image Processing (DIP)

Computer vision refers to any automated procedure designed to extract useful information from a digital image via DIP. Whilst still relatively young as a scientific discipline, an explosion of interest beginning in the 1970s has since resulted in dramatic growth in both its theory and application. Image analysis techniques are used throughout the food processing industry for the purposes of Quality Assurance (QA). In fact, in many cases they have demonstrated to be a reasonable substitute for employing trained, at-line, quality inspectors; as well as being inherently more cost effective and objective. Thus, it has become one of the top ten industries to employ computer vision systems as part of the manufacturing process [7, 8, 9].

One of the most powerful DIP strategies within the food industry is the utilisation of colorimetry, the science of quantifying and describing colour, in order to asses key product attributes, such as: texture, ripeness or flavour etc. This information may then be used to retain or discard produce as part of an in-line sorting strategy. Food can also be rejected based purely on aesthetics alone, as outer appearance has long been demonstrated to strongly influence buyer behavioural patterns.

One of the central tenets of colorimetry is to first define the colour space, i.e. set of coordinates, that will be used as reference. A commonly used gamut within industrial applications is the ‘1976 L*a*b* Colour Space’, presumably as it has been demonstrated many times to offer a high degree of accuracy for the purposes of food classification based upon colour. In fact, in 2006 a particularly interesting study compared it with 2 other commonly used colour spaces, for the purposes

of inspecting agricultural products with curved surfaces, and found it to be the most accurate and consistant performer [10, 9].

What follows is a brief history of colorimetry with respect to the '1976 L*a*b* Colour Space', as may be found within many academic sources including the book: 'Colour in Food - Improving Quality' published in 2002 [11]. Colorimetry, the science of colour measurement, began in earnest during the early part of the 20th century when the International Commission on Illumination (Commission Internationale de l'Éclairage, CIE) began establishing colour measurement standards that still form the basis of many systems used within industry today. The metrics formulated were based upon an earlier investigation into how the average person perceives colour, and were underpinned using current physiological understanding of the human eye (i.e. that colour vision, as perceived by a person, is facilitated via three colour sensors located within the retina; collectively named 'cone cells').

Cone cells, then as now, are thought to be particularly sensitive to specific regions of the Electromagnetic (EM) spectrum. It is for this reason that they are often referred to as either: blue (short-wave), green (medium-wave) or red (long-wave) cones. Consequently, these early experiments consisted of additive mixing of three different light sources, in order to assess the intensities needed to produce a vast array of colours, which in turn corresponded to intervals across the breadth of the visible EM spectrum. Accordingly, primary colours were chosen as the light sources, namely: blue, green and red, in order to coordinate with these naturally occurring cone cells.

During the experiments observers were asked to confirm whether a particular colour had been formulated as a result of light intensity alteration. This, in effect, allowed the researchers to quantify the magnitudes of primary colour light intensities needed, in order to produce every colour perceptible to the human eye. These intensity values were subsequently designated the 'tristimulus' values. Furthermore, by plotting the tristimulus values vs. wavelength, three colour matching functions could be composed. These curves were thought to approximately correlate with the sensitivity to wavelength displayed by each type of cone cell, and were discovered to be very broad and overlapping.

The obvious weakness with this methodology is the subjective nature of gathering results based upon an observation of colour. However, as colour perception is in itself an inherently subjective phenomena, being both physical and psychological in nature, calculating average response was deemed the most accurate strategy for quantifying human colour recognition. In fact, although these experiments have since been refined and supplemented, the method described previously was still the basic approach used by investigators.

The theory of colour perception suggests that any perceivable colour can be closely approximated through a three component vector, i.e. via the magnitudes of: red, green and blue within its composition. In colorimetry this is known as the 'RGB (Red, Green and Blue) Colour Space'. The CIE further developed this idea by proposing three imaginary primary colours: X, Y and Z, which were derived by linearly transforming the three colour matching functions from the 'RGB model' into the imaginary tristimulus values: $\bar{x}(\lambda)$, $\bar{y}(\lambda)$, $\bar{z}(\lambda)$ (the 'Colour-Matching Functions of the 1931 CIE Standard Observer') which has been provided as Figure 1.1.

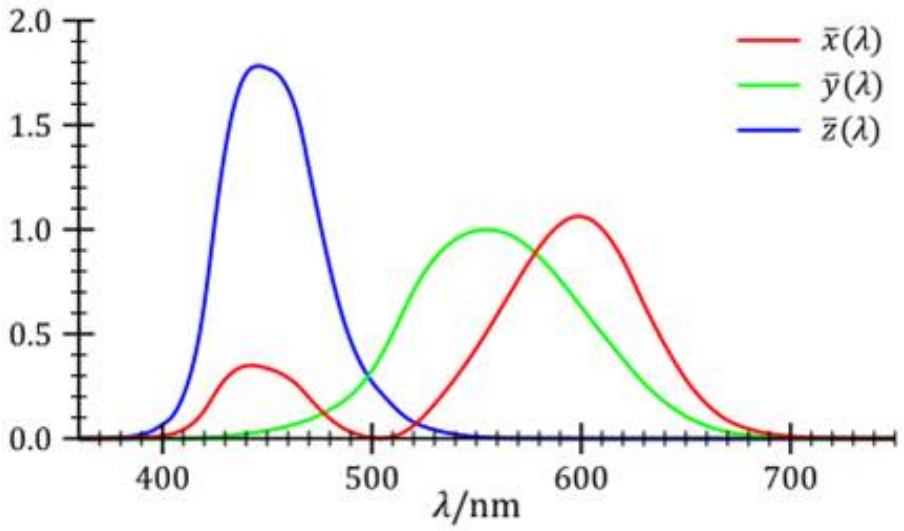

Figure 1.1: The Colour-Matching Functions of the 1931 CIE Standard Observer [12].

The linear transformation was chosen so that the $\bar{y}(\lambda)$ was set equal to the previously derived 'luminous efficiency function', which had been calculated by ranking equally luminous colours, corresponding to intervals across the breadth of the visible EM spectrum, in terms of perceived brightness to an observer. This, in effect, decoupled the effects of luminosity from the X and Z axis, with the full effects of brightness being incorporated entirely along the Y dimension. Figure 1.2 displays the 'CIE 1931 XYZ Colour Space' plotted in three dimensions.

Whilst the 'XYZ Colour Space' was, at its heart, an attempt to classify colour in a similar fashion to the physiological nature of the human eye, the CIE were still not entirely satisfied. This was because the spread of each colour within 'XYZ' 3D space was not perceptually uniform, which is to say the similarity between colours bore little resemblance to their proximity within the Cartesian coordinate system.

Therefore, to compensate for this the 'CIE 1976 L*a*b* Colour Space' was developed, where 3 functions were used to change the axis X, Y and Z scales into the L*, a* and b* axis, where: L*

represented the lightness component, a* green to red and b* blue to yellow. This has also been displayed as Figure 1.2. The 'L*a*b* Colour Space' was also formulated to be 'device independent', which meant it was standardised so a colour's coordinates within the space are the same, regardless of the device used to read or display the image.

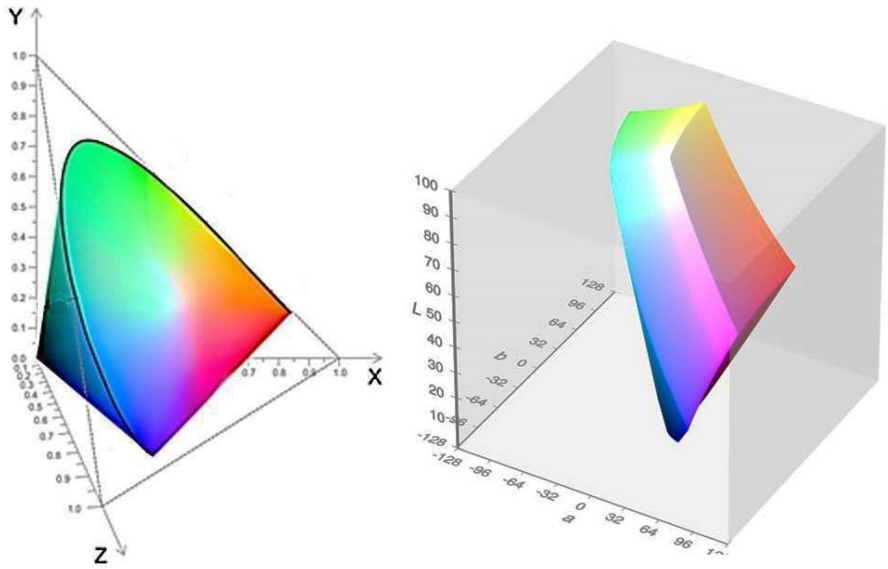

Figure 1.2: (Left) The CIE 1931 XYZ Colour Space [13]. (Right) The 1976 CIE Chromatogram [14].

As mentioned previously, within the L*a*b* Colour Space 3 values are needed to describe any individual colour, namely: the L*, a* and b* component. The L* value describes how light a particular colour is, with 0 being the darkest value and 100 the brightest. The a* component describes the level of green or red within the colour (both may not be present within this gamut), with -100 to 0 indicating 'greenest green' to 'no green', and 0 to 100 indicating 'no red' to the 'reddest red'. Similarly, the b* component describes the level of either blue or yellow within the colour being described (as before both may not be present within this gamut), with -100 to 0 indicating 'bluest blue' to 'no blue', and 0 to 100 indicating 'no yellow' to the 'yellowest yellow'.

These properties have in turn has led to Euclidean distances being utilised in order quantify how closely colours match. This metric is called ΔE for which the formula has been provided as Equation 1.1. The ΔE threshold that is commonly suggested to be distinguishable to the average person is ≈ 2.3 [15].

$$\Delta E = \sqrt{(L_1^* - L_2^*)^2 + (a_1^* - a_2^*)^2 + (b_1^* - b_2^*)^2} \tag{1.1}$$

RTD is a critical metric for characterising a materials flow profile during a continuous, or series of continuous, unit operations. A more in-depth discussion regarding the theory and application

shall be addressed in Section 3.2. However, put simply, the RTD is a probability distribution of the time a small element of solid/fluid may spend within a system [16]. In order to generate the index a pulse or step change of tracer, assumed to have no effect upon the flow properties of the process overall, is added to the system. The change in concentration is subsequently monitored over time at the outlet. Finally, by plotting the tracer concentration (recast as a percentage) vs. time, the overall objective is achieved.

Intuitively, the sampling protocol used is an important consideration when fabricating these experiments. For solids applications some methods found within literature incorporate colorimetry within the overall strategy. This was the case in 2003, when Ziegler et al. [17] conducted experiments using a small scale TSM to process chocolate formula.

The trials were performed as follows:

- The ingredients were altered mid-manufacture from white chocolate formula to milk chocolate formula, whilst keeping all other process variables constant. This was in order to take advantage of the obvious colour change (white to brown), combined with very little changing in regards to material flow properties (which was assumed as the formulations were extremely similar).
- Samples taken from the TSM's discharge were collected and measured by colorimeter. A linear relationship had previously been established between the amount of white chocolate formula (relative to milk chocolate) and the magnitude of the L reading (discerned via the colorimeter), with an R^2 value of 0.988. This meant the concentration of white chocolate formula could be inferred.
- The researchers were therefore able to discern the length of time needed for 100% white chocolate formula to be dispatched at the TSM's exit, for a given set of process parameters.

The L in this instance was presumably referencing the 'Hunter 1948 Lab Colour Space', which is a similar gamut to the 'CIE 1976 L*a*b* Colour Space', with both being slightly different transformations of the 'CIE 1931 XYZ Colour Space' (undertaken in an attempt to achieve perceptual uniformity). However, of the two, the latter is generally thought to be superior within DIP applications [11].

Despite colorimetry being a major component of DIP within the food industry, the development of tracer measurement methodology for the purposes of RTD fabrication has rarely been undertaken within academic literature. Of the few studies that have been conducted on the topic three

of them, published in: 2006, 2007 and 2009 [18, 19, 20] respectively, used extrusion processes to investigate its potential.

All three extolled the virtues of using a DIP based approach to measuring coloured tracer concentration, such as being: non-labour intensive, non-destructive, inexpensive (as only a standard digital camera and computer are needed), and rapid.

The three publications were similar in that they utilised the L*a*b* colour space within their methodologies. Furthermore, each document cross-validated their results to ensure a linear relationship existed between the concentrations of red tracer and the magnitude of red present within a processed digital image (with R^2 values of at least 0.86 being achieved).

Gao et al, commented on these methods in their 2012 [16] review, ascerting that whilst measuring RTD in this fashion has been clearly demonstrated to yield a high degree of accuracy, these procedures could only be completed off-line. However, whilst this may be true within some solid processing applications, for a loose granular material, it is this authors opinion that there is no insurmountable barrier to incorporating a similar approach in-line (provided an adequate automated sampling procedure can be fabricated).

This view would seem to be greatly supported by the success enjoyed within the food industry, where in-line DIP driven automated processes are routinely used for the purposes of QA. Therefore, an exploration of the potential of using DIP to measure RTD, in-line, within a continuous granular process forms a major component of this report.

1.3 Twin-Screw Mixing

Twin-Screw processing is commonly cited as possessing many advantages for carrying out solid and viscous fluid unit operations when being compared to alternatives such as: fluidised bed and continuous high-shear. These advantages include: shorter residence times, handling larger fluctuations in feed rate and an intimate mixing of formulation ingredients. They are also to some degree self-cleaning, as the entire surface of screw and barrel are continuously scraped by the screw flights. In turn this reduces the time needed for cleaning and may even allow up to 24 hour production (although this is likely to be highly dependent on formulation). Twin-screw manufacturing also offers a similar level of flexibility to high-shear batch processes, owing to their inherently modular design. A systems alteration therefore, becomes a relatively simple and rapid endeavour [21, 5].

Whilst much research has been conducted using twin-screw technology with regards to extrusion and to a lesser extent granulation, with both being reviewed in Chapter 2, there currently exists a severe lack of literature addressing the fundamentals of dry powder transport within these machines. To the best of this author's knowledge, the most relevant publications in this regard were a series written (by various authors) under the tutelage of Professor Theodore Heindel, from Iowa State University [22, 6, 23, 24, 25]. These documents are in full agreement with the notion that literature pertaining to granular flow within TSMs, or indeed regarding TSMs in general, are minimal at best. Therefore, this state of affairs needs to be seriously addressed in order that the promising technology may progress.

Two such studies, published in 2014 [22, 6], used red oak chips (particle sizes between 500 μm - 6350 μm and a true density of 1350 kg/m^3 as measured by a pycnometer) and glass beads (particle sizes between 300 μm - 500 μm and a true density of 2510 kg/m^3) as particulates. These materials were employed to compare the mixing effects of a TSM, in response to alterations in: screw pitch, rotational direction of the screws and rotation speed. The three rotational regimes investigated were labelled: co-rotational (CoR), counter-rotating up-pumping (CtrR UP), and counter-rotating down-pumping (CtrR DP). This has been displayed in Figure 1.3.

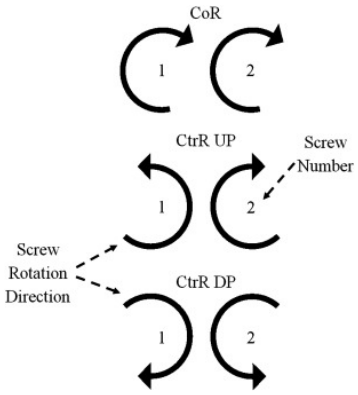

Figure 1.3: Screws direction of rotation: Co-rotating (CoR), counter-rotating up-pumping (CtrR UP), and counter-rotating down-pumping (CtrR DP), respectively [6].

The screw mixer was fabricated with two non-contact, single flight, intermeshing screws of 2.54 cm in diameter and a screw root diameter of 0.79 cm (a thorough explanation on screw terminology may be found within Chapter 2). Two volumetric auger feeders were used to input the particulates into two separate injection ports, with port 2 being situated 5.08 cm downstream of port 1. They were both positioned above the screw housing and centrally between the screws. After transport through the system the granular material exited under the force of gravity through a dividing mechanism situated below the barrel. This served to separate the exiting granules into four

separate streams, as show in Figure 1.4.

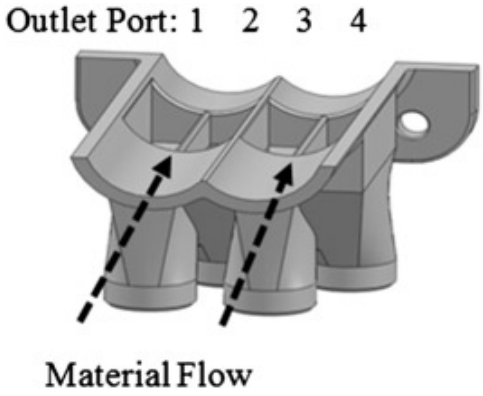

Figure 1.4: The screw mixer's dividing mechanism used to section the granular flow's exit into four separate streams [6].

The mixing length was measured to be 24.4 cm from the end of the second inlet port (inlet port 2) to the beginning of the outlet port, as displayed in Figure 1.5. The barrel was constructed of a transparent plastic to allow a visual assessment of the flow.

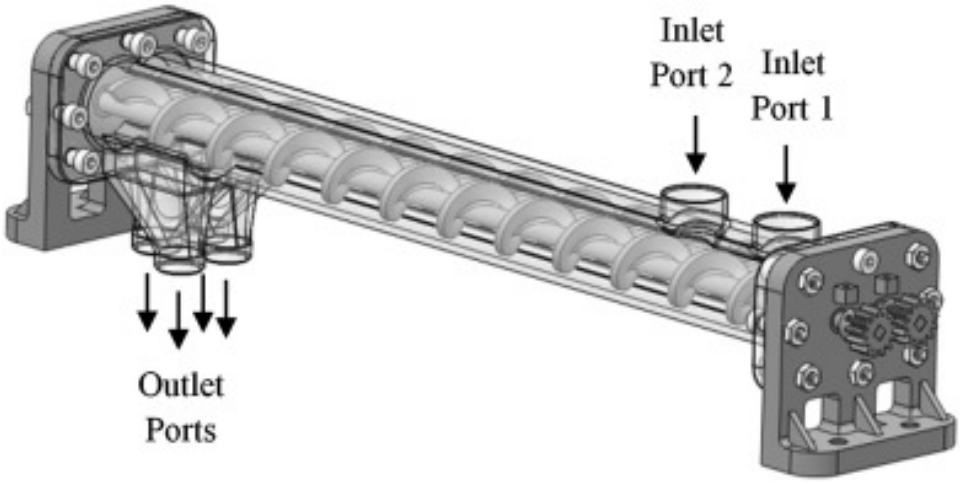

Figure 1.5: TSM used to perform granular mixing studies [6].

The first study sought [22] to analyse the changes in mixing efficiency in response to changes in screw rotation speed (either: 20, 40 or 60 RPM) and screw pitch (either: 1.91, 3.18 or 4.45 cm). The screws rotated using the co-rotational regime, and a 65% volumetric fill level was maintained throughout at a ratio of 10:1 mass flow rate of glass beads (ranging from 11.3 - 57.5 kg/hr) to red oak chips (ranging from 1.13 - 5.75 kg/hr).

The degree of mixing was ascertained by first formulating an empirical relationship between a

samples density and the mass fraction of red oak chips contained therein. Subsequently, four mass fraction values could be obtained per experiment, owing to the design of the outlet port. These values were inserted into Equation 1.2 to find the weighted composition variance.

$$s^2 = \frac{\sum_{i=1}^{i=n} m_i(x_i - \overline{x_w})^2}{(\frac{N-1}{N})\sum_{i=1}^{i=n} m_i} \tag{1.2}$$

Where: s^2 is the mass weighted composition variance, m_i is the mass of the i^{th} sample, x_i is the mass weighted composition of the i^{th} sample, $\overline{x_w}$ is the mass weighted mean composition of the samples and N is the total number of samples (in this case four).

Therefore, if the mass fraction of red oak chips contained within each sample was equal, this would represent perfect mixing and s^2 would be zero. Subsequently, during the investigation the lower the value of s^2 the better mixing had been accomplished within the binary granular system.

Whilst comparing the effect of process variable alteration upon the compositional variance, the best results were achieved using the mid-rotational speed of 40 RPM coupled with the largest screw pitch of 4.45 cm. The reason given for mid-screw speed being optimum was attributed to it being the best trade-off between how vigorously the material undergoes rotation (facilitating distributive mixing) and residence time (allowing the powder more time within the barrel to mix).

Larger screw pitch playing a key role in the mixing dynamics was concluded to be the consequence of increased granular rotational velocity (as well as larger screw pitch giving greater axial distance per revolution). This would appear to be a strange conclusion however, as it could be hypothesized that an increase in screw pitch would do more to increase the axial velocity rather than the rotational. Perhaps a more suitable explanation would be that a larger screw pitches were more adept at promoting back-mixing within each individual pitch section of the shafts length.

A visual inspection of the flow also displayed an inverse relationship between screw pitch and residence time. It is this author's opinion therefore, that as both larger pitch and faster revolutions decrease residence time, it suggests some fine tuning of the system may be accomplished through the adjustment of both factors in parallel. Optimising this arrangement to achieve the best mixing dynamics available however, is likely to be highly system dependent (being reliant on other factors such as: formulation, screw length and fill level etc.).

The second study [6] again sought to analyse the changes in mixing efficiency in response to changes in screw rotation speed (either: 20, 40 or 60 RPM) and screw pitch (either: 1.91, 3.18 or 4.45 cm). Also, as before, a 65% volumetric fill level was maintained throughout at a ratio of 10:1 mass flow rate of glass beads (ranging from 11.3 - 57.5 kg/hr) to red oak chips (ranging from 1.13 - 5.75 kg/hr).

This time however, the screws rotational direction was adjusted in order to examine either the: co-rotational, counter-rotational down-pumping or counter-rotational up-pumping (as displayed in Figure 1.3) regimes. The effects of changing the order in which the two granules were added, i.e. whether inlet port 1 was used to add glass beads and inlet port 2 to add oak chips and vice versa was also investigated (in the previous experiment red oak chips were always inserted via port 1 and glass beads via port 2).

The effect of rotation speed on the compositional variance varied greatly depending on: screw rotation regime, screw pitch and the order in which the particles were added to the system. For example, whilst using the smallest pitch screws (1.91 cm) during a co-rotating regime, the degree of mixing was found to decrease with screw speed. In contrast, for the counter-rotating down-pumping regime, best mixing for the largest pitch elements (4.45 cm) was achieved at the highest rotation rate. To complicate matters still further, whilst operating at medium screw speed adding oak chips first followed by glass beads maximised compositional variance (and thus decreased mixing).

The authors also noted that mixing became more efficient during the co-rotational regime as pitch was increased (in agreement with the findings of their previous study). However, the opposite was true for the counter-rotating up-pumping regime and pitch had hardly any influence at all for the counter-rotating down pumping regime (although mixing did improve slightly with an increase in pitch).

The most intriguing finding was that mixing was best accomplished under counter-rotational down-pumping conditions, whilst also being most consistent (discerned through repeat experimentation). This was attributed to the strong down-pumping action of the screw flights upon the less dense wood chip particles into the granular matrix, which meant their tendency to rise to the top and agglomerate through sedimentation happened less frequently, in comparison to the other rotational regimes.

The influence of material injection order was also examined visually and found to be extremely important at short distances from the injection ports. This effect became dampened however, as the material travelled axially downstream. The dampening phenomenon became most pronounced during the counter-rotating down pumping regime, which was put forward as another reason this regime facilitated superior mixing.

In 2015 [23] the same equipment was used to characterise material flow patterns via X-ray particle tracking, using an oak particle physically modified to act as a tracer. This was achieved by soaking the granule in potassium iodide solution, coating with silver paint, then adding a layer of

fingernail polish. Therefore, the modified particle became much more absorbent to radiation and contrasted sharply within the system whilst being monitored under X-ray stereography.

In this fashion the researchers were able to discern particle journeys both spatially and temporally during TSM operation. Particle velocities were also calculated via a simple derivation between adjacent particle positions with respect to time. The resolution of the system was given as $\pm$ 3.1 mm in 3D space and tracer readings were taken every 55 ms.

The study concluded that if constant: fill level, screw pitch and screw rotational regime were maintained, the path lengths travelled by the tracers remained remarkably similar, regardless of screw speed. This has been displayed within Figure 1.6, where the top schematic shows tracer data collated during counter-rotational down-pumping conditions, whilst the screws operated at 60 RPM. Whereas, the bottom part of the schematic displays tracer readings within a similar system, except this time the screws are rotating at 20 RPM.

Within Figure 1.6 the y axis denotes the axial direction from TSM inlet to outlet, the x axis denotes the horizontal plane as viewed from the front of the TSM and the z axis denotes the vertical plane as viewed from the front of the TSM. Transverse speed denotes the two dimensional particle velocity at position y, within the x vs. y plane. The axial speed on the other hand denotes one dimensional particle velocity in the y direct at position y.

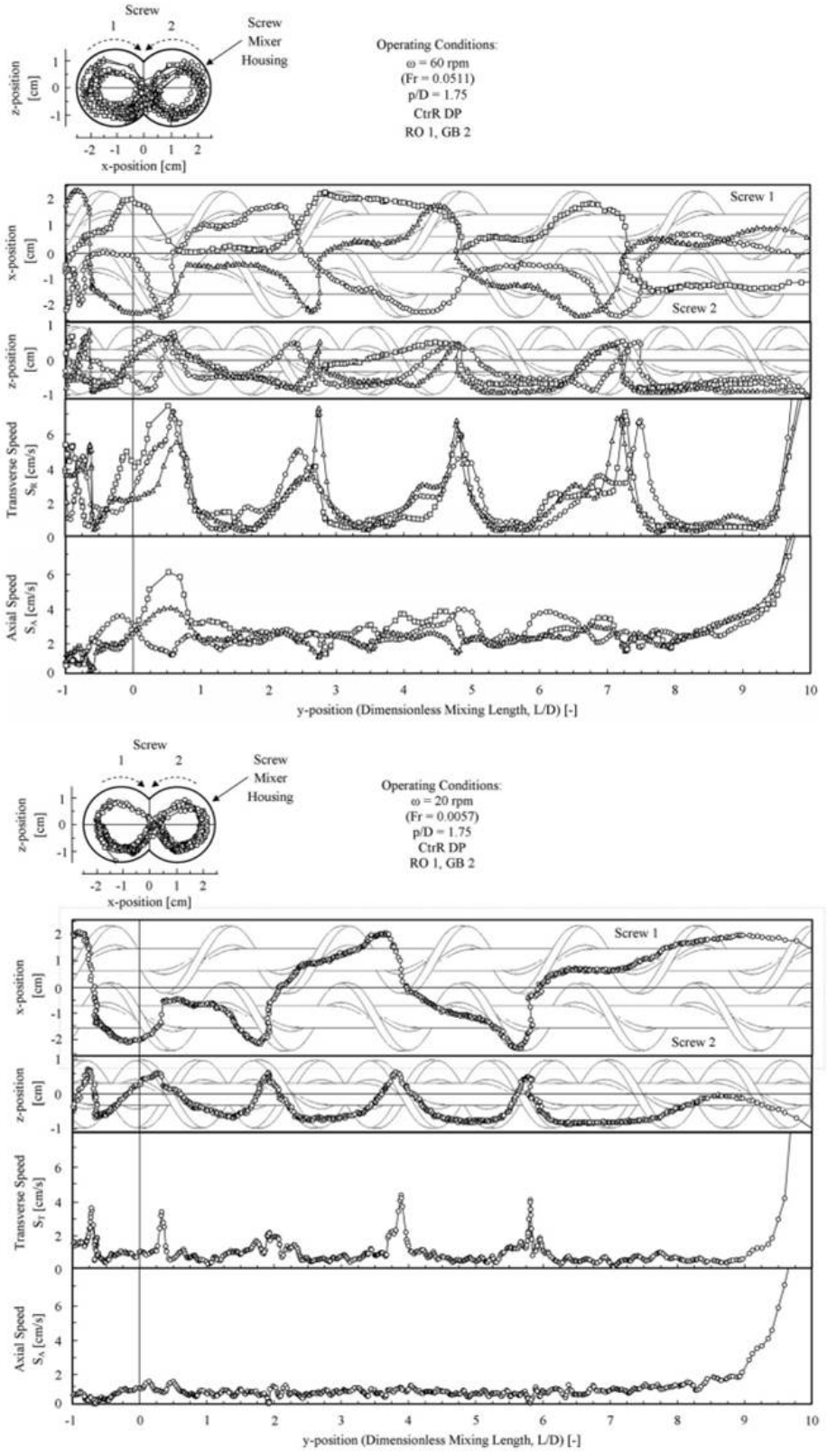

Figure 1.6: (Top) X-ray tracking position and speed profiles for 3 particle tracers travelling within the counter-rotating, down-pumping, 60 RPM operating regime. (Bottom) X-ray tracking position and speed profile of 1 particle tracer travelling within the counter-rotating, down-pumping, 20 RPM operating regime [23].

The authors also noted that in the counter-rotational down-pumping regime the tracer particles translated between screws several times before leaving the mixer. The particle positional data also displayed peaks in the z direction, as particles were lifted by the screw flights. These events were accompanied by sharp peaks in the x direction, towards the central point above and between the two screws (in a manner matching flight movement).

The axial velocity was said to be fairly constant as the tracer flowed downstream, until approaching the outlet. Here, the mixture became more free flowing as it poured out through the discharge ports under the influence of gravity. Another flow phenomena was noted as granules entered the system through the injection ports, causing the particles to behave differently at the start. Thus, the researchers identified three separate flow regimes namely: granules entering the system, flow within the main body of the TSM and granules exiting the system. These three flow regimes were noted to some degree within all screw rotational directions investigated.

As mentioned previously, the biggest changes were discerned after altering the rotational direction of the screws. The co-rotating regime and the counter-rotating up-pumping regime (with the counter-rotating up-pumping regime being displayed as Figure 1.7) revealed shorter flow path lengths being travelled and smaller residence times whilst being compared to the counter-rotating down-pumping regime. This was attributed to the tracer being more commonly passed between screws in the latters case, and so therefore undergoing a longer journey. The particle being passed between screws was the primary reason put forward for why work completed within Professor Heindel's group [22, 6, 23, 24, 25] always concluded the counter-rotational down-pumping regime exhibited the best mixing [23].

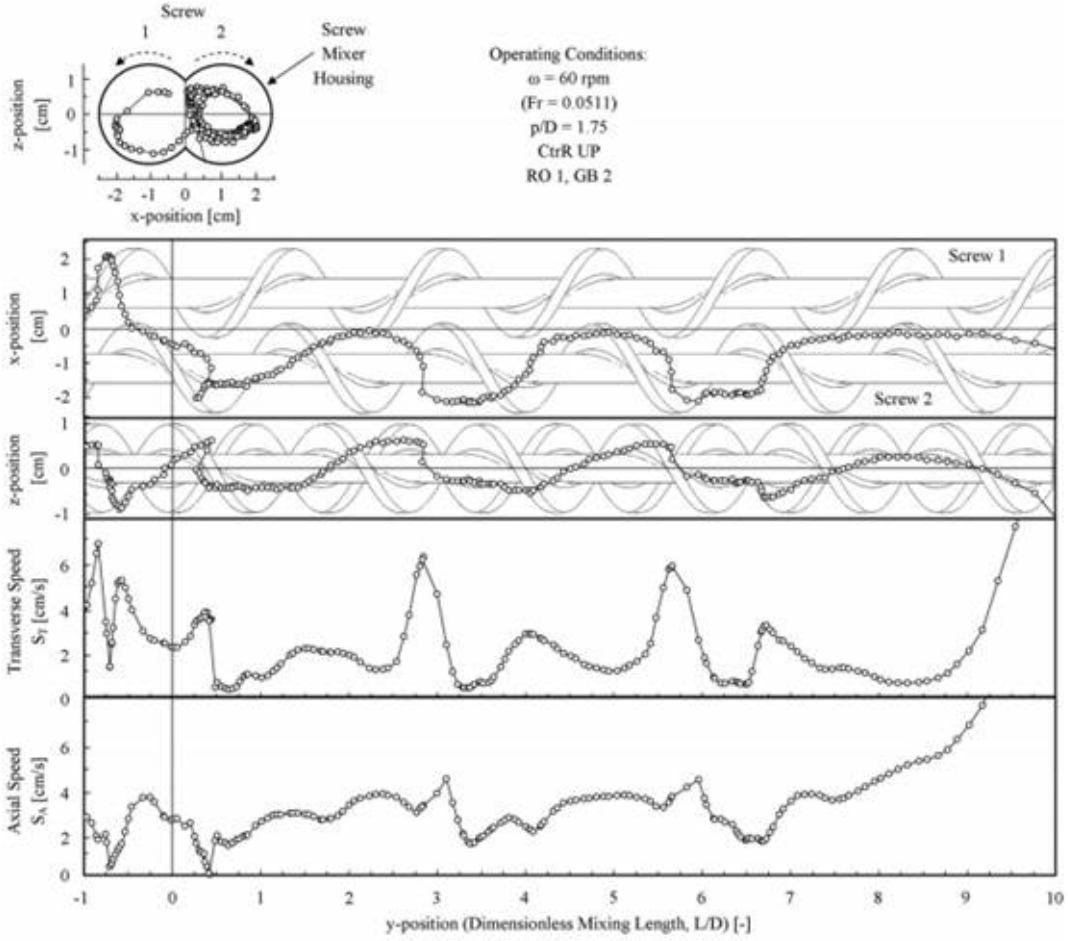

Figure 1.7: X-ray tracking position and speed profiles within a counter-rotating up pumping TSM [23].

In 2016 Marmur [24] built on the previous publications using the same equipment, but this time investigated the effects of varying granular size and density. The conclusions drawn were that the counter-rotational regime again achieved the best mixing results for every system examined.

Other interesting observations included: (1) reducing average particle size tended to greatly improve the mixing efficiencies for all screw rotation directions, and (2) mixing efficiencies were improved still further if the 2 types of particles used displayed similar densities [24].

The Discrete Element Method (DEM) was employed to model the same TSM in a paper published in 2017 [25]. The authors however, only simulated the counter-rotational down pumping regime. Within this study they ratified the expectation that screw speed in this regime has little influence on the degree of mixing as long as the fill volume remains constant [25].

This is an interesting point to note, as all previous TSM trials discussed maintained a static fill

volume of 65% by volume. The authors went on to assert that decreasing fill level by volume resulted in biomass particles separating out from the mixture's bed (via sedimentation effects), which they assumed was created by free space developing under the screw shafts.

Overall whilst this series of papers has shed some light on particle motion within the Twin-Screw regime, there is still much to be addressed. Not least, as is this reports intention, to look at the properties of powder flow (instead of biomass and glass beads) at the rate of hundreds of kg/hr, rather than tens of kg/hr. In fact, these changes in formulation and flow rate may create very different results to the ones discussed here. This is because as Bridgwater discussed in his 2012 [2] review, robust rules addressing flow do not exist for granular processes owing to their inherent complexity.

In summation nothing can be assumed or taken for granted with regard to granular flow behaviour within these complex machines. Therefore, whilst the knowledge gained through this discussion offers a useful basis in which to compare and contrast the results generated within this report, proceeding in a cautious meticulous fashion in an attempt to thoroughly characterise the basics of granular motion (within TSMs of this scale) was the approach adopted in this thesis.

1.4 Thesis Structure and Objectives

This thesis contains details of research undertaken in partial fulfilment of the Engineering Doctorate (EngD) award in Chemical Engineering from Newcastle University, in collaboration with Procter & Gamble (P&G). Therefore, the investigation needed to align with the companies interests, whilst simultaneously being of suitable academic rigour. Each subsequent chapter will now be summarised in terms of its benefit to P&G, as well as the contribution to academic literature.

- Chapter 2: A literature review regarding twin-screw processing has been conducted. The review focussed mainly on TSE and TSG as these technologies represent the only twin-screw processes to have acquired a substantial publication history within academia. Subsequently, the review proved invaluable in allowing insight into methods and terminology used previously by researchers for developing twin-screw technology. This aided considerably in the experimental design that was ultimately adopted. The analysis also allowed a good basis for comparing and contrasting key findings relating to powder flow mechanics.

  Furthermore, of the two twin-screw regimes discussed in this section, it is TSG that has been most heavily addressed. This is because granulation of fine powder is one of the more

obvious procedures that may be conducted within a TSM, with the main difference between the two machines being the scales involved. TSG is also the subject of much scrutiny within industry for its pharmaceutical applications. Thus, sharing key findings from the review with industry directly addressed one of the main objectives of the AMSCI (a large financial contributor to the project), i.e. to open up new markets for particle based products manufactured in existing UK plants.

- Chapter 3: This Chapter outlines the materials and methods utilised during the investigation.

- Chapter 4: The results of this chapter include validation for measuring a granular RTD via an in-line DIP algorithm. This will not only be an academically novel use of DIP, as it is the first time this method has been conducted on a granular flow, but may also be utilised by P&G to accurately and quickly measure the critical RTD index across a range of continuous powder processes.

  Key metrics gained from the RTD results have also been analysed using statistical Response Surface Models. These models formed the basis of an investigation into powder flow, whilst also being highly desirable to P&G in terms of planning future experiments, and proving the concept of using them within an advanced process control strategy. A Tanks-in-Series model investigation has also been conducted to further assess axial flow.

- Chapter 5: The TSM has been analysed via the advanced diagnostic technique PEPT. Detailed knowledge of how individual particles behave is highly desirable in terms of further process development. It is also the first time a TSM has been monitored using the technique at such large scales.

- Chapter 6: By examining a geometrically similar, but larger, TSM with the techniques pioneered in Chapter 4, an insight into how powder motion alters during scale-up can be investigated. This is one of the most important things to address, as even though these machines are large by the standards of twin-screw processing discussed in previous Chapters, they not as large as the company would need for full scale operations. An investigation into a change in internal geometry has also been conducted. It is easy to see how these findings will be of equal interest to the academic community.

- Chapter 7: presents a summary of the key findings within this thesis.

- Chapter 8: This Chapter gives suggestions in regards to how research should proceed in order establish the technology as a viable option for full manufacture.

Chapter 2

Literature Review

2.1 Granulation

Granulation is the process where fine powders are agglomerated together to form larger permanent/ semi-permanent aggregates known as granules. The procedure is also often referred to as: agglomeration, pelletisation or balling. A particular subset of granulation, known as 'wet granulation', is where liquid binder is (usually) sprayed onto a bed of agitated particulates. This creates a combination of capillary and viscous forces causing particles to coalesce. Further sintering or drying methods may be subsequently applied in order to create more permanent interstitial bonding within the granules [1]. Intuitively, the choice of binder is dependent on the temperature of the process and the final product requirements [26].

Wet granulation may also refer to procedures in which particle augmentation is no longer governed via agglomeration phenomena, instead growth is achieved through a layering effect caused by the addition of: a melt, solution or slurry; which coats the surface of seeded particles. Once coated, the additional layer proceeds to solidify or crystallise to form an 'onion skin' effect [1]. This review will not seek to address these particular techniques, instead it will confine itself to particle growth methodologies dominated by breakage and agglomeration mechanisms.

In essence granulation is an example of particle design that seeks to improve the inherent physical characteristics of the primary particulates, these include: flowability, which aids in precise measurement and handling of the product; reduced dust formation, which decreases: loss, inhalation and explosion risks and increased end product homogeneity [1, 27].

In order to fully realise these physical improvements 2 output parameters usually must be kept under stringent control, these being: (1) the Particle Size Distribution (PSD), which must be kept very narrow, and (2) particle homogeneity, which must be kept very high. This is especially true within pharmaceutical applications, as any variability in active ingredient concentration could lead to safety concerns.

This inflexibility of the product's output requirements can result in even slight disturbances within the particle processing environment leading to an unacceptable deviation from set point [28, 27]. High sensitivity to ambient conditions is further exacerbated by the complex array of underlying physical phenomena taking place during the granulation procedure [29].

Granulation processes are big business. The technique has been practised for decades in its modern form; within an ever increasing array of applications. Some of these include: pharmaceuticals (as mentioned previously), fertilizers, food processing, minerals and detergents [30, 31, 32]. In fact, to give some sense of scale, the report written by Iveson and Litster in 2001 [1] disclosed that 60% of products in the chemical industry alone undergo some form of agglomeration; with a further 20% of products using agglomerated powders within the ingredients.

Around the turn of the 21st century the process of wet granulation was commonly thought to be inadequately understood. This was because the fabrication of control systems and scale-up methods for the technique were largely driven via heuristics, rather than by any great understanding of the process. This state of affairs was assumed largely responsible for the high inefficiencies incurred whilst carrying out the procedure. Thus, poor recycle ratios, in the region of 2-6:1 recycle/product, was seen as a routine occurrence [33, 1, 34].

Today, there seems to be little change in the commercial sector with regards to the fabrication and control of granulation processes, as the heuristic approach remains the industry staple [26, 35]. As a result, many processes are still deemed to be operating far from optimally. This is despite a significant amount of research being completed on the subject; driven by the substantial economic incentive [28, 32, 36].

As granulation techniques are usually not underpinned through scientific understanding, Towler and Sinnott surmised in 2013 [26] that the process was still not well understood. As mentioned previously, this was a view shared by many at the beginning of the new millennium, and would seem to be at odds with the notion that much research and development had taken place since.

However, Cameron and Wang writing in 2007 [37] offer what seems to be a reasonable explanation for the prevalence of heuristic methods being adopted in industry. They assert that whilst the study of particle technology has been covered extensively on the macro-scale (unit operation level) and the micro–scale (particle level), there is still much to be addressed within intermediate stages, such as the granular scale and granular bed scale. It was theorised that by adopting a 'multi-scale' approach, the various regimes associated with granulation may be adequately modelled and subsequently linked together within a suitable systems framework. Figure 2.1 displays the various process length scales that were identified.

The same article concluded that by developing an advanced control system, for an already established well operated process, a 5% benefit in turnover costs could routinely be delivered, or better if currently operating under a poor control scheme [37].

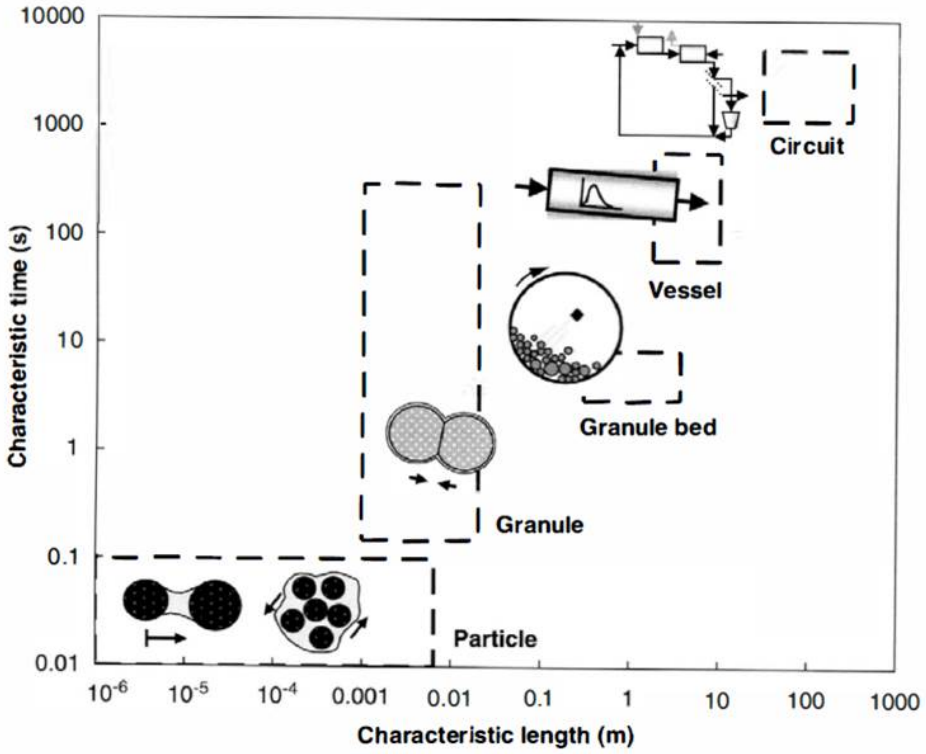

Figure 2.1: Scale map for granulation processes [37].

Many authors since have agreed with Cameron and Wang's [37] assertion that the problem needs to be addressed at multiple levels of scale in order to construct suitably accurate process simulations. A popular example of this approach being applied within literature is the Population Balance Model (PBM). This technique uses kernels developed from microscopic properties, such as the material's kinetics and thermodynamic parameters, together with macroscopic properties, such as: mixer geometry, temperature and shear forces, to describe properties on the mesoscopic scale, such as particle porosity and the PSD [29, 38, 39].

Whilst using PBMs to try and model granulation is nothing new, Poon et al. argued in 2009 [32] that only since recent advances in modern computer technology have they become a viable proposition. This is because of their inherent complexity when trying to incorporate all the necessary phenomena to adequately describe the system.

It is perhaps reasonable for Poon et al. to reach this conclusion [32], as computer processing power has increased dramatically within the past few decades and therefore solutions for complex equa-

tions can be achieved in a more timely and cost effective fashion, as would be needed for an effective process control scheme. It also means that the potential to fabricate and solve ever more complex simulations, using PBMs (or indeed other simulation techniques such as DEM), have become more accessible to the research community at large. Therefore, progress for arriving at a suitably complex system framework, able to adequately describe the granulation process, could be advanced more rapidly.

Batchwise wet granulation techniques have been used extensively over the last few decades. However, development of continuous granulation equipment has been the subject of much research due to the inherent advantages associated with this operating within this regime. These include increased automation leading to a reduction in labour costs, as well as a reduction in batch to batch variability and processing time [40].

Twin-Screw Extruders (TSEs) commonly utilised within the polymer and food sectors have recently become the subject of much interest within the pharmaceutical industry. This is due to their inherent mixing ability, allowing them to continuously process fine powders into larger agglomerates. When utilised in this fashion they have begun to be referred to as TSGs. TSGs have been noted as displaying significant advantages over other continuous granulation techniques such as fluidised bed and continuous high-shear. These advantages include: equipment design flexibility, shorter residence times, a wider range of throughputs and intimate mixing of formulation ingredients [3]. They are also self-cleaning, as the entire surface of the screw and barrel are continuously scraped by the screws, thus saving on cleaning time and allowing up to 24 hour production [41].

This Chapter contains a comprehensive review of twin-screw extrusion technology in regards to granulation. Twin-screw technology being utilised for this purpose has recently received a vast degree of attention, which has led to a large body of work being assembled in a relatively short space of time. Therefore, knowledge of key findings and development methodology for these machines is an invaluable commodity for this study, due to Twin-Screw mixing being a far less developed yet closely related discipline. Furthermore, utilising TSMs for large scale granulation processes is one of their more obvious applications, which adds further relevance to the knowledge collated and analysed within Chapter 2.

2.2 Twin-Screw Extrusion (TSE)

In order to obtain a greater understanding of how environmental factors and system geometry may contribute to particle mixing and agglomeration within TSGs (and so subsequently TSMs), a review of viscous fluids and solids blending within TSEs has been undertaken. Twin-screw extrusion is a similar, yet even more mature and developed discipline, than twin-screw granulation, and so may offer greater insight into the various internal operating regimes that all matter may experience during operations.

In 1980, an interesting paper was published by Booy [42], who asserted that to truly understand flow within TSEs, first a detailed examination of the internal geometry was deemed necessary. The author asserted that for simplicity, as had earlier been the case when developing single-screw extrusion models based on system geometry, an in depth analysis should commence by first addressing the isothermal flow of incompressible, Newtonian fluids, within the twin-screw operating regime. Subsequently, the author stated that the models could later be modified to include: temperature, pressure and non-Newtonian effects.

Figure 2.2 shows a cross section of two symmetrical double-flighted intermeshing conveying elements. The cross section was divided into two separate zones in which process fluid may longitudinally flow toward the die, these being: (1) the intermeshing area where the flights of the screws come together, which was referred to as the 'nip zone', and (2) the remaining annular free space. Subsequently, mechanical models for the two sections were constructed in order to predict both regions individual contributions to overall fluid flow rate.

In Figure 2.2, the nip region has been represented as a parallelogram; with points labelled O_1SO_2T. The average free area for fluid flow was calculated using the cross sectional geometry and how this changed with respect to rate of screw rotation. It was assumed that for a full screw revolution, the fluid was transported axially within the nip region at a rate equal to the lead of the screw thread. To determine the overall axial flow rate of fluid in the annular spaces, an equation was developed that utilised the 2 opposing parameters of: (1) forward drag pressure, and (2) back pressure, which were calculated using values relating to system geometry and fluid viscosity. For this reason it was surmised that material flow in the nip region would be more rapid than within the annular spaces.

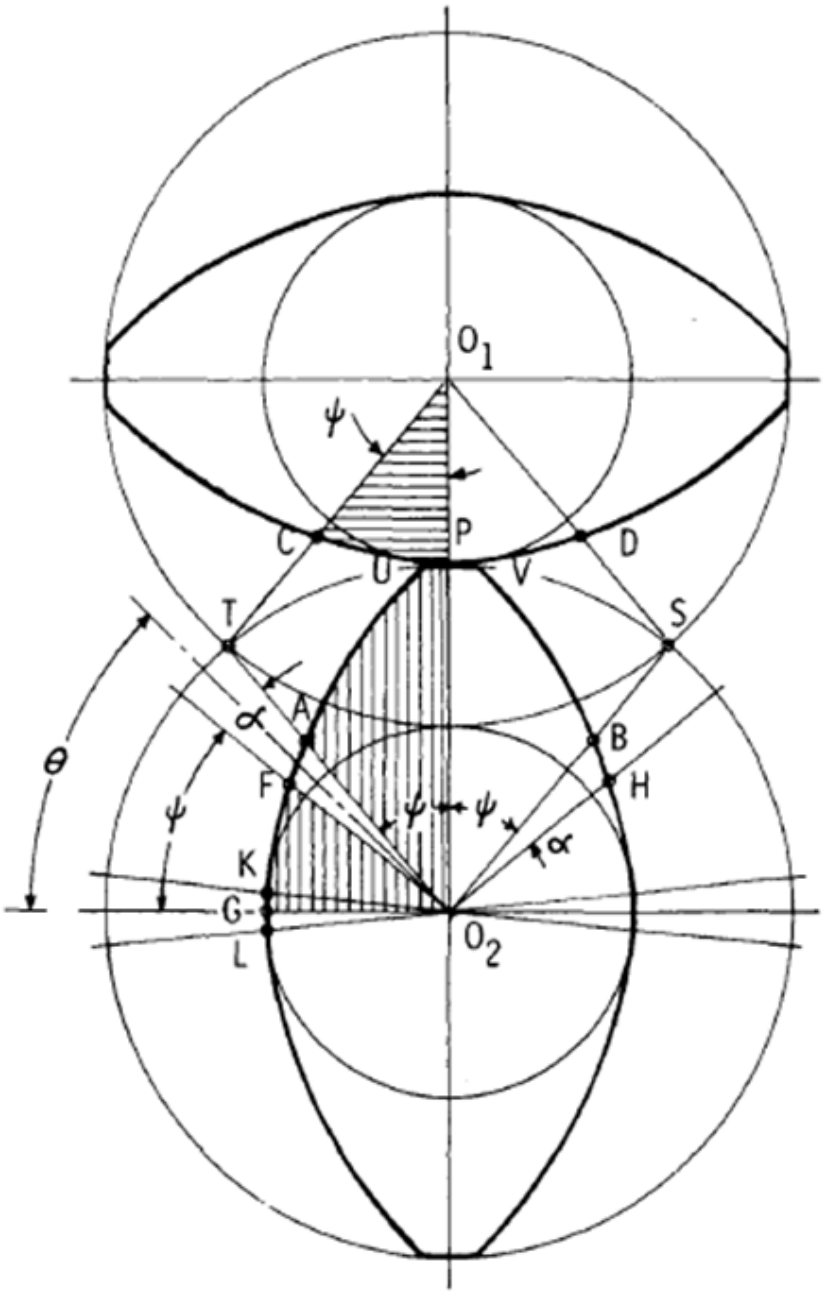

Figure 2.2: Free cross section within nip zone O_1SO_2T [42].

Bakalis and Karwe expanded on Booy's work in 2002 [43], by attempting to prove analytically the flow rate within the nip region. The experimental equipment was assembled to mimic the conditions laid out in the latter publication for 2 different screw rotational speeds (60 and 120 RPM). The annular space area was referred to throughout the publication as the 'translational region'.

A four-beam 300 mW argon-ion Laser Doppler Anemometry (LDA) system recorded the velocity data of the fluid within each of the two flow regions; and an encoder was employed to keep track

of the angular position of the screw root. Figure 2.3 displays the two regions that were tracked as a top view and a cross sectional view; analogous to the cross sectional view displayed in Figure 2.2.

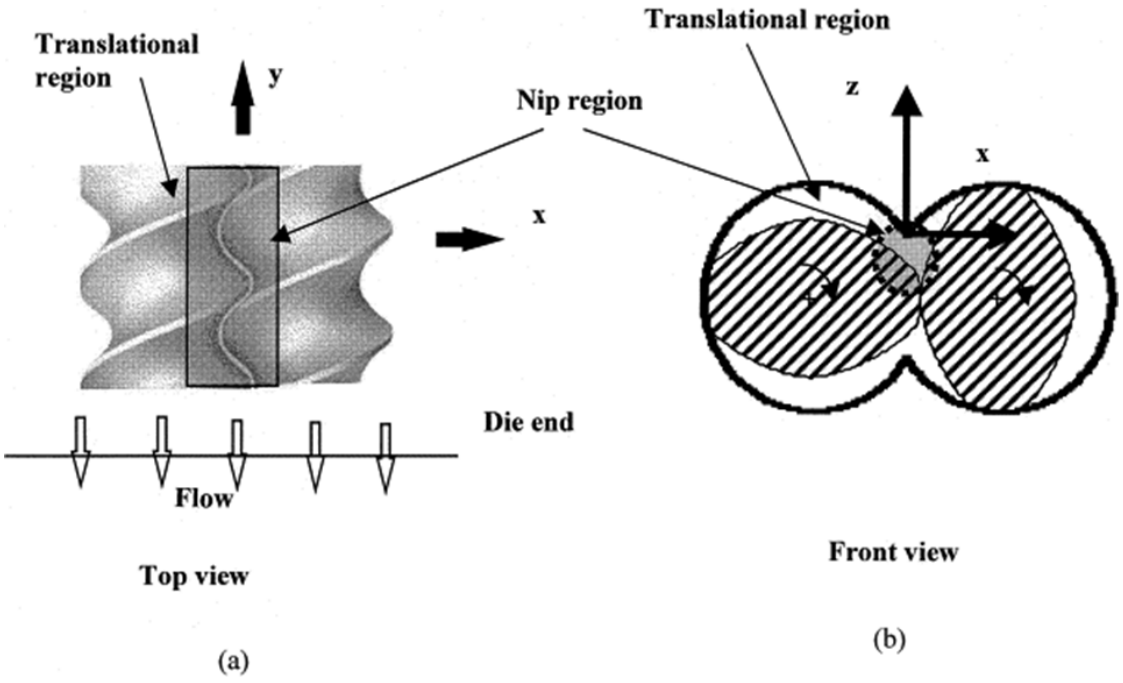

Figure 2.3: (a) Shows a top view of the screws and (b) is a cross sectional view of the same screws [43].

A co-rotating intermeshing TSE was employed for the investigation, with L/D ratio of 9.7; where L=300 mm and D=30.85 mm. The screws were composed entirely of 28 mm pitch double-flighted conveying elements, and fully filled with fluid. The fluid examined was corn syrup, a Newtonian fluid of 1400 kg/m^3 density, a 1.49 refractive index and shear viscosity of 4.7 Pa.s at 30°C. The process was carried out in isothermal conditions at 30°C.

Using the experimental data, Bakalis and Karwe [43] were able to identify Booy's [42] proposed nip region, and reveal the flow as being around 3.8 times higher than the flow within the translational region. It was thus claimed that a clear indication was given of the positive displacement effect that Booy had previously identified. However, whilst the analytical flow rate in the nip region compared well with that of the theoretical flow rate calculated using Booy's equation, 2.41×10^{-6} m^3/s and 2.12×10^{-6} m^3/s respectively, the nip region was much less uniform, and larger, than the parallelogram predicted (displayed in Figure 2.2).

The flow in the nip region was described as being similar in appearance to that observed from a positive displacement pump, with the material being pushed towards the die. This was predicted

by Booy, with both publications postulating it being caused by the phase difference in the angular positions of the two screw lobes. Additionally, the authors also noted a wide distribution of velocity values in the translational region, which were all considerably lower in magnitude than in the nip region (around 3.8 times lower). The flow discovered in the translational region was considered to be the result of a combination of drag and pressure effects.

It is clear from the work completed by Bakalis and Karwe [43] that Booy's [42] assumption that, due to the positive displacement pump action in the nip zone, fluid is transported axially at a rate roughly equivalent to one screw lead for a complete rotation (at least when the pitch is filled with the Newtonian fluid under investigation). However, the geometrical calculations developed by Booy have been shown to be too simplistic to accurately model flow within an extruder; as the nip region identified by experiment was much larger than predicted (and velocity profiles in the translational region were far more complex).

This indicates that large flow velocities within the nip must in some fashion be responsible for large flow velocities in small parts of the translational region. Subsequently, this too may also be a function of the figure of 8 flow pattern observed within the bulk, as liquid is passed between the lobes (which many authors conclude is the usual mode of mass transport within co-rotational intermeshing extruders), the specific fluid/powder being processed and the degree of channel fill. Therefore, dividing the model into two separate zones may turn out to be a gross over-simplification, when seeking to adequately describe a TSE's internal flow phenomena.

In 1999, Carneiro et al. [44] conducted an investigation using an intermeshing co-rotating Leistritz LSM 30.34 twin-screw extruder, with a transparent 40 cm long barrel. An L/D ratio of 29 was used for the screws and temperatures were reported as being typical for a polymer melt operation; but not included. The investigation used silicon oil as the extrudant, which is a Newtonian fluid of 1000 Pa.s viscosity, also thought to be in the usual range for polymer melts. Once steady state had been achieved, a yellow ink tracer was injected at the entrance of the extruder and the flow patterns were subsequently monitored using a conventional video recorder under indirect artificial light [44].

The screw profiles for the series of experiments conducted utilised the same upstream and downstream double-flighted transport elements, whilst varying the geometry of a central kneading block, which was usually followed by a reverse conveying element. An individual conveying element used within the system was either: 20, 30 or 45 mm in pitch; and was of: 30, 60 or 120 mm in length respectively.

A kneading block is a series of bi-lobal discs (as displayed in Figure 2.8, geometrically defined by

their staggering angle with relation to the adjacent disc. A positive conveying effect was thought to be created for positively staggered angles at +30° and +60°, due to the geometrical effect of creating a discontinuous right hand helix screw flight, and a neutral/no conveying effect was expected for +90° staggered angles. A negative conveying effect was expected for negatively staggered angles at -60° and -30°, as this gave the effect of a discontinuous left hand helix screw flight. Figure 2.4 displays the basic screw configuration, complete with the code for the modules used to construct the complete screw geometry.

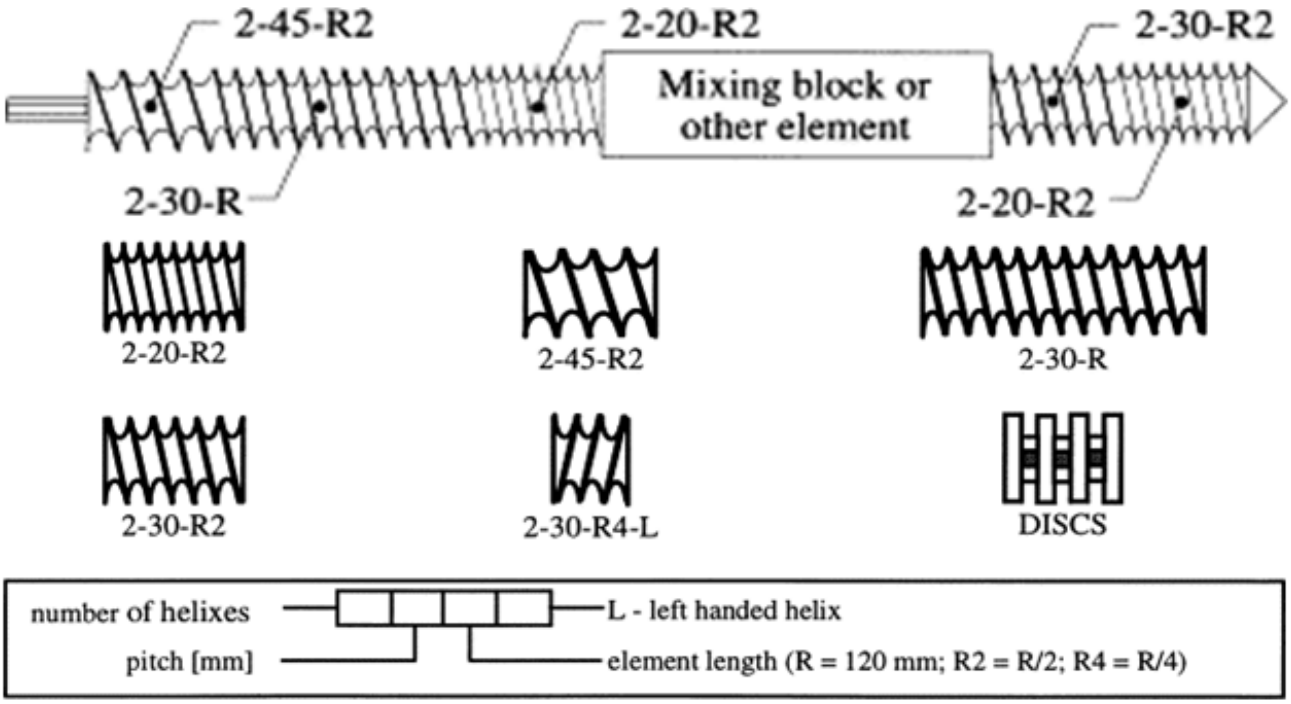

Figure 2.4: The basic screw configuration used in Carneiro et al. visualisation experiments and the module codes used to define the screw geometry [44].

The second half of the experiments carried out focussed on monitoring the RTD using equivalent extruder geometries to that of the first half of the investigation. During operations, pressure readings were logged using five melt-pressure transducers situated at various points along the barrel. A polypropylene extrusion grade (Borealis HB 121 J) was used as the throughput material, and the machine was operated at 150 RPM, with feed rates between 8 – 10 kg/hr. After feeding 10 g of a silica tracer through the hopper throat at the beginning of the experiment, collection points were used to determine tracer concentration via weight. The screw configuration, complete with the location of the collection ports and pressure transducers has been included as Figure 2.5.

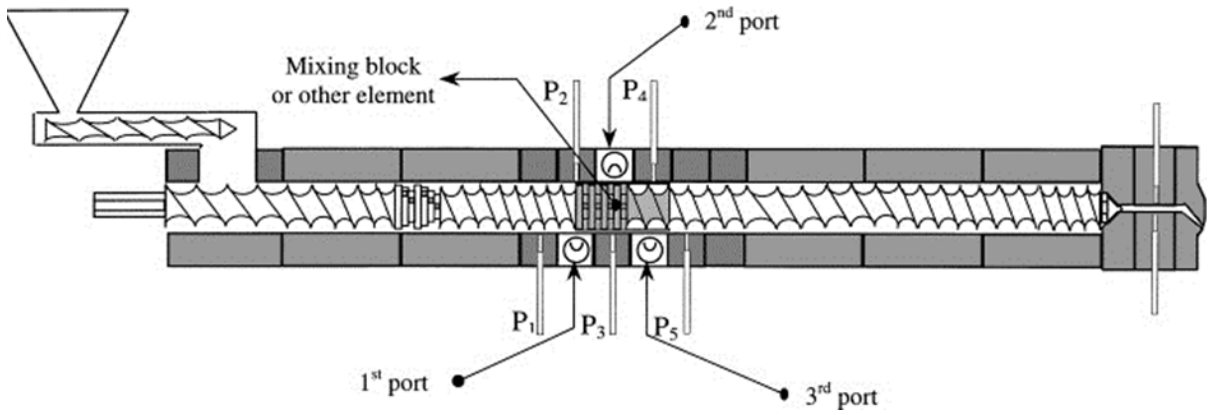

Figure 2.5: The basic screw configuration used in extrusion experiments and location of the collection ports and pressure transducers [44].

The average residence time and cumulative normalised residence time function was computed using Equations 2.1 and 2.2.

$$\boldsymbol{\tau} = \frac{\sum_0^t tC\Delta t}{\sum_0^\infty C\Delta t} \tag{2.1}$$

$$F(\theta) = \frac{\sum_0^t C\Delta t}{\sum_0^\infty C\Delta t} \tag{2.2}$$

Where: $\boldsymbol{\tau}$ is the mean residence time, $F(\theta)$ is the cumulative normalised residence time function, C is the concentration of tracer, Δt is the time interval and θ is the normalised time ($\theta = t/\boldsymbol{\tau}$).

During the visualisation studies, the flow patterns and flow time were found to be highly dependent on the staggering angle of the discs. The time required for the tracer to reach the kneading block module, then flow across the kneading block module, was also recorded and discussed at length.

A figure of 8 tracer flow pattern was observed visually for conventional positive conveying screw elements, this ratified the authors (and many others) expectations of fluid flowing helically across the screws towards the die. The observation may serve as a good indication of how the bulk material flows between the screws. However, to discern flow properties within interesting areas such as the central nip zone, more complex recording equipment such as that employed by Bakalis et al. [43] would be needed.

When the feed rate was kept constant, and the kneading elements set in a neutrally conveying +90° configuration, it was discovered that flow time from the extruder entrance to the mixing

module was inversely proportional to an increase in screw revolution speed. However, once the fluid reached the kneading elements the time taken for the liquid to traverse the geometry, for any given feed rate, did not seem to decrease significantly with lowering the rate of revolution.

The publication decided these findings may be due to screw revolution speed being independent of pressure generation and thus, also independent of inducing drag flow across the mixing block. However, this may also imply that the screws were fully filled within the kneading block throughout all of the trials. This is because residence time is a function of the volume, divided by volumetric flow rate. This means that if the volumetric flow rate was always equal to the kneading zone volume then the residence time would also remain unchanged.

Increasing the feed rate under constant screw revolution speed led to a decrease in the time taken for fluid to reach the mixing block. A probable reason for this was that by increasing the fluid-barrel contact area, more efficient axial transport was experienced.

The increase in the time taken for fluid to traverse the mixing block, for analogous experiments, always increased with the number of discs inserted, although not in a linear fashion. This was proposed as being a consequence of the drag force required for flow to commence over the block increasing with each kneading disc addition (although it may also be the result of the increase in material needed to to fully fill the zone as mentioned previously). This was intuitive, however, the non-linear nature suggests that by adding discs the flow patterns became ever more complex.

The authors also noted that when the kneading block geometry consisted of neutral conveying elements, not coupled with a reverse conveying block, a slight positive pressure gradient developed between P1 and P2 (displayed in figure 2.5). It was postulated that this created the drag pressure necessary to induce flow across the block. Subsequently, this was followed by a slight negative gradient between P2 and P3. For positive kneading block geometries, with no subsequent reverse conveying elements, no pressure gradients were observed.

On the other hand, once a negative kneading element arrangement had been incorporated (without a reverse element), an even greater pressure gradient was recorded between P1 and P2, which in turn was able to overcome the negative resistance and create forward drag flow. Intuitively, this was also followed by a negative pressure gradient from P2 to P3. The effect also became much more pronounced when a reverse element was included for all mixing block geometries.

The experiments also revealed that as the staggering angle was increased from +30° to +60° and finally +90°, the time needed for tracer to cross the block became increasingly longer. The publication stated that this was the result of a kneading block resembling a pair of discontinuous conveying screws, which incorporated progressively smaller positive flow channels from +30° to

+60°, and that by +90° the discontinuous positive conveying effect was removed. A schematic of this geometry can be seen in Figure 2.6. The positive flow channel is labelled α, and is larger than the negative flow channel, β, at +60° . The opposite is true at -60°, whilst at +90° both channels are equal.

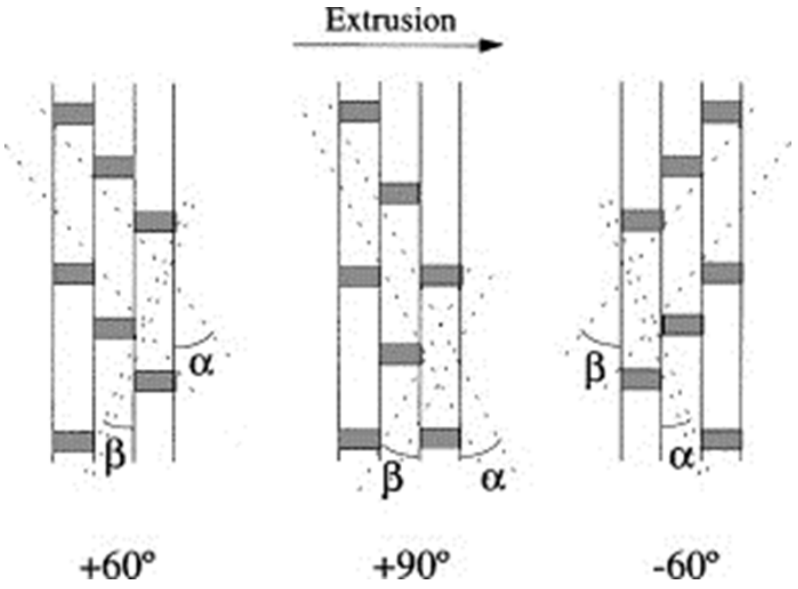

Figure 2.6: Flow channels defined by adjacent discs of a mixing block for different staggering angles [44].

This negative conveying action meant that at -60° configurations the tracer took longer to cross the kneading block than for the neutrally conveying +90°. However, at -30°, time time taken was equal to that of +60°. The reason given for tracer flow time at -30° being equal to +60° was that the -30° set-up had an inherently large carrying capacity within its respective α channels, so upstream pressure was able to rapidly overcome the negative conveyance effect. It is this author's opinion that it is highly unlikely that these opposing effects would balance themselves for every system, and would be dependent on system variables such as: temperature, material and screw speed etc. Nonetheless, it represents an interesting consideration whilst determining material residence time.

The RTD function was plotted for experiments where the mixing block was set at a staggering angle of +60° or +90° with no reverse conveying elements. Carneiro et al. [44] asserted that when the mixing block was set at neutral (+90°), overall axial mixing within the extruder displayed a reasonable approximation to plug flow type behaviour. This conclusion was arrived upon by obtaining a relatively steep sigmoidal curve when $F(\theta)$ was calculated from the tracer concentration in the fluid extruded from the die (which was also slightly steeper than the experiment at +60°). The authors decided this was a consequence of material accumulating upstream during drag flow

pressure generation leading to homologous tracer/fluid mixing during flow across the kneading block.

However, this may be a false conclusion as a slight gradient was obtained in the data, indicating some degree of axial mixing; although the gradient was steeper than for RTD graphs plotted from samples taken at previous sections from the same experiment (samples taken from ports 1-3 in figure 2.5) and at a +60° configuration. Furthermore, others have deduced axial mixing upon examination of RTD graphs whilst investigating systems containing kneading blocks, at both positive or negatively staggered angles, through measuring tracer concentrations taken from samples obtained at the die [45].

Therefore, it perhaps would have been useful to include a comparison of RTD graphs plotted from samples taken at the die whilst using a wider selection of mixing block geometries in order to fully support this conclusion, i.e. if a similar graph had been obtained for forward conveying kneading blocks at +30° staggering angle, or for forward conveying elements only, this would easily nullify the hypothesis.

As in the publication by Carneiro et al., [44] Gautam and Choudhury [45] also asserted that RTD graphs are an excellent indicator of axial mixing during extrusion processes. Furthermore, the authors revealed these graphs had been used to improve equipment design and scale-up since at least the 1970s. The power of the RTD graph was in using them to assess the effects of independent variables, such as: throughput, screw speed, moisture content and barrel temperature upon the extrusion process. Gautam and Choudhury [45] further corroborated Carneiro et al. [44] by revealing that the kneading elements can be utilised to influence these graphs though their inherent mixing properties.

During the experiments that were carried out, Gautam and Choudhury [45] calculated a normalised function, $E(\theta)$, unlike Carneiro et al. [44] however, they were not plotted cumulatively as $F(\theta)$. Therefore, they obtained unimodal curves rather than sigmoidal functions, with broadening and lowering of the curves peak demonstrating axial mixing. Throughout their experiments this effect was observed in response to adding flow restricting mixing elements to the extrusion geometry [45].

The investigation focussed on extruding rice flour within a Model BC 21, Clextrel, Firminy Cedex, intermeshing co-rotating twin-screw extruder. The barrel was 800 mm long, and bored with two 25 mm diameter holes. The screws were composed of conveying elements, reverse conveying elements and kneading blocks and had an overall L/D ratio of 32:1. A die was used, as with all extrusion processes, which had an orifice of 5 mm in diameter.

Thermal energy was also provided through 8 equally sized induction heaters (100 mm in length each) mounted externally to the barrel, which rose in temperature in the following progression: 0, 30, 30, 30, 70, 100, 150 and 150° C. The extruder was divided into a non-experimental (beginning at the feed) section and an experimental section (beginning at the non-experimental section and ending at the die).

The length and pitch of the conveying elements in the 600 mm non-experimental section were kept constant throughout the experiments and progressed from the feed in the following fashion: 50/50/3, 33.5/50/4, 25/50/3, 25/25/3 and 16/25/1, with the numbers representing pitch (mm), length (mm), and number of elements. The 200 mm experimental section consisted of a combination of: kneading blocks, forward conveying blocks or reverse conveying blocks, that were arranged in various configurations and positions along the barrel. The kneading elements of the blocks were orientated at +77 or -77° with respect to each other, in order to alter their overall conveying capacity in the forward or backward direction. Both conveying elements utilised had pitches of 16.6 mm and were of 25 or 50 mm in length.

Residence time was determined by measuring the electrical conductivity of the material in the die, after inserting a tracer prepared by mixing air dried rice flour with saturated $NaNO_3$ solution. The moisture content of the mixture was adjusted to 20 % (w/w) and the voltage across the material measured. A baseline voltage reading was recorded at steady state, without tracer, and was used to complete the calibration. From this, a relationship between voltage and concentration of tracer could be discerned.

The mean residence time, $\boldsymbol{\tau}$, and the cumulative residence time normalised function, $F(\theta)$, could be calculated using the same relationships found in Equations 2.1 and 2.2. Furthermore, the residence time function, $E(t)$, was also calculated using the relationship found in Equation 2.3 and plotted as the RTD.

$$E\left(t\right) = \frac{C}{\sum_{0}^{\infty} C\Delta t} \tag{2.3}$$

During the experiments the dimensionless Peclet number was also calculated as another method of measuring the extent of axial mixing. This number is equal to the reciprocal of the dispersion number, Da/uL, used to measure how much a material spreads out longitudinally as it travels through a tube, where: Da is the axial dispersion coefficient characterising the degree of back mixing during flow, m^2/s; u is the fluid flow rate, m/s; and L is the length of the entire vessel/screw, m. Using this metric, large values of Da equate to rapid spreading of material unilaterally. Thus, when Da is equal to zero, this equates to no unilateral spreading, i.e. plug flow has transpired. In essence

this is simply a method to gain a comparison in the magnitude of axial dispersion occurring between each experiment.

Diffusivity was calculated from the $E(t)$ curve using the relationship found in equation 2.4. This equation was derived by Levenspiel in 1972 [46], and stated that curve variance obtained during fluid flow, through a vessel with stagnant pockets, was a function of the dispersion number [46].

$$\sigma_\theta^2 = \frac{\sigma^2}{\boldsymbol{\tau^2}} = 2\frac{Da}{uL} - 2\left(\frac{Da}{uL}\right)^2\left(1 - e^{-uL/Da}\right) \tag{2.4}$$

Where: σ^2 is the variance of the $E(t)$ curve. This was determined using equation 2.5.

$$\sigma^2 = \frac{\sum_0^\infty t^2 C\Delta t}{\sum_0^\infty C\Delta t} - \boldsymbol{\tau^2} \tag{2.5}$$

During the experiments when no kneading elements were present, the mean residence time was 29.84 s rising to 41.7 s when a 25 mm long kneading block was placed at the die. This residence time increased further to 48.71 when a reverse screw element replaced the kneading block at a similar length and position. Incorporation of kneading blocks and reverse screw elements both lowered the height and increased the spread of the $E(t)$ curves, with the reverse screw elements having a more profound effect.

The material was subjected to increased temperatures from the heating elements as it flowed toward the die, and as such the viscosity decreased. Viscosity had an effect upon the resistance to flow through a kneading, or reverse screw element which meant the further upstream an element was placed, regardless of type, the more easily the extrudant was able to flow into the geometry and fill the channel.

Increasing the mixing element length from 25 to 50 mm increased the mean residence time considerably due to the higher degree of channel fill needed to develop enough pressure to create flow. Or perhaps more likely the increase in residence time was due to the increase in material now needed to fully fill the larger kneading zone. As mentioned previously, this is because residence time is a function of the systems volume divided by the volumetric flow rate. So increasing the kneading zone would be another way to increase residence time.

Again the kneading block had a milder effect than the reverse screw element. The Peclet number analysis further ratified these findings by discovering that a lower number was achieved (indicating better axial mixing) for reverse element screws over kneading blocks. Axial mixing was also found to be improved by increasing element length, as deduced by the dispersion number. Split-

ting a kneading block into two separately spaced entities had a similar effect as one long element for all the data [45].

In the work of Zuilichem et al., [47] the effects of altering mixing elements in single and twin-screw extruders were investigated. The authors asserted that mixing in all extruders occurs through 3 mechanisms, namely: (1) longitudinal/axial mixing, (2) dispersive or comminution of the disperse phase and (3) distributive mixing or radial mixing. If a particle is subjected to axial mixing, as demonstrated in the experiments by Gautam and Choudhury [45] and Carneiro et al., [44] this could be measured by alterations in the Residence Time Distribution (RTD), such as the broadening and shortening of the $E(\theta)$ functions peak. Therefore, in the extreme case of plug flow (when particles all have the same residence time), this is indicative of no axial mixing [47].

The authors [47] went further in their explanation into mixing mechanisms by stating that the second mechanism, dispersive mixing, was caused by the break-up of agglomerates within the disperse phase into smaller particles driven by extensional and shear stresses. Distributive mixing on the other hand was described as being caused by screw elements distributing the concentration of the disperse phase over the total volume of a chamber or channel so that each volumetric unit within a block becomes more homogeneous i.e. combating the effects of sedimentation.

Although the 3 mechanisms were described as being different, it was proposed that they could never be totally independent of each other. Designing screws that promoted certain types of mixing, or various combinations of the three, was seen as being important for designing an individual manufacturing process. In order to observe these operating principles in action, it was asserted that a model could be utilised to aid in further understanding of how changes in geometry may affect the finished product.

To model axial mixing, the authors [47] discussed a method where an RTD could be modelled using two parallel series of Continuously Stirred Tank Reactors (CSTR), used to represent the two screws of a twin screw extruder. This, they explained, had been carried out in a series of publications produced by the Wageningen research group in the late 1980's and early 1990's. A schematic of this model has been provided as figure 2.7.

In figure 2.7 the boxes represent the two parallel series of CSTRs which together represent the two screws of the extruder. In this system a number of leakage flows were identified that opposed the overall mass transport of material downstream. This includes the flows through the following gaps: calendar gaps, Q_{c}, the side gaps, Q_{s}, the flight gaps, Q_{f} and the tetrahedron-gaps, Q_{t}.

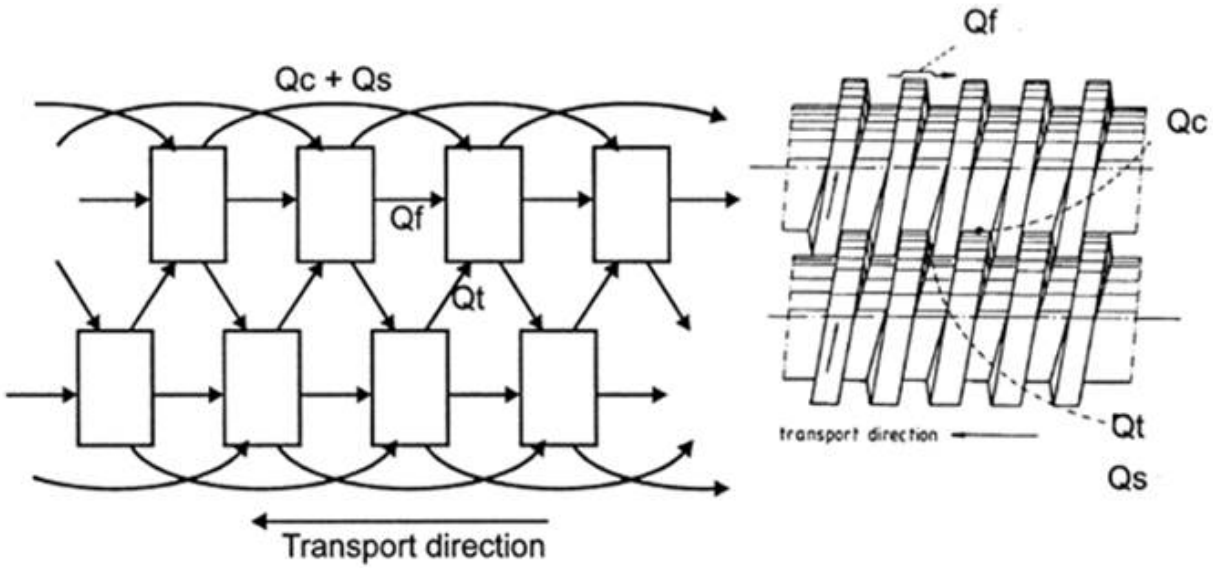

Figure 2.7: (Left) CSTR Model and actual leakage flows, Q_c, Q_s, Q_f and Q_t in a co-rotating TSE simulation. (Right) The TSE system the CSTR model with leakage flows is seeking to simulate [47].

However, Zuilichem et al. [47] proposed that RTD graphs produced by real data tended to be more asymmetrical than those produced using the method proposed by the Wageningen group. Thus, a model was discussed that had been produced by Jager et al. in 1988, which was described as producing a more accurate shape. This simulation imagined material flowing through a succession of CSTR's from feed port to die, where chamber volumes changed in size and each chamber lost some degree of material in the opposite direction [48].

Zuilichem et al. [47] went on to describe all RTD models to date as being calculated through one of three methods: (1) curve fitted exercises, such as using numerical methods to calculate a number of CSTRs in series; or (2) a more descriptive and/or predictive approach, with an example being given describing a Plug Flow Reactor (PFR) model, that incorporates axial mixing deduced from the Peclet number, or (3) a mixture of both [47]. The authors then recounted two models that could predict dispersive and distributive mixing, but conceded both mechanisms were highly dependent on the effects of shear so could not be examined fully independently.

According to Zuilichem et al., [47] RTD graphs are used to discern axial mixing within a TSE, which is mainly driven through screw rotation. However, as RTD is simply a probability distribution of the time material may spend within an extruder, they may also be able to capture some information regarding distributive and dispersive mixing as the three mixing mechanisms may

never be completely decoupled.

Thus, by considering how RTD function shapes may alter with differing: geometries, environmental factors and thermodynamic parameters, may lead to greater understanding of the mixing process as a whole. The knowledge gained could consequently be incorporated within other mechanical or analytical models, in order to predict characterisation properties of the product, such as: the PSD or the porosity of granules.

It is clear that the internal environment of a TSE is well understood in a very qualitative fashion. This has been demonstrated throughout literature, where there is general agreement with regards to the effects of altering: screw geometries, material types and environmental factors (such as temperature), upon the final products characterisation. This includes interesting phenomena with regards to the nip region, as well as the various modes of mixing driven by screw elements such as: the kneading block and reverse screw elements.

However, the flow regimes within these machines are clearly very complex, with attempts to develop scale-up rules based on geometric models undoubtedly being a very difficult task to accomplish. What may prove more useful is utilising the qualitative knowledge when deciphering changes in the RTD function in a more quantitative fashion. These graphs are easily obtainable for the equipment, which will greatly aid in this pursuit. Finally, once this has been achieved, investigations into developing RTD models, such as a Tanks-in-Series model, able to directly relate system features to function shape could prove invaluable for more easily developing models for scale-up and control purposes.

2.3 Twin-Screw Granulation (TSG)

In a review published by Thompson in 2015 [49] it was established that, for well over half a century, the food and plastics industries have been by far the largest contributors to the Research and Development (R&D) of various single- and twin-screw extrusion technologies. It was revealed that the technique has been widely utilised due to its inherent mixing properties, whilst simultaneously conveying material axially along the screw/s. A common application of this technique involves the melt and mix of viscous fluids and/or solid particles in order to form a homogeneous melt. Pellets are subsequently formed through a pressurised expulsion of the product though a die situated at the end of the extruder's barrel [49].

The history of extrusion asserted by Thompson [49] was further ratified by Djuric and Kleineb-

udde [21], who established within a piece published in 2008 that the technique has been performed within the plastics industry since the 1950s. The article went on to declare that the process, due to the inherent modularity of the internal screw geometry, has led to the common procedure of consecutive adjustments being applied to the configuration until product is produced displaying the desired characteristics [21]. As a result of its long history, it is now commonly accepted that extrusion is able to deliver consistent and repeatable high-quality end product, within what has become the two core sectors of food and polymer manufacture [4].

In addition, extruders have also been investigated for other particulate processing operations such as the granulation of munitions powder. However, most of the more recent research into extrusion technology has largely been driven from within the pharmaceutical sector for the purposes of creating sophisticated dosage forms of Active Pharmaceutical Ingredients (APIs) blended with excipient [49].

Pharmaceutical production is dominated by processes that operate within a batchwise regime; largely propagated within the industry by two widely held beliefs, namely: (1) that continuous operations cannot hope to match the flexibility offered by batch processes, where procedural alterations are routinely applied in response to changing demand for low quantities of expensive product; and (2) more easily fulfilling the rigorous requirements made by regulatory authorities with regard to historically profiling the environment in which all materials used within drug manufacture have been subjected.

With respect to the latter however, the industry has become increasingly more disposed to continuous operation, after the concepts of Quality by Design (QbD) and Process Analytical Technology (PAT) were introduced by the Food and Drug Administration (FDA) in 2003 [50]. Furthermore, continuous twin-screw manufacturing in particular would seem to neatly address the former concern, as it offers a similar level of flexibility owing to the machines inherently modular design. A system alteration therefore, becomes a relatively simple and rapid endeavour.

Consequently, if sufficient research is conducted in order to provide a robust proof of concept, the adoption of twin-screw technology in place of batch techniques could allow the industry to enjoy numerous benefits. As mentioned within Section 1.3 these include: reduced labour costs, less batch to batch variability and shorter processing times. Additionally, assuming that PAT and QbD methodology has led to a well understood process (as is its purpose), continuous processing has the further advantage of eliminating the need to discard entire batches of material, as a result of unacceptable deviations incurred by the process variables.

The earliest paper to examine extrusion for pharmaceutical purposes was written by Gamlen and

Eardley in 1986 [51]. The authors studied the effects of formulation parameters upon single-screw extrusion of paracetamol extrudates [51]. This was followed by Lindberg et al., [52, 53, 54] who produced a series of papers seeking to characterise the process of effervescent granulation via twin-screw extrusion. These early papers mainly focussed on the mean residence time of the material and the influence of process parameters on the granular porosity and liquid saturation point [52, 53, 54].

The Lindberg et al. publications [52, 53, 54], along with most of the early work on pharmaceutical TSE granulation that was completed subsequently, involved the use of a die plate situated at the outlet of the appliance as is common during spheronisation. The result was the densification of the output material leading to larger agglomerates being formed, thought to be a direct consequence of the increased pressure that material experiences as it is expelled through the orifice [3].

This was the state of affairs until a paper by Keleb et al. in 2004 [55], demonstrated that by removing the die plate, optimising process parameters and replacing the extrusion elements with larger conveying elements, a granulation process could be established that required no extra milling step. The publication went on to report that subsequently, it became possible to produce granules of acceptable characterisation and yields. Interestingly, the authors even ran the experiments for 8 hour intervals and deduced no discernible deviation in quality. Furthermore, the power consumption never deviated from 26 to 30% capacity and the barrel temperatures remained between 56 and 66°C [55].

In response to these findings, most research in the field has been conducted using die-less TSEs in order to investigate the possibility of using it as a one-step wet granulation procedure. Therefore, as was defined in the review by Thompson in 2014 [49], a TSE being used without a die plate to produce granules shall henceforth be referred to as a TSG.

Since the work by Keleb [55], most of the interesting work regarding TSGs has been completed using a co-rotating twin-screw set-up (where both screws rotate in the same direction), rather than the single-screw configuration. In fact, Martin [4] wrote within a 2013 book detailing advances in pharmaceutical processes that the co-rotating inter-meshing TSE now dominates the market, with 90% of extruders utilised within the pharmaceutical industry being of this design [4].

Undoubtedly the reason for this development is the increased flexibility offered by the twin-screw system in terms of responding to fluctuations within feed characteristics, such as the: flow rate, particle size and moisture content. It is also commonly suggested that the process offers a wider selection of material output properties, such as alterations to granular: size, shape and porosity. The reason for these assertions are the result of greater options with regard to internal geometry,

mainly the screw design, in conjunction with the positive displacement pumping action created as the two screws intermesh.

The pumping phenomenon mentioned previously has been shown in various studies to allow greater variation in the feed rate, with no discernible drop in quality, as well as the option to run on numerous degrees of channel fill. Whereas in contrast, it is commonly suggested that single-screw extruders must be full of material in order to operate efficiently. The positive displacement action also offers higher heat transfer rates (and thus a better control of temperature) and is more competent at handling viscous materials that may more readily slip at the screw/wall interface within a single-screw design. The main drawback of using the twin-screw arrangement over single screw is the higher maintenance and capital costs, which in many cases may more than double [56].

The general design of a TSG may be described as 2 co-rotating intermeshing screws enclosed within a barrel. The intermeshing nature of the screws leads to many throughout literature referring to the arrangement as being 'self-wiping'. However, Thompson contends in his 2015 review [49] that this is only partially true, as intuitively some material residue will likely remain. The barrel may also act as a heating/cooling jacket, which can be used to keep the process isothermal via pumped fluid. The heating/cooling jacket may also be divided into individual elements, subjecting the material to changes in temperature as it propagates axially downstream.

At the entrance to the barrel raw material is fed into a transport zone consisting of multiple conveying elements which together are referred to as a conveying block. It is within this section that liquid binder is usually supplemented via two nozzles (one per screw) to initiate the aggregation process. There are a number of feeders that may be selected to add the material to the machine, including: screw feeders, gravity feeders and vibratory feeders, with the choice being dependent upon the flowing properties of the primary particulates [50].

The material is subsequently transported to a mixing zone which generally consists of a combination of 3 elemental blocks, namely: (1) kneading, (2) conveying (which may be assembled in a reverse configuration to promote back-mixing) and (3) combing; these have been displayed within Figure 2.8. A screw design may consist of multiple conveying and mixing blocks, which span the complete length of the barrel. The number and type of element contained within each block can be easily adjusted giving the equipment overall a high degree of modularity.

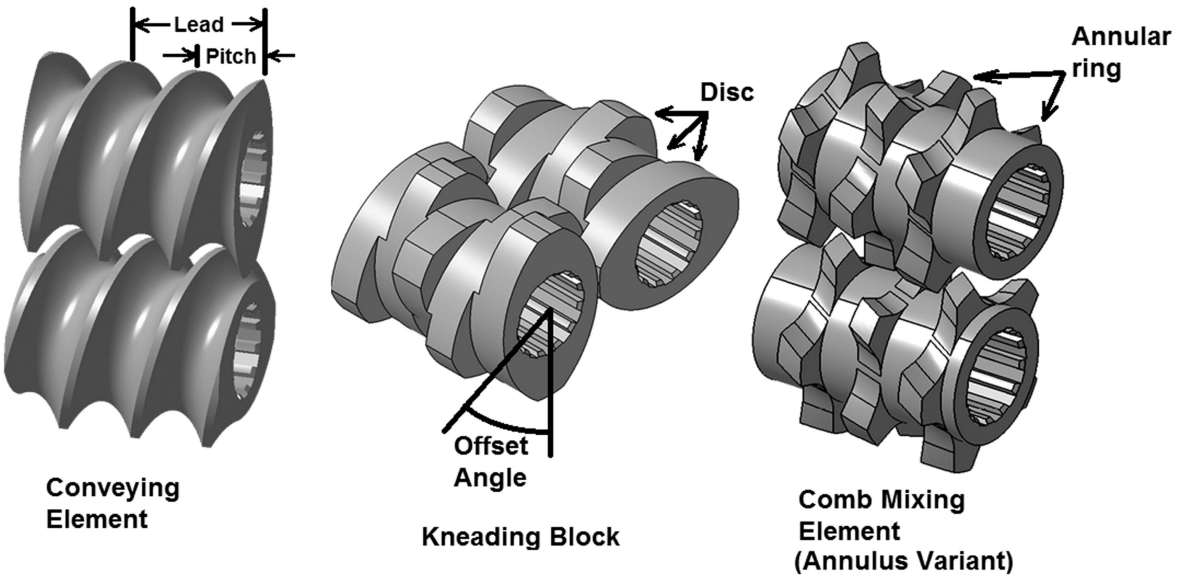

Figure 2.8: The 3 most common TSG screw elements in a side-by-side arrangement [49].

As the material travels in a sequential manner across the various blocks, granulation is able to proceed via a combination of capillary and viscous forces that bind particles together in a wet state. The compacting and elongation that occurs in each section converts the particulate morphology from a microstructure to a macrostructure [57].

Figure 2.9 displays an example of an elemental arrangement inside a TSG barrel (taken from the investigation by Kumar et al. 2015 [57]). The screw geometry elements have been arranged into 5 modular blocks, namely: (1) 1st conveying block, (2) 1st kneading block, (3) 2nd conveying block, (4) 2nd kneading block and (5) 3rd conveying block.

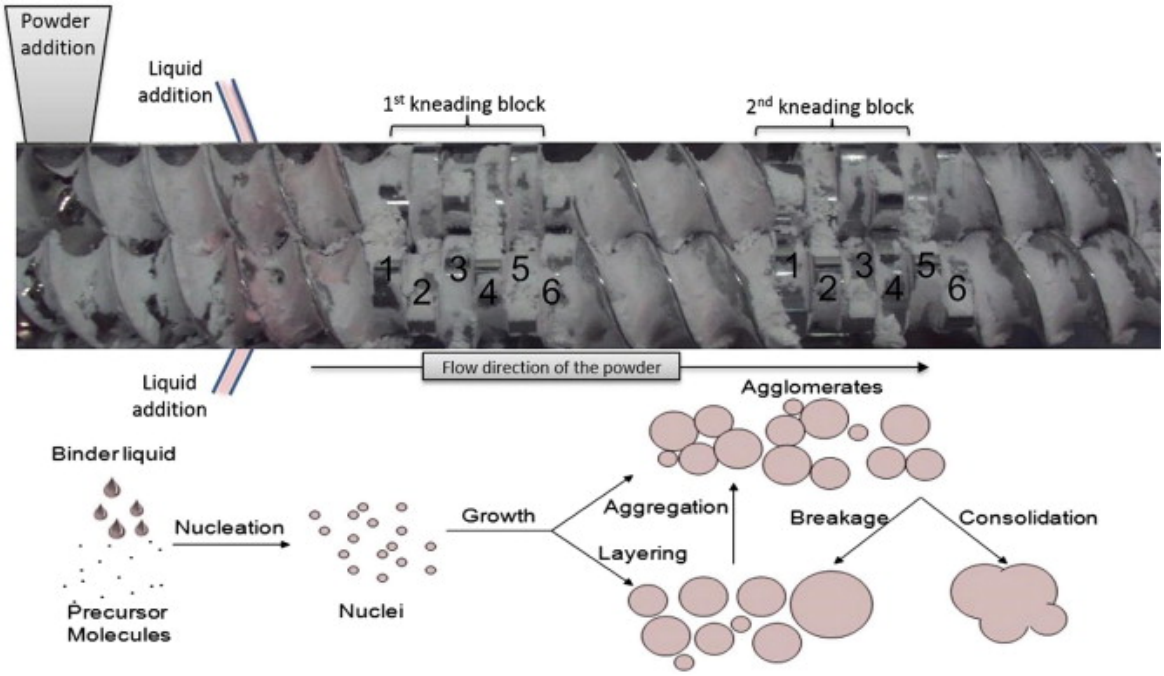

Figure 2.9: Screw configuration with 12 kneading discs (2 blocks containing 6 kneading discs each) indicating the geometry and flow of material inside the TSG barrel [57].

Unlike for the mixing zones, conveying elements primary function is to transport material in an axial direction, and so impart much less mechanical energy upon the material [50]. These elements are composed of a flight wound helically around a screw shaft, the shaft otherwise being known as a screw root. By far the most commonly encountered conveying element, the double-flighted conveying element, is constructed of two flights wound 180° off axis from one another. This creates a bi-lobal cross sectional geometry, as can be seen in Figure 2.2. For one complete screw revolution the distance a flight traverses axially along the screw is known as the flight lead. The axial distance between two adjacent flights is called the flight pitch and so for a double-flighted element this distance will be twice that of the lead. It is usually this type of conveying element that composes the majority of a screws length [49].

The mixing block elements are designed to produce much higher mechanical forces than within the conveying sections in order to aid in compaction and distributive mixing [50]. They generally offer little or no forward conveying capacity (and sometimes reverse conveying) and so rely on pressure developed upstream to stimulate axial downstream flow across the block. Sometimes a mixing block is coupled with a downstream reverse conveying element. This serves to increase further the degree of channel fill and back pressure within the block, facilitating compaction and distribution of material.

Whilst describing the dimensions of a granulator/ extruder, a typical value supplied throughout literature and by manufacturers is the 'length over the diameter', L/D, where L is the length of a screw and D is the outer flight diameter. Screw flights typically have small clearances within the bore of the barrel, giving rise to a relatively small cross sectional area through which the material is transported. This allows a more homologous application of stress to be imparted by the machine. By way of comparison, within high-shear batch processes profiling the stress history imparted by the machine upon the material is much more difficult to accomplish, owing to the complex variations in flow regimes encountered which are a function of proximity to the impeller [49].

As noted in the review by Seem et al., [50] powder passing through a TSG with a lower free cross sectional area, and by extension lower free volume, may be expected to encounter higher shear stresses and undergo a higher degree of compaction. The authors subsequently asserted that a good metric to consider whilst calculating the free cross sectional area is the ratio of inner (Di) to outer (Do) screw diameter. Consequently, the ratio of Di:Do was deemed of great importance. However, it was also revealed as having little attention paid to quantifying it throughout literature [50]. Furthermore, Thompson [49] reported serious concern for the lack of consideration given to degree of channel fill. This was in strong agreement with Seem et al. [50], as at any given flow rate the degree of channel fill would be a function of the Di:Do ratio [49]. The authors of both reviews seem to raise an excellent point regarding the free volume present within a TSG, as intuitively the degree of compaction may greatly affect the characterisation of the granules produced and so is worthy of much more investigation.

Thompson [49] also revealed that depending on: flow rate, screw speed, liquid binder to solid ratio (L/S) and concentration of a binding polymer in solution, well lubricated TSGs typically saw a rise in temperature between 5 and 15 $^{\circ}C$. Poorly lubricated operations meanwhile had been known to witness temperature rises of around 70 $^{\circ}C$. Moreover, longer mixing zones were described as being responsible for larger temperature rises [49]. This is perhaps intuitive and was again ratified by Seem et al., [50] who discussed temperature increases being propagated by friction created between the material and barrel/kneading blocks [50].

The same author cited temperature excursions within a TSG being a point of concern within the pharmaceutical industry regarding thermal degradation of materials. However, as an increase in temperature may be mitigated to some degree with cooling jackets, this coupled with small residence times (of the order of a few seconds), may in most cases be enough to prevent drug damage from occurring. Thompson did concede however, that not enough research had been completed to reach any solid conclusions regarding this potential complication [49].

Despite being less numerous, Martin also asserted within his 2013 publication [4] that the counter-rotating intermeshing TSE (where both screws rotate in opposite directions), has also shown great promise within many pharmaceutical applications. The author went on to explain that in contrast to the intermeshing co-rotating TSE, this regime could be fabricated to produce a much closer approximation to plug flow and were also more efficient at pumping material into a die i.e. extrusion.

This was a view ratified by Shah and Gupta [58], who developed two models displaying 3D flow of polymer, within either: (1) a co-rotating, or (2) counter-rotating; intermeshing TSE. The models demonstrated that during a complete screw rotation within the former, polymer mostly transferred directly from one lobe to the other, as materially flowed axially along the barrel length. However, this was not always true for the latter, as greater pressure was generated within the intermeshing zone, which tended to propagate flow toward the die far more directly (by material forcing its way axially between the 2 screws calendar gaps).

Due to the two different flow regimes demonstrated within the models, it was assumed better mixing would be enjoyed within the co-rotating set-up (and therefore presumably a lesser degree of plug flow, as asserted by Martin [4]). However, Shah and Gupta [58] decided, also in strong agreement with Martin [4], that the greater pressure generated within the counter-rotating screw intermeshing region (as a consequence of internal calendar action), may be the preferred mechanism depending upon application. An instance of which was given as being the direct extrusion of viscous polymer through a die [58].

The perceived wisdom of co-rotational intermeshing TSEs having ‘superior mixing qualities’, and counter-rotating intermeshing TSEs being ‘better suited to direct extrusion of viscous material’, has also been ratified by many other authors throughout literature. This includes Wiedmann and Holzel [59], who concluded that co-rotating intermeshing TSEs make more efficient mixers due to the way material flows internally, in both an axial and tangential direction (i.e. a figure-of-eight flow pattern as material is passed between the lobes of the two screws). Whereas in contrast, the counter-rotating intermeshing TSEs were described as being relatively poor mixers, but performing well as pumps for forcing viscous material axially through the calendar gaps of the screws and eventually through the extruders die plate [59].

As should have become evident whilst reading this Chapter most (if not all) of the work regarding TSE/TSG has been conducted using co-rotating intermeshing extruders rather than the counter-rotating intermeshing type and so by default this is the operating regime that has been more thoroughly addressed within Chapter 2. Presumably this is a result of the prevalent view throughout literature that the regime offers better mixing and so may be more conducive to a wider range of

processing applications.

However, the subject is worthy of an empirical investigation to discover conclusively that this is the case especially as the decreased pressure in a TSG, as a result of removing the die plate, may alter the internal flow patterns (from that witnessed in polymer extrusion) and thus potentially prove more conducive to granulation. This was certainly the conclusions drawn by Professor Heindel's group [22, 6, 23, 24, 25] during their investigations into TSM technology, as discussed within section 1.3, as the researchers insisted the counter-rotating down pumping arrangement was most conducive to mixing, at least for the systems they investigated using glass beads and wood chippings as primary particulates [22, 6, 23, 24, 25].

Van Melkebeke et al. [60] published a paper in 2008 in which they set out to build on the work of Keleb et al., [55] by: (1) examining the effects of screw configuration upon granular characteristics and (2) examining the mixing quality, both within a modified TSE. The same basic formulation was also utilised, α-Lactose monohydrate as excipient and 2.5% (w/w) PVP solution as the liquid binder. The extruder model was a co-rotating TSE MP 19 TC 25 APV Baker, which had the die removed to create a TSG. The L/D was 25:1. All the experiments were performed using 5.6 kg/hr as the feed rate, 250 RPM as screw speed, and the barrel was kept isothermal at 25°C. The granules produced were dried in an oven at 25°C for 24 hours before being analysed.

Within the publication it was revealed that for the first part of the investigation they had adapted the screw configuration used by Keleb [55] (screw configuration 1 in Figure 2.10), to include only 1 mixing block, which was placed either at the end of the screw length (screw configuration 2 in Figure 2.10), or just before an additional conveying zone (screw configuration 3 in Figure 2.10). The kneading block for both consisted of ten kneading elements, each 4.7 mm thick, with the staggering angle for the kneading block set-up described as increasing from +30° (for the first four elements), to +60° (for the next 5 elements) and finally at 90° (for the last element) using the kneading block construction terminology as discussed in Section 2.2, whilst discussing the work by Carneiro et al., [44] (displayed in figure 2.6). Liquid binder was added just before the kneading block, as noted by the arrows in figure 2.10. The binding solution was added by peristaltic pump at 7.5% (w/w) of dry powder weight.

For the second part of the investigation an examination of mixing efficiency was conducted. This was achieved through adjusting the staggering angle of the kneading block so that all 10 discs were set at either: +30°, +60° or +90°. The mixing block generated for this part of the trials was always positioned at the end of the screw length, at the same position as displayed within Figure 2.10 (configuration 2). The trials were conducted both wet and dry and so during the wet trials binding solution was added by peristaltic pump at 8.5% (w/w) of dry powder weight. A dry pow-

der tracer was continuously added for the dry experiments as opposed to a tracer solution during the wet trials. Tracer concentrations were measured off-line from the granular samples taken from the extruder's outlet every minute, by dissolving the granules and measuring the solution spectrophotometrically ($\lambda = 267nm$).

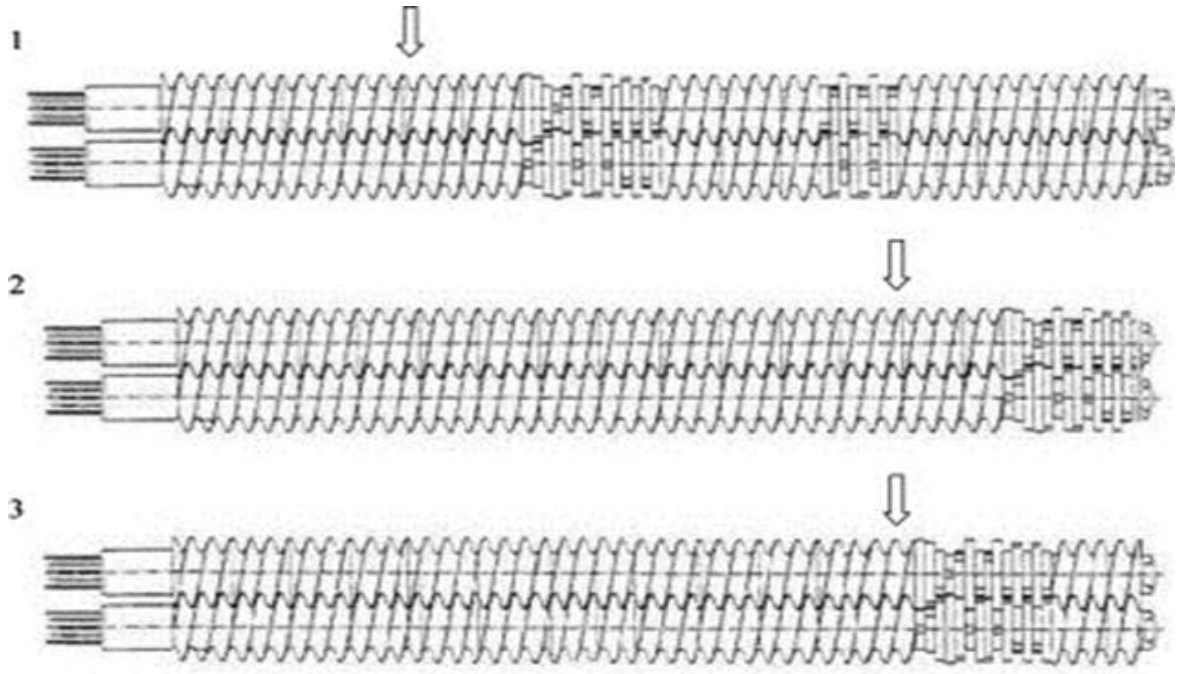

Figure 2.10: Screw configurations used for twin-screw granulation: (1) screw configuration used by Keleb et al. (2004); (2) screw configuration with mixing block positioned at the end of the screws; (3) screw configuration with mixing block proceeded by a conveying section. The arrow indicates point of liquid addition [60].

For the first part of the investigation, inclusion of a conveying element after the kneading block was discovered to have a significant influence on the amount of oversized agglomerates produced. With oversized agglomerates (defined as being particles >1400 μm in diameter) dropping from 11.9% (without a proceeding conveying element after the mixing block), to 1.1% (with a proceeding conveying element after the mixing block). Additionally, the overall yield (defined as being particles >1000 μm and <1400 μm in diameter) increased from 46% to 73%. The authors concluded that the extra conveying element must have broken down a large proportion of oversized agglomerates produced within the kneading block in order for this to occur. The porosity and friability of the granules however, was not significantly affected by either of the two configurations.

The granule friability (deduced by subjecting 10 g of granules to 10 minutes within a friabilator, at speeds of 25 RPM together with glass beads, and subsequently measuring the percentage loss in mass through a 250 μm sieve), decreased as the geometry of the kneading block staggering an-

gle was increased from: +30°, to +60° (from 23 to 21% friability) and finally making a significant drop when staggering was increased to +90° (11 % friability). This was thought to be caused by the increase in shear developed in the neutrally conveying +90° mixing block. Thus, more even distribution of the binding liquid was realised leading to better overall bonding. All the friability values for the granules produced, during both parts of the experiments, were less than 30%, which the authors stated was the maximum value acceptable for tabletting. During the mixing trials the authors also found tracer concentrations remained within acceptable tolerances and consistent, regardless of the conditions tested, this led to them conclude that TSG was a robust mixing process [60].

Djuric and Kleinebudde [21] also set out to build on the work by Keleb and colleagues in their 2008 publication. Like Van Melkebeke and colleagues [60] they also conducted twin-screw granulation (i.e. extrusion without a die plate) using α-lactose monohydrate as the primary powder, but this time used purified water only as the binder. The extruder used was a Leistritz Micro 27GL/28D. The main focus of the study was to examine the effects of different screw elements upon granulation. Therefore, the: screw speed, binder addition rate and powder feed rate, were kept at a constant: 100 RPM, 3 g/min and 33 g/min, respectively. The barrel was kept at a constant 25°C, and the granules collected were oven dried at 60°C for 4 hours before being analysed.

For all the experiments the length of the screw was 330 mm, and was divided into two zones; described as: (1) the feeding, and (2) the variation zone. The feeding zone configuration was held constant throughout the investigation at 180 mm in length and was constructed of a series of 40 mm pitch conveying elements. The variation zone however, was adjusted between experiments in order to assess the effects of the changing geometry. The length of the variation zone therefore, was 150 mm in length (the remaining length of the total screw), which was fabricated into one of the following arrangements:

- Conveying elements with a different sized pitch used for the entire length, namely: 15, 20, 30 or 40 mm.
- Combing elements of two different pitches/lengths: 15/60 mm and 20/90 mm respectively. For these experiments one of these was placed just after the feeding zone. The remaining length of the variation zone was always composed of 40 mm pitch conveying elements.
- Kneading blocks of either 30 (using 5 discs) or 60 (using 10 discs) mm's in length. The staggering geometry was set at either: -30 (for 30 mm of the TSG's length only), +30, +60 or +90° between adjacent elements (for 60 mm of the TSG's length). The blocks were situated after 210 mm of total screw length, and the remaining length was composed of 40 mm

pitch conveying elements.

The researchers reported that whilst using conveying elements only, the smaller pitch elements (15 and 20 mm) produce a lower yield in comparison to the 40 mm pitch elements which was defined as the granule fraction between 125 and 1250 μm in diameter. Therefore, it was proposed that a smaller conveying pitch provided less free chamber volume, so the granules tended to bypass the elements in an uneven manner leading to increased lumps and fines.

They also found that combing elements produced higher yields when compared to the same pitch conveying elements. This, they assumed, was due to the increased space created by the longitudinal slots leading to homogenous feeding and filling of the barrel. This may be a false assumption, as combing elements are known to produce higher mechanical forces than conveying elements, which may in turn create better interstitial bonding within the granules leading to less fines.

Kneading element experiments led to almost no fines compared to conveying and combing, almost certainly caused by the bulk experiencing larger compactive and distributive forces. The highest yields were obtained with a 30 mm long +90° staggering angle. This was attributed to the highly dispersive mixing characteristics of the block, which were also not large enough to produce a significant amount of oversized agglomerates. The 60 mm long kneading block staggered at +90° and the reverse conveying 30 mm long -30° experiments displayed similar behaviour, but this time produced large amounts of oversized agglomerates. The authors thought this may be caused by the development of the largest mechanical stresses upon the bulk for all kneading configurations investigated.

The highest porosity of granules (discerned via a helium pycnometer) was found for conveying elements alone, followed by the combing then kneading blocks. This was to be expected, because as the mechanical forces are increased the material would become more compacted. The porosity of the granule displayed a strong inverse relationship with granule friability, which again is a function of stronger bonds being formed.

Next in 2009, Djuric [61] and colleagues conducted a comparison between two TSE's, with the die plates removed, in order to directly compare how they performed whilst processing either water insoluble (dicalcium phosphate anhydrate), or soluble (α-lactose monohydrate 200 M) granules. The two extruders under investigation were the Leistritz Micro 27GL/S8D co-rotating TSE, with a screw diameter of 27 mm and the second was a MP19 TC25 APV Baker co-rotating TSE, with a screw diameter of 19 mm. The authors explained that this was the first publication to directly compare the performance of two different TSGs under similar conditions.

After granulation, 2 kg of wet material, i.e. the granules, were oven dried at 60°C for 4 hours.

Both extruders had analogous screw configurations based on the L/D ratio. The screw length for both was 24 D. The geometry began with a conveying zone, 20 D in length, and the binder was added at the end of this section via peristaltic pump. This was followed by a granulation zone 4 D in length.

For the insoluble powder 11% (w/w) liquid binder was input into the process and for the soluble powder 7.5% (w/w) liquid binder was added. To prepare the binder for both 2.5 % (w/w) of povidone was dissolved in demineralised water.

The granulation zone for the Leistritz extruder contained 2.2 D long kneading blocks. The staggering geometry was described as starting as +30° and finishing at +60°. However, the number of kneading elements in the geometry along the entire length of the block was not given. The granulation zone was followed by a 1.8 D long conveying section to the outlet.

For the APV extruder the kneading block was 2.5 D in length and consisted of ten discs. These had a staggering angle increasing from +30° (4 discs) to +60° (5 discs) and finished on +90° (1 disc). The block was followed by a conveying section of 1.5 D long leading to the outlet.

A full 2^3 factorial DoE was completed for each machine using each of the 2 powders. The design examined 2 variables (powder feed rate and screw speed) at 3 levels (2, 4, 6 kg/hr and 150, 225, 300 RPM respectively), with the centre point being repeated 4 times. Once the dried granules had been obtained the granule fraction between 125-1250 μm were compacted into tablets.

The dimensionless Froude, Fr, number was used to compare the extruders, which roughly transcribes as the ratio of centrifugal force developed in the machine to gravity. It was explained that traditionally the correlation is used to assess high-shear granulation, in relation to granular properties vs. shear. The Froude numbers calculated were much lower than for a typical high-shear batch process, which adds credence to the idea the technique may be more suitable for preparing formulations containing a fragile API.

Equation 2.6 displays the Froude number equation. The Leistritz extruder displayed higher Froude numbers than the APV as the screw diameter was larger, meaning higher tip speed. This in turn was thought to input higher mechanical stresses on the material during processing.

$$Fr = \frac{N^2 D}{g} \tag{2.6}$$

Where: N is the number of revolutions, s^{-1}, D is the diameter of the impeller (when examining high-shear batch processes) or screw, m; and g is the gravitational constant, m/s^2.

For the insoluble granulation experiments it was discovered that increasing the total input rate of

powder for both machines decreased the fines fraction (granules <125 μm). This was possibly the result of increased compaction experienced by the bulk as the overall mass within the barrel increased.

Larger insoluble granules were produced when increasing the feed rate of the Leistritz, but this was only mildly observed in the APV. The authors decided this was due to the difference between the two machines free volume, as the increased space within the APV meant the compaction effects were less pronounced. This could have been proven more conclusively, if the authors had examined changes to the Di:Do ratio discussed by Seem [50], rather than using the same flow rates for both.

The Leistritz extruder also produced much larger granules overall. Djuric et al. [61] also mentioned that the increased compaction in the Leistritz extruder led to better defined granules. This would seem to be in agreement with previous sources who found increases in shear and pressure led to less fines and spherical well defined granules.

During the insoluble powder trials higher input rates for both yielded granules with lower friability. Also thought to be a function of higher densification, with the Leistritz extruder producing less friable granules as would be expected. Flowability of the granules was also described as being good. No significant difference in the flowability of the insoluble granules could be detected between the machine utilised.

Whilst examining the PSDs of the lactose experiments the granule sizes were found to be significantly affected by both the machine used and the feed rate. In fact, the APV extruder produced almost no oversized agglomerates (>3150 μm) at all when compared to the Leistritz. However, higher fill levels resulted in more oversized agglomerates within both machines thought to be due to the densification effects.

The experiments also revealed that the lactose granules produced were slightly larger and more defined than insoluble dicalcium phospate. This was thought to be due to lactose possessing more moderate agglomeration behaviour in response to high-shear and overwetting conditions than dicalcium phosphate.

As agglomeration was almost complete for all lactose experiments, the flowability of the granules was also said to be of a high standard regardless of granulator used. This was attributed to the lack of fines as had been noted previously, but may have been more related to overall granule porosity. As had been noted in previous work by Djuric et al. [21] using lactose, the more porous (APV produced) granules produced higher tensile strength tablets after compaction than the less porous (Leistritz produced) granules; 2.1 to 2.2 MPa vs. 1.9 to 2 MPa respectively.

The reverse was true for insoluble powder which is an interesting point to consider when designing a granulation process. This is because it highlights that, as with all solid processing procedures, formulation is undoubtedly one of the most critical parameters. However, in all cases and for both powders the granular properties were thought to be of an acceptable standard.

The final conclusion was that choice of machine used played a vital role in the differences noted between both granules and tablets produced [61]. This would again seem to back up Seem [50] and Thompson's [5] point that the degree of channel fill is an important consideration, as channel size was the key difference between the two.

In 2010 Dhenge and colleagues [62] conducted an investigation into the effect of varying the: liquid to solid ratio (L/S), screw speed and powder feed rate upon the granular: residence time, size, shape, structure, flow and strength. The feed powder consisted of 73.5% α-Lactose monohydrate, 20% microcrystalline cellulose, 5% hydroxypropyl cellulose, HPC, and 1.5% crosscarmellose sodium. Water was used as the liquid binder. They also employed the use of a torque meter, so they were able to monitor changes in screw torque during the trials.

The authors found that the torque increased with L/S, which was attributed to the material becoming a pasty substance (but could also have been due to extra mass). The PSD also became monomodal at the highest L/S value investigated (0.4). High L/S also produced the most spherical particles, attributed to better liquid bridges being formed within the granules, thus creating stronger binding [62]. This again shows the importance of formulation, not just on granular properties but also on the energy need to run the procedure.

It is clear from the review of literature that TSG is a very promising technique that offers much promise in the field of continuous powder processing, especially for the pharmaceutical industry. The flexibility offered by the procedures inherently modular design, coupled with a more intimate and gentle application of shear, means it would be relatively facile to incorporate within the FDA's QbD framework. Whilst its continuous nature should lead to a high degree of process controllability when used in conjunction with PAT.

It is also clear however, that there is still much to be addressed before the technology can enjoy widespread use. This is despite a general consensus regarding system behaviour being achieved in a qualitative fashion, as there is still little in regard to more quantitative methodology. This includes being able to predict properties such as granular: PSD, flowability and porosity, based entirely upon adjustable parameters such as: geometry, formulation, feed rate, temperature and screw speed.

The literature is also heavily reliant on methodology adopted during TSE fabrication, such as: be-

ing dominated by the co-rotational screw regime, adopting similar screw elements and the use of Di as the characteristic dimension. Ultimately this may, or may not, be the most effective approach to take whilst researching and deploying these machines. The reason for this assertion is because of large differences in internal ambient pressures between the two techniques (as a result of removing the die plate), which may in turn create vast differences in the bulk's rheology.

These were certainly the findings of Professor Heindel's group whilst working with TSMs, as discussed in Section 1.3 [22, 6, 23, 24, 25]. As they discovered that counter-rotating down pumping arrangements were more conducive to better mixing of oak chips and glass beads in small scale TSMs, in contrast to the generally agreed upon conclusion that the opposite is true for typical formulations used within a TSE.

In the context of this report, of the three twin-screw regimes researched: TSM, TSE and TSG, all have key differences to that of the large scale TSM processes being investigated within Chapter 3 and beyond. The TSM research discussed in Section 1.3, for example, utilised oak chips and marbles, whilst the TSE investigations, by and large, analysed the transport of viscous fluids. These properties alone undoubtedly played a significant role in the results found in literature, as it is abundantly clear that formulation is a critical consideration during any semi-/ solid processing procedure.

Furthermore, all three technologies reviewed were addressed at similar scales, adopting mass flow rates of either kg/hr or tens of kg/hr, rather than the hundreds to thousands of kg/hr that shall be investigated in this report. Nevertheless, the equipment represents the closest approximation to a large scale TSM that has been examined to any degree of depth within literature. Subsequently, knowledge gained from how these similar technologies have been investigated has proved invaluable in fabricating the research methodology for this report.

It was also of great importance to the Project Chariot consortium to address TSG in particular, as: (1) granulation is one of the key processes that could be adopted within a the TSM, and (2) the procedure is currently the subject of much scrutiny within the pharmaceutical industry. Therefore, sharing key findings with the industry at large is helpful for addressing the AMSCI's key remit of opening up new markets for particle based products, manufactured in existing UK plants.

The most important lesson learned from literature regarding complex twin-screw process development is the need to keep process parameters relatively simple at the start. This is because it is vital to gain a thorough understanding of the more basic configurations before the researcher can confidently proceed to add higher levels of complexity. For this reason the investigation focuses upon dry powder flow, and how it responds to changes in: TSM size and length (especially

as scale-up/out are major considerations for P&G), screw speed and feed rate.

Finally, it was only possible in this report to thoroughly investigate one of the screw rotational regimes available. Therefore, the counter-rotating up pumping regime is the one that has been selected. In reality any of the three on offer could have been chosen, as it was very unclear how powder may behave within a large scale TSM, regardless of rotational direction. However, it is recommended that each rotational regime be addressed in future studies.

Chapter 3

Materials and Methods

3.1 Residence Time Distribution (RTD) Trials

A series of RTD trials were conducted using two geometrically similar counter-rotational up-pumping (to use the parlance from figure 1.3 to describe screw rotational regime) TSMs at two different scales. This was achieved by monitoring the change in concentration with respect to time of a pulse of tracer (added to the system whilst operating under steady-state conditions, using the strategy discussed in Section 3.2).

Two different TSMs were investigated, either having a Di of 75 mm or 125 mm. Henceforth, they shall be referred to as either the TSM 75 or TSM 125 to denote this change in outer screw flight diameter. As the characteristic dimension, Di, of the two machines has been defined, this translates to a Di scale-up ratio between the machines of 3:5. The screw root diameter however, Do, was 20 and 32 mm for the TSM 75 and 125 respectively, which translates to a scale-up ratio of 5:8. The clearances between screw tip and TSM barrel meanwhile was 5 (TSM 75) and 7.5 mm (TSM 125) and so the scale-up ratio was 10:14. Therefore, all the key characteristic lengths scaled-up at a ratio of between 1:1.5 - 1:1.67 between the two machines.

Using the dimensions supplied by the TSM's manufacturer, scale diagrams of each system were constructed in Matlab using the 'patch' function [63], and have been displayed as Figures 3.1 and 3.2. Subsequently, the 'polyarea' function in Matlab was utilised to discern the free area in the front facing view, the z vs. y axis on the diagrams, making sure that space occupied by the 2 screw shafts was removed from the total [64].

Both machines were designed by the manufacturer to have larger than normal head space, for the purposes of R&D. These areas have been highlighted and labelled within the schematics, and were not included in the free volume calculation for each TSM.

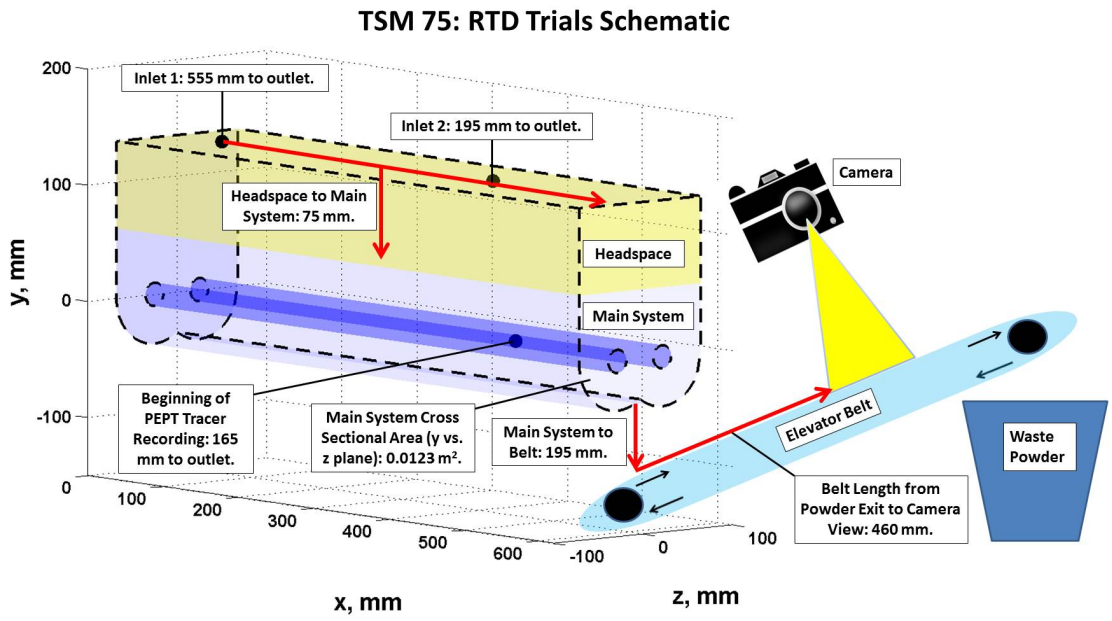

Figure 3.1: The TSM 75 RTD experimental set-up. The internal dimensions of the TSM are displayed to scale. The beginning of the PEPT tracer recording (the method for which is discussed in Section 3.5) has also been displayed.

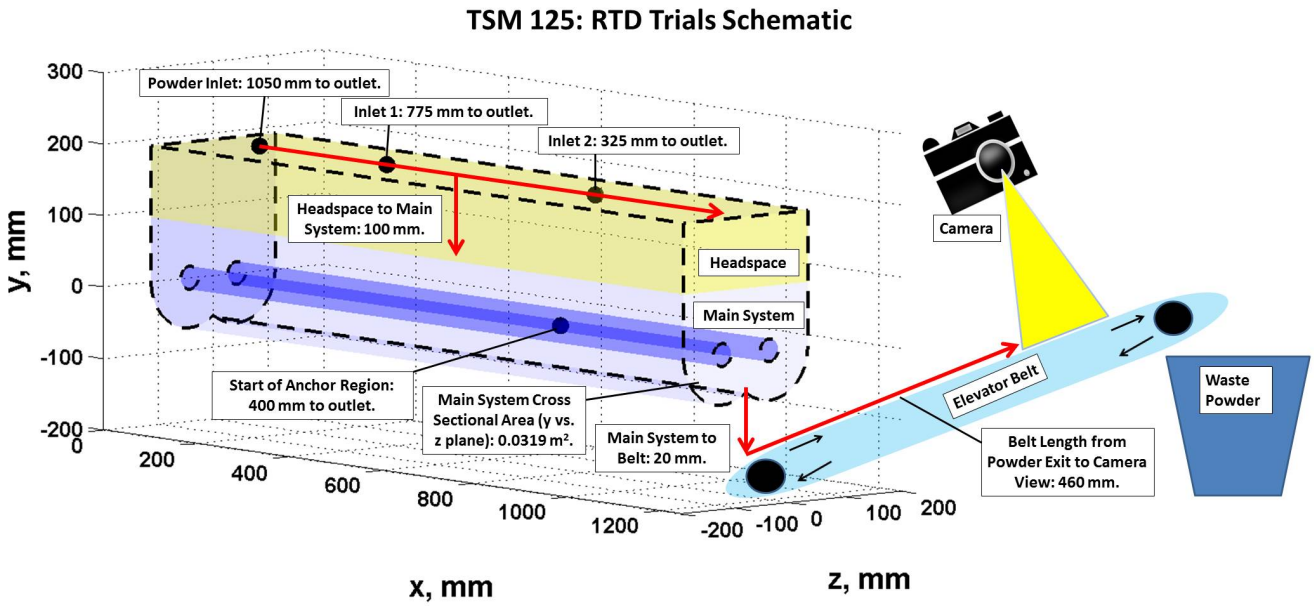

Figure 3.2: The TSM 125 RTD experimental set-up. The internal dimensions of the TSM are displayed to scale. The location where quadrant paddles are replaced with anchor paddles, for the purposes of analysing geometrical alterations within the system, has also been indicated.

The free frontal area (the z vs. y plane displayed in figures 3.1 and 3.2) of the TSM 75 was calculated to be 0.0123 m^2 and for the TSM 125 it was 0.0319 m^2. This meant the frontal area of the TSM 125 was 2.59 times bigger than the TSM 75 (or at a ratio of 1^2:1.61^2, which agrees well with the characteristic length scaling discussed previously).

The centre point of Inlet Port 1 and 2 for the TSM 75 was positioned 55.5 and 19.5 cm from the powder exit respectively. They were also positioned above the system and centrally between the 2 screws along the z axis. Inlet Port 1 for the TSM 75 was also positioned at the same point the primary particulates were fed into the system. Both systems fed primary particulates via a volumetric screw feeder attached to a hopper, which was manufactured by AJAX Equipment.

The centre point of Inlet Port 1 and 2 for the TSM 125 was positioned 77.5 and 32.5 cm from the powder exit respectively. As before, they were also located above the system and centrally between the 2 screws along the z axis. However, this time Inlet Port 1 was not combined with the primary particulate feed, which was located 105 cm from the TSM exit.

The injection ports used were chosen in order to ensure a similar L/D ratio was achieved in both machines for the purposes of scale-up comparisons. Therefore, Inlet Port 1 had an L/D of 7.4 and 6.2 for the TSM 75 and TSM 125 respectively. Whereas Inlet Port 2 had an L/D of 2.6 for both machines.

The tracer particles chosen for the experiments consisted of red sodium carbonate granules, measured as having a typical D_{50} of 0.78 mm (calculated from a PSD obtained using the Ro-Tap sieve shaker method [65]) and a bulk density of 1064 kg/m^3 (calculated by weighing samples of a known volume).

The primary particulates used in the trials were anhydrous sodium sulphate powder, a common filler used during detergent manufacture [66] and measured as having a typical D_{50} of 0.18 mm (calculated from a PSD obtained using the Ro-Tap sieve shaker method [65]) and a bulk density of 1408 kg/m^3 (calculated by weighing samples of known volume). This tracer/primary particulate pairing is commonly utilised within the NIC during experimentation, as they are thought to be of comparable magnitude and density (and so are believed to behave similarly in terms of their motion).

The pulse of tracer consisted of a 200 g cup of the red granules, dropped instantaneously into the TSM at the start of an RTD experiment. This was conducted for a range of different primary particulate flow rates and screw speeds, which were chosen according to the DoE strategy outlined in Section 3.4. Each condition was repeated twice, with the tracer being added at two different injection ports. This was to assess how the RTD function evolves with respect to the axial distance

travelled within the system.

There will of course be some error associated with adding the 200 g cup of tracer. As no tracer can be added such that: 1) it is all added completely instantaneously into the flow, 2) the corresponding bulk is at the same time removed instantaneously from the main flow, and 3) that the tracer is only added at one exact axial location. These issues may work to distort the RTD function from it's true value.

The method assumes therefore: 1) the rate of tracer addition is suitably fast compared to the overall system dynamics, 2) the mass of tracer is negligible compared to overall flow and 3) the difference in axial width in which the tracer lands in the system is suitably small. To test this assumption the method shall be validated using PEPT, which may be viewed in Chapter 4.1.1.

The time stamps associated with each samples concentration value was adjusted to account for: (1) initial fall time for tracer to enter the system, (2) fall time for the tracer/powder mix to exit the system and land on the elevator belt, and finally (3) time taken for the elevator belt to carry the tracer sample into the camera's field of vision (displayed in Figures 3.1 and 3.2). The camera itself was utilised as an inferential tracer concentration sensor, using the method outlined in Section 3.2.

The time adjustment to account for the tracer/powder mix's journey on the elevator belt was calculated simply by dividing the distance travelled by belt velocity. The two time adjustments to account for tracer falling into the system and the tracer/powder mix falling out of the system was calculated by measuring the distances involved and rearranging Equation 3.1 [67], to obtain equation 3.2.

$$d = v_0 t + \frac{1}{2} g t^2 \tag{3.1}$$

$$t = \sqrt{\frac{2d}{g}} \tag{3.2}$$

Where: v_0 is initial velocity (in this case always zero), m/s; t is time taken for the tracer to fall into/out of the system, s; d is the distance travelled, m; and g is acceleration due to gravity, m/s^2.

Figure 3.3's left hand panel displays a photo of the experimental set-up in CPI. The middle panel and the right panel display photos of the internal set-up of the TSM 75 and 125 respectively.

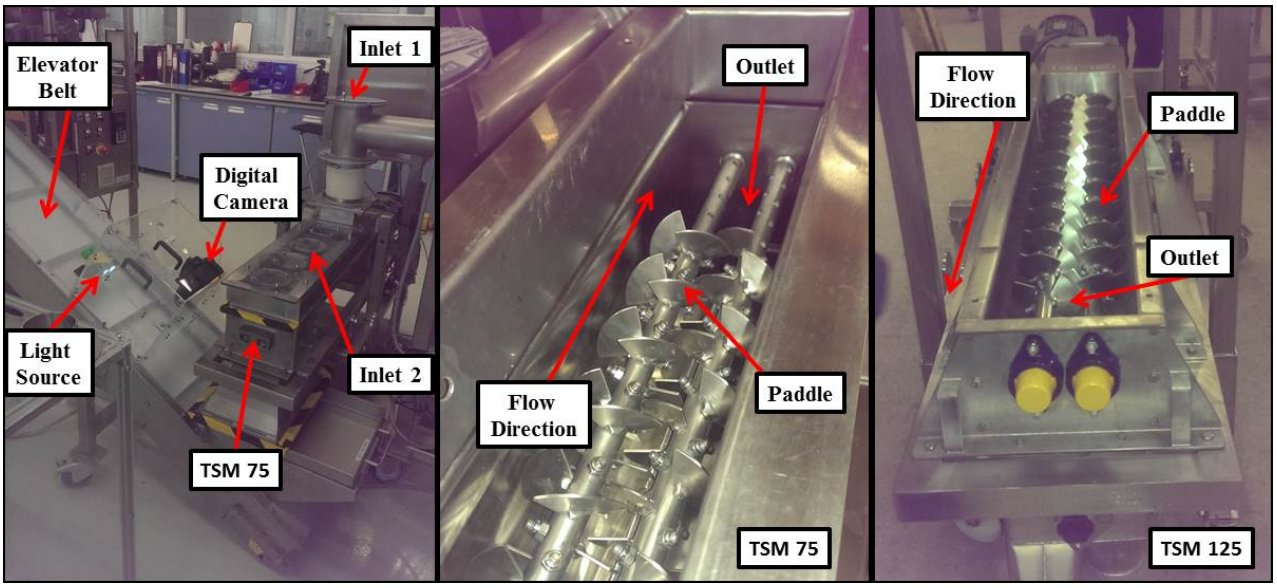

Figure 3.3: (Left) A photo of the experimental set-up in CPI. (Middle) A photo of the TSM 75 internal geometry. (Right) A photo of the TSM 125 internal geometry.

The screw arrangement consists of a series of paddles adjusted to resemble a discontinuous double helix screw thread set at a helix angle of 22°. This has been displayed in figure 3.4 part b of the blueprints provided by AJAX Equipment.

The helix angle selected was selected to be greater than 0 and less than 90°, as this facilitates the axial propulsion of powder flow through the system. Furthermore, the angle was also chosen according to best practice whilst designing a typical TSE process, by using an angle between 17.66 and 30° (which has demonstrated many times to be conducive to good radial mixing [68]). However, a more thorough examination of the effects of helix angle upon a granular mix should be addressed in the near future in order to confirm that the same is true in a TSM.

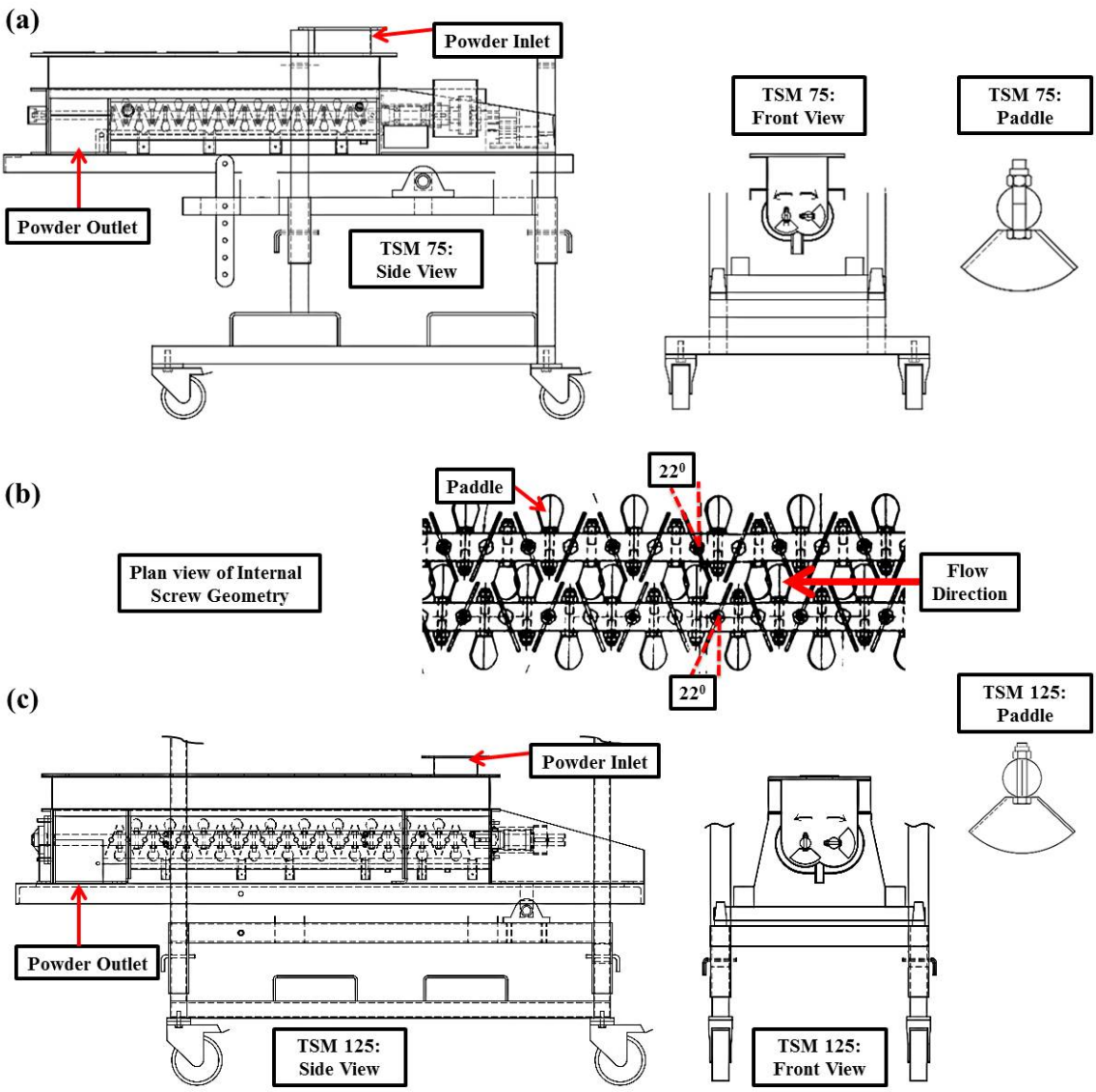

Figure 3.4: Part of the blueprints used by AJAX Equipment to fabricate the TSM's. (a) Is the TSM 75, (b) Is the screw configuration used in both machines and (c) is the TSM 125.

As alluded to in Figure 3.2, a second set of analogous experiments were conducted upon the TSM 125 after an alteration in the system's geometry. This involved replacing some of the quadrants with anchor type paddles. The anchor paddles were of the same size as the quadrants, and positioned in the same helical arrangement, but were of smaller surface area. A photo of the two types of paddles can be viewed as Figure 3.5.

This geometrical alteration only took place from a position of 40 cm along the TSM 125's x axis to the system outlet. The preceding paddle geometry was left unchanged for both TSM 125 trials conducted.

Figure 3.5: The TSM 125 paddles: quadrant and anchor photo.

The powder sampling was conducted by the elevator belt in an automated fashion, as it collected the falling powder from the outlet and carried it into the inferential sensor's (the camera's) field of view. The elevator was set at a gentle angle of 20° with respect to the floor, and at a belt speed of 0.28 m/s. After the powder reached the top of the elevator it fell under the influence of gravity into a large waste sack.

The belt was sub-divided by flaps into sections that were: 27 cm in width, 29.5 cm in height and 3.5 cm in depth. This was in order to prevent powder tumbling back down the belt into the camera's field of view; as the elevator, and therefore belt, was set at a slight angle as mentioned previously.

The frequency of the measurements was every 0.96 s, set to line up with a full sub-section of the belt entering within the cameras field of view (a subsection of the belt was 0.27 m in height and the belt ran at 0.28 m/s). The duration of a measurement (or film frame) was 0.03 s. The lowest concentration of tracer that could be measured in this fashion will be the direct equivalent of what the human eye is able to detect in terms of colour changes in the sample (from white to red). Previous RTD measurement techniques have always found very strong linear correlations between colour change and concentration, as discussed in Chapter 1.2.

Knowing the absolute concentration of tracer is not important, as long as the relative changes in concentration are consistent within each individual trial (i.e. that the R value in RGB space increases and decreases linearly with tracer concentration), and therefore features of the RTD function are captured.

To ensure the resolution of tracer concentration measurement in this fashion is fit for purpose, the RTDs generated will be examined to ensure most/all have tails of some description, and will be compared with the PEPT data in Chapter 4.1.1.

Whilst a model could be calibrated between magnitude of red in the pixels and tracer concentration, it would be subject to change depending on external lighting conditions. As an overall concentration measurement of tracer is not necessary, one of the strengths of this RTD measurement technique is ambient light does not need to be strenuously controlled, as recalibration takes place using red tracer images generated within an individual run. This will be discussed in more detail in Section 3.2.

The digital images recorded were inspected for visual quality, and found to be more than capable of recording a non-blurry view of powder upon the belt at the speeds used.

This automated approach to sampling ensured Allen's [69] two golden rules of sampling were being thourougly observed. Namely: (1) The powder should be sampled while the system is in motion, and (2) the whole powder stream should be taken for many short time increments. These rules are put in place to ensure that sedimentation effects do not corrupt the final results [69].

3.2 Digital Image Processing (DIP) of Residence Time Distribution (RTD)

Each RTD experiment began by operating either the TSM 75 or 125 at the predetermined screw tip speed and feed rate, and subsequently waiting for five minutes until steady-state had been attained (which included a visual inspection that powder fill level had become constant). The parameter settings were chosen according to the strategy discussed in section 3.4. After the system had stabilised, the coloured tracer was added to the system (as described in detail within Section 3.1).

As shown in Figures 3.1 and 3.2, a digital camera was used to record the entire width of the elevator belt as it carried powder from the TSM outlet to the waste sack. The camera utilised was a Nikon D5200 Digital SLR Camera with 18-55 mm lens. Torchlight was used to illuminate the cameras field of view in order to keep the belt well lit.

The .MOV files produced by the camera were opened in Windows Movie Maker [70] and a series of images were carefully extracted from the film and given a time stamp (with respect to the length of time expired since the pulse of tracer had been added). The time stamp was subsequently adjusted to account for: tracer falling into the system, tracer/powder mix falling out of the system

onto the elevator belt, and time spent travelling on the elevator belt to the cameras field of view (as discussed in Section 3.1). Each image was chosen such that they displayed an entire individual elevator belt partition, and subsequently saved as a .PNG file.

A series of images for each experimental condition under investigation were collated in this fashion. These became the individual samples used to calculate the RTDs. An example of a sample being processed can be seen in Figure 3.6.

A digital image processing algorithm was fabricated in Matlab to process each series of samples acquired into a corresponding RTD. The algorithm was a prototype developed off-line in order to provide proof of concept. However, the strategy could easily be adapted to extract a series of samples from the .MOV files automatically, therefore making it a fully in-line procedure. The digital image processing strategy used shall now be described in detail.

Each image consisted of $\approx$ 400,000 pixels. Therefore, as the images were saved in the sRGB gamut, the standard colour space used to record digital images [71], the information in each data file consisted of 3 matrices describing the magnitudes of: (1) Red, (2) Green and (3) Blue contained within each pixel.

Image segmentation is another important step in a DIP strategy, as it can improve the visibility of key features in order to aid in the subsequent analysis [9]. To this end, images needed to be pre-processed so only pixels containing tracer particles were retained for analysis. To achieve this an image segmentation strategy adapted from the work of the 'Image Analyst' (a prolific and highly respected contributor to the MathWork's file exchange community [72]) was incorporated within the RTD measuring algorithm. Within this work the histogram thresholding approach was used to facilitate image segmentation. It is the thresholding approach that trains the software to recognise tracer present within the images.

Thresholding, and therefore training, begins by sorting all the pixels in an image into histogram bins based upon a parameter such as colour. The peaks and valleys in the histogram may then be utilised to locate analogous pixel clusters [73]. A step-by-step description of how the DIP algorithm computes an individual RTD, from a series of images, shall now be discussed.

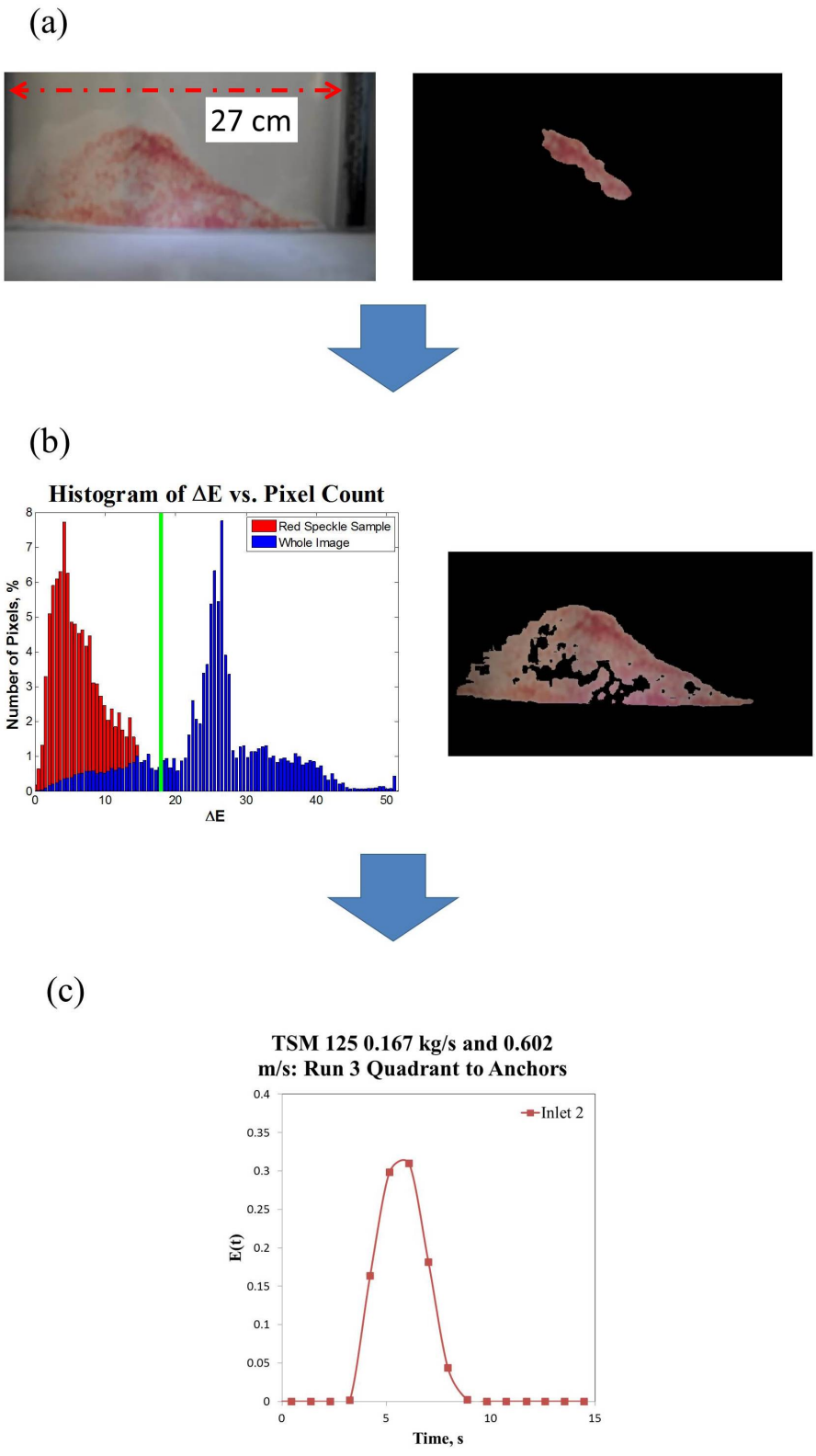

Figure 3.6: (a) Select training data. (b) Removing pixels that do not represent tracer using a ΔE threshold (determined via the training algorithm). (c) Use the processed images to calculate tracer concentration and subsequently an RTD.

Fives curves were generated using the procedure displayed in figure 3.6. The five curves generated for this example have been provided as figure 3.7.

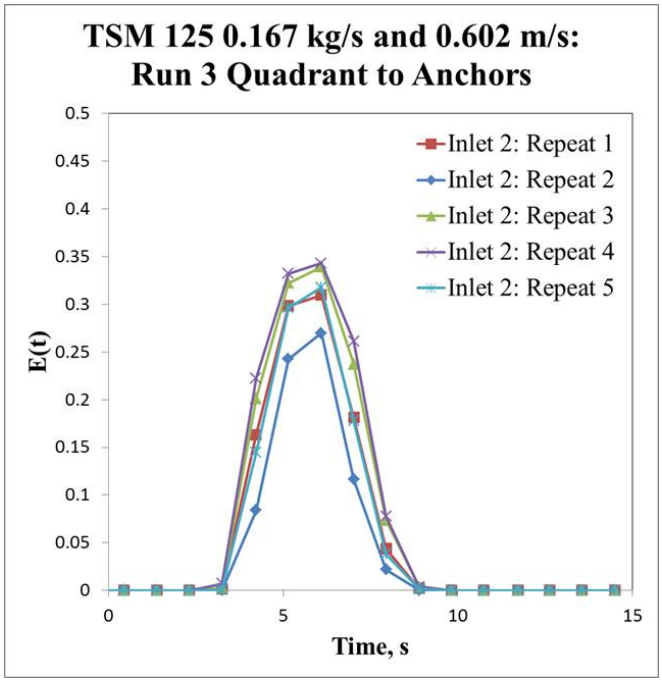

Figure 3.7: The 5 RTD curves used to generate the final curve in figure 3.6.

Two more examples of the procedure shown in figure 3.6 have been provided as figure 3.8.

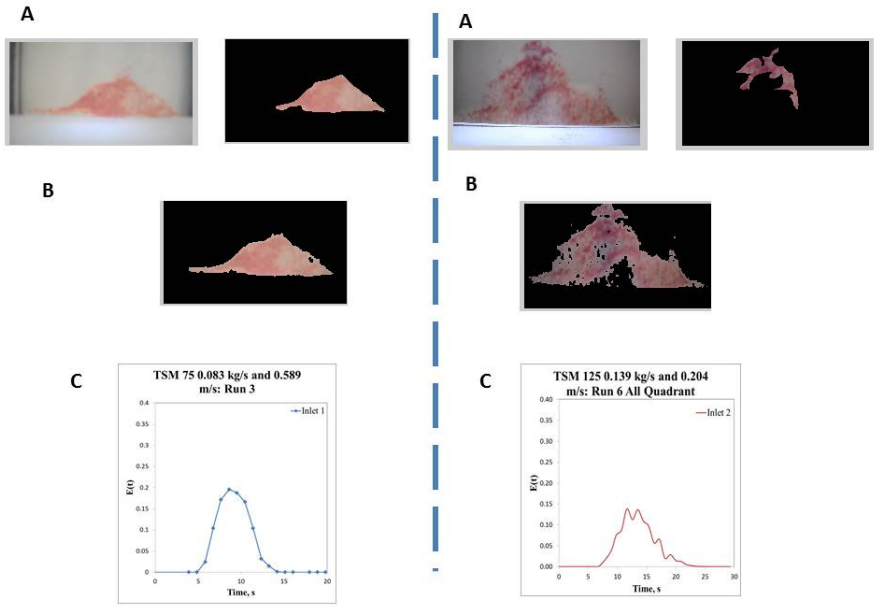

Figure 3.8: Two more examples of the procedure shown in figure 3.6 have been provided.

As can be seen in Figure 3.6 part (a), the first step to processing a series of images is to first choose one frame to act as training data. The image is selected such that it contains large regions of the tracer particles (which is determined by visual inspection). Once the image is chosen, one such region is selected by the user using Matlab's 'imfreehand' tool [74].

The training image is then converted from the sRGB colour space into the 1976 CIE L*a*b* colour space, via the 1931 CIE XYZ colour space, using functions available in Matlab's Image Processing toolbox [75]. These functions assume an observer angle of 2°, which is recommended for evaluating colour images [76].

The gamut transformation took place after specifying the reference white as the CIE standard illuminant D65 (the colour of white generated by noon sunlight [77]). This was because the images were recorded in sRGB format by the camera, which by definition uses this reference as its white-point [78], and so therefore would facilitate a more consistent transformation into L*a*b* space.

Next, the average pixel values of L*, a* and b* within the 'imhandtool' selected region were calculated. These averages were subsequently used as: L_1^*, a_1^* and b_1^*, whilst determining each pixels value of ΔE (as displayed in Equation 1.1).

A histogram of pixels within the 'imhandtool' region was then constructed based upon their ΔE values, using the L*a*b* value of each as: L_2^*, a_2^* and b_2^* within the equation. The x axis of the histogram was given as a percentage of the total number of pixels. Subsequently, a similar histogram was calculated for the pixels in the entire training image, and was overlaid on top of the first. This has been displayed on the left hand side of Figure 3.6 part (a).

The two histograms were then compared to discern a threshold ΔE with which to discard parts of the image that did not contain tracer particles. A first approximation for this value was given as 2 standard deviations of the first histogram (red speckle sample) histogram, as in theory this should capture 95% of the relevant pixels assuming a Gaussian distribution. The tolerance value was then adjusted manually to the nearest valley within the second (whole image) histogram. Pixels that generated ΔE values above this threshold were subsequently discarded. This can be seen in the right hand side of Figure 3.6 part (b). In this fashion the software has been trained to recognise red tracers in a pixel by thresholding according to ΔE.

Thresholding is necessary as it improves the accuracy of the concentration measurements. This is because all pixels in an image will have some degree of R in them (as digital colour is stored as 3 values, R, G and B). Therefore, by only considering pixels containing tracer, much of the noise is cut from the image, which in turn leads to far smoother curves without the need for further filtering. In addition, thresholding also returns the curve neatly to the baseline.

The algorithm then proceeded to cycle through the whole series of images, removing pixels according to this threshold ΔE value. The images were subsequently converted back to sRGB space, and the average value of R computed for each in series. These values were subsequently converted to an RTD using the relationship found in equation 2.3 and an example of the results given can be seen in Figure 3.6 part (c).

A visual check was then completed, by examining the curve generated against the series of images to ensure a sensible result had been obtained. Subsequently, a sensitivity analysis was conducted for each RTD, by repeated the procedure five times for each using different training images and/or training regions. For each of the five repeats τ and σ^2 were recorded, using equations 2.1 and 2.5. These values were recorded to two decimal places, as this was the level of precision afforded by the camera.

Finally, of the five curves generated per experiment (an example of which can be seen in figure 3.7), an average RTD was generated (by averaging each concentration value with respect to time) and this was retained for further analysis. This was completed to ensure the curve conformed closely to the average values of τ and σ^2. The Standard Error, as a result of using different frames and/or pixel regions as training data, was also calculated from the five repeats using Equation 3.3. These values have been reported in the results.

$$SE = \frac{S}{\sqrt{n}} \tag{3.3}$$

Where: SE is the Standard Error of the sample mean, S is the standard deviation of the sample and n is the number of samples.

3.3 Tanks-in-Series (T-i-S) Modelling of Residence Time Distribution (RTD)

Using a T-i-S approach to model RTD curves is useful for characterising flow and making equipment comparisons to aid in scale-up studies [46]. However, as Fogler states, a certain amount of engineering judgement should be employed when selecting which model to use, in order to ensure it is capable of describing the physical processes at hand [79].

One such approach is to approximate the RTD as a series of CSTRs. Should this model adequately describe the system, the number of CSTRs generated can give an indication of axial dispersion (with a small number of CSTRs demonstrating high amounts of axial dispersion). Conversely, if the model of best fit generates a high number of CSTRs, this indicates an approximation to plug

flow. The CSTRs in series model has been provided as Equation 3.4 [79].

$$E(t) = \frac{t^{n-1}}{(n-1)!\,\tau_i^n} e^{\frac{-t}{\tau_i}} \tag{3.4}$$

Where: E(t) is the RTD function, t is time, n is the number of CSTRs (the only adjustable parameter for this model) and τ_i is the residence time the material spends in each individual CSTR.

In order to compare across different pieces of equipment, time is normalised to ensure that the average residence time, τ, is always situated at 1 along the normalised RTD's x axis (where normalised time is defined thus: θ=t/τ). The normalised CSTRs in series model is derived using Equations 3.5, 3.6, 3.7 and 3.8.

Multiplying both sides of Equation 3.4 by τ yields:

$$E(\theta) = \tau E(t) = \frac{\tau t^{n-1}}{(n-1)!\,\tau_i^n} e^{\frac{-t}{\tau_i}} \tag{3.5}$$

Then realising that:

$$\tau_i = \frac{\tau}{n} \tag{3.6}$$

Simplifies the equation as follows:

$$E(\theta) = \frac{n\tau_i t^{n-1}}{(n-1)!\,\tau_i^n} e^{-n\frac{t}{\tau}} \tag{3.7}$$

And finally:

$$E(\theta) = \frac{n(n\theta)^{n-1}}{(n-1)!} e^{-n\theta} \tag{3.8}$$

Expanding on this model in 2015, Kumar and colleagues [57] developed a T-i-S model with 3 fitting parameters to model flow within a TSG. This model included a Plug Flow Volume Fraction, p, followed by a series of CSTRs, n and finally a Dead Zone Volume Fraction, d.

This model imagined some fraction, p, of the TSG initially behaving as a Plug Flow Reactor, with the steeper (and therefore faster) the RTD curve ascended to τ, the closer this parameter to unity. Next, the number of CSTRs parameter, n, gave a direct measure of how spread out the main part

of the curve was, and so therefore how much the material axially dispersed within the system during transport (in the same fashion as the 1 parameter model given in Equation 3.4). Finally, the Dead Zone Fraction, d, gave a measure of material spending an excessive amount of time within the system (normally twice τ) and therefore represented the RTD's tail. The schematic of this model can be viewed as Figure 3.9 and Equations 3.9 and 3.10.

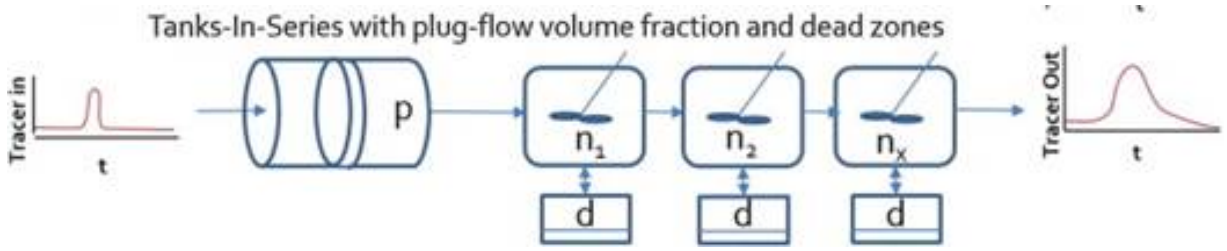

Figure 3.9: Schematic diagram of the conceptual model used by Kumar et al. for an RTD within a TSG. Where: p is the Plug Flow Volume Fraction, n is the number of CSTRs in series and d is the Dead Zone Fraction [57].

$$E(\theta) = \frac{b[b(\theta - p)]^{n-1}}{(n-1)!} e^{-b(\theta - p)} \tag{3.9}$$

Where:

$$b = \frac{n}{(1-p)(1-d)} \tag{3.10}$$

Within this thesis the T-i-S plus Dead Zone model, developed by Kumar et al. [57] for describing flow within a TSG, proved most adequate at describing the physical systems under investigation here (the 2 TSMs). The reasons for this shall be discussed in more detail within Chapters 4 and 6.

However, to summarise, even though the model has three adjustable parameters (breaking Fogler's rule of not using a T-i-S model with any more than 2 to prevent over fitting [79]), the shape of the curves, and the consistency in which the parameters were approximated, was strikingly consistent. Furthermore, the model rarely needed to use all 3 parameters in order to provide excellent results (usually only needing the same 2 parameters for Inlet 1 curves and the same 1 parameter for Inlet 2; across both TSMs and geometries).

To calculate the model of best fit for every RTD measured (using the method described in section 3.2), first the curves were transformed into the Normalised Time Domain (by multiplying the y axis, E(t), by τ and dividing the x axis, t, by τ). Next, to calculate model parameters, the robust

Generalised Reduced Gradient (GRG) algorithm within Excels Solver was used to find the solution [80].

This was obtained by minimising an Objective Function (the Residual Sum of Squares (RSS) between data and model) through adjustment of the models parameters: n, p and d. The algorithm was constrained such that: n must be a integer, p and d must be some value between 0-1 and no parameter may be negative.

As the optimisation problem is non-linear in nature, as equation 3.9 is not a linear model, it is impossible for any solving algorithm to guarantee it has found the best solution (as the algorithm may have converged on a local, rather than global, minima). To combat this, the solving algorithm was set to run 1000 times, using different randomly generated parameter starting positions, and then retain the best solution overall [80]. The values of R^2 for each was also reported in the results.

Finally, the Solver was used again in the same fashion, but this time minimising the Objective Function across all the RTDs from a particular: Inlet, geometry and scale. This allowed an investigation into how the TSM behaves overall across a range of powder: Fill levels, Feed rates and Screw Speeds, as well as linking axial length to the position of the theoretical tanks in the model.

The model of best fit for the RTD curves was also generated with p and d term set to zero. This was to see if the curves could be adequately described using CSTRs in series only. This would be useful as using CSTRs only would give a cleaner interpretation of axial mixing whilst comparing between different machines and operating conditions.

Axial mixing was also assessed by using the solver to calculate the Peclet number from RTD curves variance according to equation 3.11. This equation was derived by Levenspiel in 1972 [46], and stated that curve variance obtained during fluid flow, through a vessel with stagnant pockets, was a function of the Peclet number [46]. Lower Peclet numbers mean more axial mixing, this has been discussed in more detail in Section 2.2.

$$\sigma_\theta^2 = \frac{2}{Pe} - \left(\frac{2}{Pe^2}\right)\left(1 - e^{-Pe}\right) \tag{3.11}$$

Where σ_θ^2 is the curves variance and Pe is the Peclet number.

3.4 Response Surface Models (RSM)

Whilst generating RTDs using the strategy described in Section 3.1 and 3.2, the process settings were selected based on the popular Central Composite Design (CCD) methodology. A CCD is a particular type of Response Surface Model (RSM), seeking to efficiently analyse the process design space by approximating it to a second order Taylor Expansion [81].

The overall purpose of this strategy was to construct 6 sets of models (namely: (1) TSM 75 Inlet 1, (2) TSM 75 Inlet 2, (3) TSM 125, All Quadrants, Inlet 1, (4) TSM 125, All Quadrants, Inlet 2, (5) TSM 125, Quadrants to Anchors, Inlet 1 and (6) TSM 125, Quadrants to Anchors, Inlet 2), using the 2 Independent Variables (IVs) of Screw Speed and Feed Rate, to predict the key RTD metrics of σ^2 and τ (and so by extension Average Fill Volume % using the bulk density of the material at rest).

These models have then been thoroughly examined within Chapters 4 and 6 in order to improve process understanding. The models are also extremely useful for P&G to aid in more efficient planning of future TSM experimentation.

A schematic diagram of a two dimensional CCD (such as would be needed here) has been provided as Figure 3.10. This design is based upon a 2^2 Factorial DoE, with 2 Factors operating at 2 levels. In order to complete the design, 3-5 centre points are added, as well as 4 additional star points (at $\pm\alpha$). These extra experiments are included in order to widen the design space further in each direction, so that the data structure can more accurately be approximated to a second order regression [82]. The second order regression takes the form of Equation 3.12.

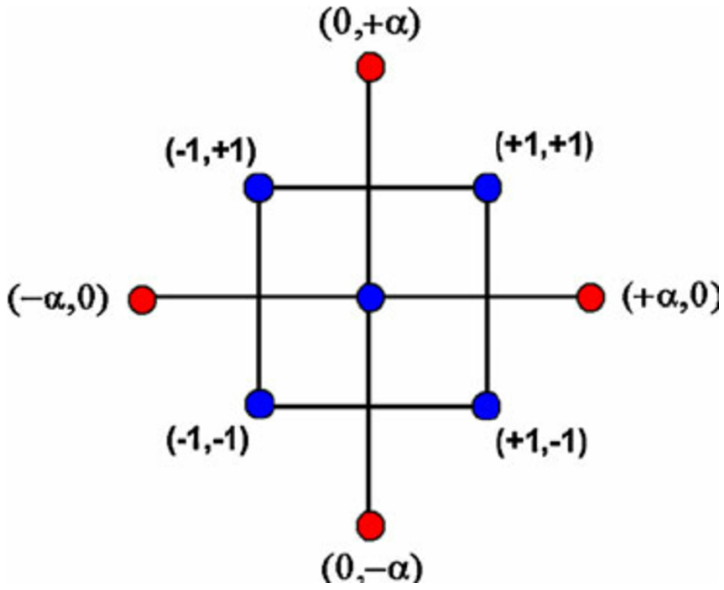

Figure 3.10: A schematic of the design space being investigated for a CCD with 2 Independent Variables (IVs) [83]. The IV levels used in the experiment are given the coded units: -α, -1, 0, 1 and α.

$$\begin{aligned} y = \beta_0 &+ \beta_1 Tip\ Speed,\ m/s + \beta_2 Feed\ Rate,\ kg/s \\ &+ \beta_3 (Tip\ Speed,\ m/s)^2 + \beta_4 (Feed\ Rate,\ kg/s)^2 \\ &+ \beta_5 (Tip\ Speed,\ m/s) \times (Feed\ Rate,\ kg/s) + \varepsilon \end{aligned} \tag{3.12}$$

Where: y is the RSM Dependent Variable, the β terms are the RSM constant parameters that are adjusted to find the model of best fit (by minimising the RSS between data and model) and ε is the RSM error.

A randomly generated experimental run order, with 3 centre points, was constructed in the Minitab 17 software package, and has been provided as Table 3.1. In this table the coded units for the IV levels have been replaced as follows: -α is Very Low, -1 is Low, 0 is Mid, 1 is High and α is Very High. This formed the basis of IV level selection for all 6 sets of RTD trials.

Table 3.1: The DoE Levels. In this table the coded units for the IV levels have been replaced as follows: -α is Very Low, -1 is Low, 0 is Mid, 1 is High and α is Very High.

Run	***Tip Speed Level***	***Feed Rate Level***
1	Mid	Mid
2	Mid	Very High
3	High	Low
4	Very Low	Mid
5	High	High
6	Mid	Very Low
7	Low	Low
8	Mid	Mid
9	Low	High
10	Mid	Mid
11	Very High	Mid

The next stage of the procedure was to select the magnitudes for the 5 levels, for both IVs and all 3 systems, namely: 1) TSM 75, 2) TSM 125 (All Quadrant) and 3) TSM 125 (Quadrants to Anchors). Ideally, the levels should be spaced apart in such fashion as to give the model rotatable properties. This means the response surface should be most accurate at its centre, where multiple repeat centre point experiments have been performed, and that the accuracy of the model should decline at the same rate (no matter which direction is travelled from the RSM's centre). These properties are thought to add a layer of consistency to the model, and are especially useful when the design space is largely unknown, and the researcher is attempting to locate key features [81].

However, as with all statistical analysis, the perfect method must sometimes give way to prior process knowledge and logistical considerations [81]. In this case, it was known that a minimum fill level was needed in order for powder to be lifted over the shafts by the paddles. This fill level has been displayed in Figure 3.11 as the dashed green line within the TSM 75 (N.B. the same was also true for the TSM 125, for both geometrical configurations).

Subsequently, it was decided that some combination of Screw Speed and Feed Rate, that produces this 'green line' Fill Level, should be chosen as the repeated RSM centre point. This is because this level of fill represents a change in the way the bulk flow behaves (as below this fill level no material can be seen flowing over the top of the screw shafts), and so would benefit from an increase in precision at this location. Unfortunately, this regime could not be generated in any of the systems whilst Screw Speed and Feed Rate were adjusted to their middle settings, so compro-

mises needed to be made (as is often the case for many RSM investigations [81]).

It is also true however, as long as a reasonable distribution of levels is observed throughout the design space, any issues that may arise due to non-rotatability should be negligible [81]. In any case, the models Goodness-of-Fit were vigorously assessed using the methods that shall be described further along within this Section, and were found as a whole to be excellent. Tables 3.2, 3.3 and 3.4 show the levels used for each system, at both Inlet 1 and 2. A description of how full the system looked visually from the centre of the barrel has also been provided.

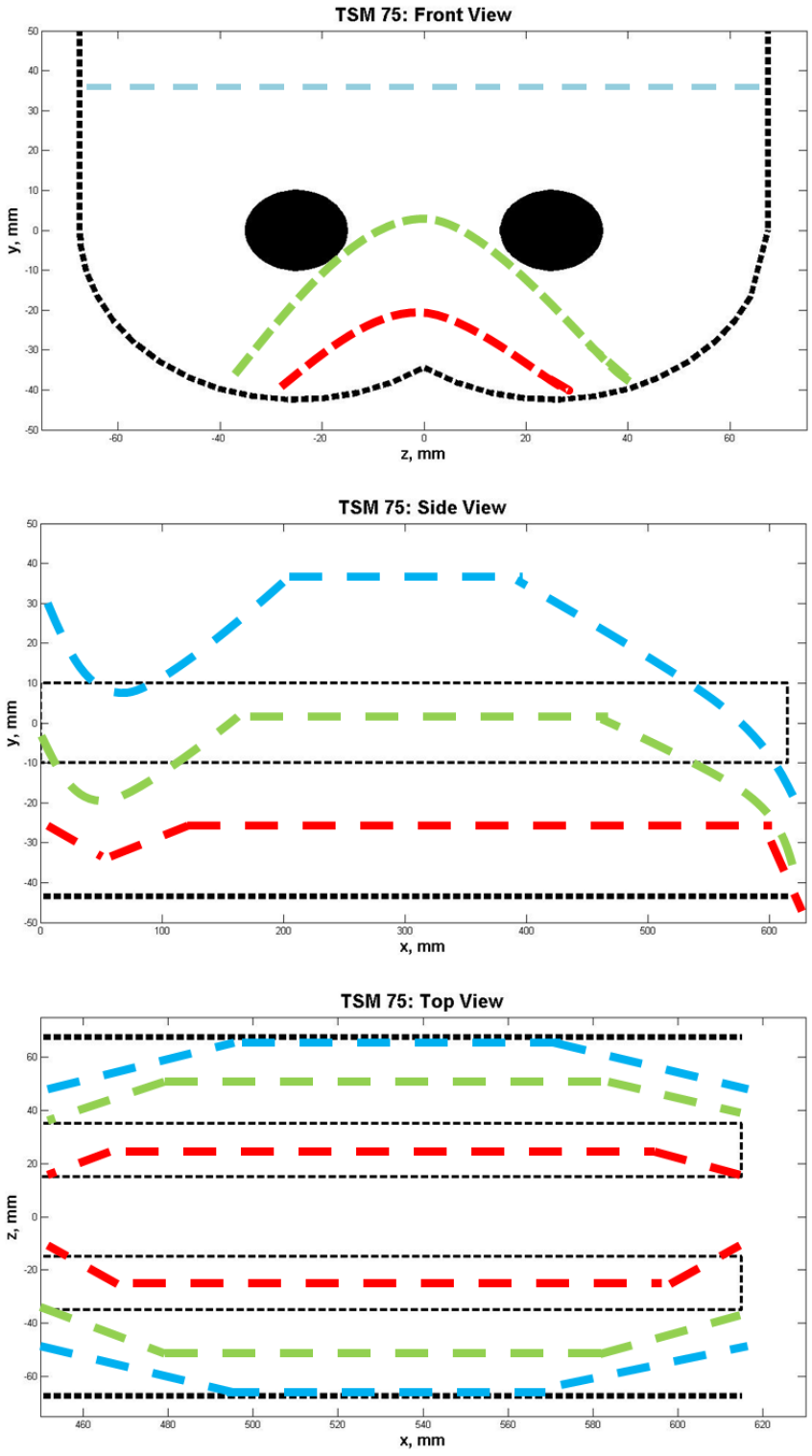

Figure 3.11: A schematic to show how different powder fill levels appeared to an observer within the TSM 75. The blue dashed line represents an almost full TSM, the green dashed line represents the minimum level of fill needed for powder to be pushed over the shafts and the red dashed line represents a starved fill level (the same phenomena could be seen in the TSM 125 using both geometrical configurations).

It was interesting to note that the visual fill levels displayed in Figure 3.11 seems to corroborate the work of Kingston and colleagues, as discussed in Section 1.3 [23]. This is because three separate flow regimes are inferred, namely: (1) At the Inlet, where powder initially tapers up to maximum, (2) the main powder flow regime along the barrel and (3) the Outlet, where free flowing powder, under the influence of gravity, creates a tapering down effect.

The experimental trials were started from empty (for each of the 3 systems) and run sequentially in the run order noted in tables 3.2, 3.3 and 3.4. Each experiment was allowed 5 minutes to stabilise after changing the process parameters (feed rate and screw speed) to ensure steady state before adding the tracer to the system.

Table 3.2: The TSM 75 DoE Screw Speed and Feed Rate Levels. A visual description of the fill level from the centre of the barrel has also been included.

Run	***Tip Speed*, m/s**	***Feed Rate*, kg/s**	***Fill Level Description.***
1	0.295	0.125	Mid fill level. Powder just beginning to be pushed over screw shafts.
2	0.295	0.258	Very high fill level. Powder is almost covering screws to the tip.
3	0.589	0.083	Very starved fill level.
4	0.153	0.125	Very high fill level. Powder is almost covering screws to the tip.
5	0.589	0.208	Starved fill level. Powder occasionally thrown over shaft due to tip speed.
6	0.295	0.067	Very starved fill level.
7	0.232	0.083	Mid fill level. Powder just beginning to be pushed over screw shafts.
8	0.295	0.125	Mid fill level. Powder just beginning to be pushed over screw shafts.
9	0.232	0.208	Very high fill level. Powder is almost covering screws to the tip.
10	0.295	0.125	Mid fill level. Powder just beginning to be pushed over screw shafts.
11	0.939	0.125	Very starved fill level. Powder violently thrown around inside due to tip speed.

Table 3.3: The TSM 125 DoE All Quadrant Screw Speed and Feed Rate Levels. A visual description of the fill level from the centre of the barrel has also been included.

Run	$TipSpeed, m/s$	$FeedRate, kg/s$	$FillLevelDescription$
1	0.204	0.278	Mid fill level. Powder just beginning to be pushed over screw shafts.
2	0.204	0.486	Very high fill level. Powder is almost covering screws to the tip.
3	0.602	0.167	Very starved fill level.
4	0.125	0.278	Very high fill level. Powder is . almost covering screws to the tip.
5	0.602	0.417	Starved fill level.
6	0.204	0.139	Starved fill level.
7	0.185	0.167	Just below shaft. Slight instances of powder being pushed over screw shafts.
8	0.204	0.278	Mid fill level. Powder just beginning to be pushed over screw shafts.
9	0.185	0.417	Very high fill level. Powder is almost covering screws to the tip.
10	0.204	0.278	Mid fill level. Powder just beginning to be pushed over screw shafts.
11	0.702	0.278	Very starved fill level.

Table 3.4: The TSM 125 DoE Quadrant to Anchors Screw Speed and Feed Rate Levels. A visual description of the fill level from the centre of the barrel has also been included.

$\boldsymbol{Run}$	$\boldsymbol{TipSpeed, m/s}$	$\boldsymbol{FeedRate, kg/s}$	$\boldsymbol{FillLevelDescription}$
1	0.204	0.278	Mid fill level. Powder just beginning to be pushed over screw shafts.
2	0.204	0.486	Very high fill level. Powder is almost covering screws to the tip.
3	0.602	0.167	Very starved fill level.
4	0.105	0.278	Very high fill level. Powder is almost covering screws to the tip.
5	0.602	0.417	Starved fill level.
6	0.204	0.139	Starved fill level.
7	0.185	0.167	Just below shaft. Slight instances of powder being pushed over screw shafts.
8	0.204	0.278	Mid fill level. Powder just beginning to be pushed over screw shafts.
9	0.185	0.417	Very high fill level. Powder is almost covering screws to the tip.
10	0.204	0.278	Mid fill level. Powder just beginning to be pushed over screw shafts.
11	0.702	0.278	Very starved fill level.

As the algorithm will attempt to approximate the system to a second order model, it is good practice to inspect the structure of data to ensure this is a suitable framework. Subsequently, with the aid of process knowledge, a decision must be taken as to whether a second order model can pro-

vide a reasonable approximation, or if a transformation of the data set is required [81]. For reasons that will be discussed further in Chapters 4 and 6, both dependent variables τ and σ^2 displayed strong inverse relationships with Screw Speed, so it became clear that they would need to be transformed.

Subsequently, τ was transformed to Average Velocity (axial distance divided by τ) and σ^2 was recast as $1/\sigma^2$. As the digital camera used to calculate these metrics (using the method described in Section 3.2) recorded at a rate of 30 frames/second, the precision of the instrumentation was deemed to be in the region of between a tenth and a hundredth of a second. Therefore, the results τ and σ^2 have been reported to 2 decimal places within the results (which usually meant 3 or 4 significant figures). Once the terms had been transformed for use in an RSM however (via the divisions mentioned previously), a more conservative 3 significant figures was always applied. RSM error, as a result of random variations in the method, will therefore be quantified within metrics such as R^2.

The next step in the procedure is to remove terms from Equation 3.12 using the backwards elimination approach. Term removal is deduced via an ANOVA, where each term is given associated P-values, which are used to determine with 95% confidence (usually, but the user may specify any percentage) whether they are significant. This is an iterative process, where the least significant term is removed from the model each time, before proceeding to re-calculate the model and subsequently perform another ANOVA on the remaining terms in the model [84]. The method is also hierarchical in the sense it will not remove a first order term, regardless of significance, if the IV is present in some form within a second order term. The procedure terminates once all the highest order IV terms that remain in the model are deemed statistically significant by the ANOVA.

Backwards elimination (from second, to first, to zero order terms) was preferred for eliminating terms from 3.12, as this allows the algorithm to assess every term in the model (and only retain curvature or interaction terms if statistically significant). If the first order terms were not present in the model from the start of the ANOVA, then the model may deduce higher order terms are required (falsely concluding a statistically significant curved relationship and/or interaction).

Furthermore, the model has been given in terms of coded and uncoded units. Coded units are the interpretation of the model where each predictor and dependent variable has had it's mean subtracted before the model has been calculated. This has the effect of bringing the constant term in the coded model to the estimated mean value of the dependent variable.

This method centres the variables such that the models coded coefficients represent the expected

magnitude of the response to a one unit change in the predictor. When all predictors are at their mean value the mean value of the response is estimated to be the models constant term.

Therefore, in the coded model the positive and negative signs present in front of the models first order terms will indicate to the researcher if the predictor is having a positive or negative effect upon the overall outcome. The uncoded units on the other hand calculate the dependent variable magnitude directly. It is for these reasons that the first order terms sometimes change signs between coded and uncoded models. As the first order terms are retained preferentially this also has the effect of the second order and interaction term coefficients remaining identical for both coded and uncoded unit models.

Once the RSM has been constructed, the following properties must be inspected in order to further validate if: (1) any further data transformation is required, and/or (2) if the correct number and type of model terms have been retained:

- The model's residuals plots should be examined. This includes: a check that the error is approximately normally distributed via a Normal Probability Plot and Histogram; ensuring that the error is randomly distributed by ensuring no underlying structure through a Residual vs. Fits Plot; and finally, ensuring there is no correlation between error and experimental run order via a Residual vs. Observation Order Plot. A example of these plots for the TSM 75: Velocity Inlet 1 RSM has been provided as Figure 3.12. The overall objective here is to ensure that the amount of error is consistent across the model (by examining distribution) and that the overall structure of the error is random.

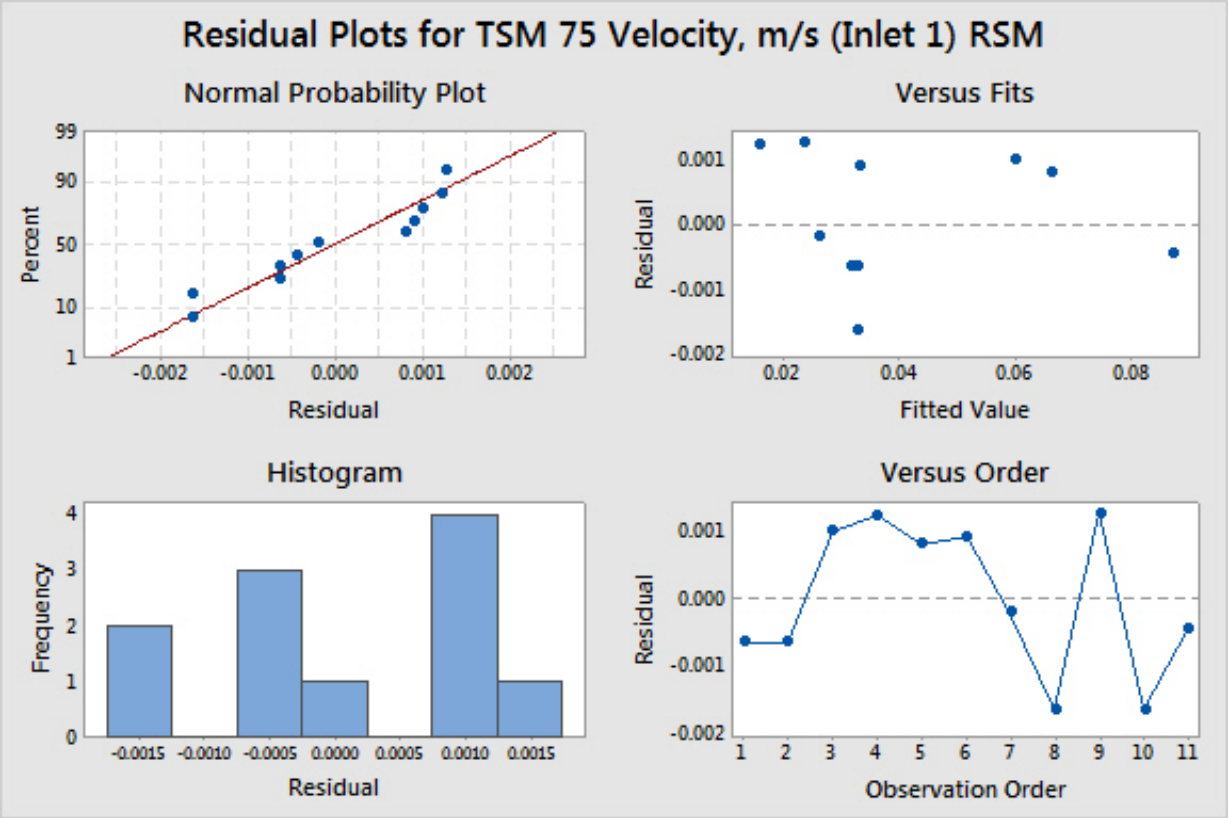

Figure 3.12: An example of the Residuals Plots for an RSM.

- R^2: a measure of how closely the RSM predictions match the data.
- Adjusted R^2: a modified version of R^2 that penalises the user for including terms that do not improve the model any more than would be expected by chance [85].
- Predicted R^2: with this term Minitab systematically removes every data point in the model and recalculates the model of best fit. The new sub-models are then assessed to see how accurately they would predict the 'unseen' data point [85].
- Lack-of-Fit (L-o-F): this metric is calculated during the ANOVA and is another means of measuring how accurate the model will be at predicting new data points. It is performed by partitioning error into pure error (which is estimated from variation in the repeated centre points) and error due to Lack-of-Fit. From here it calculates the probability, using the P-Value, that the model accurately predicts the data. A good level to aim for is a L-o-F P-Value of 0.05 or greater (or a 95% probability that the model is accurately fitting the data set).
- Variance Inflation Factors (VIF). This is a measure of multicollinearity between the regression coefficients. A good value to aim for is anything less than 5.

It is important to note that whilst these metrics and precautions are useful whilst trying to construct the most robust model possible, they will never fully supersede a researchers background knowledge and intuition. Therefore, for a few of the models constructed some of these guidelines and tolerances were slightly relaxed, and model terms either retained or removed.

Each models Coded Coefficient tables has been provided in Chapter 4 and 6. These contain the β coefficients for each term retained in the model, complete with P-Values and VIFs. The values are coded as the models are constructed in Minitab using means centred data points. These tables are always followed by the actual equation, where the β constant values have been rescaled to predict the dependent variable magnitude directly. Furthermore, the Velocity models have been combined with the volumetric internal measure of both TSMs (determined after constructing each system to scale within Matlab as discussed in Section 3.1), to produce models of the overall Fill Level %. This has been given as equation 3.13.

$$Fill\ Level,\ \% = \frac{\tau \times \frac{Feed\ Rate,\ kg/s}{\rho}}{Vol} \times 100 \tag{3.13}$$

Where: ρ is the powder bulk density, kg/m^3 and Vol is the total volume of the TSM from Inlet to Outlet, m^3.

3.5 Positron Emission Particle Tracking (PEPT)

Positron Emission Particle Tracking (PEPT) is a powerful technique first pioneered in the 1980s within the University of Birmingham. The procedure may trace it's roots to Particle Emission Tomography (PET); widely used as an imaging technique within the field of medicine. In summary, the PEPT procedure seeks to analyse and understand an industrial process, via the monitoring of radioactively labelled particle movements during process operation [86].

The tracers selected for these trials were spherical resin particles, made radioactive through an anion exchange procedure [87]. The true density of these particles was 1.1 g/ml, and they were measured as being between 0.25-0.3 mm in diameter.

These tracers were selected from the ones on offer, as they bore the closest physical resemblance to the model powder under investigation; anhydrous Sodium Sulphate. As mentioned in Section 3.2, this material was measured as having a D_{50} of 0.18 mm, and has a true density of 2.68 g/ml [88].

One of the main assumptions of PEPT is that these tracer particles will behave like a typical particle of the model powder, Sodium Sulphate. However, whilst every care was taken to select a tracer that most closely matched the powder under investigation, the fact there will be differences with respect to: density, size, electrostatic properties and geometry, may introduce some unavoidable error into the results.

The tracers were subsequently tracked in time and space, during TSM 75 operation, by 2 radiation sensing detectors. The radiation sensing area encapsulated by each detector was 500 by 400 mm^2, which meant the TSM 75, with a total axial length of 750 mm, could not fit completely within the recording range. Therefore, only the last quarter of the mixing zones axial length, from 450-615 mm, could be accurately recorded. This section incorporates 11 of the total 39 mixing paddles per shaft. This has been displayed within Figure 3.13.

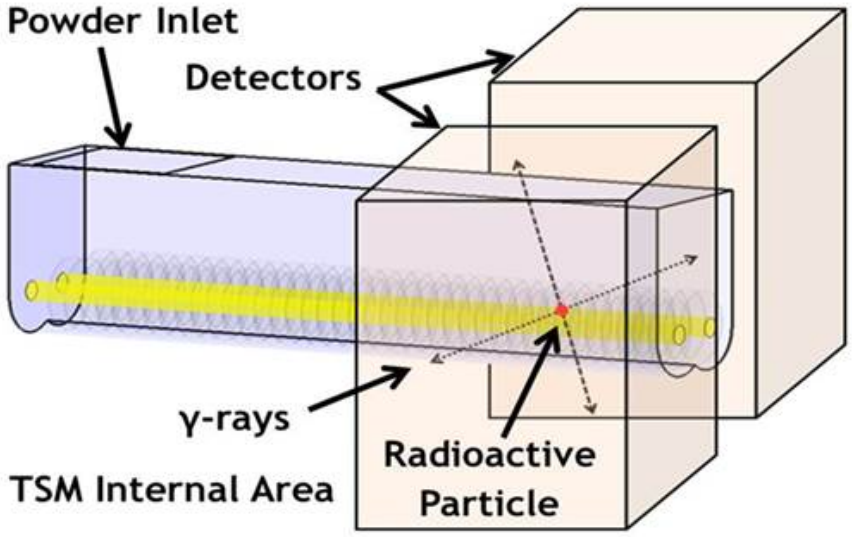

Figure 3.13: A schematic of a radioactive particle's position being recorded during TSM 75 operation.

The trials consisted of 4 experiments, where the Feed Rates and Screw Speeds were operated at either low or high levels. The low/high Feed Rates utilised during the trials were 0.067 kg/s and 0.125 kg/s respectively. Whereas, the low/high TSM 75 Screw Tip Speeds were 0.3 and 0.6 m/s. As the 4 trials lay within the design region investigated in Chapter 4, this allowed both investigations (i.e. that discussed in Chapter 5) to corroborate and expand upon each others findings.

Positron emission is a subset of β decay involving a proton inside the nucleus converting to a neutron. This triggers the release of a positron, the antimatter equivalent of an electron. The positron then rapidly collides with an electron causing both to be annihilated. This in turn causes the pro-

duction of a pair of back-to-back 511 keV γ rays to be emitted in almost opposite directions (180°$\pm$ 0.5°) [89].

The γ detectors are then able to detect where γ rays hit their surface, with 2 such coincident events defining a Line of Response (LoR). The assumption is then made that the annihilation site, and thus particle position, lies at some point along this line. In theory, only two such LoRs are needed at a given time in order to deduce particle position; as can be seen in the way the γ rays cross in Figure 3.13. Each LoR is also given a time stamp, the average of which being used to eventually give each particle location a time stamp.

In practice however, a number of events become corrupt due to Compton scattering and random coincidences (where two annihilation events are detected almost simultaneously). To reduce the noise that these events create in the dataset, an in-house procedure has been developed by the Positron Imaging Centre at the University of Birmingham, which shall now be summarised.

As the amount of spurious data is system dependent (being largely related to wall material and thickness), a radioactive tracer particle was first placed inside the TSM 75 under static conditions and monitored for 5 minutes. Whilst processing the data file, using the in-house 'Track' algorithm, the user is invited to select the fraction of LoRs to retain, f, and the number of LoRs used to determine each position, N.

The algorithm then proceeds to march through the dataset in time calculating a set of particle locations. For a set of N LoRs this involves: firstly calculating a position in space that lies the closest to all N LoRs, and secondly retaining a fraction f of the LoRs, that lie closest in proximity to the initial estimate, and recalculating the particle position in order to attain the final value.

In this investigation the commonly used N value of 250 was utilised, and the data re-processed using a variety of different f values. As the particle is stationary, any variation in particle position is assumed to be caused by error. Therefore, to minimise this error, the Root Sum of Squares Standard Deviation for all 3 spacial dimensions (x, y and z) was calculated according to Equation 3.14, and plotted with respect to the f value, and a global minima region located. This has been displayed as Figure 3.14.

$$\sigma = \sqrt{\sigma_x^2 + \sigma_y^2 + \sigma_z^2} \tag{3.14}$$

Where: σ is the Root Sum of Squares Deviation for all 3 spacial dimensions, σ_x is the Standard Deviation of the tracer along the x axis, σ_y is the Standard Deviation of the tracer along the y axis and σ_z is the Standard Deviation of the tracer along the z axis.

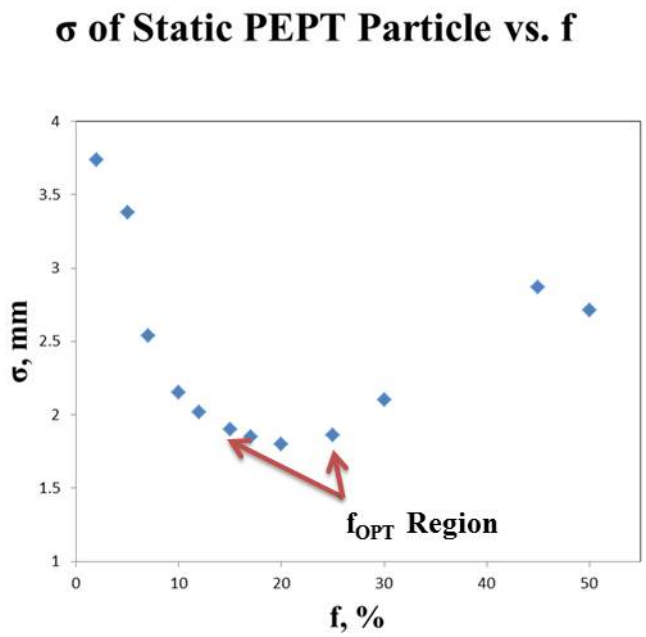

Figure 3.14: A plot of Root Sum of Squares Standard Deviation for all 3 spatial dimensions (x, y and z) vs. f to find f_{OPT} for the TSM 75 experiments.

For this system any f value within the local minima region of approximately 15-22% could be utilised, without making any real difference to the overall accuracy, as can be seen in Figure 3.14. Therefore, an f value of 17% was used to process all subsequent experimental data, and so this became known as f_{OPT}.

As the f_{OPT} value gave a Standard Deviation of 1.85 mm, for the stationary tracer's location, this gives an indication of the error associated with the PEPT procedure when monitoring particles within the TSM 75. However, as the particle is moving during the actual experimentation this may also increase error. Despite this, experience shows that particles travelling up to 1 m/s may be tracked to within an accuracy of 1 mm [86]. Therefore, as long as this speed is not exceeded, the error would not be expected to increase significantly from the stationary case; if at all.

The next stage in the process was to standardise the: x, y and z coordinate system, and remove any spurious particle locations that fall outside the systems boundaries. Figure 3.15 shows an example of the original dataset for the Low Screw Speed and High Feed Rate being treated in this manner within Matlab.

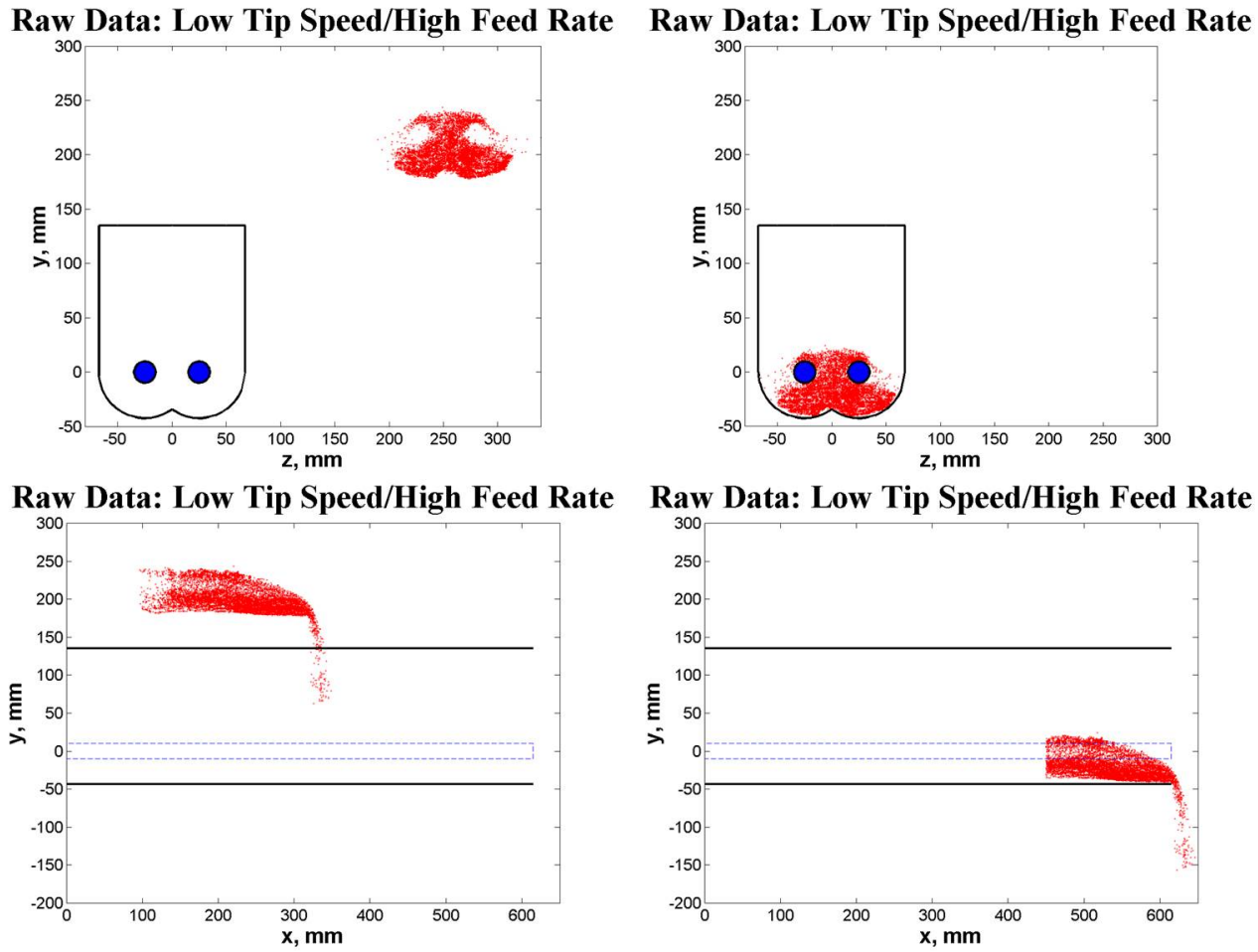

Figure 3.15: The PEPT data for the Low Tip Speed and High Feed Rate regime being moved to within the TSM 75 system boundaries, and spurious data points being cut.

The next stage in processing the raw data involved visually inspecting each tracers path in order to discern and remove spurious particle locations from within the system, and to ensure there were no large gaps. If a large gap was identified, then the tracer path in question had to be discarded.

The particle journeys were then augmented, through straight line interpolation, with extra particle locations to ensure that the gaps never exceeded 1 mm. This was completed in order to replace missing data points, and ensure each tracer's path was equally data rich, in order to generate accurate Occupancy and Velocity Plots. An example of this procedure being carried out has been displayed in Figure 3.16.

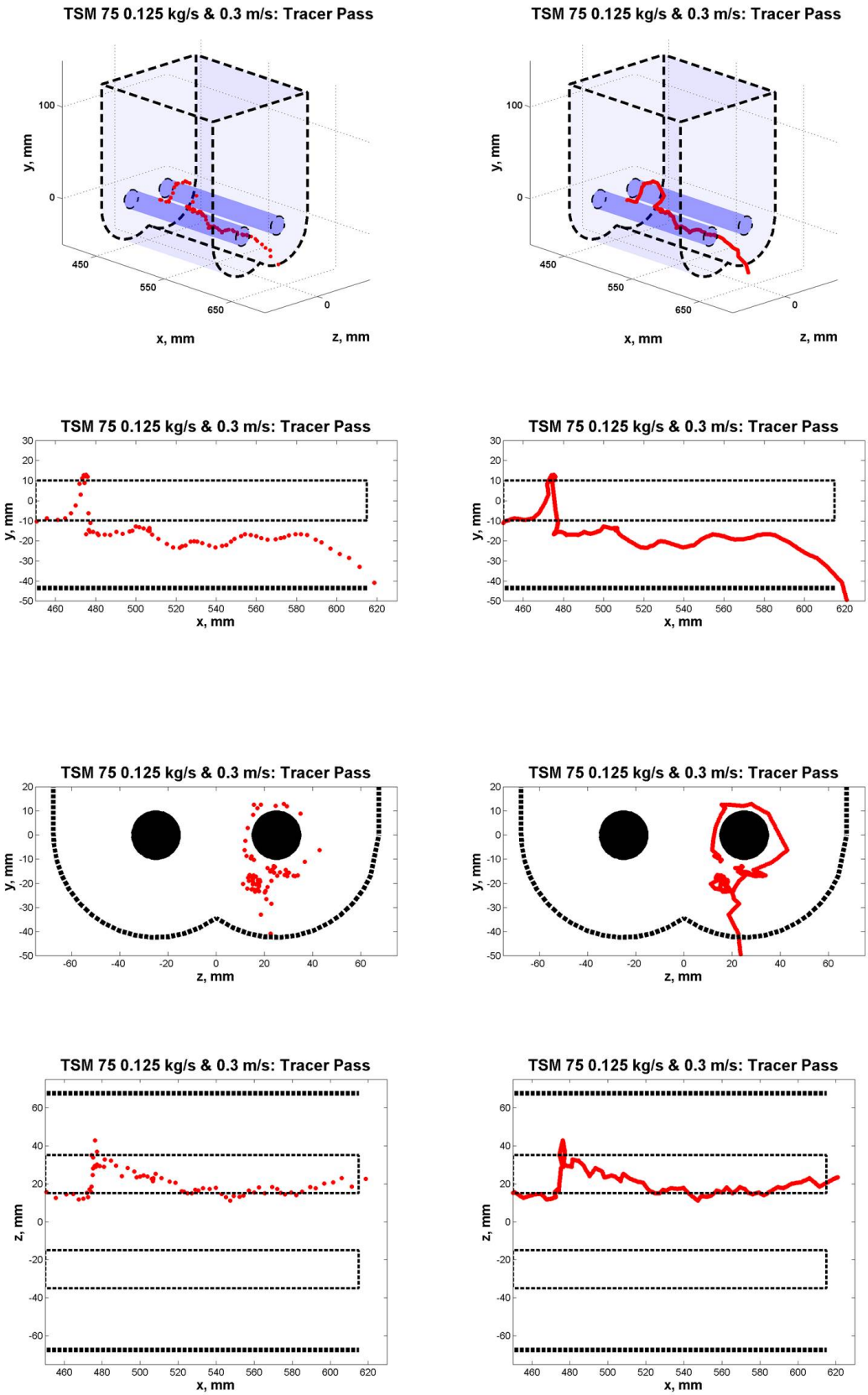

Figure 3.16: (Left) Firstly, a particle journey was visually inspected. (Right) Secondly, the particle path was augmented with extra locations, through linear interpolation, to ensure no gap exceeded 1 mm.

The radioactive particles were recycled through the system multiple times in order to achieve between 80-100 passes per experiment. This was essential in order to capture the various particle paths that may be taken during transit through the system. Each system was then divided into equally sized voxels of 25 mm x 25 mm x 25 mm within Matlab. As this was the discovered to be the smallest size to usually yield at least 30 different visits, across all 4 PEPT experiments (if the voxel was visited by a tracer at all).

Having 30 different tracer passes per voxel is generally seen as enough to ensure a close approximation to ergodicity, whilst generating Occupancy and Velocity Plots [89]. An example of the system being discretised has been provided as Figure 3.17.

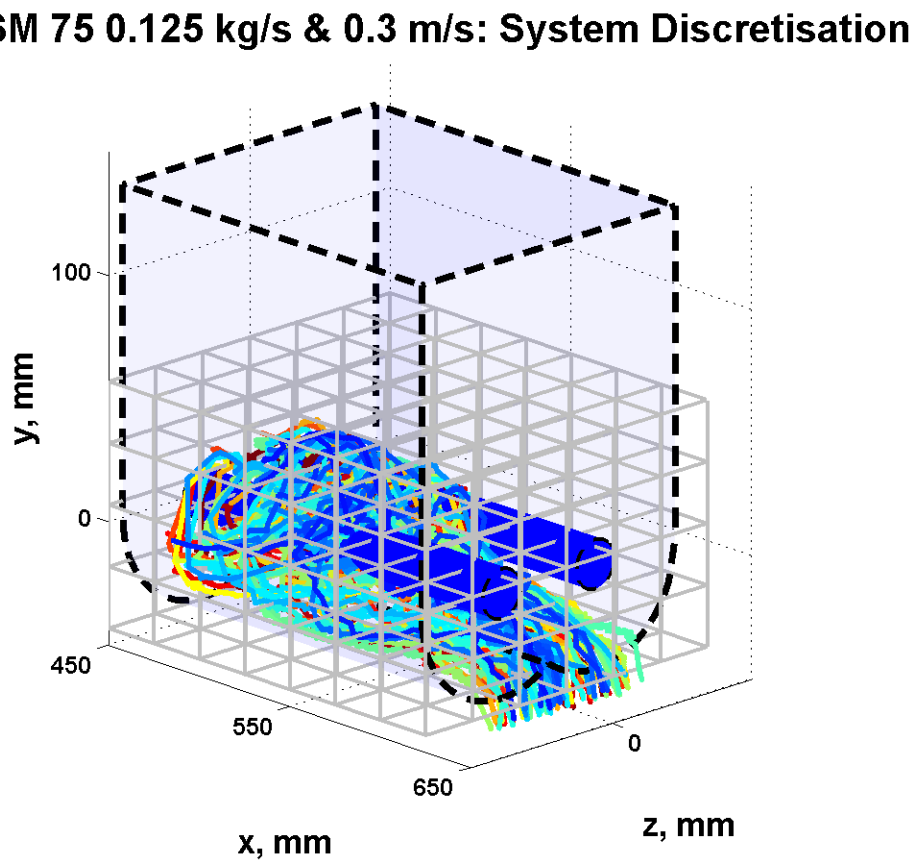

Figure 3.17: The system was discretised into 25 mm x 25 mm x 25 mm, to approximate ergodicity for the Occupancy and Velocity Plots.

Bespoke software was then written by the author in Matlab, able to slice the system along any plane of voxels desired, and to subsequently generate either: Occupancy or Velocity Plots, for the subsection being viewed.

The Occupancy Plots display, as a percentage, the total amount of time the tracers spent within

each of the voxels being viewed (in the form of a Colour Map). This information is then used to infer where the bulk spends the majority of its time during transport.

On the other hand, the Velocity Plots display, in m/s, the average velocity of the tracers within each of the voxels in the third spacial dimension, also in the form of a Colour Map (i.e. if the voxels displayed are within the x vs. y two dimensional plane, then the Colour Map would represent average velocity along the z axis).

Additionally, the velocity of the other 2 spacial dimensions is represented using Matlab's 'Quiver' function [90]. This function displays the 2 dimensional direction the particles are travelling through the use of an arrow, that emanates from the centre of each voxel. It also describes this 2 component velocity's magnitude through adjusting the arrows lengths, and by displaying the magnitude within each box as a number in m/s.

This information is then used to infer flow patterns of the bulk within the TSM 75. To calculate each particle locations velocity, in all three spacial dimensions (x, y and z), the robust 6-point method, developed specifically for PEPT [89], was employed. This has been provided as Equation 3.15.

$$\begin{aligned}\overrightarrow{v_i} = 0.1\left(\frac{\overrightarrow{P_{i+5}} - \overrightarrow{P_i}}{\overrightarrow{t_{i+5}} - \overrightarrow{t_i}}\right) + 0.15\left(\frac{\overrightarrow{P_{i+4}} - \overrightarrow{P_{i-1}}}{\overrightarrow{t_{i+4}} - \overrightarrow{t_{i-1}}}\right) + 0.25\left(\frac{\overrightarrow{P_{i+3}} - \overrightarrow{P_{i-2}}}{\overrightarrow{t_{i+3}} - \overrightarrow{t_{i-2}}}\right) \\ +0.25\left(\frac{\overrightarrow{P_{i+2}} - \overrightarrow{P_{i-3}}}{\overrightarrow{t_{i+2}} - \overrightarrow{t_{i-3}}}\right) + 0.15\left(\frac{\overrightarrow{P_{i+1}} - \overrightarrow{P_{i-4}}}{\overrightarrow{t_{i+1}} - \overrightarrow{t_{i-4}}}\right) + 0.1\left(\frac{\overrightarrow{P_i} - \overrightarrow{P_{i-5}}}{\overrightarrow{t_i} - \overrightarrow{t_{i-5}}}\right)\end{aligned} \tag{3.15}$$

Where: $\overrightarrow{v_i}$ is the particle velocity for the ith particle, $\overrightarrow{P_i}$ is the position of the ith particle along either the: x, y or z axis (depending on which of the 3 velocity components is being calculated) and $\overrightarrow{t_i}$ is the time stamp of the ith particle.

Finally, a short mixing study was conducted, which was modelled on the work carried out by Kingston and colleagues, and discussed in Section 1.3 [22, 6]. To achieve this, all the 80-100 PEPT tracers used for a particular experiment were divided into either 'blue' or 'red' groups; based upon whether they entered the system on the positive side of the z axis or the negative side.

The particles were then monitored until leaving the system at 615 mm along the x axis. Next, the tracers were divided into 2 'samples', determined by where they were located along the z axis, being either in the positive or negative half of the axis. Equation 1.2 was then used to determine how well mixed the particles became, after travelling axially through the TSM 75 from 450 to 615 mm along the x axis.

Chapter 4

Validating a Digital Image Processing (DIP) strategy used to analyse axial flow of dry powder within a large-scale, counter-rotational, intermeshing Twin-Screw Mixer (TSM).

4.1 Results and Discussion

4.1.1 Validation of Digital Image Processing (DIP) Algorithm and Response Surface Model (RSM) Investigation for TSM 75.

The aims of this Section are twofold:

- To validate the the DIP strategy discussed in Section 3.2 for measuring a RTD.
- Once validated, to use the RTD data to analyse the TSM 75 using Response Surface Methodology.

RTD metrics generated by the methods discussed in Chapter 3 have been displayed in Tables 4.1 and 4.2. As discussed previously, this method involved recording the outlet of the TSM under various different Screw Speeds and Feed Rates. For each set of conditions a pulse of tracer was added to the system and the concentration of red tracer was measured using digital image analysis. This concentration could then be plotted with respect to time to obtain the concentration curve.

The concentration curve data was then recast as the residence time function, $E(t)$, as per equation 4.1. From this function the mean residence time, τ, and the curve variance, σ^2, could be calculated from equations 4.2 and 4.3 respectively.

$$E(t) = \frac{C}{\sum_0^\infty C\Delta t} \tag{4.1}$$

$$\boldsymbol{\tau} = \frac{\sum_0^t tC\Delta t}{\sum_0^\infty C\Delta t} \tag{4.2}$$

$$\sigma^2 = \frac{\sum_0^\infty t^2 C\Delta t}{\sum_0^\infty C\Delta t} - \boldsymbol{\tau^2} \tag{4.3}$$

Upon examining the data, one of the first things to note is the SE of τ, as a result of the DIP processing strategy, generally increases at lower screw speeds. This could could be because the tracer is being distributed into more video frames (as the curve variance tends to increase with increased residence time). Consequently, the algorithm is called upon to discern sample concentrations of lower magnitudes (as the same amount of tracer is spread across more frames), leading to increased variability in the RTD metrics generated. It is encouraging to note however, that no SE could be detected to three decimal places after recasting the values to represent Average Velocity in m/s.

The σ^2 metric follows a similar pattern for the associated SE generated as the SE generated for τ, and for similar reasons. However, in this instance the issue is compounded by the σ^2 calculation being more sensitive to slight variations in tracer concentration in the samples. The precision still seems more than acceptable however, with only two of the slowest screw speeds (Runs 4 and 9) yielding a standard error above 1 s^2, and even then only for results generated from Inlet 1.

The Fill % SE, being a transformation of τ, is also acceptable, as the associated SE is never greater than 2% (and in the majority of cases less than 1%). It can be concluded therefore, through the examination of the SE, that the method detailed in Section 3.2 shows a high degree of precision in terms of repeatability.

As described in Section 3.4, Fill Volume % refers to how full the TSM would be should the powders bulk density remain the same as at rest as it is at steady state (for a given bulk axial velocity). This was chosen because it would be nearly impossible to remeasure the bulk density at various different screw speeds and feed rates, so the bulk density of the powder at rest offers a good baseline for comparison between different experiments (and later different sized TSMs to assess if the powder has a tendency to consolidate more at larger volumes, see Chapter 6).

Table 4.1: The TSM 75 Inlet 1 RTD metrics. The curves were generated 5 times using the procedure outlined in Section 3.2, this allowed a calculation of the SE for τ and σ^2, and so subsequently the SE of the Fill % and Velocity. The code refers to the TSM 75 Screw Tip Speed and powder Feed Rate used in the DoE discussed in Section 3.4, which may be referenced in Tables 3.1 and 3.2.

$\boldsymbol{Run\ (Code)}$	$\boldsymbol{\tau, s}$	$\boldsymbol{SE(\tau), s}$	$\boldsymbol{\sigma^2, s^2}$	$\boldsymbol{SE(\sigma^2), s^2}$	$\boldsymbol{V, m/s}$	$\boldsymbol{Fill, \%}$
$\mathbf{1\ (Mid \backslash Mid)}$	17.39	0.07	5.08	0.19	0.032±0.000	22.62±0.50
$\mathbf{2\ (Mid \backslash V.High)}$	17.91	0.06	6.64	0.31	0.031±0.000	48.07±0.94
$\mathbf{3\ (High \backslash Low)}$	9.13	0.01	2.74	0.06	0.061±0.000	7.88±0.05
$\mathbf{4\ (V.Low \backslash Mid)}$	31.97	0.26	15.76	2.58	0.017±0.000	41.58±1.96
$\mathbf{5\ (High \backslash High)}$	8.27	0.01	1.59	0.05	0.067±0.000	17.90±0.14
$\mathbf{6\ (Mid \backslash V.Low)}$	16.48	0.06	5.42	0.59	0.034±0.000	11.49±0.26
$\mathbf{7\ (Low \backslash Low)}$	21.45	0.09	8.37	0.57	0.026±0.000	18.53±0.44
$\mathbf{8\ (Mid \backslash Mid)}$	17.70	0.21	4.45	0.61	0.031±0.000	23.02±1.55
$\mathbf{9\ (Low \backslash High)}$	21.81	0.08	8.09	1.40	0.025±0.000	47.20±0.96
$\mathbf{10\ (Mid \backslash Mid)}$	18.00	0.08	5.31	0.31	0.031±0.000	23.41±0.61
$\mathbf{11\ (V.High \backslash Mid)}$	6.35	0.00	1.86	0.15	0.087±0.000	8.26±0.01

Table 4.2: The TSM 75 Inlet 2 RTD metrics. The curves were generated 5 times using the procedure outlined in Section 3.2, this allowed a calculation of the SE for τ and σ^2, and so subsequently the SE of the Fill % and Velocity. The code refers to the TSM 75 Screw Tip Speed and powder Feed Rate used in the DoE discussed in Section 3.4, which may be referenced in Tables 3.1 and 3.2.

$\boldsymbol{Run\ (Code)}$	$\boldsymbol{\tau, s}$	$\boldsymbol{SE(\tau), s}$	$\boldsymbol{\sigma^2, s^2}$	$\boldsymbol{SE(\sigma^2), s^2}$	$\boldsymbol{V, m/s}$	$\boldsymbol{Fill, \%}$
$\mathbf{1\ (Mid\backslash Mid)}$	5.57	0.12	2.93	0.19	0.035±0.000	20.63±0.80
$\mathbf{2\ (Mid\backslash V.High)}$	5.60	0.05	1.75	0.10	0.035±0.000	42.80±0.82
$\mathbf{3\ (High\backslash Low)}$	3.41	0.01	1.12	0.02	0.057±0.000	8.38±0.03
$\mathbf{4\ (V.Low\backslash Mid)}$	7.58	0.10	6.93	0.41	0.026±0.000	28.07±0.77
$\mathbf{5\ (High\backslash High)}$	3.06	0.00	0.45	0.00	0.064±0.000	18.85±0.00
$\mathbf{6\ (Mid\backslash V.Low)}$	6.15	0.02	2.53	0.04	0.032±0.000	12.20±0.06
$\mathbf{7\ (Low\backslash Low)}$	7.85	0.01	4.35	0.04	0.025±0.000	19.29±0.04
$\mathbf{8\ (Mid\backslash Mid)}$	5.88	0.07	2.30	0.16	0.033±0.000	21.77±0.50
$\mathbf{9\ (Low\backslash High)}$	5.31	0.01	2.87	0.02	0.037±0.000	32.68±0.11
$\mathbf{10\ (Mid\backslash Mid)}$	6.69	0.05	2.53	0.12	0.029±0.000	24.78±0.38
$\mathbf{11\ (V.High\backslash Mid)}$	1.98	0.02	0.40	0.03	0.098±0.000	7.34±0.13

As the final intention was to approximate the results to a second order model, using the procedure outlined in Section 3.4, good practice dictates that a visual examination of the data structure should first be conducted. This was in order to assess any obvious trends that would not be captured using a second (or first) order approximation and so necessitate a data transformation. The model equation has been provided as equation 4.4.

$$\begin{aligned} y = \beta_0 &+ \beta_1 Tip\ Speed,\ m/s + \beta_2 Feed\ Rate,\ kg/s \\ &+ \beta_3 (Tip\ Speed,\ m/s)^2 + \beta_4 (Feed\ Rate,\ kg/s)^2 \\ &+ \beta_5 (Tip\ Speed,\ m/s) \times (Feed\ Rate,\ kg/s) + \varepsilon \end{aligned} \tag{4.4}$$

Whilst examining τ and σ^2, by plotting the values with respect to Screw Tip Speed, it became clear that both cases displayed a strong inverse relationship between the variables. This can be seen in the left hand side of Figure 4.1.

Intuitively, it made sense that the speed of the screws and τ are to some degree inversely proportional, as it is the screws turning motion that drives powder flow through the system. The extent

to which this factor dominates, regardless of Feed Rate (and so Fill Level), was nevertheless a very interesting observation.

The σ^2 metric being inversely proportional to screw speed may also be considered to be intuitive. The reasons for this assertion are twofold: (1) the longer the powder remains in the TSM 75 (due to an increased τ) the more opportunity it has to spread in an axial fashion, and (2) the particle momentum generated at higher speeds may result in more uniform flow patterns, and therefore less variation in the particle path lengths travelled (due to an increase in bulk momentum facilitating a smoother flow regime, rather than being bumped along in a more piecemeal fashion by the paddles). At this initial glance however, it appears that Screw Tip Speed may not dominate the dependent variable to the degree witnessed previously for τ, and therefore Feed Rate (and subsequently Fill Level) may have a much larger role to play in the final results.

Armed with this knowledge it became clear that both RTD metrics (τ and σ^2) should be transformed to remove any inverse structure before undergoing the statistical regression described in Section 3.4. Therefore, instead of τ, the regression was performed using the Average Velocity as the dependent variable, which is simply τ^{-1} multiplied by a constant (the axial distance from the tracer inlet to the TSM 75 outlet). Using Average Velocity rather than residence time also had the welcome convenience of allowing direct comparisons between bulk axial flow speed variation between Inlet 1 and Inlet 2 (as well as for making direct comparisons with the TSM 125 in Chapter 6).

For the σ^2 metric no convenient, easy to conceptualise, inverse transformation exists. For this reason the statistical regression was simply performed upon σ^2 in its inverse form. Both these inverse transformations can be viewed, plotted with respect to Screw Tip Speed, on the right hand side of Figure 4.1.

The data was then fitted to equation 4.4 and an ANOVA performed to remove terms should they not be statistically significant. The models are presented in two ways within this section: 1) in coded units when all the variables have been mean centred so the output becomes how far the prediction falls from the mean response value and 2) uncoded units where the output of the model is the actual response prediction in the units given. Mean centering the data set can sometimes lead to the first order terms changing sign between coded and uncoded versions of the model due to the centering of the data sets.

The first order terms are always retained within the model if they feature in a higher order term, so that the curvature terms and higher order terms are only retained if statistically significant during the ANOVA procedure. The coded version of the model is given as it allows the researcher to

see if the independent variable generally has a positive or negative effect upon the response (by looking at the sign of the first order terms coefficients).

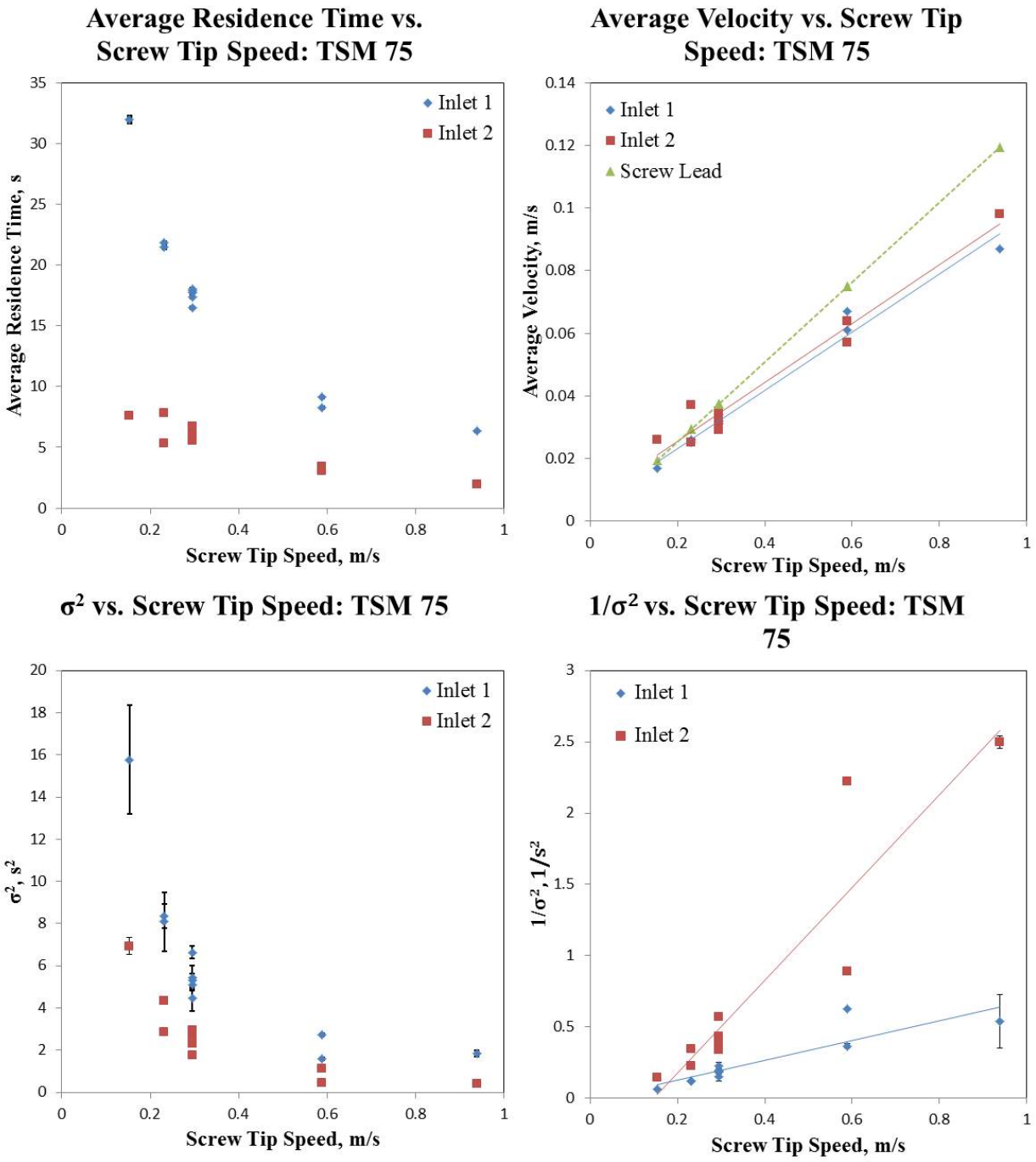

Figure 4.1: The RTD metrics for the TSM 75 plotted vs. Screw Tip Speed. The error bars denote the SE (the error bars are present for all data points but some are so small they cannot be clearly distinguished). A straight line regression has been generated in Excel for the two graphs on the right hand side, and the associated constants have been provided in Table 4.3.

The extent to which the RTD data, displayed on the left hand side of Figure 4.1, exhibited inverse behaviour with respect to Screw Tip Speed was also examined. This was achieved using Excel to compute straight line equations of best fit, for each of the inverse data transformations (which have been provided on the right hand side of Figure 4.1).

As Screw Lead is the measure of how rapidly the screw flight orientation propagates axially downstream, this has also been provided within the Velocity vs. Screw Tip Speed plot. This is in order to ascertain how closely related the moving geometry tracks bulk powder Average Velocity. This is because if axial transport was 100% efficient, then the bulk would be expected to move axially the distance of the screw lead for every screw revolution. The straight line equation parameters generated by Excel have all been provided within Table 4.3.

Table 4.3: TSM 75: Screw Speed vs. RTD metrics straight line equation parameters (as displayed in 4.1).

Dependent Variable	**Gradient**	**Constant**	$\boldsymbol{R^2}$
$\boldsymbol{Screw\ Lead, m/s}$	0.13	0.00	N/A
$\boldsymbol{V(Inlet, 1), m/s}$	0.09	0.00	0.98
$\boldsymbol{V(Inlet, 2), m/s}$	0.09	0.01	0.96
$\boldsymbol{1/\sigma^2(Inlet, 1), 1/s^2}$	0.70	-0.01	0.79
$\boldsymbol{1/\sigma^2(Inlet, 2), 1/s^2}$	3.25	-0.47	0.85

The R^2 values for both Velocity equations given in Table 4.3 show a large degree of correlation, with numbers in excess of 0.96. This again demonstrates how largely dominated this parameter is to the overall Screw Tip Speed, regardless of the Feed Rate. The gradients for both equations are also equal to 2 decimal places. However, the constant value in the straight line equation is slightly higher from Inlet 2 than Inlet 1 (0.01 and 0.00 respectively).

This may be explained by the Velocity results within the TSMs second section not being influenced by the phenomenon witnessed as the bulk enters the system. Within this region (at the beginning of the TSMs axial length) a tapering up to maximum fill level can be seen visually, as the powder is brought up to maximum speed by the screws (as described in Figure 3.11).

Conversely, at the TSMs exit a tapering down effect can be discerned, as powder falls out of the system under the influence of gravity. This phenomena not only creates a rapid increase in Velocity along the downward trajectory, but the sudden reduction in mass also creates the tapering down effect, as the bulk tries to leave the system as rapidly as possible. This in turn causes an increase in flow in the axial direction.

The equations also reveal that the Average Velocity measured at Inlet 1 is always about 70% of the screw lead, showing that to some degree the two tapering effects described previously must cancel each other out. Whilst the Average Velocity at Inlet 2 begins at around 90% of Screw Lead for the lower Screw Tip Speeds, and dropping to around 77% for the higher Screw Tip Speeds (within the screw speed region examined). This indicates that at higher Screw Tip Speeds more bulk powder (as a proportion of the total) will slip through the gaps between the paddles and the TSM wall. Furthermore, at extremely high screw speeds, powder will be thrown haphazardly into the air, as noted in Table 3.2 Run 11.

The curve variance is less adequately described by Screw Speed alone, because the R^2 values for the straight line transformations drop to around 80%. Furthermore, as the straight line gradients for the reciprocal of σ^2 equations are very different, axial transport distance travelled by the bulk must play a far greater role for this parameter. This is a logical deduction, as the longer the powder stays in the system, the more chance it has to disperse in an axial fashion.

Once the data had been transformed to remove non-first and second order behaviour from the dependent variables, i.e. using Average Velocity and σ^2 in its inverse form, the RSMs could then be constructed. Table 4.4 displays the RSM model for Average Velocity at Inlet 1 in its coded coefficient form and Equation 4.5 shows the same model in uncoded units. The model scores very highly on all the statistical metrics used to measure the Goodness-of-Fit and so should be highly accurate.

Table 4.4: Coded Coefficient Table for TSM 75 Inlet 1, Velocity Model. The hierarchical model retained terms using 95% confidence, determined via the P-values. Metrics to determine the Goodness-of-Fit included: R^2 of 99.74%, Adjusted R^2 of 99.57%, a Predicted R^2 of 92.77% and a Lack-of-Fit P-value greater than 0.05.

Term	**Coefficient**	**P-Value**	**VIF**
$\boldsymbol{Constant}$	0.042332	0.000	
$\boldsymbol{Tip\ Speed}$	0.10800	0.000	3.12
$\boldsymbol{Feed\ Rate}$	0.00949	0.270	1.09
$(\boldsymbol{Tip\ Speed})^2$	-0.04296	0.003	3.25
$(\boldsymbol{Tip\ Speed}) \times (\boldsymbol{Feed\ Rate})$	0.1944	0.014	1.16

$$Velocity,\ m/s\ (Inlet\ 1) = 0.00375 + 0.1138 Tip\ Speed,\ m/s - 0.0649 Feed\ Rate,\ kg/s \\ -0.04296(Tip\ Speed,\ m/s)^2 + 0.1944(Tip\ Speed,\ m/s) \times (Feed\ Rate,\ kg/s) \tag{4.5}$$

For Inlet 1, the coded units reveal that an increase in Tip Speed and Feed Rate both generally increase the velocity overall. There is also an interaction between Tip Speed and Feed Rate.

Table 4.5 displays the RSM model for the inverse of σ^2 at Inlet 1 in its coded coefficient form and Equation 4.6 shows the same model in uncoded units. As before, the model scores very highly on all the statistical metrics used to measure the Goodness-of-Fit and so should again be highly accurate.

Table 4.5: Coded Coefficient Table for TSM 75 Inlet 1, $(\sigma^2)^{-1}$. The hierarchical model retained terms using 95% confidence, determined via the P-values. Metrics to determine the Goodness-of-Fit included: R^2 of 99.21%, Adjusted R^2 of 98.41%, a Predicted R^2 of 73.84% and a Lack-of-Fit P-value greater than 0.05.

Term	**Coefficient**	**P-Value**	**VIF**
$\boldsymbol{Constant}$	0.3223	0.000	
$\boldsymbol{Tip\ Speed}$	1.0508	0.000	3.23
$\boldsymbol{Feed\ Rate}$	0.830	0.003	1.70
$\boldsymbol{(Tip\ Speed)^2}$	-0.955	0.002	3.70
$\boldsymbol{(Feed\ Rate)^2}$	-6.36	0.050	1.99
$\boldsymbol{(Tip\ Speed) \times (Feed\ Rate)}$	6.515	0.001	1.24

$$1/\sigma^2,\ 1/s^2\ (Inlet\ 1) = -0.1114 + 0.874 Tip\ Speed,\ m/s + 0.110 Feed\ Rate,\ kg/s \\ -0.955(Tip\ Speed,\ m/s)^2 - 6.36(Feed\ Rate,\ kg/s)^2 \\ +6.515(Tip\ Speed,\ m/s) \times (Feed\ Rate,\ kg/s) \tag{4.6}$$

For Inlet 1 the inverse curve variance is also effected by an interaction between the Tip Speed and Feed Rate. The Tip Speed and Feed Rate will also generally have a positive effect upon the response (as the first order coded units are positive). Therefore, this means the reverse will be true when the inverse curve variance is recast as σ^2.

The top two plots in Figure 4.2 show three dimensional data plots and RSMs for Inlet 1 of the TSM 75 Average Velocity and inverse of σ^2 experiments. Below this in the same figure is the two dimensional response surface plots of the same models. However, the inverse curve variance plot has been converted back to its non-reciprocal σ^2 form.

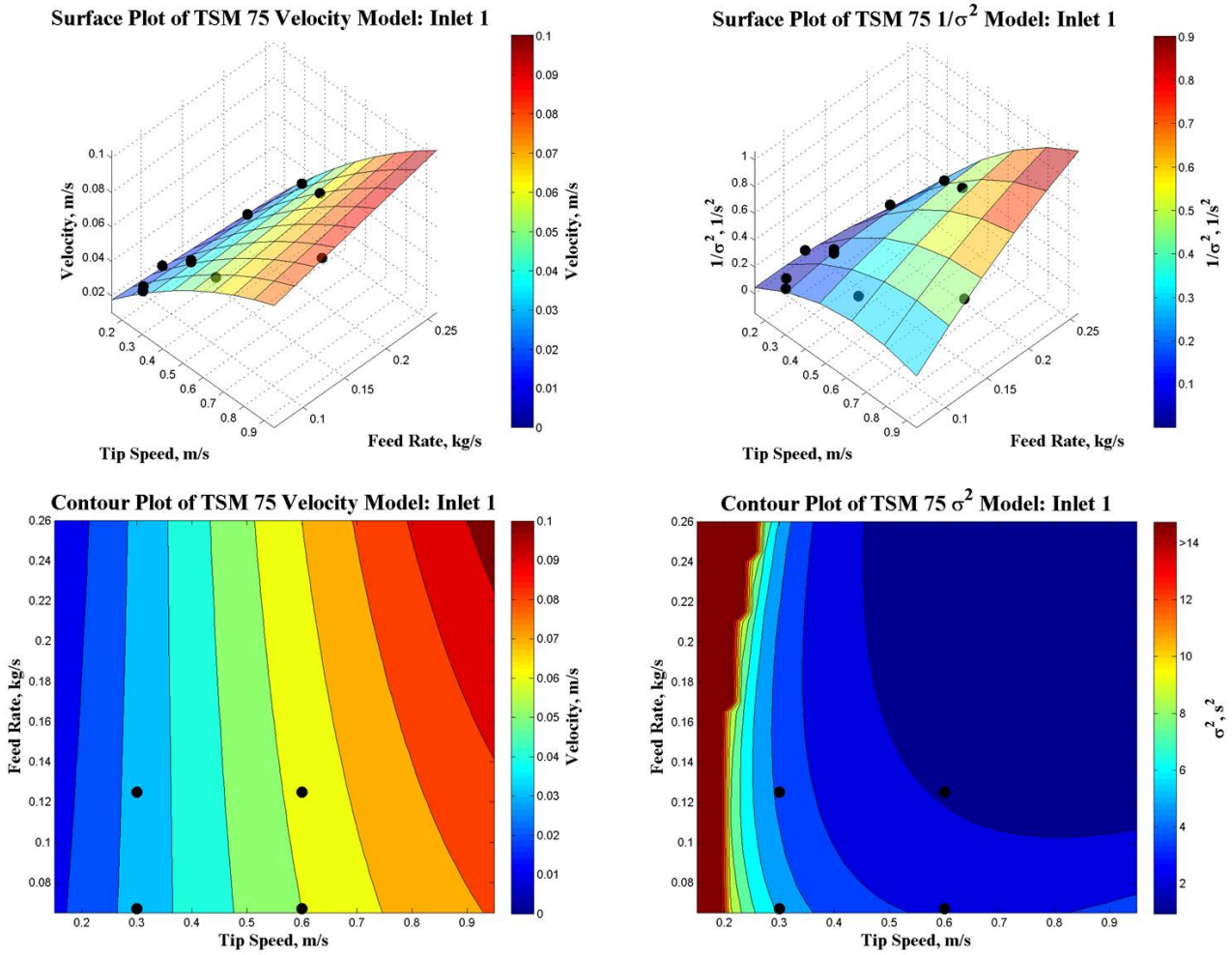

Figure 4.2: (Left) The TSM 75 Inlet 1 Velocity Model, displayed as a 3D surface plot (top) and a 2D contour plot (bottom). (Right) The TSM 75 Inlet 1 $1/\sigma^2$ Model, displayed as a 3D surface plot (top), and displayed in non-reciprocal form as a 2D contour plot (bottom). The black dots displayed in the contour plots represent the four regimes investigated during the PEPT trials, whereas the black dots in the 3D plots are the RTD metrics obtained via the DIP obtained RTDs.

The Inlet 1 Average Velocity Response Surface shows clearly how the response variable is dominated by screw speed within most of the range examined. However, this becomes less true over Screw Tip Speeds of around 0.8 m/s, as the model suggests the values then tend toward becoming equally important as the models interaction term begins to dominate.

These findings may be because at very high screw speeds extreme levels of system starvation are encountered, unless compensated for by an increase in feed rate. This indicates that a certain level of fill is necessary to ensure the paddles have enough bulk surface area to ensure flow remains efficient. Another reason for this observation is that very high screw speeds displayed a tendency to throw random jets of powder into the air, which in turn may disrupt axial flow (as mentioned in the descriptions in Table 3.2).

Conversely, to a lesser extent, for values below approximately 0.3 m/s Tip Speed, increasing the Feed Rate actually begins to slow down the overall Average Velocity (this is as a result of the negative second order Tip Speed term in the model). This may be explained by very High Fill levels leading to the development of stagnant regions at the top corners of the TSMs x vs z axis, where the paddle tips are unable to reach. This is because small amount of speckled tracer could be visually discerned taking longer than usual to incorporate themselves into the flow during the trials. These results may also be indicative of the propensity for the powder to be bumped along in a more piecemeal fashion at lower Tip Speeds which may be exacerbated by increased powder mass.

Meanwhile, σ^2 is dominated by Tip Speed alone from the minimum Screw Speed to around 0.3 m/s. This demonstrates that reducing the Tip Speed to within the region where powder tends to be bumped along, rather than flowing smoothly due to an increase in bulk momentum, causes an exponential increase in curve variance (as a result of the interaction term). Above 0.3 m/s however, the influence of Screw Tip Speed and Feed Rate seem to be roughly equivalent. This indicates that Fill Level must be an important factor whilst determining the bulks level of axial dispersion.

Table 4.6 displays the RSM model for Average Velocity at Inlet 2 in its coded coefficient form and Equation 4.7 shows the same model in uncoded units. The model scores very highly on all the statistical metrics used to measure the Goodness-of-Fit and so should be highly accurate.

Table 4.6: Coded Coefficient Table for TSM 75 Inlet 2, Velocity Model. The hierarchical model retained terms using 95% confidence, determined via the P-values. Metrics to determine the Goodness-of-Fit included: R^2 of 98.51%, Adjusted R^2 of 97.88%, a Predicted R^2 of 87.59% and a Lack-of-Fit P-value greater than 0.05.

Term	**Coefficient**	**P-Value**	**VIF**
$\boldsymbol{Constant}$	0.04050	0.000	
$\boldsymbol{Tip\ Speed}$	0.07899	0.000	3.12
$\boldsymbol{Feed\ Rate}$	0.0432	0.038	1.01
$(\boldsymbol{Tip\ Speed})^2$	0.0480	0.051	3.14

$$Velocity,\ m/s\ (Inlet\ 2) = 0.01128 + 0.0423 Tip\ Speed,\ m/s + 0.0432 Feed\ Rate,\ kg/s + 0.048(Tip\ Speed,\ m/s)^2 \tag{4.7}$$

At Inlet 2 the coded coefficients for the first order terms show that increasing Tip Speed and Feed Rate generally increases the bulks average velocity.

Table 4.7 displays the RSM model for the inverse of σ^2 at Inlet 2 in its coded coefficient form and Equation 4.8 shows the same model in uncoded units. As before, the model scores very highly on all the statistical metrics used to measure the Goodness-of-Fit and so should again be highly accurate.

Table 4.7: Coded Coefficient Table for TSM 75 Inlet 2, $(\sigma^2)^{-1}$. The hierarchical model retained terms using 95% confidence, determined via the P-values. Metrics to determine the Goodness-of-Fit included: R^2 of 99.05%, Adjusted R^2 of 98.65%, a Predicted R^2 of 97.49% and a Lack-of-Fit P-value greater than 0.05.

Term	**Coefficient**	**P-Value**	**VIF**
$\boldsymbol{Constant}$	0.7835	0.000	
$\boldsymbol{Tip\ Speed}$	3.535	0.000	1.06
$\boldsymbol{Feed\ Rate}$	4.204	0.000	1.07
$(\boldsymbol{Tip\ Speed}) \times (\boldsymbol{Feed\ Rate})$	30.08	0.000	1.12

$$1/\sigma^2,\ 1/s^2\ (Inlet\ 2) = 0.448 - 0.654 Tip\ Speed,\ m/s - 7.3 Feed\ Rate,\ kg/s + 30.08(Tip\ Speed,\ m/s) \times (Feed\ Rate,\ kg/s) \tag{4.8}$$

As was the case at Inlet 1, the inverse curve variance from Inlet 2 is positively effected by the Tip Speed and Feed Rate (as seen by positive coded coefficient values). Therefore, this means the reverse will be true when the inverse curve variance is recast as σ^2.

The top two plots in Figure 4.3 show three dimensional data plots and RSMs for Inlet 2 of the TSM 75 Average Velocity and inverse of σ^2 experiments. Below this in the same figure is the two dimensional response surface plots of the same models. However, the inverse curve variance plot has been converted back to its non-reciprocal σ^2 form.

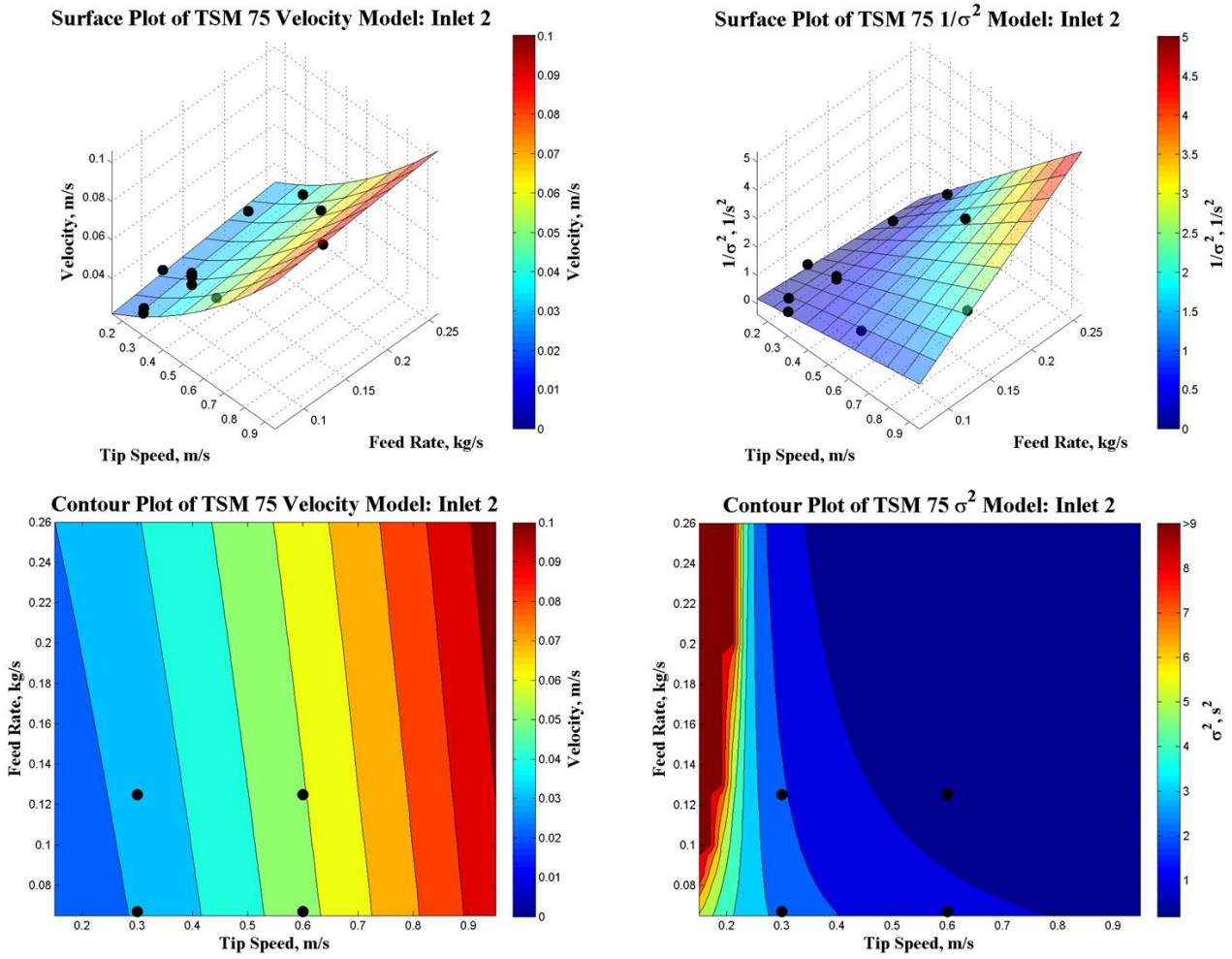

Figure 4.3: (Left) The TSM 75 Inlet 2 Velocity Model, displayed as a 3D surface plot (top) and a 2D contour plot (bottom). (Right) The TSM 75 Inlet 2 $1/\sigma^2$ Model, displayed as a 3D surface plot (top), and displayed in non-reciprocal form as a 2D contour plot (bottom). The black dots displayed in the contour plots represent the four regimes investigated during the PEPT trials, whereas the black dots in the 3D plots are the RTD metrics obtained via the DIP obtained RTDs.

The Inlet 2 models tell a similar story to that of the Inlet 1 models. However, where the bulk is bumped along by the paddles in a more piecemeal fashion, begins to dominate σ^2 at a slightly lower Tip Speed than the 0.3 m/s noted in the Inlet 1 models. Conversely, the region where Screw Speed alone stops dominating Average Velocity is also higher than the 0.8 m/s previously discerned from the Inlet 1 model.

There is also the possibility that some of the differences between Inlet 1 and Inlet 2 are down to method. This is because at Inlet 1 the tracer is added to the system at the same location as the

bulk. Whereas, at Inlet 2, tracer only is added at this location on top of bulk flow.

The static Fill Volume models for Inlet 1 and 2 have been provided as Figure 4.4. These have been calculated from the Average Velocity data using the method described in Section 3.4. By comparing the static Fill Volume, calculated via Equation 3.13, to the visual Fill Level description noted in Table 3.2, it was possible to deduce design space regions where Screw Speed and Feed Rate settings would yield one of four distinct Fill Levels (static Fill Volume refers to how full the system would be at rest if it contained the same amount of material as at steady state).

These included: 1) Starved Fill Level, where powder travelled under the shafts only (<18% static fill volume); 2) Mid Fill Level, the minimum fill level needed for the bulk to be pushed over the screw shafts (around 18-22% static fill volume); 3) High Fill Level (around 22-48% static fill volume) and 4) system flooding (>48% static fill volume). These Fill Level regime maps proved extremely useful to P&G in terms of planning future experimentation. A schematic of how this appears visually is provided as figure 4.5.

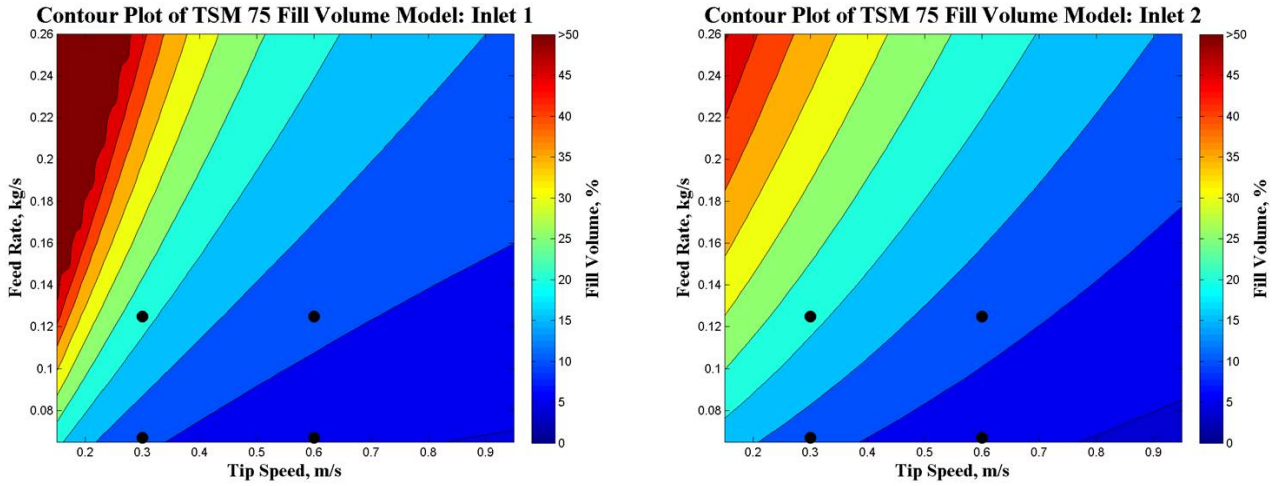

Figure 4.4: (Left) The TSM 75 Inlet 1 Fill Volume Model, calculated using the Inlet 1 Velocity Model, displayed as a 2D contour plot. (Right) The TSM 75 Inlet 2 Fill Volume Model, calculated using the Inlet 2 Velocity Model, displayed as a 2D contour plot. The black dots displayed in the contour plots represent the four regimes investigated during the PEPT trials. The Fill Volume was calculated from bulk density, so is a measure of how full the system would be at rest should it contain the same amount of material as at steady state for a given average bulk velocity.

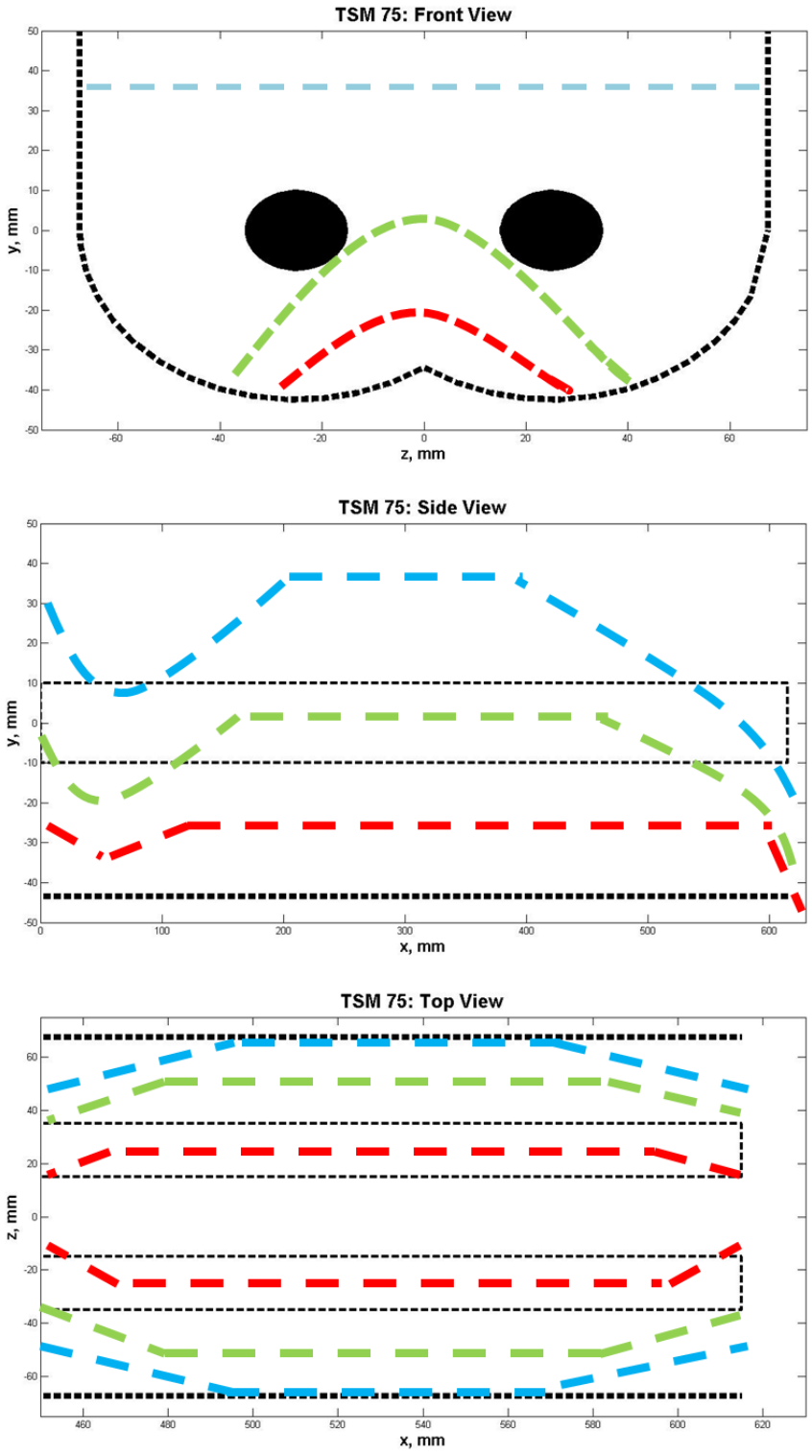

Figure 4.5: A schematic to show how different powder fill levels appeared to an observer within the TSM 75 whilst it was in operation. The blue dashed line represents a High Fill Level (around 22-48% static fill volume), the green dashed line represents the Mid Fill Level needed for powder to be pushed over the shafts (around 18-22% static fill volume) and the red dashed line represents Low Fill Level (<18% static fill volume).

It is clear from Figure 4.4 that at no point in the design space investigated for Inlet 2 does Screw Speed and Feed Rate combine to induce system flooding (as denoted by static Fill Volume percentages above 48). This is in contrast to that displayed for Inlet 1, where there is a very clear flooding region in the top left hand corner. This is caused by an increase in Velocity at Inlet 2 compared to Inlet 1 whilst operating at either low Screw Speeds or high Feed Rates (or both), which leads to the tapering down effect mentioned previously and displayed in Figure 3.11.

The accuracy displayed by all the statistical models built within this Chapter, using data generated by the DIP RTD measuring strategy, would seem to all be highly accurate. This is because they show a high level of consistency in terms of: visual inspection of system behaviour (i.e. the shape of the model curves and data curves are usually very similar), conceptual understanding, consistency between the Inlet 1 and 2 models, RTD shapes are usually asymmetrical as they mostly have tails (see Section 4.1.2), as well as scoring highly on the statistical Goodness-of-Fit metrics.

However, as a final check, the models were also compared to the PEPT data generated using the method discussed in Section 3.5. This was achieved by examining all the tracer particles, for the 4 regimes investigated, axial journey (x axis) with respect to time. This has been provided as Figure 4.6.

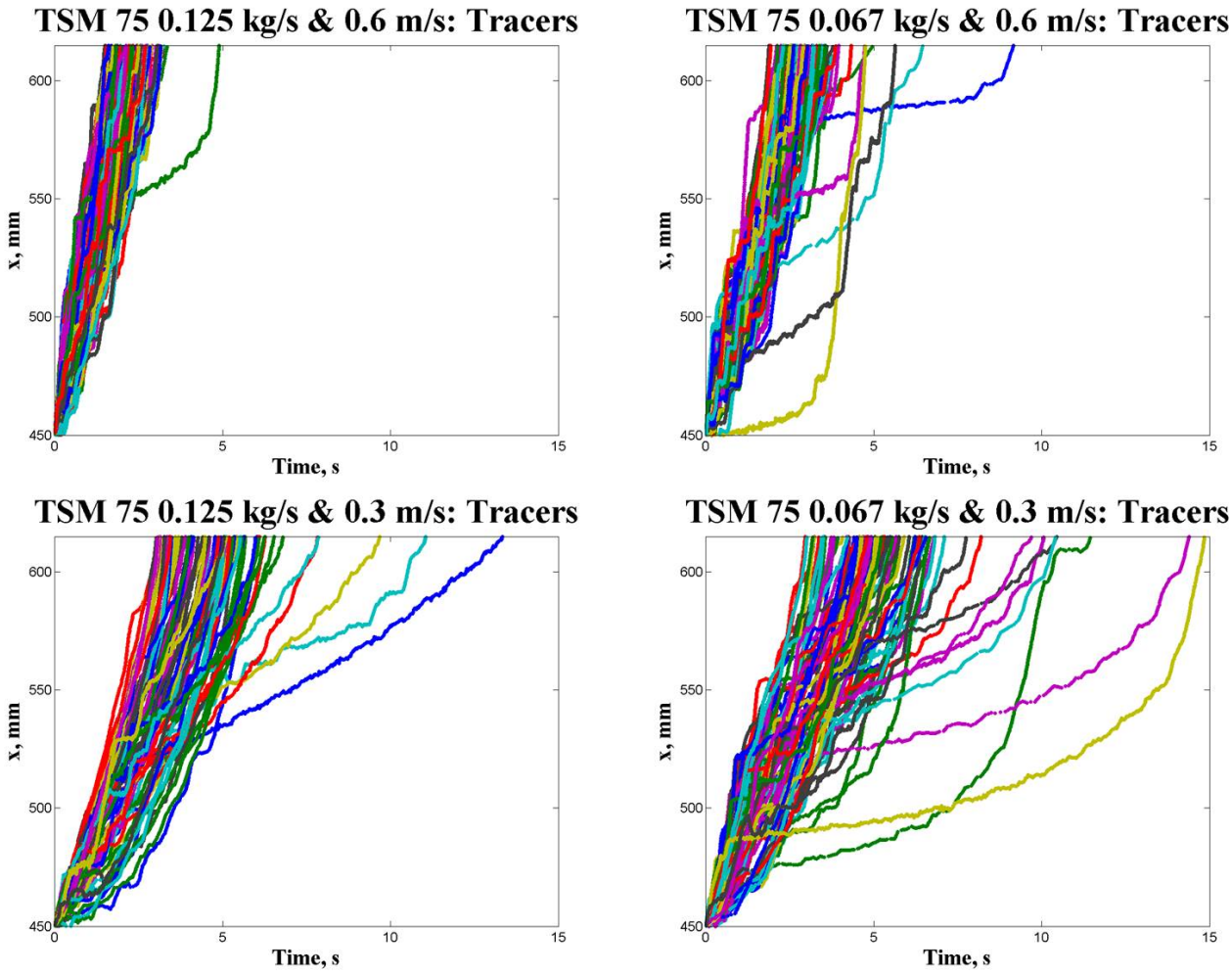

Figure 4.6: All PEPT tracer positions along the x axis with respect to time. Different colours represent different particle journeys.

The PEPT Feed Rate and Screw Speed settings used have been marked upon all the surface plots within this Section (on Figures: 4.2, 4.3 and 4.4). The degree to which the axial particle journeys differ in Figure 4.6, between each of the 4 regimes, corresponds well to the changes in σ^2 predicted by the models from a visual perspective. With the highest Screw Speed and Feed Rate settings leading to the smallest variation in particle journeys, and the lowest settings vice versa. The Fill Level for the PEPT regimes, as displayed as Figures 5.1, 5.2 and 5.3, are also consistent with the models predictions.

Finally, the average axial velocity was calculated for each PEPT regime and compared with that predicted by the models. This has been provided in Table 4.8.

Table 4.8: RSM comparison to PEPT results.

PEPT Trial	Tip Speed m/s	Feed Rate kg/s	PEPT Velocity m/s	Inlet 1 Model Velocity m/s	Inlet 2 Model Velocity m/s
1	0.6	0.125	0.068	0.063	0.059
2	0.6	0.067	0.052	0.060	0.059
3	0.3	0.067	0.030	0.034	0.034
4	0.3	0.125	0.036	0.033	0.034

As the RSM Average Velocity values compare well with that of the PEPT values, it can be concluded that (along with all the other evidence presented) the DIP RTD measuring strategy constructed for this report has demonstrated a remarkable accuracy. This should make the algorithm a useful tool for P&G to characterise not only TSMs, but other continuous systems they may wish to examine in the future.

4.1.2 Tanks-in-Series (T-i-S) Models Investigation TSM 75.

The TSM 75 curves provided in Figure 4.8, in every case, display higher peaks for Inlet 2 than their Inlet 1 counterparts. This is to be expected, considering that powder has spent less time in the system and so has had less opportunity to spread out overall. This is also the reason that the curves positioned toward the left hand side of the time axis present thin tall sharp peaks, whereas, the opposite is generally true for curves positioned towards the right hand side of the time axis.

The variability in the process can be also be discerned to some extent through an examination of the 3 repeated experiments: Run 1, Run 8 and Run 10, these may be viewed in Figure 4.7. From a visual perspective it is clear that some inherent variation is present in bulk transport, owing to slight differences in the shape of the RTDs. Nevertheless the RTDs do look remarkably similar, especially in terms of where they peak and the curve variance (which is why the residence time and curve variance described in the previous section is so similar).

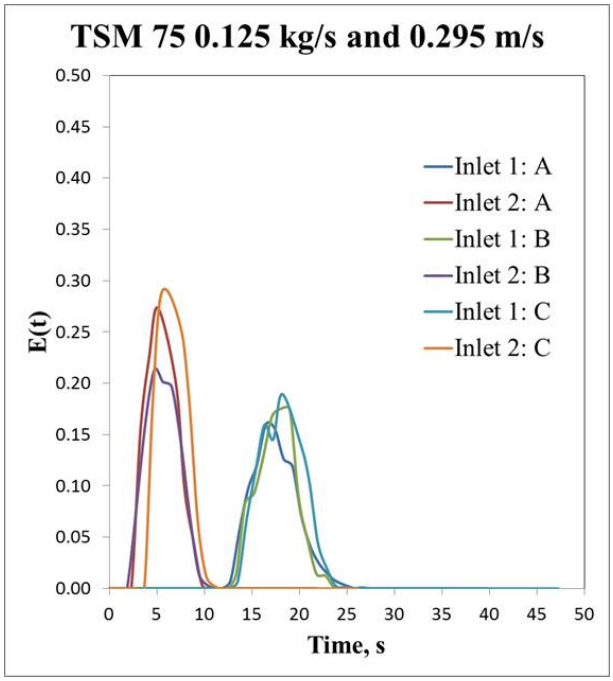

Figure 4.7: Comparison between TSM 75 Inlet 1 repeats: Run 1 (A), Run 8 (B) and Run 10 (C).

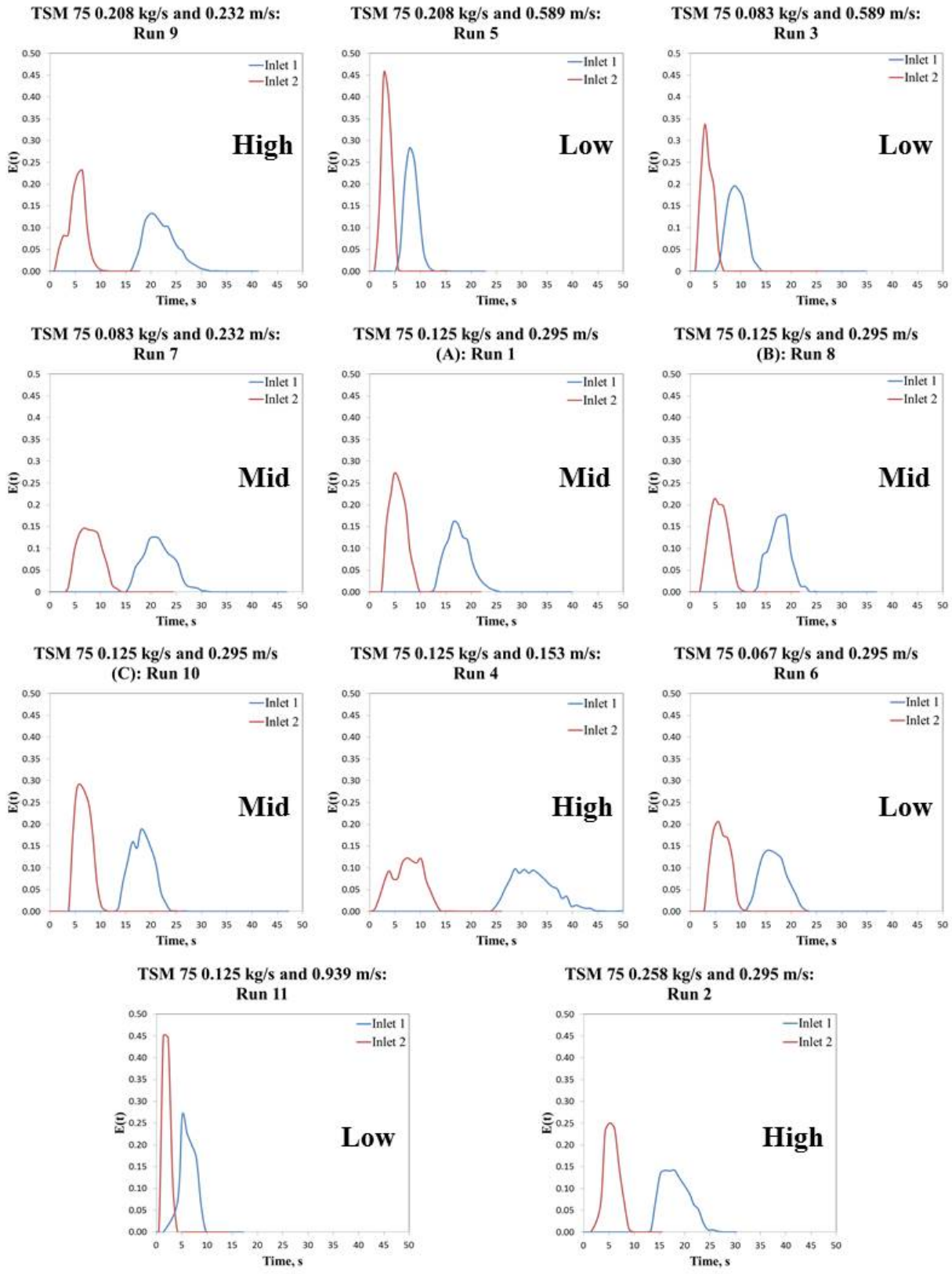

Figure 4.8: TSM 75 Residence Time Distributions. The terms: Low, Mid and High give a brief description of visual fill level within the TSM, for a more in depth description refer to Table 3.2.

The normalised TSM 75 Inlet 1 RTDs have been displayed as Figure 4.9, complete with the corresponding T-i-S models, fabricated using the approach described in Section 3.3. The T-i-S model parameters have also been provided in Table 4.1. It is clear from a visual inspection that the models correlate well with the actual data (i.e. the model and data curves generally appear very similar). This is further corroborated by all R^2 values between model and data being 0.95 or above.

As described in Section 3.3 the T-i-S model has again been given as equations 4.9 and 4.10. In these equations: p is the plug flow fraction, n is the number of CSTRs in series and d is the dead zone fraction [57]. The models of best fit have been fitted to the data by using the Solver function within Excel to minimise a cost function.

$$E(\theta) = \frac{b[b(\theta - p)]^{n-1}}{(n-1)!} e^{-b(\theta - p)} \tag{4.9}$$

Where:

$$b = \frac{n}{(1-p)(1-d)} \tag{4.10}$$

The Inlet 1 model parameters show the systems tendency to produce plug flow. This is because all values have either a large plug flow fraction (p$\geq$0.62), or many CSTRs in series (n$\geq$55), or sometimes a moderately large number of both. As well as a dead time fraction of 0.00, which denotes no stagnant regions and/or excessive back mixing. The lack of a dead time fraction is also consistent with the TSM fill levels always visually being as expected.

Whilst examining the 3 repeat experiments: Run 1, Run 8 and Run 10 model parameters, it is clear some variability has been picked up in the way powder flows within the system. With Run 1 having a medium sized plug flow fraction (p=0.28) followed by 25 CSTRs and Runs 8 and 10 displaying the behaviour of 63 or 55 CSTRs in series only. However, all these results point to a system that displays a stronger approximation towards plug flow type behaviour, rather than that of a CSTR.

Table 4.9: TSM 75 Inlet 1 Tanks-in-Series Model parameters.

$\boldsymbol{Run}$	$\boldsymbol{n}$	$\boldsymbol{p}$	$\boldsymbol{d}$	$\boldsymbol{R^2}$
1	25	0.28	0.00	0.99
2	6	0.62	0.00	0.96
3	23	0.00	0.00	0.99
4	8	0.62	0.00	0.98
5	30	0.12	0.00	1.00
6	28	0.15	0.00	0.99
7	38	0.09	0.00	0.99
8	63	0.00	0.00	0.96
9	6	0.65	0.00	0.99
10	55	0.00	0.00	0.96
11	8	0.32	0.00	0.95

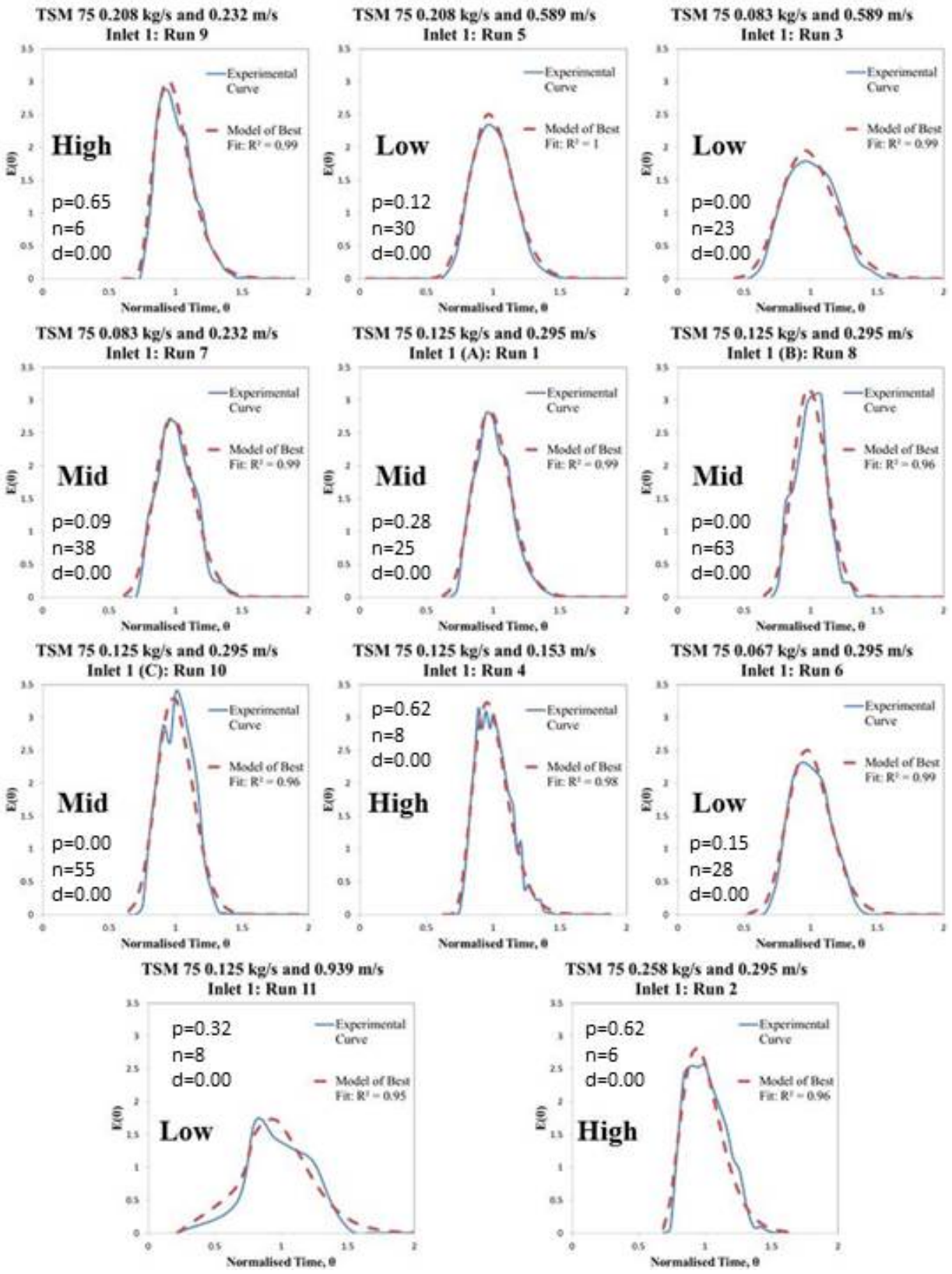

Figure 4.9: TSM 75 Normalised Residence Time Distributions with the best fitting Tanks-in-Series Models: Inlet 1. The terms: low, mid and high give a brief description of visual fill level within the TSM, for a more in depth description refer to table 3.2.

The normalised TSM 75 Inlet 2 RTDs have been displayed as Figure 4.10 complete with the corresponding T-i-S models, fabricated using the approach described in Section 3.3. The T-i-S model parameters have also been provided in Table 4.2. As with the Inlet 1 results it is clear from a visual inspection that the models correlate well with the actual data (i.e. the model and data curves generally appear very similar). This is further corroborated by most R^2 values between model and data being 0.96 or above.

The Inlet 2 model parameters show the systems tendency to produce a transitional flow resembling something in between a CSTR and a PFR. This is because most values have either no plug flow fraction (p=0.00), and a small to intermediate quantity of CSTRs in series ($8 \leq n \geq 15$); as well as the dead time fraction, which denotes stagnant regions and/or excessive back mixing, always being 0.00. This is not true for Run 11 however, which is the very high screw speed, which has a large plug flow fraction (p=0.66). This may be caused by the the speed in which the powder passes through the short length of system being better approximated to plug flow.

The second case this is also not true is for Run 10, one of the 3 repeat experiments (that also includes Run 1 and Run 8). It is clear some variability has been picked up in the way powder flows within the system, causing Run 10 to tend slightly more toward plug flow than Runs 1 and 8.

Table 4.10: TSM 75 Inlet 2 Tanks-in-Series Model parameters.

Run	***n***	***p***	***d***	$\boldsymbol{R^2}$
1	10	0.00	0.00	0.96
2	14	0.00	0.00	0.98
3	8	0.00	0.00	0.98
4	5	0.00	0.00	0.78
5	15	0.00	0.00	0.96
6	11	0.00	0.00	0.97
7	10	0.00	0.00	0.96
8	10	0.00	0.00	0.98
9	9	0.00	0.00	0.83
10	12	0.19	0.00	0.98
11	2	0.66	0.00	0.99

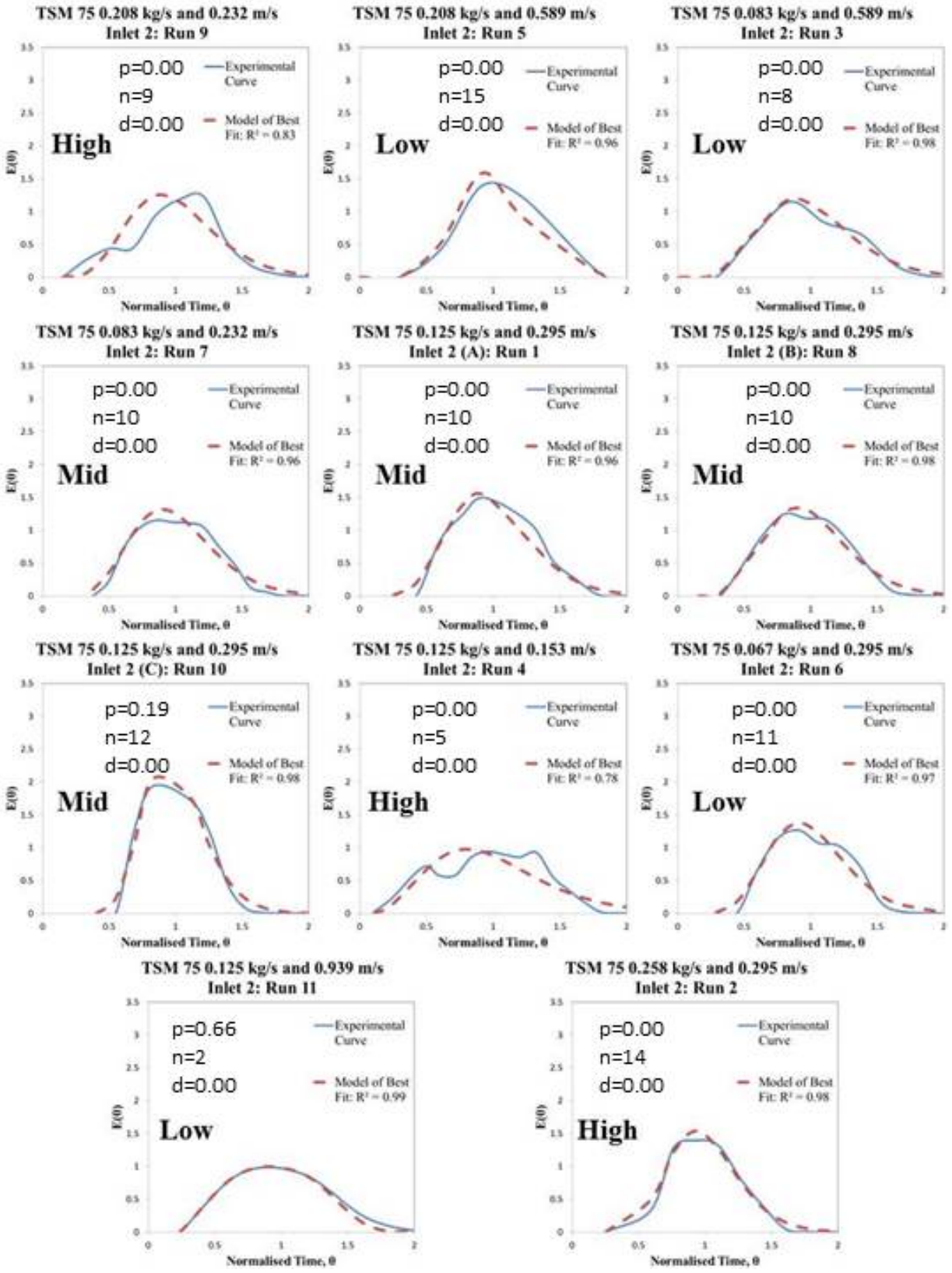

Figure 4.10: TSM 75 Normalised Residence Time Distributions with the best fitting Tanks-in-Series Models: Inlet 2. The terms: Low, Mid and High give a brief description of visual fill level within the TSM, for a more in depth description refer to table 3.2.

Figure 4.11 shows the two T-i-S models, with plug flow and dead time, that best fit the system over the entire design space examined, calculated using the method described in Section 3.3. The Inlet 1 model shows that within the system, in general, flow resembles a plug flow reactor for 32% of the journeys length (p=0.32), followed by a series of 22 CSTRs in series (n=22). As the total length from Inlet 1 to the exit is 555 mm, this gives the initial PFR a length of 117.6 mm, followed by 22 CSTRs, each being 19.88 mm in diameter.

The Inlet 2 model corroborates this, by inferring that the final 10 CSTRs occupy a length of 195 mm from Inlet 2 to the exit. This corresponds to each CSTR being 19.5 mm in length, which is extremely close to the 19.88 mm predicted for Inlet 1. There is however, a very small plug flow fraction of 2%, which corresponds to a length of 3.9 mm. Removing this value of p however,does not make any difference to the RSS up to 2 decimal places, so may easily be attributed to error.

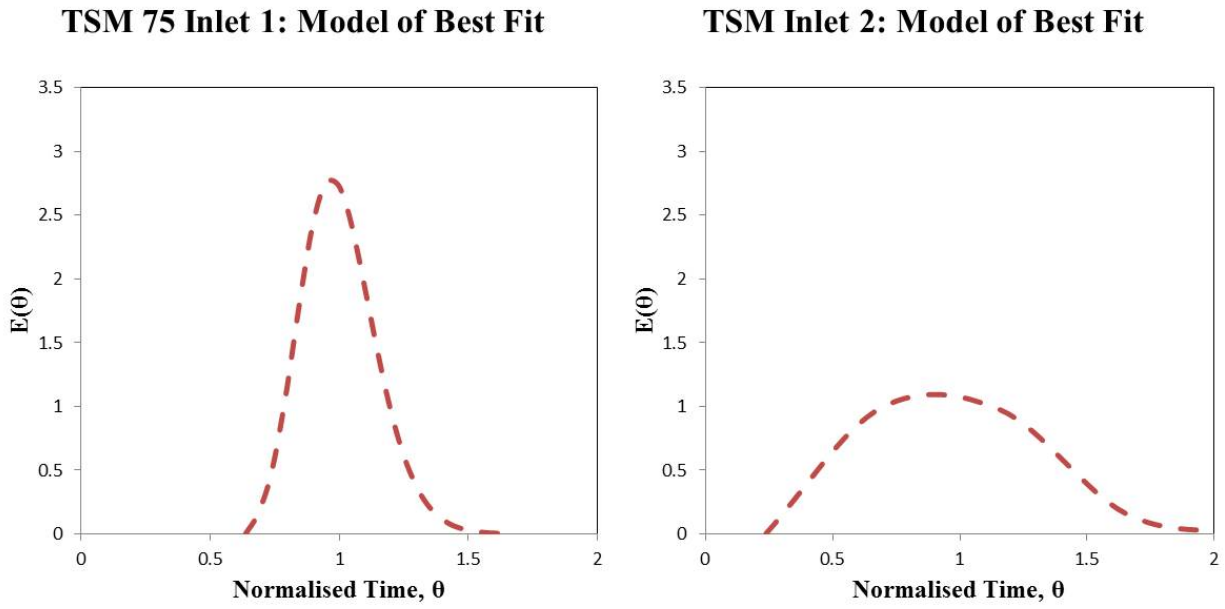

Figure 4.11: The Tanks-in-Series (T-i-S) Models that best describe flow in the TSM 75. (Left) From Inlet 1 to exit model parameters are: n = 22, d = 0 and p = 0.32, the Residual Sum of Squares (RSS) = 14.40. (Right) From Inlet 2 to exit model parameters are: n = 10, d = 0 and p = 0.02, the Residual Sum of Squares (RSS) = 4.30.

Now that the system has been characterised using the T-i-S with plug flow model it is clear that the system generally does not need the dead zone, d, to be described. However, now the system shall be described in terms of T-i-S alone (i.e. with p and d set to 0). This is to ensure that the p term is really a necessary parameter. It will also make comparisons between each experiment much easier to deduce as it is easier to compare number of CSTRs than to estimate the effects of

p and n in tandem. The Peclet number shall also be derived for each system using equation 4.11.

$$\sigma_\theta^2 = \frac{\sigma^2}{\tau} = \frac{2}{Pe} - \left(\frac{2}{Pe^2}\right)\left(1 - e^{-Pe}\right) \tag{4.11}$$

The T-i-S parameters shown in Table 4.11 and Figure 4.12 seem to fit the data just as strongly as the T-i-S plus plug flow and dead time models discussed previously. This is because they visually appear to fit the data just as strongly (as the model and data curves generally appear similar) and have similar R^2 values.

Furthermore, the Peclet numbers also tend to correspond to the rise and fall of n in the T-i-S models, as expected. This is because the number of T-i-S and Peclet Numbers are known to be roughly equivalent at describing the same thing (axial dispersion) with the choice of which metric to use being down to personal preference [46].

Therefore, by realising that: a Peclet number of infinity is perfect plug flow, Pe = 500 is a small amount of dispersion, Pe = 40 is an intermediate amount of dispersion, Pe = 5 is a large amount of dispersion and Pe = 0 is a perfect CSTR, axial mixing can be described with respect to process parameters [79].

Table 4.11: TSM 75 Normalised Residence Time Distributions with the best fitting, n only, Tanks-in-Series (T-i-S) Models and Peclet Numbers: Inlet 1.

Run	***n***	$\boldsymbol{R^2}$	Pe
1	49	0.99	118.08
2	43	0.94	95.62
3	23	0.99	59.92
4	60	0.96	128.68
5	35	0.99	84.91
6	40	0.99	99.17
7	46	0.99	108.95
8	63	0.96	139.86
9	50	0.96	116.55
10	55	0.96	121.06
11	16	0.95	42.31

Intermediate dispersion, tending towards a low amount of axial dispersion, is demonstrated at Inlet 1 for all experiments run at mid screw speed, 0.295 m/s (Pe range 95.62 - 139.86). This is true

for the lower Screw Tip speeds, 0.153 m/s and 0.232 m/s, but tends to trend slightly lower (Pe range 108.96 - 128.68). At the much higher Screw Tip speeds, 0.589 m/s and 0.939 m/s, the Pe is much lower tending toward the centre of the Intermediate axial dispersion area (Pe range from 42.31 - 59.92).

The repeat runs 1, 8 and 10 are also all very similar. With n values ranging between 49 - 63 and Pe numbers ranging from 118.08 - 139.86.

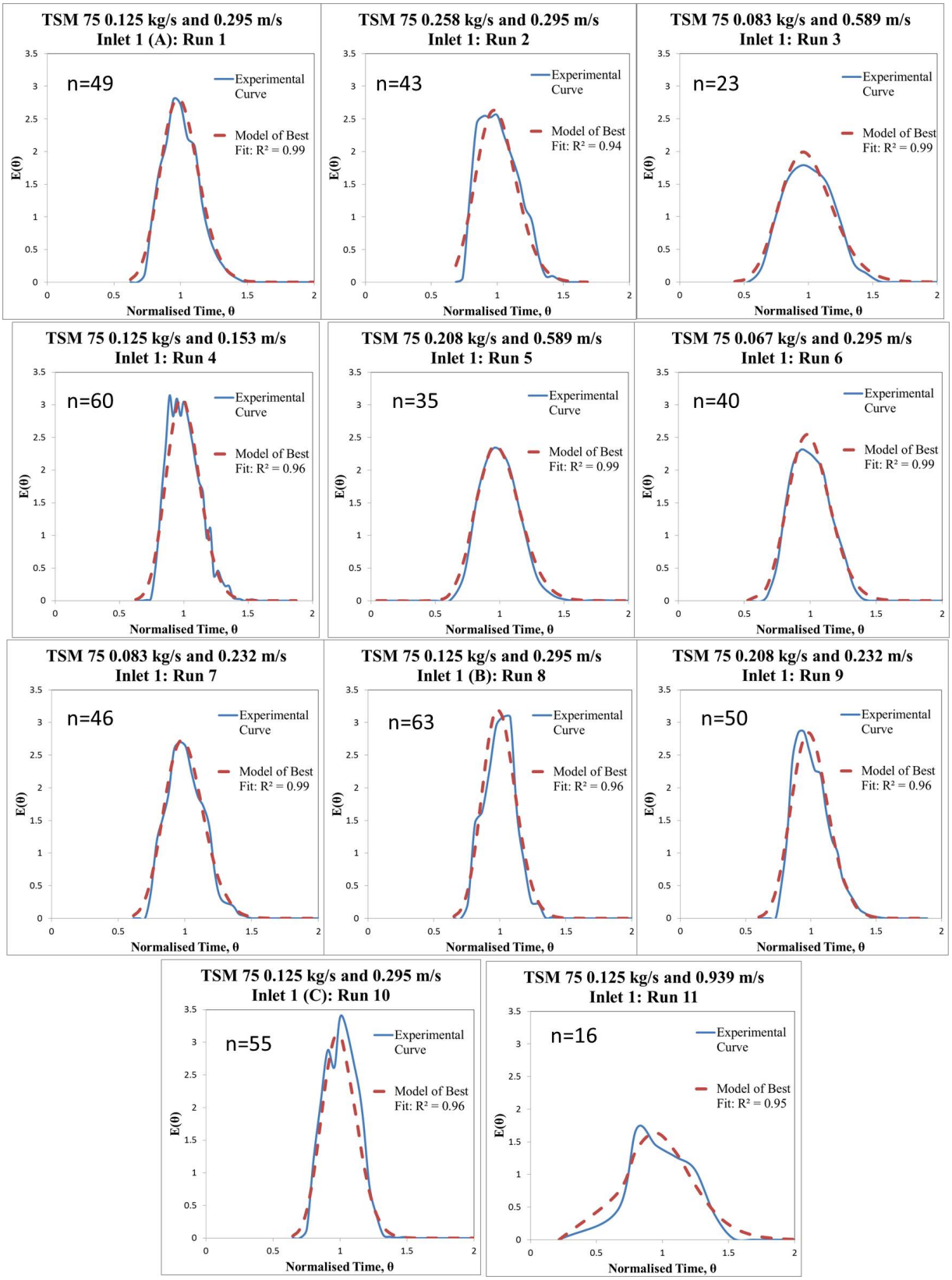

Figure 4.12: TSM 75 Normalised Residence Time Distributions with the best fitting, n only, Tanks-in-Series (T-i-S) Models: Inlet 1

The T-i-S parameters shown in Table 4.12 and Figure 4.13 also seems to fit the data just as strongly as the T-i-S plus plug flow and dead time models discussed previously. This time all regimes are in the intermediate axial dispersion range (Pe is 38.91 - 81.09). The three repeats, runs: 1, 8 and 10 have some slight discrepancies, as 1 and 8 have an n = 10 and run 10 has an n = 21.

However, this still equates to Pe numbers of Run 1 Pe = 20.14, Run 8 Pe = 29.06 and Run 10 Pe = 34.34, which are all in the same region with regards to amount of axial dispersion (as Pe = 5 is lots of axial dispersion and Pe = 40 is an intermittent amount of axial dispersion). Therefore, these differences may be caused either by slight errors in the method, or inherent variation when repeating these experiments.

Table 4.12: TSM 75 Normalised Residence Time Distributions with the best fitting, n only, Tanks-in-Series (T-i-S) Models and Peclet Numbers: Inlet 2.

$\boldsymbol{Run}$	$\boldsymbol{n}$	$\boldsymbol{R^2}$	Pe
1	10	0.96	20.14
2	14	0.98	34.80
3	8	0.98	19.61
4	5	0.78	15.52
5	15	0.96	40.96
6	11	0.97	28.89
7	10	0.96	27.25
8	10	0.98	29.06
9	9	0.83	18.59
10	21	0.97	34.34
11	8	0.99	18.63

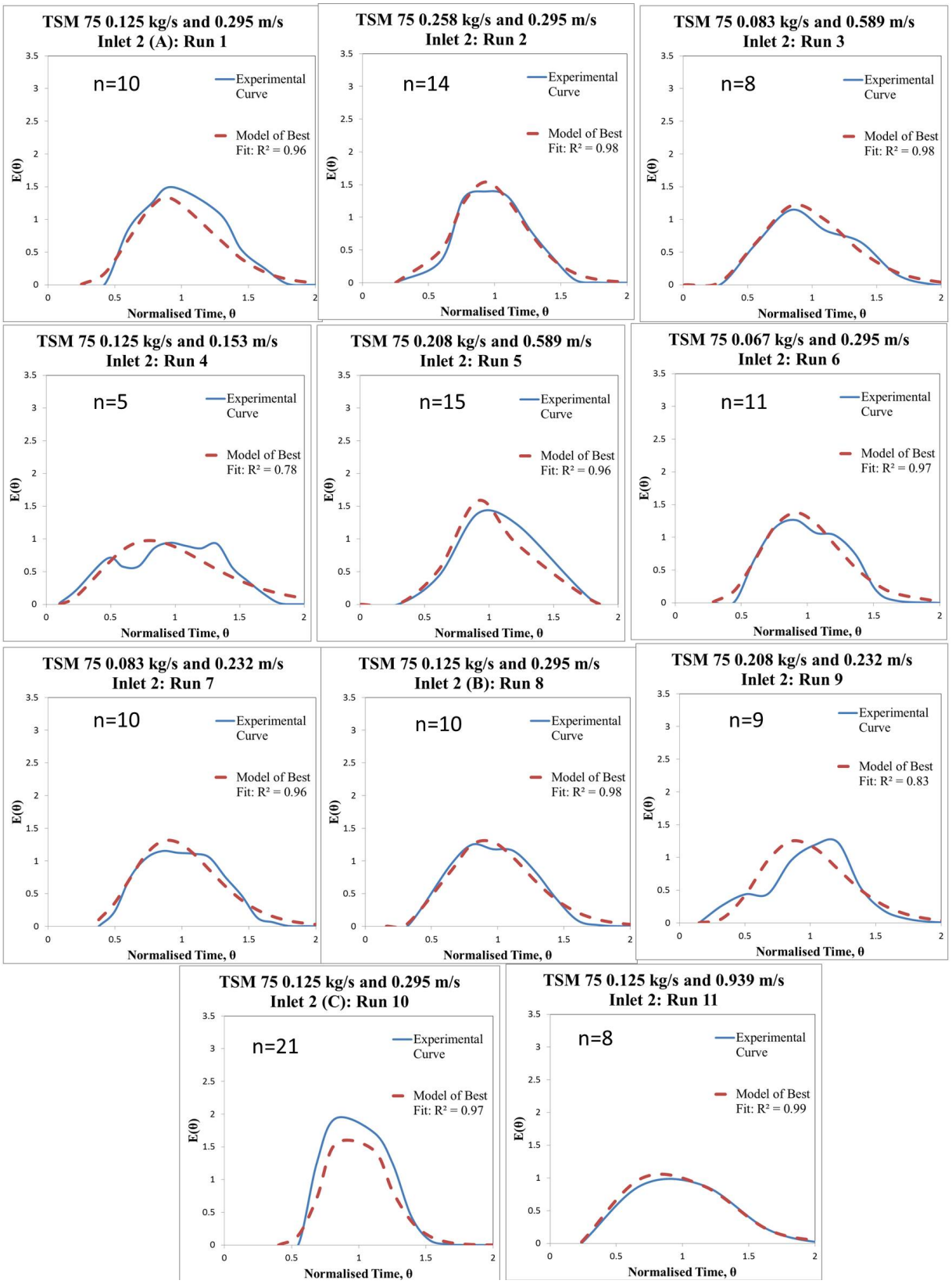

Figure 4.13: TSM 75 Normalised Residence Time Distributions with the best fitting, n only, Tanks-in-Series (T-i-S) Models: Inlet 2

Figure 4.14 shows Screw Tip speed plotted with respect to the Peclet Number for both Inlets 1 and 2. This suggests that material in these machines tend to show an intermediate amount of axial dispersion from Inlet 1. The axial dispersion also tends to have an inverse relationship with Screw Speed, with the Peclet Number ranging from about 40 - 120 (Peclet Number = 5 is lots of axial dispersion, Peclet Number = 40 is intermediate axial dispersion and Peclet Number = 500 is low amounts of axial dispersion [79]). Inlet 2 has roughly the same amount of intermediate axial dispersion regardless of Screw Speed.

This means that the amount of axial dispersion from Inlet 1 may be controlled to some degree via screw speed. However, the amount of axial dispersion from Inlet 2 is fixed within the ranges investigated, this is because the material does not remain in the system long enough to spread out in an axial fashion in response to changes in the predictor variables.

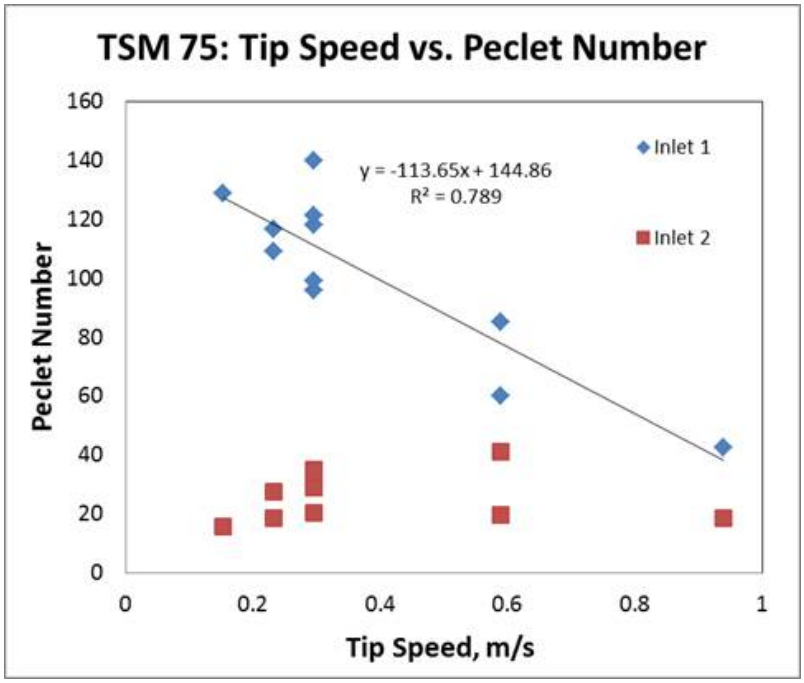

Figure 4.14: TSM 75: Tip Speed vs. Peclet Number.

4.2 Conclusions

The DIP strategy used to measure the RTD within the TSM 75 has proven to be an extremely accurate and robust methodology. This has been validated through: visual, conceptual and statistical means (including examining the residuals during RSM methodology as described in 3.4), as well as through comparison with results generated via PEPT.

Bulk Velocity, RTD curve variance and Fill Level (of the system at rest) within the machine has also been thoroughly characterised. This is invaluable, both for saving time whilst planning future experiments as well as making scale-up comparisons with the TSM 125 in Chapter 6.

The RSM models have found that Screw Tip speed tends to dominant axial bulk Velocity over most of the predictor region examined. However, above 0.8 m/s Tip Speed the Feed Rate begins to become just as important. This is because if a certain fill level is not maintained within the machine then axial flow becomes less efficient.

Curve Variance, σ^2, also tends to be dominated by Screw Speed, with the longer the powder remains in the system the further it disperses in an axial fashion. This is especially true below Tip Speeds of 0.3 m/s, where the bulk is pushed along in a more piecemeal fashion rather than smoothly flowing along.

The RTD T-i-S model is clearly just as adequate in describing axial dispersion within the TSM 75 as the T-i-S with plug flow and dead time model. Therefore, the T-i-S model is preferred as it is a simpler model that is more easily interpreted. The Peclet number also corresponds well to the number of CSTRs, so this may also be used to describe the systems axial dispersion.

The T-i-S and Peclet number show that generally the TSM 75 displays an intermediate amount of axial dispersion. Furthermore, when the bulk is added at Inlet 1 the exact amount of axial dispersion may be tuned to some degree using Screw Speed alone. Bulk added at Inlet 2 however, seems to display roughly the same amount of axial dispersion regardless of Screw Speed or Feed Rate (within the region examined). This is because the bulk does not spend enough time in the system for the axial dispersion to directly respond to the predictors.

Chapter 5

Positron Emission Particle Tracking (PEPT) analysis of dry powder flow in a large-scale, counter-rotational, intermeshing Twin-Screw Mixer (TSM) (The TSM 75)

5.1 Results and Discussion

5.1.1 PEPT Occupancy and Velocity Plots and Mixing Study.

The main objectives within this Chapter is to use PEPT to determine the following:

- To understand mass transport within the TSM 75 and how this may change with respect to changing Feed Rates and Screw Tip Speeds.
- To understand the mechanisms by which the TSM 75 mixes in a radial fashion.

Within the Side View Occupancy Plots displayed as Figure 5.1, it clearly shows that the powder bulk has a tendency to remain at the bottom of the system's y axis, for the 3 lower fill levels (TSM 75: 1. 0.125 kg/s and 0.6 m/s, 2. 0.067 kg/s and 0.6 m/s and 3. 0.067 kg/s and 0.3 m/s), as discerned visually and discussed in Chapter 3.4.

However, as a medium fill level is obtained (TSM 75: 0.125 kg/s and 0.3 m/s), and material starts to flow over the shafts, the powder begins to spend the majority of its time around 0 along the y axis (in the screw shaft region along the the vertical axis); as displayed in the TSM 75: 0.125 kg/s and 0.3 m/s regime from 450-500 mm along the x axis.

Figure 5.1 also clearly displays the tapering down effect, discussed in Chapter 4, as the powder seeks to exit the system under the influence of gravity. This effect becomes more pronounced as the system fill level increases.

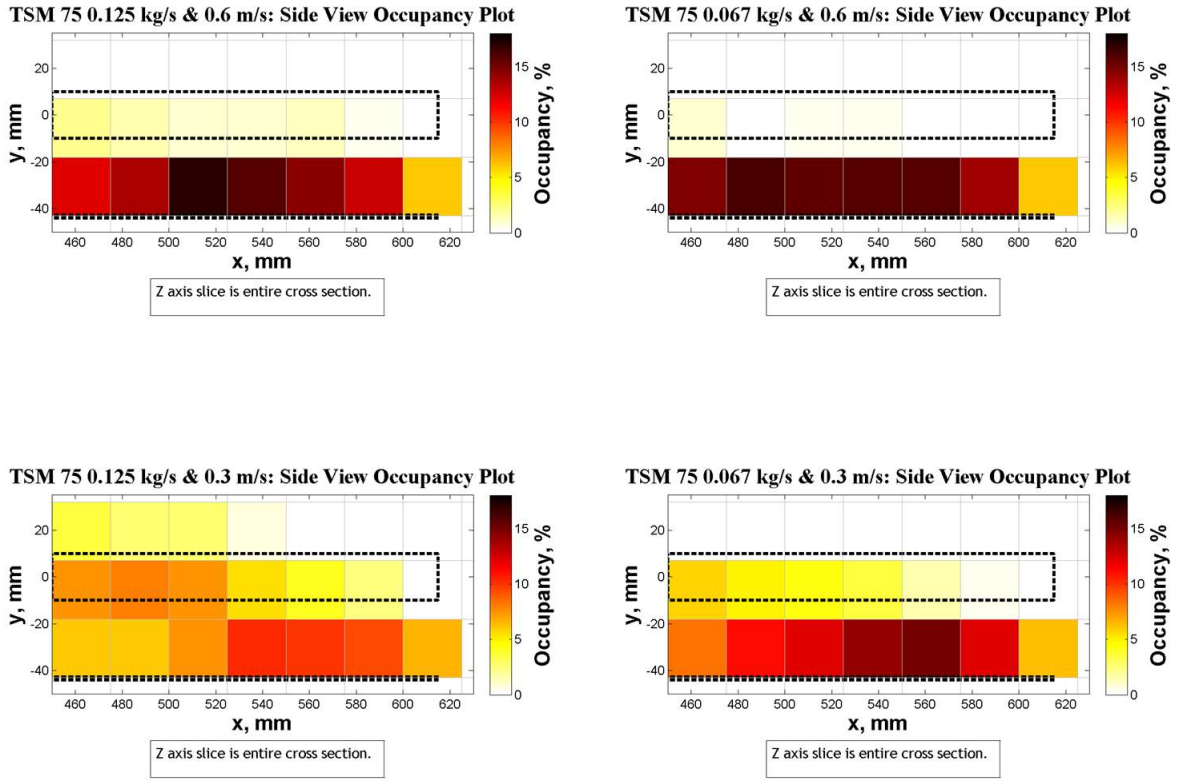

Figure 5.1: Side view occupancy plots of the 4 PEPT regimes. The cross sectional area along the x and y axis has been discretised into 25 mm^2 voxels, whereas the volume is the entire length of the z axis.

Within the Front View Occupancy Plots, displayed as Figure 5.2, the system has been divided into the constant Fill Level (left hand side) and tapering down region (right hand side) noted in Figure 5.1. These plots show that the powder, in all regimes, tends to spend the majority of its time being pushed in between both screw shafts (within the centre of the z axis; the radial axis).

It is interesting to note however, that when the powder bulk is at mid fill level (TSM 75 0.125 kg/s and 0.3 m/s), there is a very even spread of powder movement around both shafts; with there being slightly more time spent in the centre of the shafts as both circulatory streams combine. There is also slightly less time spent in the top left and right hand corner voxels, caused by these voxels not being completely filled with powder (and are therefore visited less by the tracer).

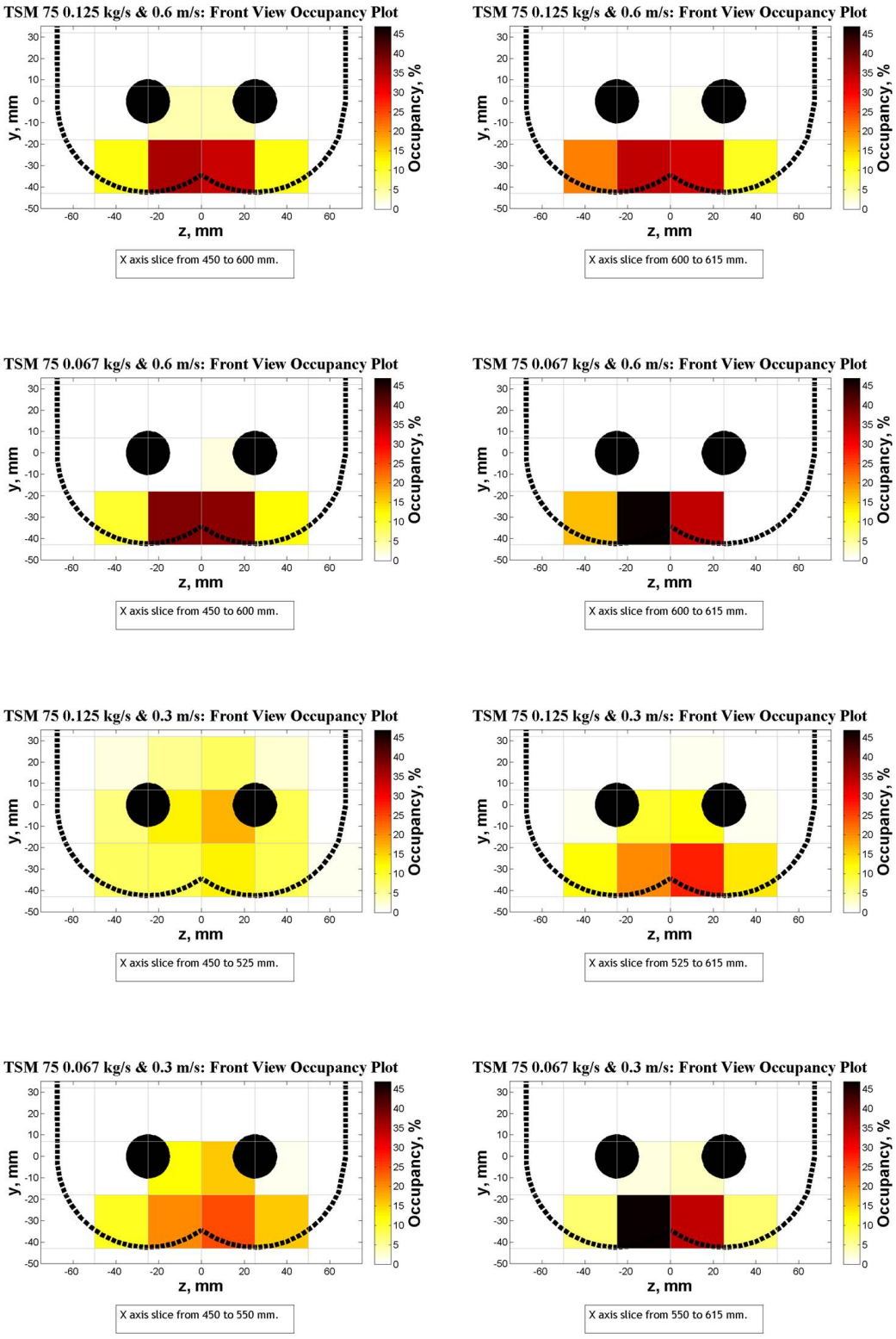

Figure 5.2: Front view occupancy plots of the 4 PEPT regimes. The cross sectional area along the x and y axis has been discretised into 25 mm^2 voxels. Whereas the left hand side diagrams volume extends from the beginning of the x axis to the beginning of the tapering down regions, and the right hand side diagrams show the tapering down regions.

Figure 5.3, the Top View Occupancy plots, confirm that the bulk tends to spend the majority of its time between the screw shafts (0 along the z axis). However, the plots also display a tapering-in effect as the material approaches the TSM exit (along the radial z axis). This can be viewed visually whilst operating the TSMs, and is described in the bottom of Figure 3.11 (which is a description of how the bulk looks visually whilst operating the TSM at different fill levels).

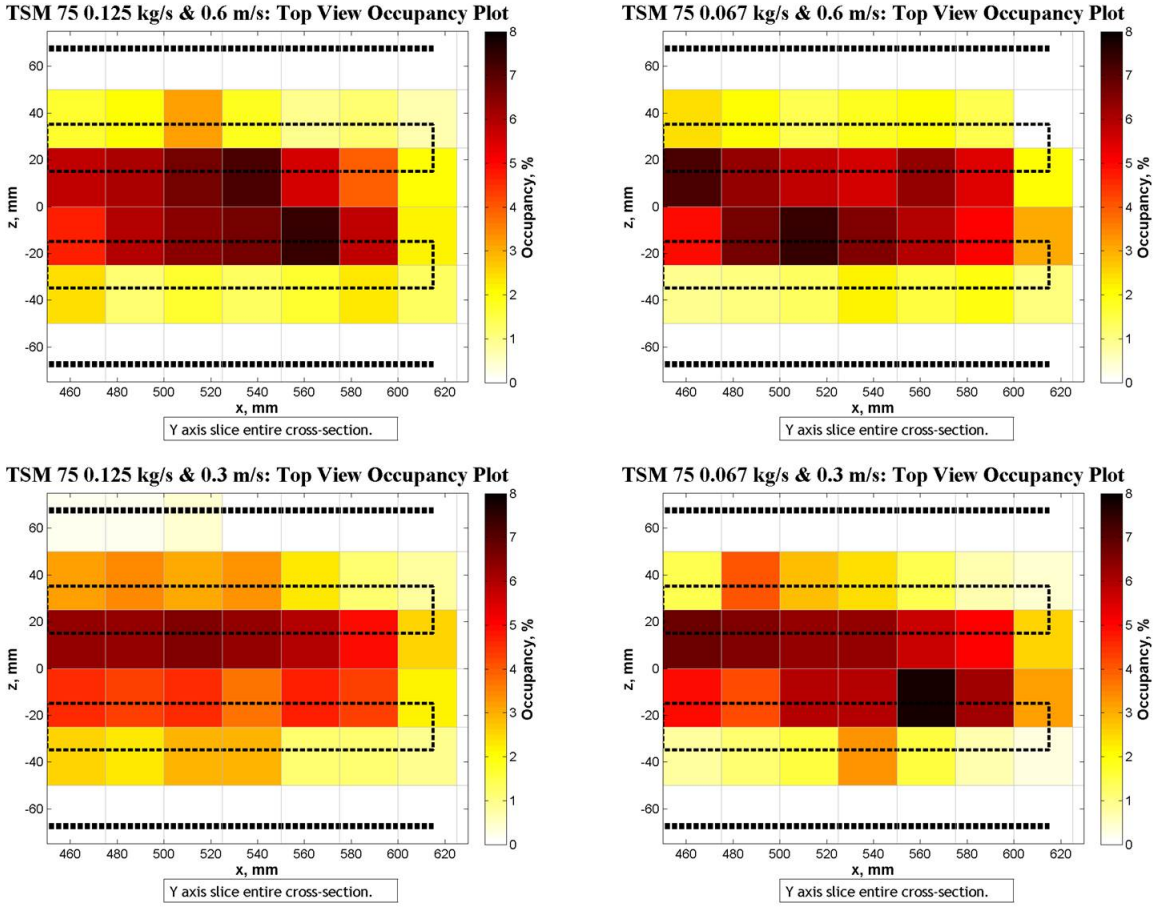

Figure 5.3: Top view occupancy plots of the 4 PEPT regimes. The cross sectional area along the x and y axis has been discretised into 25 mm^2 voxels, whereas the volume is the entire length of the y axis.

In terms of radial mixing, it is promising that the material spends the majority of its time in between the screw shafts. This indicates that the counter-rotational motion of the screw is readily combining the bulk from both sides of the TSM (the minus and positive halves of the z axis) in a radial fashion.

Furthermore, when a mid fill level is reached, the bulk seems to spend an almost even amount of time encircling the screw shafts, with a slight increase in occupancy being observed centrally between the screws (around 0 on y - vertical and z - radial axis). This complete circular flow around

the shafts of the bulk should prevent more stagnant regions forming at the z axis (radial) extremes. However, the investigation performed in Chapter 4 revealed there were no excessively stagnant regions within the machine. This means that the benefit obtained by the circular motion (when compared to the starved filled regimes) may only be very slight.

Due to these findings it is recommended that these machines should not be run starved if removing any hint of a stagnant region at the axial regimes is critical for operations. Whilst the improvement may only be slight for this model powder, obtaining the circular flow patterns may be more important if the blend is highly cohesive or adhesive. However, increasing the fill level exacerbates the tapering effect noted as the bulk exits the machine along the x axis (axial dimension). In order to prevent this from occurring, and therefore ensuring a more efficient use of the axial length of the TSM in terms of radial mixing, a weir should be incorporated near the TSM outlet in order to ensure the fill level remains high throughout the TSM length.

Figure 5.4 shows the TSM 75 Velocity plots within the y vs x plane (vertical vs. axial plane), with the left hand side showing one half of the system and the right hand side showing the other (having been split centrally between the screws through the middle of the radial z axis).

It is clear when looking at this figure, that powder flows at the bottom of the system in an axial fashion (along the x axis) at roughly the same rate as the Screw Lead (which for a Screw Tip Speed of 0.6 m/s would be 0.08 m/s and for a Screw Tip Speed of 0.3 m/s would be 0.04 m/s, as given in Table 4.3). This is until the powder reaches the tapering down region, where the axial velocity increases as the bulk leaves the system under the influence of gravity.

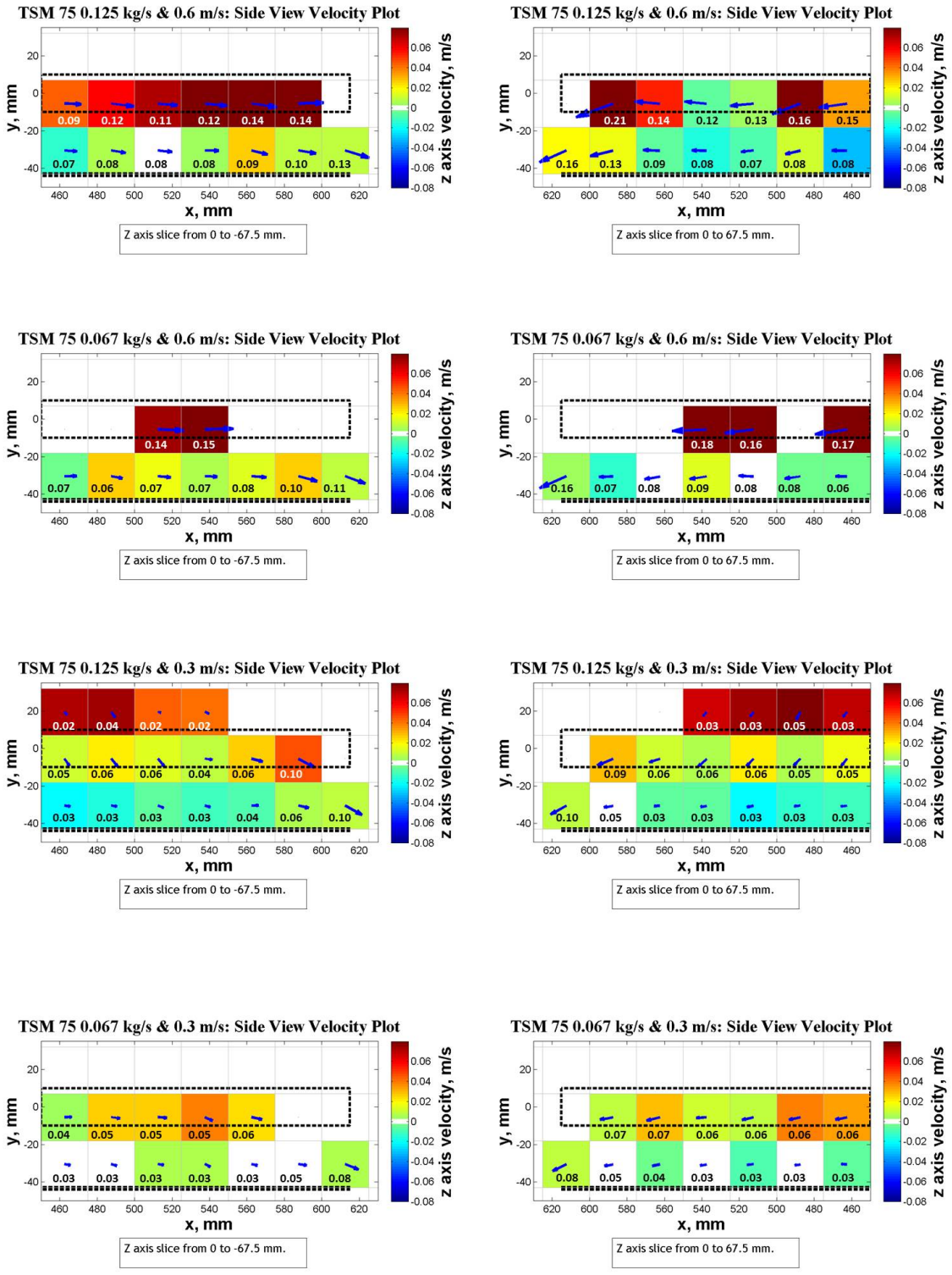

Figure 5.4: Side view velocity plots of the 4 PEPT regimes. The cross sectional area along the x and y axis has been discretised into 25 mm^2 voxels. The 2D velocity of each quiver is given in m/s.

Figure 5.5 shows the TSM 75 velocity plots within the z vs y plane (radial vs. vertical plane), with the left hand side showing the slice of the system before the tapering region starts to take effect and the right hand side being just the tapering region.

In Figure 5.5 for the 0.125 kg/s and 0.3 m/s non-tapering down section, where the X axis slice is from 450 to 525 mm, when the bulk reaches the top of the system along the y axis (vertical axis), it rapidly falls downwards under the influence of gravity, and towards the extremes of the z axis. The circular flow path of the bulk around both screw shafts can also be seen, via the quiver plots, travelling at 0.03 m/s at the bottom of the y axis and at the z axis (radial) extremes, then going down to 0.02 m/s in the centre of the z axis as the streams come together. Before finally increasing again to 0.04 m/s when reaching the top of the y axis (vertical).

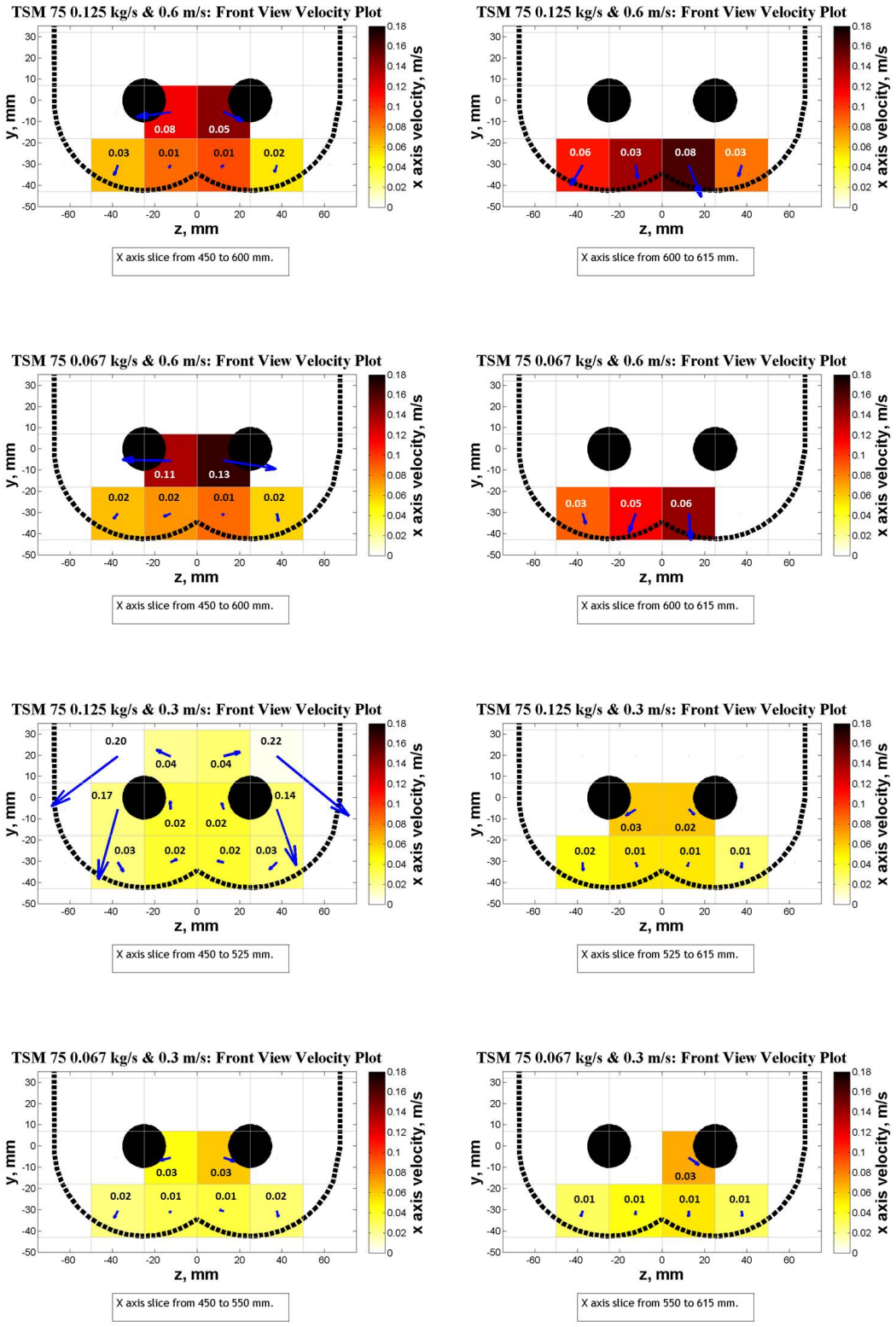

Figure 5.5: Front view velocity plots of the 4 PEPT regimes. The cross sectional area along the x and y axis has been discretised into 25 mm^2 voxels. The 2D velocity of each quiver is given in m/s.

Figure 5.6 shows a top down Velocity Plot of the two 0.6 m/s screw speed regimes. The system has been sliced 3 ways for each: 1) a whole top down view of the system, 2) a bottom slice of the system (from -43 mm to -18 mm along the y axis) and 3) a top slice of the system (from -18 to 7 mm along the y axis). This slicing captures all tracers that entered the system.

These plots clearly show that the bulk in between the screws shafts in the bottom slices (-43 mm to -18 mm along y axis) tend to travel in a axial fashion at approximately the rate of the screw lead (0.08 m/s). This is until the tapering region is reached and the axial velocity increases as the bulk leaves the system under the influence of gravity. The same plots also show that the axial velocity decreases at the extremes of the z axis before reaching the tapering region (radial axis). This means that axial transport is not as efficient in this region of the TSM.

In the top slices of the system (-18 to 7 mm along the y axis) the quivers in figure 5.6 show a change in direction and increase in velocity from that described within the bottom slice. This is caused by the tracers having reached the top of the bulk and are now tumbling down towards the extremes of the z axis (radial axis) under the influence of gravity.

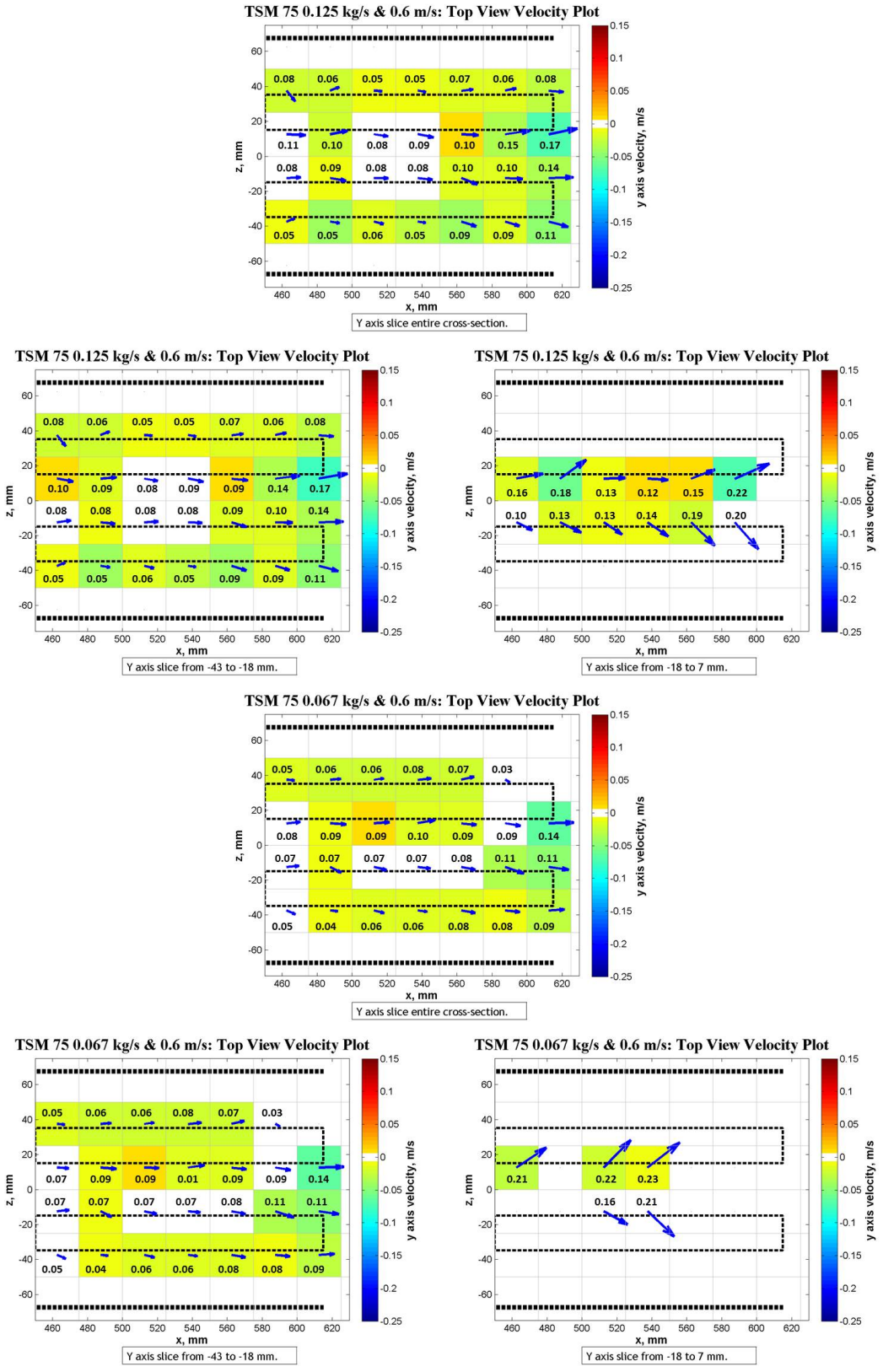

Figure 5.6: Top view velocity plots of the 2 high screw speed PEPT regimes. The cross sectional area along the x and y axis has been discretised into 25 mm^2 voxels. The 2D velocity of each quiver is given in m/s.

Figure 5.7 shows a top down Velocity Plot of the two 0.3 m/s screw speed regimes. Within the figure the 0.125 kg/s and 0.3 m/s regime has been shown in four ways: 1) a whole top down view of the system, 2) a bottom slice of the system (from -43 mm to -18 mm along the y axis) and 3) a middle slice of the system (from -18 to 7 mm along the y axis) and 4) a top slice of the system (from 7 to 32 mm along the y axis). These slices capture all the tracers that entered this system.

As within the 0.6 m/s screw speed regimes, the bottom slice of the top down view for the 0.125 kg/s and 0.3 m/s regime shows the bulk travelling axially at the same rate as the screw lead (0.04 m/s) in the region between the screw shafts. Whilst at the extremes of the z axis the bulk travels less efficiently (until the tapering region is reached and then the axial velocity increases as the tracers leave the system under the influence of gravity). As the fill level is higher there is also a middle slice that follows the same pattern in between the screw shafts (before the tapering region is reached). However, the voxels at the z axis extremes capture the tracers falling towards the extremes of the z axis, having been lifted over the shafts. The top slice of the regime shows a change of direction of the flow as all the material has reached the top of the bulk and is now tumbling to the z axis extremes.

Figure 5.7 also shows a top down Velocity Plot of the 0.067 kg/s and 0.3 m/s regime. This has been shown in three ways: 1) a whole top down view of the system, 2) a bottom slice of the system (from -43 mm to -18 mm along the y axis) and 3) a top slice of the system (from -18 to 7 mm along the y axis). The slices capture all tracers that entered the system.

This regime is similar to the others in that the axial velocity of the bulk in the bottom slice follows the speed of the screw lead (0.04 m/s) with the z axis extremes velocity being slightly less efficient (again this is until the tapering region is reached and then the axial velocity increases as the tracers leave the system under the influence of gravity). The top slice is also similar in that the bulk changes direction and velocity as the tracers reached the top of the bulk and tumble down to the z axis extremes under the influence of gravity.

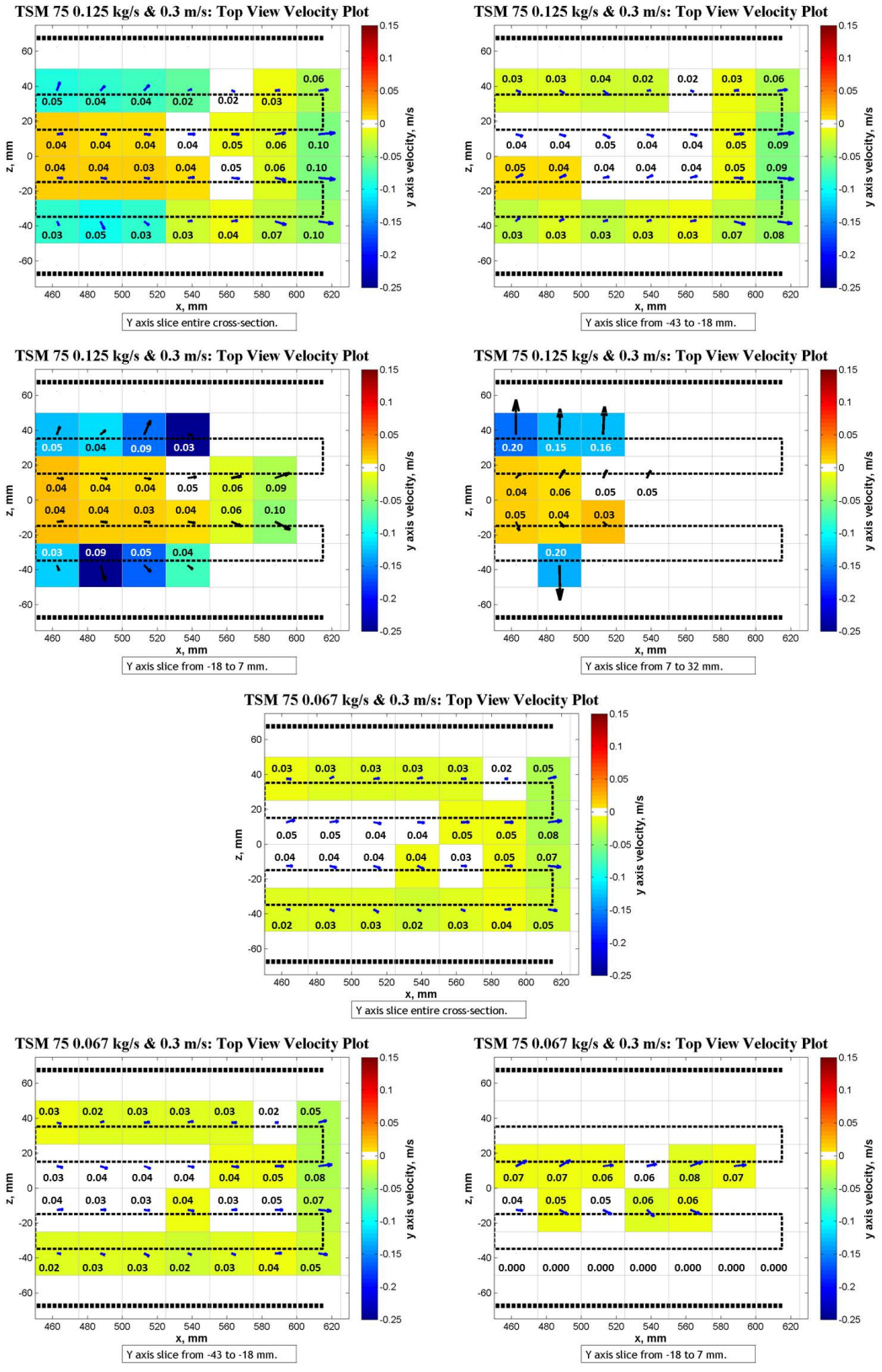

Figure 5.7: Top view velocity plots of the 2 low screw speed PEPT regimes. The cross sectional area along the x and y axis has been discretised into 25 mm^2 voxels. The 2D velocity of each quiver is given in m/s.

The Velocity plots clearly show that the powder tends to travel axially in the TSM at a rate equivalent to the screw lead in the region between the screw shafts. In the extremes of the z axis (radial axis) however, the bulk tends to travel approximately 25% more slowly than this. This is consistent with the findings in Chapter 4, where bulk velocity from Inlet 2 varies between 77% - 90% of the screw lead, depending on Screw Speed and Fill level (as different powder fill levels will mean the bulk spends various different lengths of time circulating in and out of the less efficient z axis extremes).

This may be caused by the fact that the screw flights on each shaft are set to be out of phase with one another. So, between the shafts, as the shafts rotate the flight from one will leave the bulk as the flight from the other will just be entering. This, it seems, has the effect of powder within this region tending to flow at the same rate as the screw lead, as at all times a paddle will be pushing the bulk. It is these gaps in the screw flights that may also lead to the reduction in the flow rate at the z axis extremes, as here the flow will only intermittently be driven along by a paddle.

Figure 5.8 shows two typical tracer journeys in the TSM 75 0.125 kg/s Feed Rate and 0.6 m/s Screw Speed regime. Tracer 65 in this regime (the top four panels) enters the system from a z axis extreme where it follows an axial path to around 500 mm along the x axis, whilst simultaneously ascending upwards to the top of the bulk. The tracer then tumbles down the bulk to a z axis extreme, finding itself positioned at the TSM wall. Being near the wall creates a drag force which reduces its axial velocity. The tracer then slides axially along the TSM wall before exiting the system.

In the bottom four panels tracer 39 enters the system underneath one of the screw shafts. The tracer gradually makes its way into the centre of the z axis whilst travelling axially downstream before finally exiting the system.

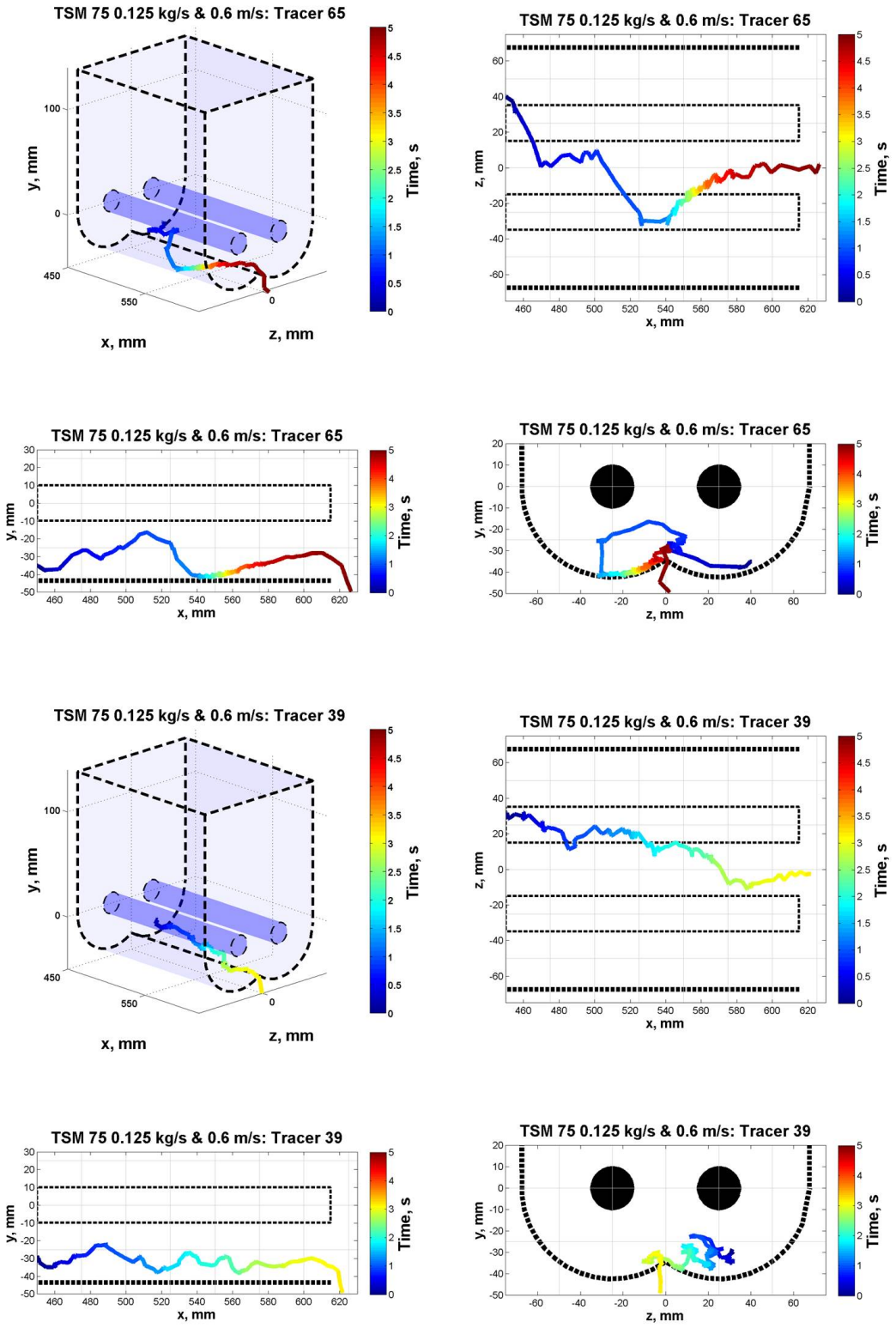

Figure 5.8: Two typical particle journeys in the TSM 75 at 0.6 m/s Screw Speed and 0.125 kg/s Feed Rate.

Figure 5.9 shows two typical tracer journeys in the TSM 75 0.125 kg/s Feed Rate and 0.3 m/s Screw Speed regime. Tracer 13 in this regime (the top four panels) enters the system from a z axis extreme where it follows an axial path to around 520 mm along the x axis, whilst simultaneously ascending upwards to the top of the bulk. The tracer then tumbles down the bulk, and over the screw shaft, to a z axis extreme finding itself positioned at the TSM wall. Being near the wall creates a drag force which reduces its axial velocity. The tracer then slides axially along the TSM wall before exiting the system.

In the bottom four panels tracer 75 enters the system underneath one of the screw shafts. The tracer gradually makes its way into the centre of the z axis, whilst gradually ascending to the top of the bulk, travelling axially downstream before finally exiting the system at the top of the tapering down region.

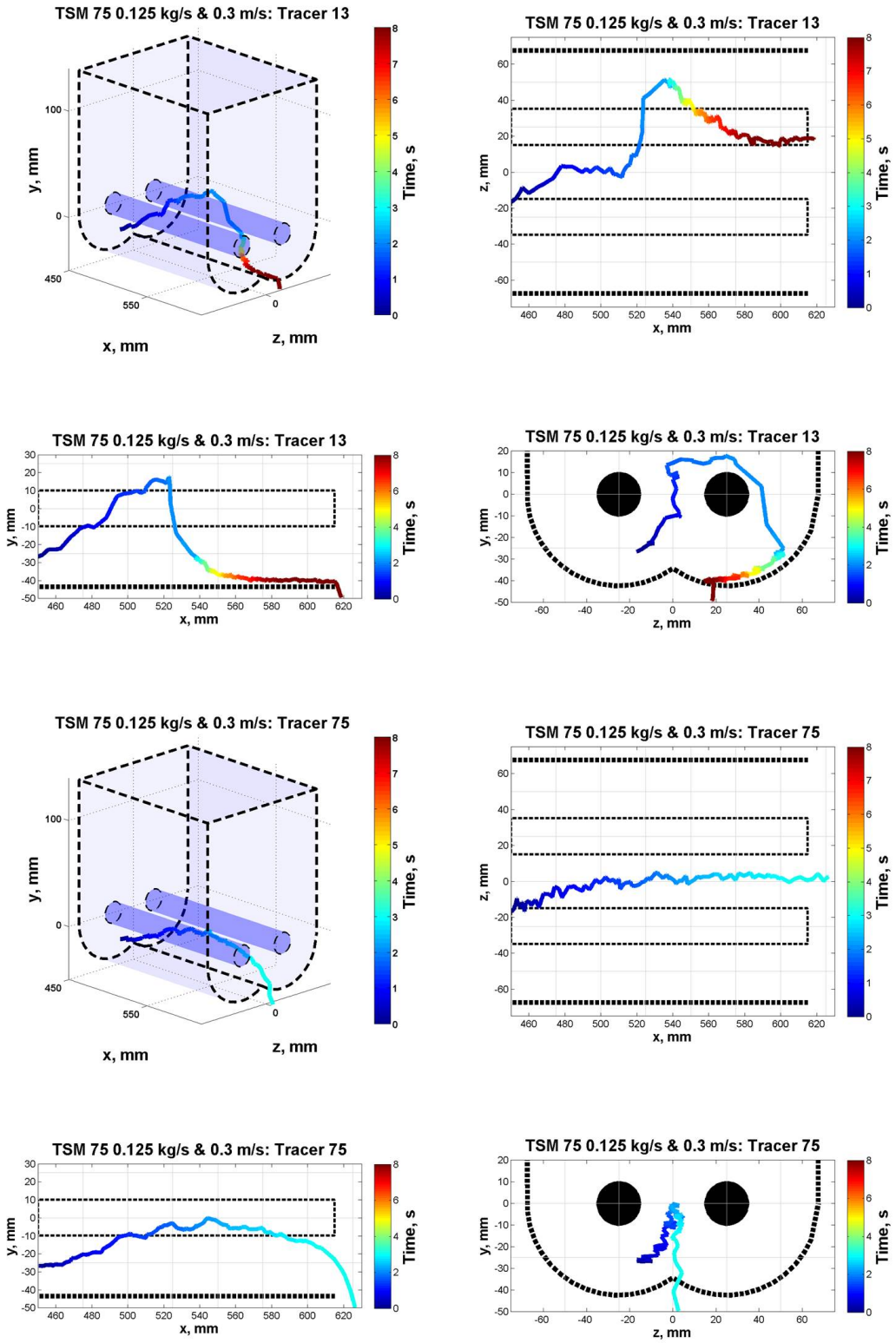

Figure 5.9: Two typical particle journeys in the TSM 75 at 0.3 m/s Screw Speed and 0.125 kg/s Feed Rate.

Figure 5.10 shows two typical tracer journeys in the TSM 75 0.067 kg/s Feed Rate and 0.6 m/s Screw Speed regime. Tracer 46 in this regime (the top four panels) enters the system from centrally along the z axis before tumbling down the bulk to a z axis extreme., whilst simultaneously ascending upwards to the top of the bulk. The tracer then finds itself at the TSM wall at around 520 mm along the x axis. Being near the wall creates a drag force which reduces its axial velocity. The tracer then slides axially along the TSM wall before exiting the system.

In the bottom four panels tracer 81 enters the system underneath one of the screw shafts. The tracer gradually travels along the x axis, making its way into the centre of the z axis as it goes, whilst also gradually ascending to the top of the bulk before exiting the system.

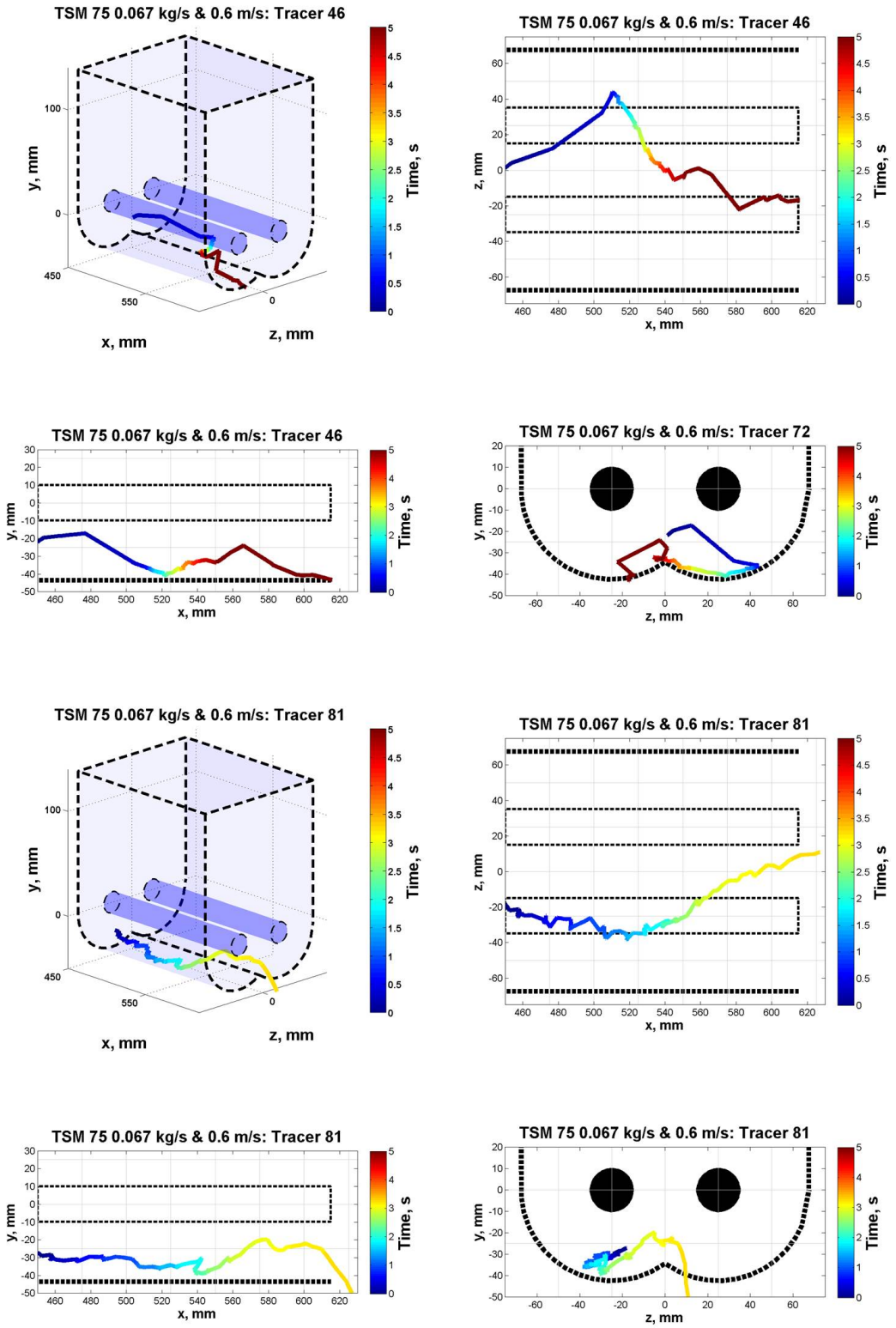

Figure 5.10: Two typical particle journeys in the TSM 75 at 0.6 m/s Screw Speed and 0.067 kg/s Feed Rate.

Figure 5.11 shows two typical tracer journeys in the TSM 75 0.067 kg/s Feed Rate and 0.3 m/s Screw Speed regime. Tracer 83 in this regime (the top four panels) enters the system tumbling down the bulk to a z axis extreme. The tracer then finds itself at the TSM wall at around 500 mm along the x axis. Being near the wall creates a drag force which reduces its axial velocity. The tracer then slides axially along the TSM wall before exiting the system.

In the bottom four panels tracer 37 enters the system centrally along the z axis. The tracer gradually travels along the x axis and upwards. It tumbles down towards the z axis extremes a few times but is pushed back towards the centre each time.

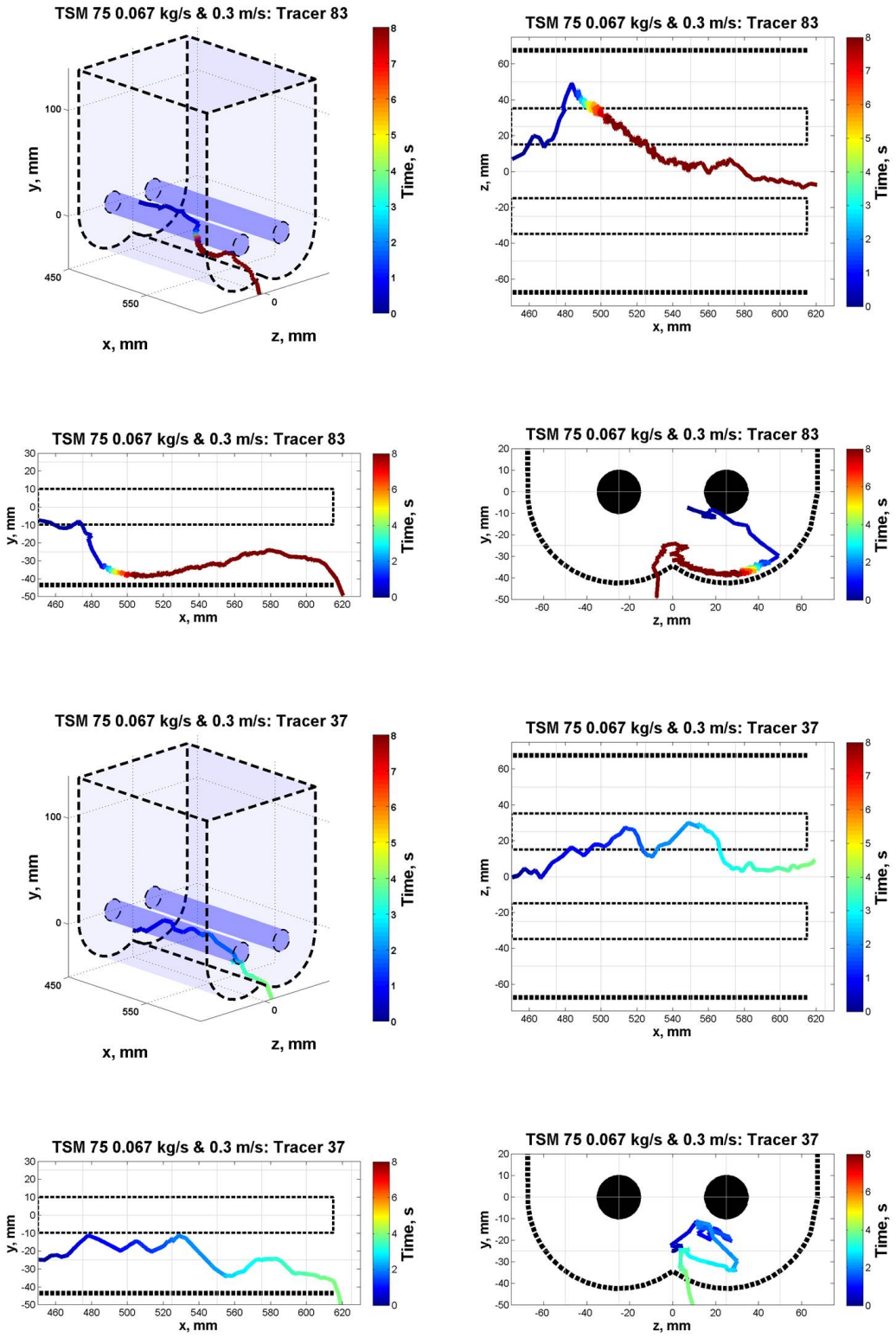

Figure 5.11: Two typical particle journeys in the TSM 75 at 0.3 m/s Screw Speed and 0.067 kg/s Feed Rate.

It is clear from analysing the particle journeys that the flow in these machines could be generally described thus: the powder tends to want to migrate to the middle of the z axis (radial) axis, and once there tends to travel axially downstream. During this axial journey the particle will normally simultaneously ascend to the top of the bulk. Once there the particle will tumble down the bulk to the extremes of the z axis.

Whilst at the extremes of the z axis the powder is also more likely to come into contact with the TSM wall retarding axial particle flow velocity. This may also be one of the factors that cause the downstream flow to be less efficient at the z axis extremes than the powder situated more centrally between the shafts (z axis centre). This means that by increasing the fill level, or using a larger TSM, increased overall flow efficiency could be created by increasing the TSM wall surface to bulk volume ratio, and therefore reduce the amount of time a unit of powder may spend at this interface.

The equation discussed in chapter 1.3 shall now be used to conduct a short mixing study. This equation has been re-written here as equation 5.1. In summary, it may be used to calculate the Mass Weighted Composition Variance s^2. The lower the value of s^2 the better mixing has taken place. With 0 being perfect mixing at the sampling scale being examined.

$$s^2 = \frac{\sum_{i=1}^{i=n} m_i(x_i - \overline{x_w})^2}{(\frac{N-1}{N})\sum_{i=1}^{i=n} m_i} \tag{5.1}$$

Where: s^2 is the mass weighted composition variance, m_i is the mass of the i^{th} sample, x_i is the mass weighted composition of the i^{th} sample, $\overline{x_w}$ is the mass weighted mean composition of the samples and N is the total number of samples (in this case four) [22] .

To adapt this equation for PEPT data the particles entering the system for each regime have been labelled blue or red depending on which half of the z axis it was initially positioned as the tracer entered the system.

As the particles migrate through the system each half (positive and negative sides of z axis) may be used as samples to see how well the particles become mixed as they travel downstream.

Therefore, m_1 is the total number of tracers in the positive half of the z axis at a given time and m_2 is the total number of tracers in the negative half of the z axis at a given time. x_1 is the fraction of particles in the positive half of the z axis that are blue and x_2 is the fraction of the particles in the negative half of the z axis that are blue. $\overline{x_w}$ is the average of x_1 and x_2 and N is the total number of samples, in this case 2.

The results for the 0.125 kg/s Feed Rate and 0.6 m/s Screw Speed regime can be found in table

5.1. The results may also be viewed visually in figure 5.12. The same is true for: the 0.125 kg/s and 0.3 m/s regime, table 5.2 and figure 5.13; the 0.067 kg/s and 0.6 m/s regime, table 5.3 and figure 5.14; and finally the 0.067 kg/s and 0.3 m/s regime, table 5.4 and figure 5.15. A top down view of all tracer particles in each regime in their final position before leaving the system has also been provided as figure 5.16.

Table 5.1: s^2, the Mass Weighted Composition Variance w.r.t. time in the 0.125 kg/s Feed Rate and 0.6 m/s Screw Speed regime.

$\boldsymbol{Time,s}$	x_1	x_2	$\overline{x_w}$	s^2
0.0	1.00	0.00	0.50	0.50
0.5	0.78	0.34	0.56	0.10
1.0	0.77	0.39	0.58	0.07
1.5	0.72	0.47	0.60	0.03
2.0	0.59	0.56	0.58	0.00
2.5	0.55	0.59	0.57	0.00
3.0	0.51	0.62	0.57	0.01
3.5	0.51	0.62	0.57	0.01
5.0	0.51	0.62	0.57	0.01

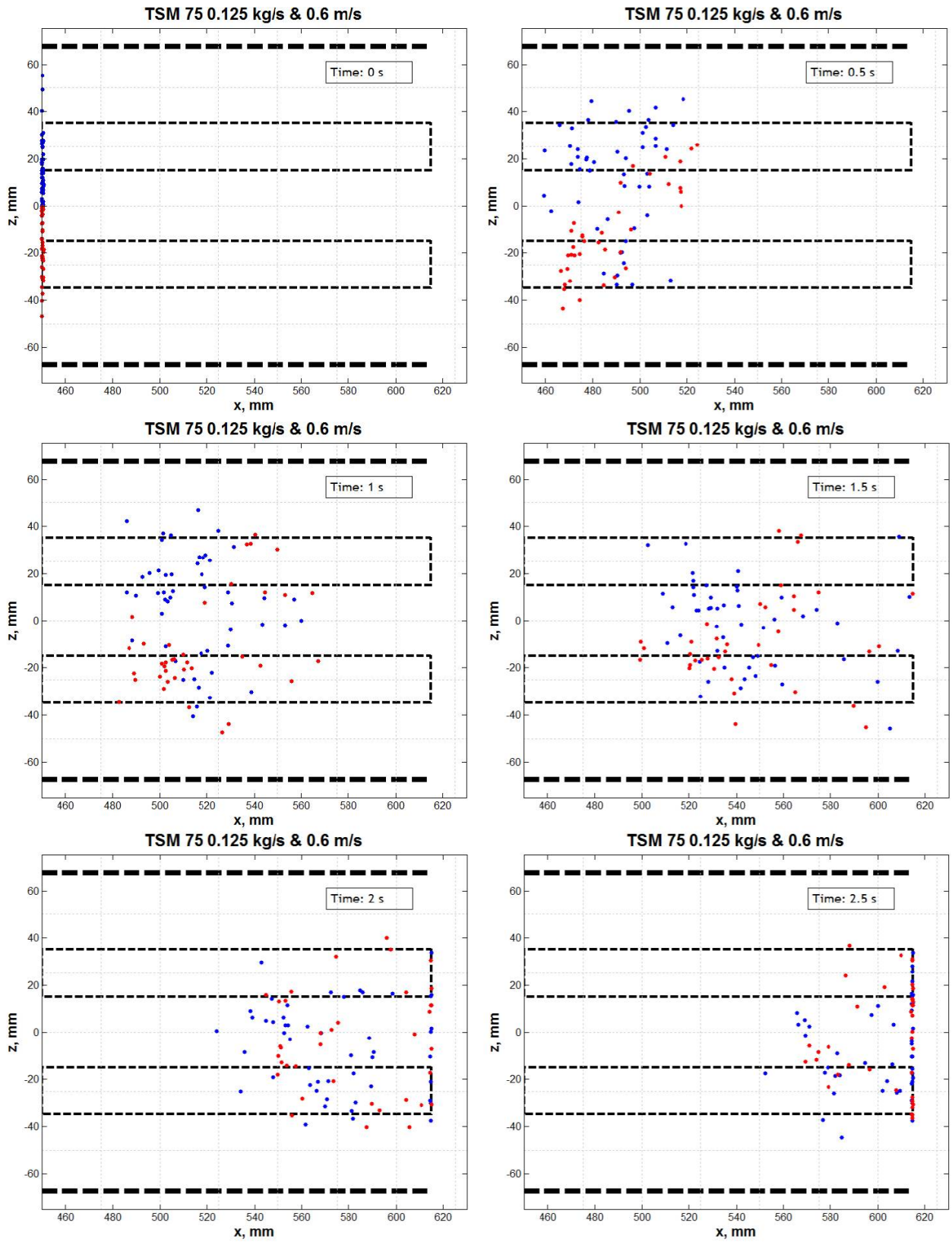

Figure 5.12: Top down view of all tracer particles travelling in the 0.125 kg/s feed rate and 0.6 m/s screw tip speed regime.

Table 5.2: s^2, the Mass Weighted Composition Variance w.r.t. time in the 0.125 kg/s Feed Rate and 0.3 m/s Screw Speed regime.

$\boldsymbol{Time,s}$	x_1	x_2	$\overline{x_w}$	s^2
0.0	1.00	0.00	0.50	0.50
1.0	0.89	0.19	0.54	0.25
2.0	0.84	0.18	0.51	0.22
3.0	0.82	0.28	0.55	0.15
4.0	0.81	0.34	0.58	0.11
5.0	0.78	0.39	0.58	0.08
9.0	0.75	0.43	0.59	0.05

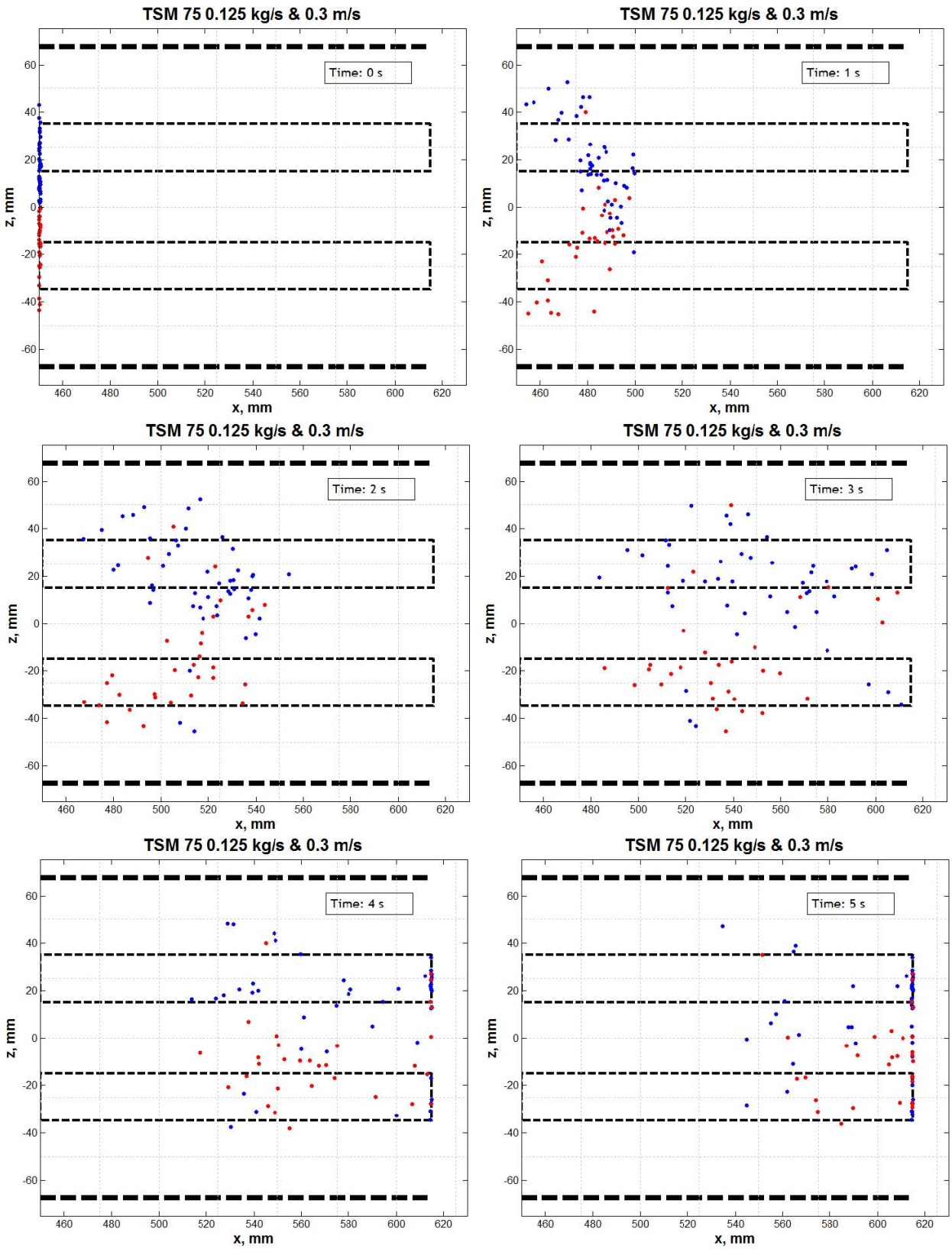

Figure 5.13: Top down view of all tracer particles travelling in the 0.125 kg/s feed rate and 0.3 m/s screw tip speed regime.

Table 5.3: s^2, the Mass Weighted Composition Variance w.r.t. time in the 0.067 kg/s Feed Rate and 0.6 m/s Screw Speed regime.

$\boldsymbol{Time,s}$	x_1	x_2	$\overline{x_w}$	s^2
0.0	1.00	0.00	0.50	0.50
0.5	0.77	0.24	0.51	0.14
1.0	0.79	0.38	0.59	0.09
1.5	0.70	0.45	0.57	0.03
2.0	0.71	0.49	0.60	0.02
2.5	0.58	0.58	0.58	0.00
3.0	0.60	0.57	0.58	0.00
3.5	0.52	0.62	0.57	0.01
10.0	0.53	0.61	0.57	0.00

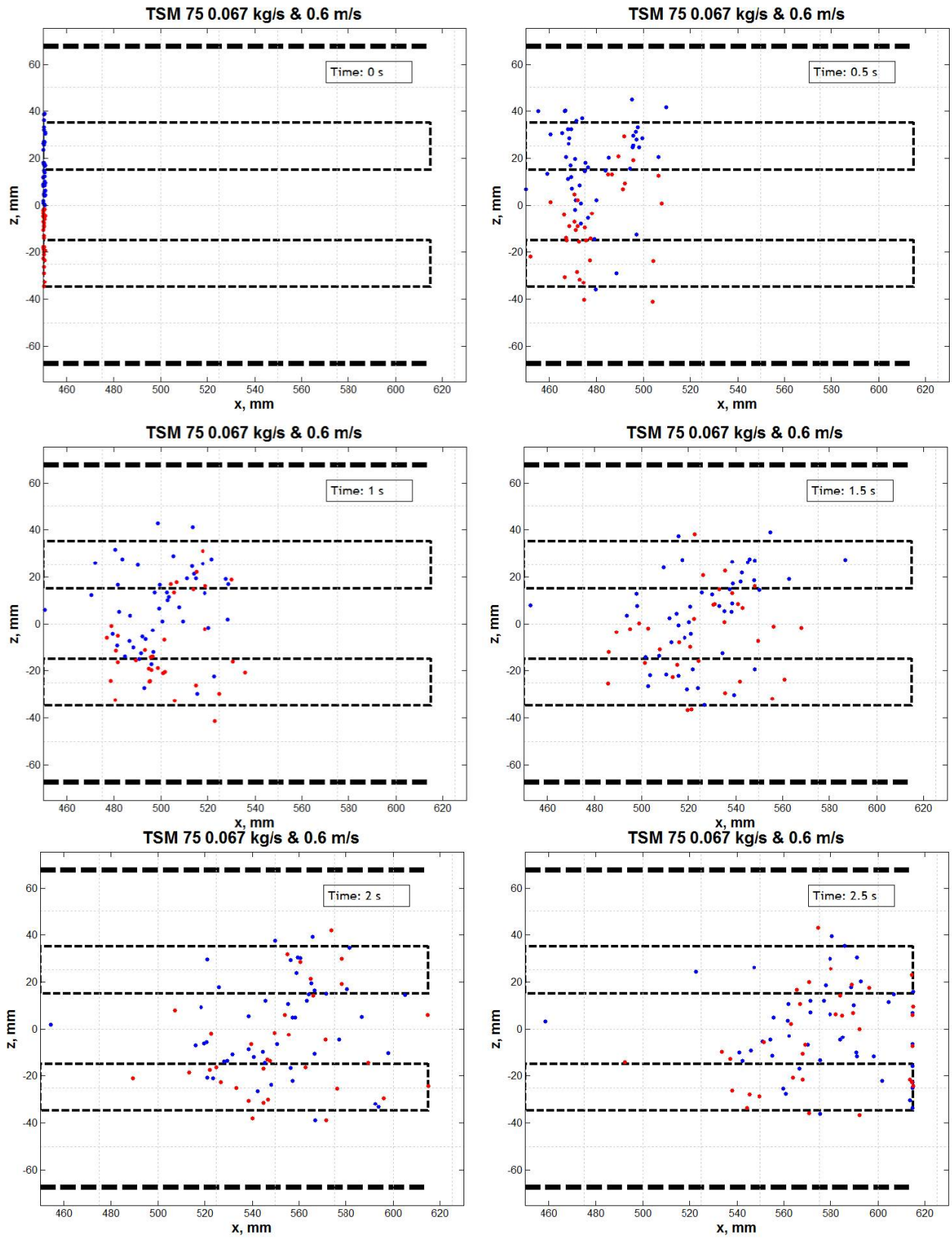

Figure 5.14: Top down view of all tracer particles travelling in the 0.067 kg/s feed rate and 0.6 m/s screw tip speed regime.

Table 5.4: s^2, the Mass Weighted Composition Variance w.r.t. time in the 0.067 kg/s Feed Rate and 0.3 m/s Screw Speed regime.

$\boldsymbol{Time,s}$	x_1	x_2	$\overline{x_w}$	s^2
0.0	1.00	0.00	0.50	0.50
1.5	0.70	0.35	0.53	0.06
2.5	0.67	0.46	0.57	0.02
3.5	0.61	0.53	0.57	0.00
4.5	0.56	0.58	0.57	0.00
5.5	0.51	0.62	0.57	0.01
6.5	0.49	0.64	0.56	0.01
7.5	0.49	0.64	0.56	0.01
12.0	0.47	0.65	0.56	0.02

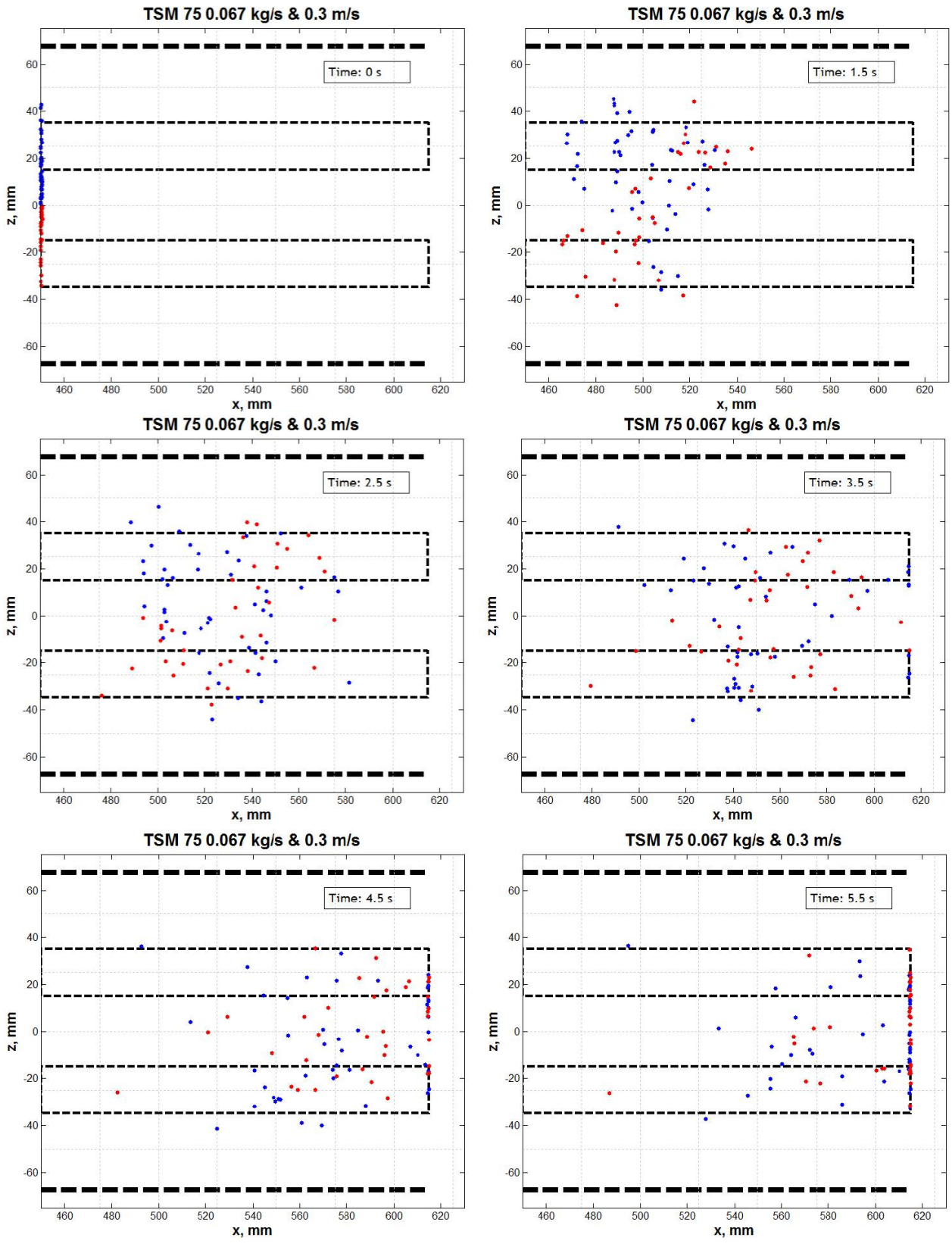

Figure 5.15: Top down view of all tracer particles travelling in the 0.067 kg/s feed rate and 0.3 m/s screw tip speed regime.

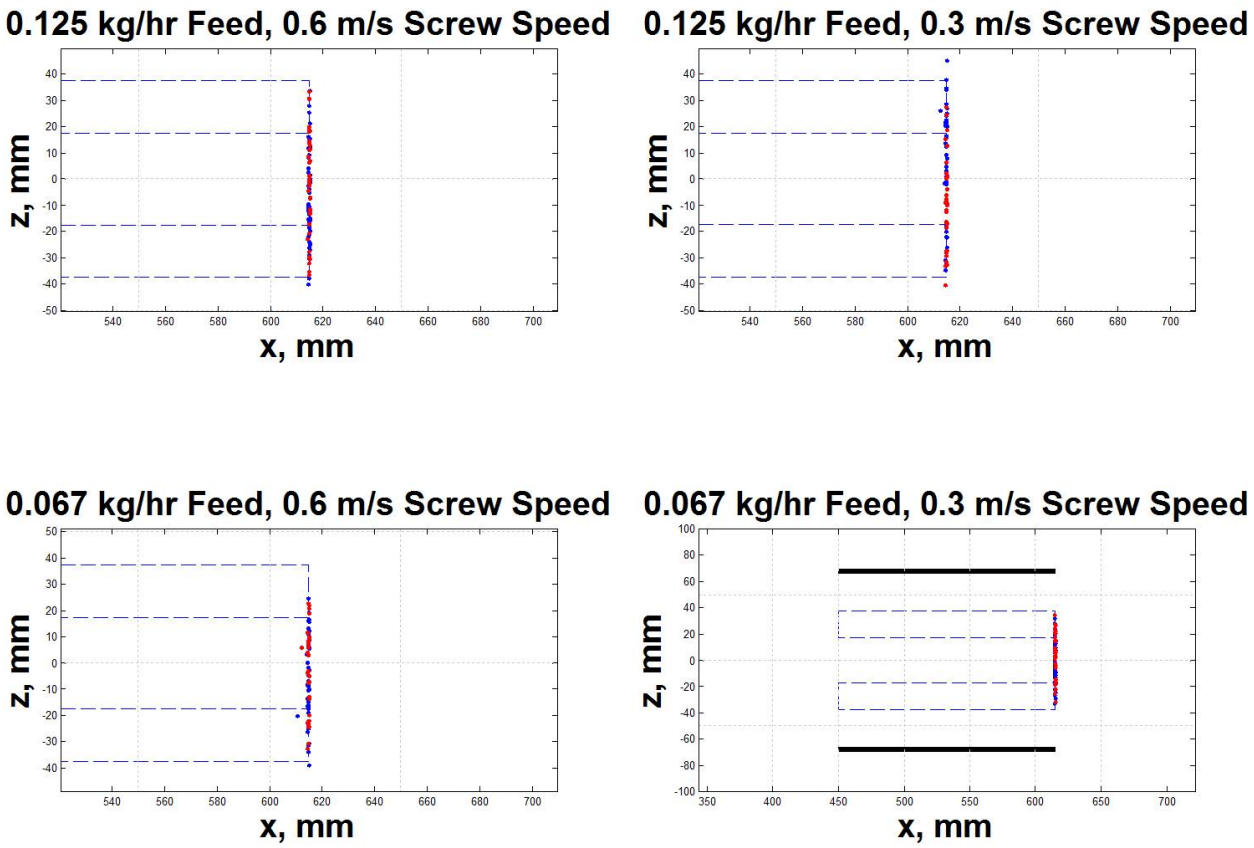

Figure 5.16: Top down view of all tracer particles for each regime in their final position before leaving the system.

s^2 has been plotted with respect to time for each of the four regimes in figure 5.17.

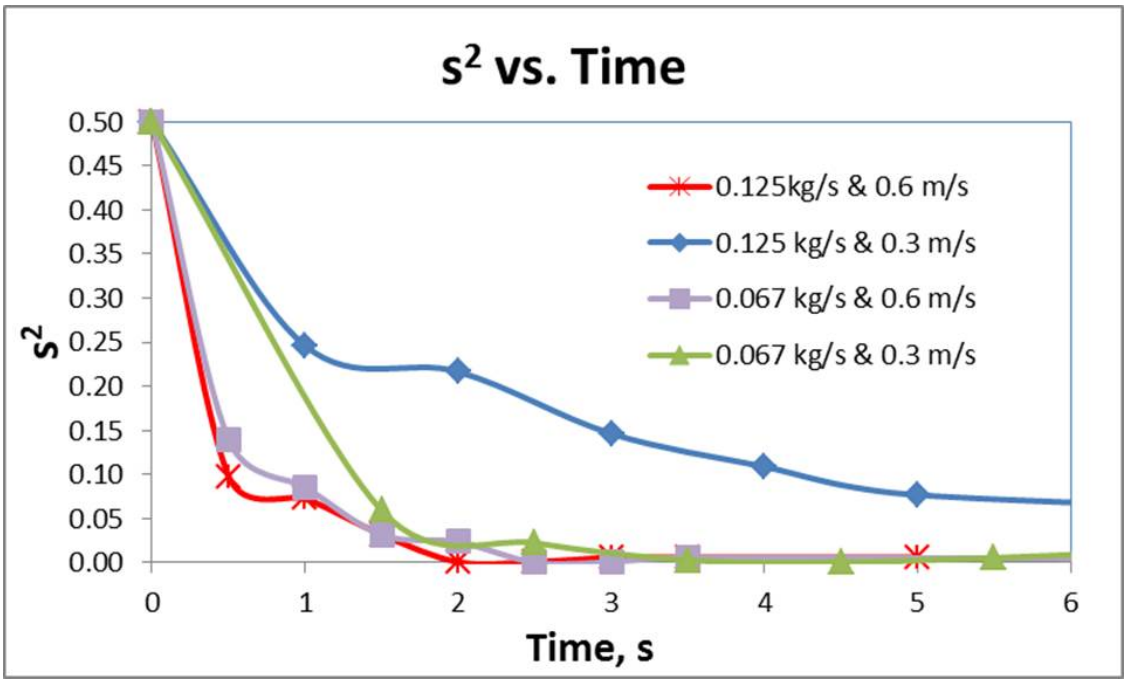

Figure 5.17: s^2 has been plotted with respect to time for each of the four PEPT regimes.

For the 0.125 kg/s Feed Rate and 0.6 m/s Screw Speed regime, figures 5.12 and 5.17 clearly show the particles very quickly mix within the first half second, in a radial fashion, as the screw flights push the particles into the center of the z axis. The mixing then slows down as some of the particles fall to the extremes of the z axis. Mixing again commences from about 1 to 2 seconds as the particles are again carried together into the z axis center. The same description may also be given to the 0.067 kg/s Feed Rate and 0.6 m/s Screw Speed regime (figure 5.14).

The two 0.3 m/s Screw Speed regimes mix at the same rate from about 1 to 2 seconds (as seen in figures 5.12 and 5.15). However, mixing is complete at around 2 seconds for the 0.3 m/s and 0.067 kg/s regime, the same as for the two 0.6 m/s Screw Speed regimes. This could be because the powder comes together more smoothly in the 0.3 m/s and 0.067 kg/s regime (so do not fall as far to the z axis extremes), and the two sides of the bulk smoothly keep recombining at the same rate until the mixing is complete.

The 0.125 kg/s and 0.3 m/s regime is the only one where the powder fill level is high enough to go over the screw shafts. This explains the sudden slow down in mixing from 1 to 2 seconds, as the tracers have fallen the furthest distance along the z axis (after being pushed over the screw shafts) and have a long distance to travel back to the center. It is this long journey over the shafts and back to the z axis center that has meant the powder has not mixed radially as well as the other starve filled regimes.

Despite the highest fill level, where the bulk encircles the screw shafts, leading to slower radial mixing, it this author's opinion that this would be the best fill level to use (of the four levels investigated in this PEPT study). This is because this flow regime is less likely to lead to stagnant regions in the z axis extremes, so whilst radial mixing may decrease overall, quality may increase (although stagnant regions do not seem to be an issue with this model powder, but could become more dominant if a more cohesive or adhesive blend was used). It is clear however, that higher fill levels require a longer axial length of TSM that that being investigated here (from 450 mm to 615 mm along the axial length) in order to fully radially mix the model powder.

5.2 Conclusions

The PEPT study has shown that the powder within the TSM 75 tends to spend the majority of its time being pushed in between the screw shafts as it travels axially downstream. In the medium fill level (0.125 kg/s and 0.3 m/s) the powder tends to keep circling around the shafts as it travels axially downstream. In all the regimes studied it is this pushing together of the powder from both sides of the z axis that induces radial mixing.

The powder has also been shown to axially flow at the same rate as the screw lead in the central region between the two screws. This is caused by the screw flights being set to be out of phase on each shaft, so as one flight enters the bulk another will be leaving the bulk. At the z axis extremes the gaps between the screw flights cause the velocity to decrease by around 25%.

Radial mixing has been shown to be least efficient in the mid fill level regime (0.125 kg/s and 0.3 m/s) and most efficient in the three starve filled regimes investigated. This is because the mid fill regime is the only one where powder is pushed over the shaft and travels a much further distance to the radial axis extremes (producing a longer route back to the radial center). However, the quality of mixing may increase overall, as this means there is less stagnant regions at these radial extremes due to the circular flow around the shafts.

Chapter 6

Investigating axial dry powder flow in large-scale, counter-rotational, intermeshing Twin-Screw Mixers (TSMs), with respect to alterations in size and internal geometry.

6.1 Results and Discussion

6.1.1 Response Surface Model (RSM) investigation of TSM 125 and comparison to TSM 75.

The main objectives within this Chapter is the following:

- To use the methodology described fully in Chapter 3 and validated and summarised in Chapter 4 to characterise a TSM 125 (a larger version of the TSM 75), using two different paddle geometries.
- To compare the findings with the TSM 75 results to assess how these machines behave upon scale-up.

The TSM 125 has been analysed using 2 different geometries via the approach described in Chapter 3, and validated in Chapter 4. This includes transforming τ and σ^2 into Velocity and $1/\sigma^2$ respectively, for the purposes of process modelling and comparisons between geometries and scale.

The RTD metrics for the All Quadrant TSM 125 has been provided as Table 6.1 for Inlet 1 and 6.2 for Inlet 2. The dependant variables have then been plotted within Figure 6.1, in the form they are calculated via the RTDs (left hand side) and their transformed state (right hand side), all with respect to Screw Tip speed.

Table 6.1: The TSM 125 Inlet 1, All quadrant, RTD metrics. The curves were generated 5 times using the procedure outlined in materials and methods, this allowed a calculation of the standard error for τ and σ^2; and so subsequently the confidence intervals of the Fill % and velocity, which were given as the Standard Error (SE). The code refers to the TSM Screw Tip Speed and powder Feed Rate used in the DoE, which may be referenced in Tables 3.1 and 3.3.

$\boldsymbol{Run\ (Code)}$	$\boldsymbol{\tau, s}$	$\boldsymbol{SE(\tau), s}$	$\boldsymbol{\sigma^2, s^2}$	$\boldsymbol{SE(\sigma^2), s^2}$	$\boldsymbol{V, m/s}$	$\boldsymbol{Fill, \%}$
$\mathbf{1\ (Mid\backslash Mid)}$	33.21	0.02	6.85	0.23	0.023±0.000	26.52±0.03
$\mathbf{2\ (Mid\backslash V.High)}$	39.75	0.01	7.36	0.14	0.019±0.000	55.50±0.02
$\mathbf{3\ (Mid\backslash Low)}$	15.27	0.00	2.68	0.08	0.051±0.000	7.33±0.00
$\mathbf{4\ (V.Low\backslash Mid)}$	67.47	0.15	32.66	0.86	0.011±0.000	53.89±0.25
$\mathbf{5\ (High\backslash High)}$	11.97	0.00	1.45	0.08	0.065±0.000	14.34±0.01
$\mathbf{6\ (Mid\backslash V.Low)}$	33.87	0.02	14.12	0.54	0.023±0.000	13.52±0.02
$\mathbf{7\ (Low\backslash Low)}$	36.76	0.01	16.46	0.70	0.021±0.000	17.64±0.01
$\mathbf{8\ (Mid\backslash Mid)}$	32.34	0.06	8.21	0.73	0.024±0.000	25.83±0.11
$\mathbf{9\ (Low\backslash High)}$	46.53	0.12	20.71	1.08	0.017±0.000	55.74±0.29
$\mathbf{10\ (Mid\backslash Mid)}$	33.01	0.02	8.66	0.25	0.023±0.000	26.37±0.04
$\mathbf{11\ (V.High\backslash Mid)}$	11.75	0.01	1.45	0.00	0.066±0.000	9.38±0.02

Table 6.2: The TSM 125 Inlet 2, All quadrant, RTD metrics. The curves were generated 5 times using the procedure outlined in materials and methods, this allowed a calculation of the standard error for τ and σ^2; and so subsequently the confidence intervals of the Fill % and Velocity, which were given as the Standard Error (SE). The code refers to the TSM Screw Tip Speed and powder Feed Rate used in the DoE, which may be referenced in Tables 3.1 and 3.3.

$\boldsymbol{Run\ (Code)}$	$\boldsymbol{\tau, s}$	$\boldsymbol{SE(\tau), s}$	$\boldsymbol{\sigma^2, s^2}$	$\boldsymbol{SE(\sigma^2), s^2}$	$\boldsymbol{V, m/s}$	$\boldsymbol{Fill, \%}$
$\mathbf{1\ (Mid\backslash Mid)}$	14.02	0.03	5.82	0.35	0.023±0.000	26.70±0.12
$\mathbf{2\ (Mid\backslash V.High)}$	14.85	0.02	4.87	0.22	0.022±0.000	49.46±0.00
$\mathbf{3\ (Mid\backslash Low)}$	6.31	0.00	1.57	0.05	0.052±0.000	7.22±0.00
$\mathbf{4\ (V.Low\backslash Mid)}$	23.23	0.04	15.93	2.04	0.014±0.000	44.25±0.17
$\mathbf{5\ (High\backslash High)}$	5.50	0.02	1.30	0.03	0.059±0.000	15.71±0.10
$\mathbf{6\ (Mid\backslash V.Low)}$	13.59	0.02	7.76	0.34	0.024±0.000	12.94±0.04
$\mathbf{7\ (Low\backslash Low)}$	16.37	0.01	12.99	0.20	0.020±0.000	18.73±0.03
$\mathbf{8\ (Mid\backslash Mid)}$	13.96	0.05	4.75	0.16	0.023±0.000	26.58±0.18
$\mathbf{9\ (Low\backslash High)}$	16.71	0.03	7.91	0.35	0.019±0.000	47.74±0.17
$\mathbf{10\ (Mid\backslash Mid)}$	13.99	0.01	4.87	0.18	0.023±0.000	26.64±0.02
$\mathbf{11\ (V.High\backslash Mid)}$	4.48	0.00	1.01	0.04	0.073±0.000	8.54±0.01

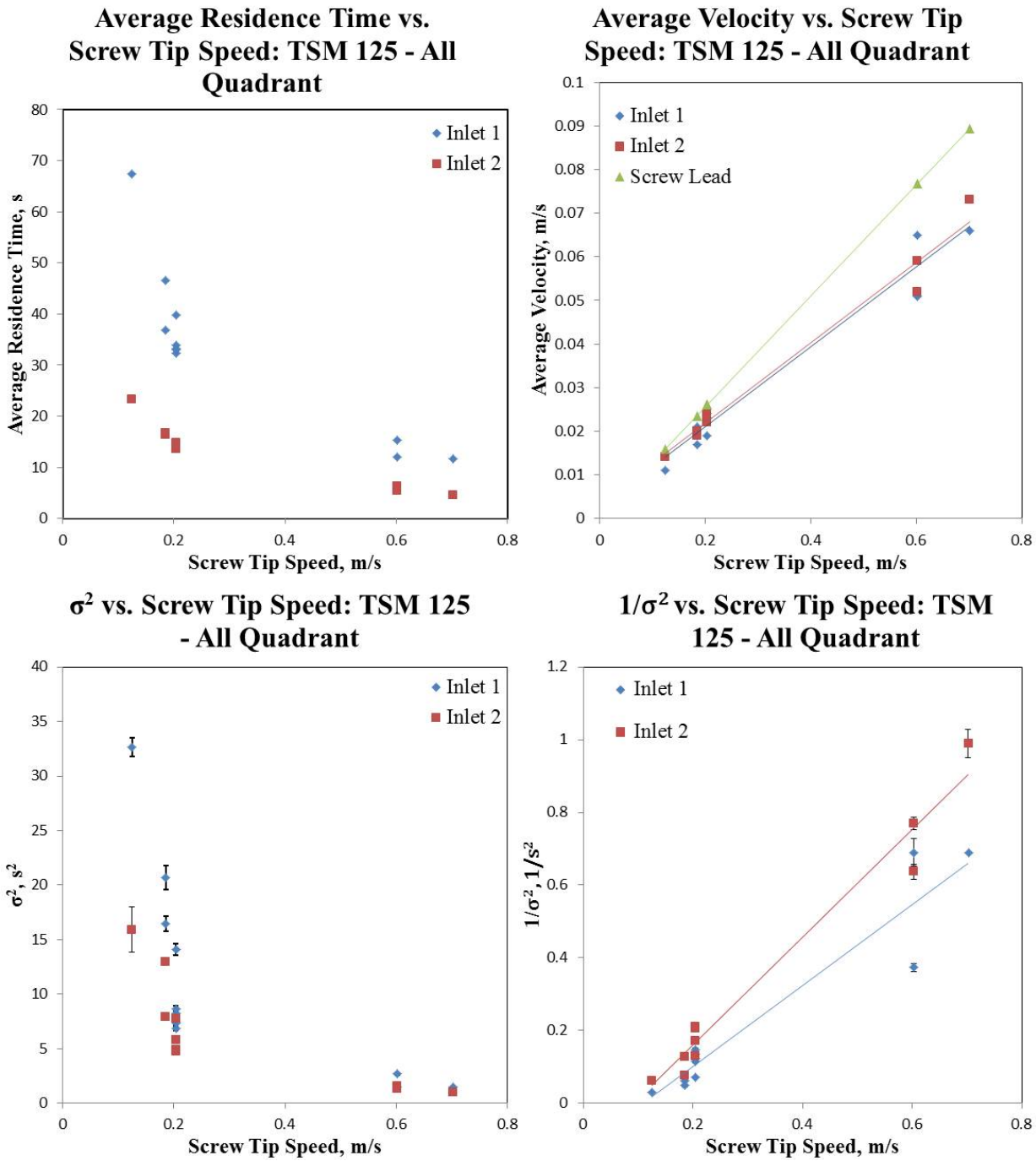

Figure 6.1: The RTD metrics for the TSM 125 - All Quadrant plotted vs. Screw Tip Speed. The error bars denote the SE (all error bars are included but some are so small they may be difficult to discern).

The straight line equation metrics in Table 6.3 can now be compared with those for the TSM 75 in Table 4.3. The Screw Lead, for different Screw Tip speeds, was calculated to be the same; which is testament to the fact both machines are geometrically similar (with a gradient of 0.13 and a

Constant of 0.00).

Even more interesting is the overall average Velocity equations between both machines are almost equal. With the only difference being a constant value of 0.01 for the TSM 75 Inlet 2 Velocity. There is however, a marked difference in the behaviour of the $1/\sigma^2$ equations from the TSM 75, as the axial length from Inlet 2 of the TSM 125 has allowed allowed the Screw Tip Speed to have more of an effect upon the response.

Table 6.3: TSM 125 - All Quadrant: Screw Speed vs. RTD metrics straight line equation parameters (as displayed in 6.1).

Dependent Variable	**Gradient**	**Constant**	$\boldsymbol{R^2}$
$\boldsymbol{Screw\ Lead, m/s}$	0.13	0.00	N/A
$\boldsymbol{V(Inlet, 1), m/s}$	0.09	0.00	0.96
$\boldsymbol{V(Inlet, 2), m/s}$	0.09	0.00	0.98
$\boldsymbol{1/\sigma^2(Inlet, 1), 1/s^2}$	1.11	-0.12	0.90
$\boldsymbol{1/\sigma^2(Inlet, 2), 1/s^2}$	1.48	-0.13	0.97

The RSMs for the TSM 125 were then constructed in the same fashion as in Chapter 4. Table 6.4 displays the Average Velocity at Inlet 1 in it's coded form and Equation 6.1 shows the same model in uncoded units. The model generally scores very highly on all the statistical metrics used to measure the Goodness-of-Fit and so should be highly accurate.

Table 6.4: Coded Coefficient Table for TSM 125 Inlet 1 all quadrant, Velocity Model. The hierarchical model retained terms using 90% confidence, determined via the P-values (the more usual 95% confidence was not used, as a visual inspection of the data indicated that the squared tip speed term should be retained). Metrics to determine the Goodness-of-Fit included: R^2 of 99.63%, Adjusted R^2 of 99.38%, a Predicted R^2 of 94.68% and a Lack-of-Fit P-value greater than 0.05.

Term	**Coefficient**	**P-Value**	**VIF**
$\boldsymbol{Constant}$	0.03348	0.000	
$\boldsymbol{Tip\ Speed}$	0.10352	0.000	7.85
$\boldsymbol{Feed\ Rate}$	0.00569	0.244	1.01
$\boldsymbol{(Tip\ Speed)^2}$	-0.0556	0.106	7.86
$\boldsymbol{(Tip\ Speed) \times (Feed\ Rate)}$	0.1698	0.000	1.01

$$Velocity,\ m/s\ (Inlet\ 1) = 0.00954 + 0.089 Tip\ Speed,\ m/s - 0.04712 Feed\ Rate,\ kg/s \\ -0.05562(Tip\ Speed,\ m/s)^2 + 0.1698(Tip\ Speed,\ m/s) \times (Feed\ Rate,\ kg/s) \tag{6.1}$$

The coded coefficients for the first order terms are both positive. This means that the impact of Tip Speed and Feed Rate upon the predictors is also generally positive.

Table 6.5 displays the RSM model for the inverse of σ^2 at Inlet 1 in its coded coefficient form, and Equation 6.2 shows the same model in uncoded units. As before, the model scores very highly on the statistical metrics used to measure the Goodness-of-Fit and so should again be highly accurate.

Table 6.5: Coded Coefficient Table for TSM 125 Inlet 1, all quadrant, $(\sigma^2)^{-1}$. The hierarchical model retained terms using 95% confidence, determined via the P-values. Metrics to determine the Goodness-of-Fit included: R^2 of 98.62%, Adjusted R^2 of 98.03%, a Predicted R^2 of 92.36% and a Lack-of-Fit -value greater than 0.05.

Term	**Coefficient**	**P-Value**	**VIF**
$\boldsymbol{Constant}$	0.2271	0.000	
$\boldsymbol{Tip\ Speed}$	1.1214	0.000	1.00
$\boldsymbol{Feed\ Rate}$	0.4289	0.003	1.00
$\boldsymbol{(Tip\ Speed) \times (Feed\ Rate)}$	2.865	0.001	1.01

$$1/\sigma^2,\ 1/s^2\ (Inlet\ 1) = 0.012 + 0.292 Tip\ Speed,\ m/s - 0.462 Feed\ Rate,\ kg/s \\ +2.865(Tip\ Speed,\ m/s) \times (Feed\ Rate,\ kg/s) \tag{6.2}$$

The coded coefficients show that both first order terms for the model are positive. This means the effect of Tip Speed and Feed Rate is also generally positive for the inverse of curve variance. Therefore the opposite is true for σ^2 in its non-inverse form.

The top two plots in Figure 6.2 show three dimensional response surface plots of the same models. However, the inverse curve variance plot has been converted back to its non-reciprocal σ^2 form.

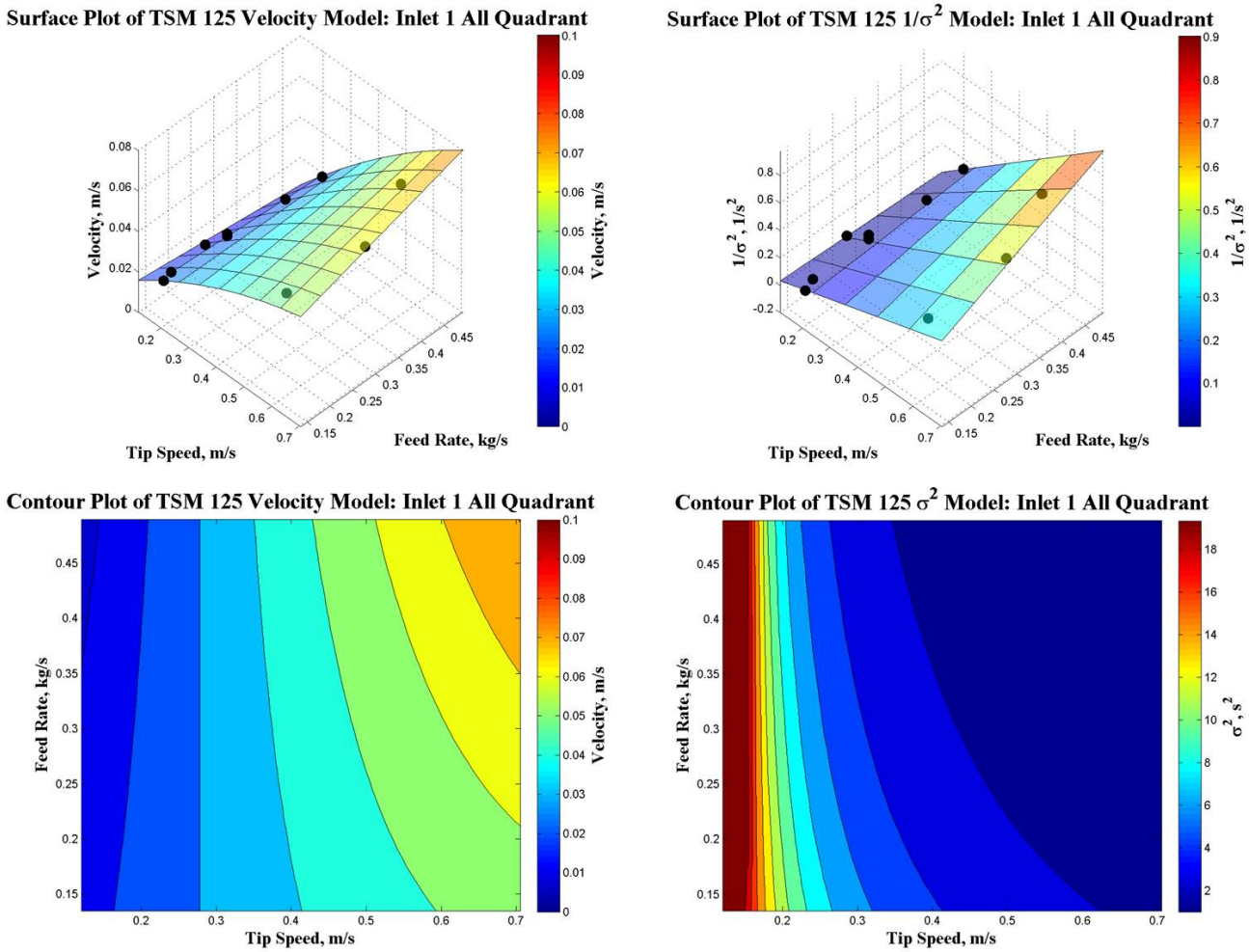

Figure 6.2: (Left) The TSM 125 Inlet 1, all quadrant, Velocity Model, displayed as a 3D surface plot (top) and a 2D contour plot (bottom). (Right) The TSM 125 Inlet 1, all quadrant, $1/sigma^2$ Model, displayed as a 3D surface plot (top), and displayed in non-reciprocal form as a 2D contour plot (bottom).

As for the TSM 75 models (displayed in Figure 4.2), the Inlet 1 Average Velocity Response Surface for the TSM 125 clearly shows how the response variable is dominated by Screw Speed within most of the range examined. However, this becomes less true over Screw Tip Speeds of around 0.6 m/s, as the model suggests the Independent Variables then tend toward becoming equally important. This is in contrast to the TSM 75, where this change happens at around 0.8 m/s.

As was the case for the TSM 75, this is again because very high screw speeds can lead to extreme system starvation and so axial flow can become more inefficient, unless compensated for by Feed Rate. However, this effect seems to be more pronounced in the TSM 125, indicating that fill level

is even more important to axial flow velocity than for the TSM 75.

Conversely (and to a lesser extent), for values below around 0.3 m/s Tip Speed, increasing the Feed Rate actually begins to slow down the overall Average Velocity; just as was witnessed in the TSM 75. This may again be explained by very High Fill levels leading to the development of stagnant regions at the top corners of the TSMs x vs z axis, where the paddle tips are unable to reach. These results may also be indicative of the flow being bumped along in a more piecemeal fashion as also described for the TSM 75.

Meanwhile, σ^2 is dominated by Tip Speed alone from the minimum Screw Speed to around 0.4 m/s, in contrast to the TSM 75, where this turning point occurs around 0.3 m/s. This again demonstrates that reducing the Tip Speed in the region when the powder is pushed along by the paddles in a piecemeal fashion causes an exponential increase in curve variance. However, this change in the flow regime appears at a higher Tip Speed in the TSM 125 compared to the TSM 75 (at 0.4 m/s rather than at 0.3 m/s).

Table 6.6 displays the RSM model for Average Velocity at Inlet 2 in its coded coefficient form and Equation 6.3 shows the same model in uncoded units. The model scores very highly on all the statistical metrics used to measure the Goodness-of-Fit and so should be highly accurate.

Table 6.6: Coded Coefficient Table for TSM 125 Inlet 2, all quadrant, Velocity Model. The hierarchical model retained terms using 80% confidence, determined via the P-values (the more usual 95% confidence was not used, as a visual inspection of the data indicated that the squared tip speed term and interaction term should be retained). Metrics to determine the Goodness-of-Fit included: R^2 of 98.91%, Adjusted R^2 of 99.18%, a Predicted R^2 of 76.55%. The Lack-of-Fit P-value could not be calculated as there was no variation in the repeated center point, so the SSPE was 0.

Term	**Coefficient**	**P-Value**	**VIF**
$\boldsymbol{Constant}$	0.02895	0.000	
$\boldsymbol{Tip\ Speed}$	0.0766	0.000	7.85
$\boldsymbol{Feed\ Rate}$	0.00416	0.600	1.01
$(\boldsymbol{Tip\ Speed})^2$	0.0757	0.181	7.86
$(\boldsymbol{Tip\ Speed}) \times (\boldsymbol{Feed\ Rate})$	0.0750	0.129	1.01

$$\begin{aligned} Velocity,\ m/s\ (Inlet\ 2) = 0.018 + 0.0078 Tip\ Speed,\ m/s - 0.0192 Feed\ Rate,\ kg/s \\ +0.0757(Tip\ Speed,\ m/s)^2 + 0.075(Tip\ Speed,\ m/s) \times (Feed\ Rate,\ kg/s) \end{aligned} \tag{6.3}$$

As for the TSM 75, the coded coefficients for the Inlet 2 model for the TSM 125 are both positive. This indicates that the effect of the predictors upon the average bulk velocity is also positive.

Table 6.7 displays the RSM model for the σ^2 model at Inlet 2 in its coded coefficient form and Equation 6.4 shows the same model in uncoded units. The model scores very highly on all the statistical metrics used to measure the Goodness-of-Fit and so should be highly accurate.

Table 6.7: Coded Coefficient Table for TSM 125 Inlet 2, all quadrant, $(\sigma^2)^{-1}$. The hierarchical model retained terms using 90% confidence, determined via the P-values (the more usual 95% confidence was not used, as a visual inspection of the data indicated that the squared feed rate term should be retained). Metrics to determine the Goodness-of-Fit included: R^2 of 98.52%, Adjusted R^2 of 97.88%, a Predicted R^2 of 94.40% and a Lack-of-Fit P-value greater than 0.05.

Term	**Coefficient**	**P-Value**	**VIF**
$\boldsymbol{Constant}$	0.3532	0.000	
$\boldsymbol{Tip\ Speed}$	1.4759	0.000	1.00
$\boldsymbol{Feed\ Rate}$	0.359	0.036	1.13
$\boldsymbol{(Tip\ Speed)^2}$	-2.29	0.106	1.13

$$1/\sigma^2,\ 1/s^2\ (Inlet\ 2) = -0.402 + 1.4759 Tip\ Speed,\ m/s + 1.686 Feed\ Rate,\ kg/s \\ -2.29(Feed\ Rate,\ kg/s)^2 \tag{6.4}$$

As for the TSM 75, the coded coefficients for the Inlet 2 model for the TSM 125 are both positive. This indicates that the effect of the predictors upon the inverse of the curve variance is positive (and thus the reverse will be true of the σ^2 in its non inverse form).

The Inlet 2 plots appear very similar for the TSM 125 and 75 at Inlet 2. However, for the σ^2 variance the TSM 125 contour plot shows that curve variance begins to increase rapidly below Tip Speeds of around 0.25 m/s rather than 0.3 m/s for the TSM 75.

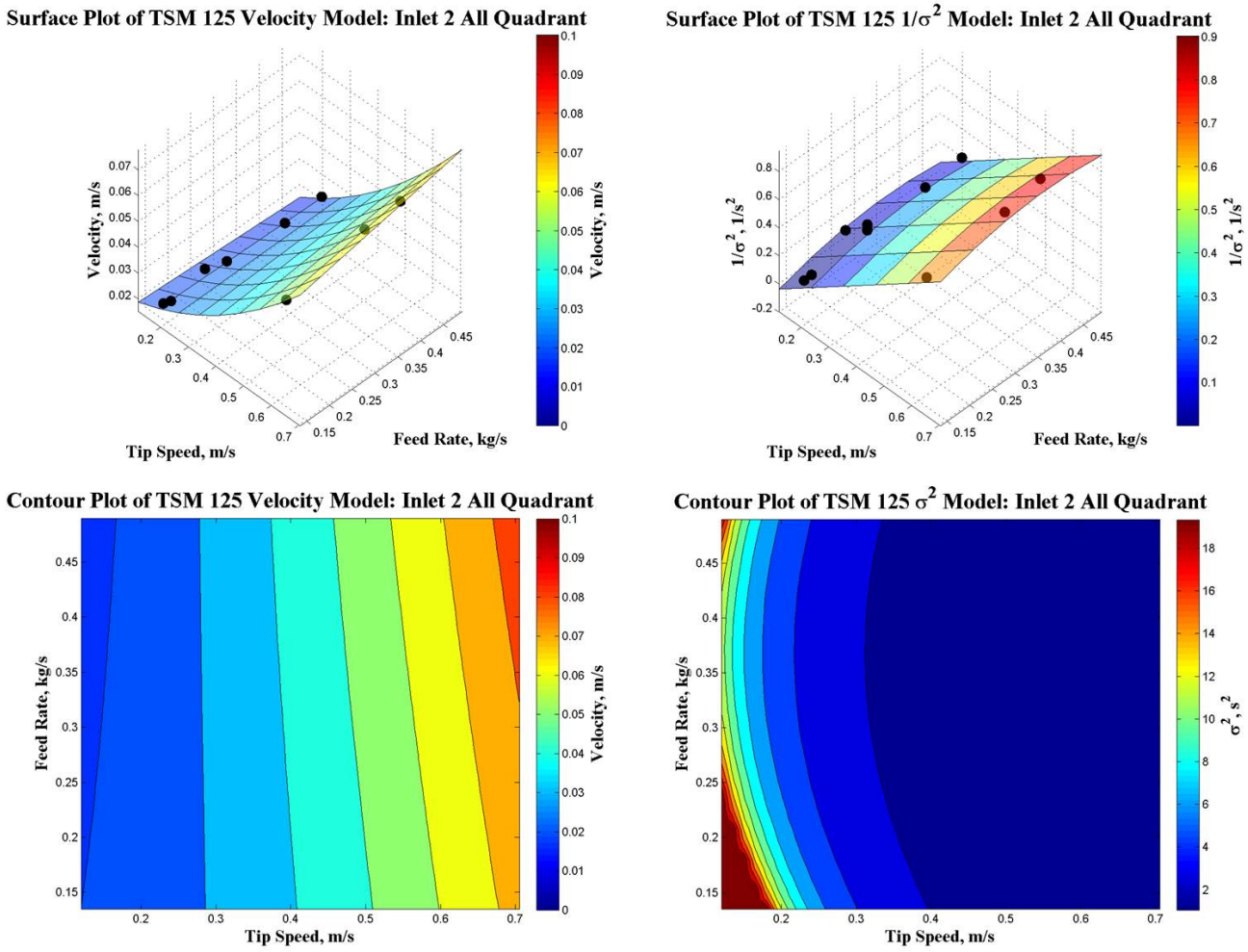

Figure 6.3: (Left) The TSM 125 Inlet 2, all quadrant, Velocity Model, displayed as a 3D surface plot (top) and a 2D contour plot (bottom). (Right) The TSM 125 Inlet 2, all quadrant, $1/sigma^2$ Model, displayed as a 3D surface plot (top), and displayed in non-reciprocal form as a 2D contour plot (bottom).

The Fill Level (Fill Level if the system was at rest) Figures for both the TSM 125 and TSM 75 are extremely similar. However, the Mid Fill Level, where the bulk just begins to be pushed over the shafts, has moved from 18-22% static fill volume to 22-26%. Furthermore, the static fill volume where the system becomes flooded has moved from values of over 48% to around 58%. This is indicative of a consolidation effect being established by the weight of the powder, that appears to become more pronounced as the system becomes more full.

This investigation indicates two important things to consider when scaling these machines: 1) the Static Fill Volume % appears to increase with an increase in mass, most likely caused by the in-

crease in weight and therefore powder consolidation, and 2) this increase in mass also impedes particles from spreading out in an axial fashion, most likely caused by a reduction in the 'Mass Volume to TSM Wall Surface Area' (this is because, within the TSM 125, particles axial Velocity is less likely to be impeded by time spent at the TSM wall (a phenomenon described in Chapter 5)) and the fact the powder has become more consolidated..

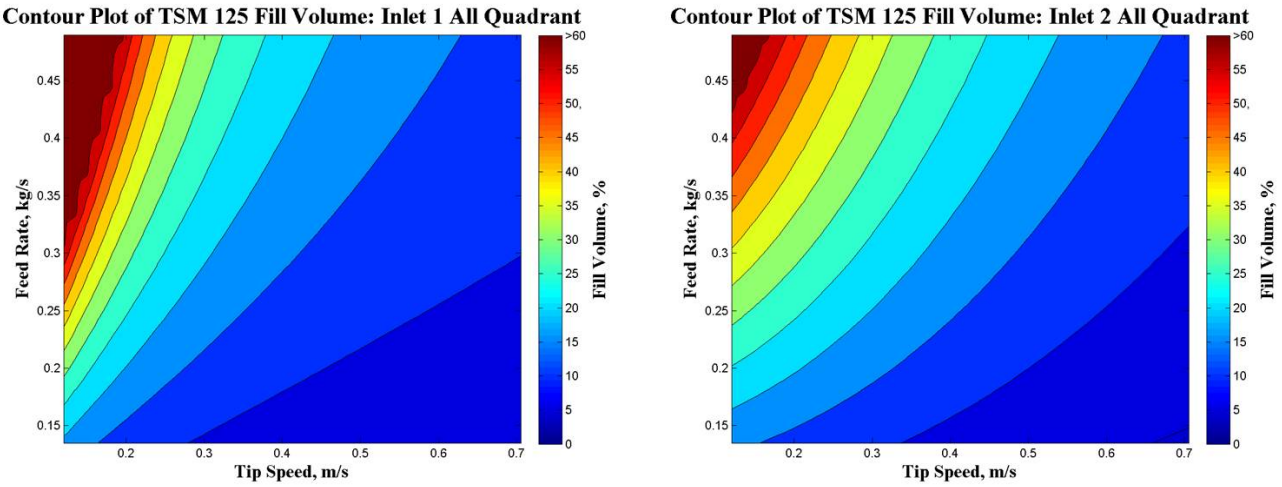

Figure 6.4: (Left) The TSM 125 Inlet 1, all quadrant, Fill Level Model, calculated using the Inlet 1, all quadrant, Velocity Model, displayed as a 2D contour plot. (Right) The TSM 125 Inlet 2, all quadrant, Fill Level Model, calculated using the Inlet 2, all quadrant, Velocity Model, displayed as a 2D contour plot.

Next, the TSM 125 quadrant to anchors paddles geometry shall be examined (see Chapter 3.1 for a full description of the TSM geometry changes). The RTD metrics for the quadrant to anchors geometry has been provided as Table 6.8 for Inlet 1 and 6.9 for Inlet 2. The dependant variables have then been plotted within Figure 6.5, in the form they are calculated via the RTDs (left hand side) and their transformed state (right hand side), all with respect to Screw Tip speed. The straight line equation parameters have also been provided in Table 6.10.

Table 6.8: The TSM 125 Inlet 1, quadrants to anchors, RTD metrics. The curves were generated 5 times using the procedure outlined in materials and methods, this allowed a calculation of the standard error for τ and σ^2; and so subsequently the confidence intervals of the fill % and velocity, which were given as the Standard Error (SE). The code refers to the TSM Screw Tip Speed and powder Feed Rate used in the DoE, which may be referenced in tables 3.1 and 3.4.

$\boldsymbol{Run\ (Code)}$	$\boldsymbol{\tau, s}$	$\boldsymbol{SE(\tau), s}$	$\boldsymbol{\sigma^2, s^2}$	$\boldsymbol{SE(\sigma^2), s^2}$	$\boldsymbol{V, m/s}$	$\boldsymbol{Fill, \%}$
$\mathbf{1\ (Mid \backslash Mid)}$	32.16	0.02	6.58	0.83	0.024±0.000	25.68±0.03
$\mathbf{2\ (Mid \backslash V.High)}$	40.20	0.06	9.22	0.61	0.019±0.000	56.13±0.18
$\mathbf{3\ (Mid \backslash Low)}$	15.96	0.03	1.67	0.05	0.049±0.000	7.66±0.03
$\mathbf{4\ (V.Low \backslash Mid)}$	71.08	0.04	22.92	0.76	0.011±0.000	56.77±0.06
$\mathbf{5\ (High \backslash High)}$	12.29	0.01	1.42	0.09	0.063±0.000	14.72±0.03
$\mathbf{6\ (Mid \backslash V.Low)}$	35.18	0.01	9.18	0.23	0.022±0.000	14.05±0.01
$\mathbf{7\ (Low \backslash Low)}$	35.18	0.02	9.40	0.62	0.022±0.000	16.88±0.02
$\mathbf{8\ (Mid \backslash Mid)}$	31.72	0.06	7.27	0.63	0.024±0.000	25.34±0.10
$\mathbf{9\ (Low \backslash High)}$	44.87	0.07	10.50	0.57	0.017±0.000	53.76±0.18
$\mathbf{10\ (Mid \backslash Mid)}$	31.59	0.02	7.60	0.39	0.025±0.000	25.23±0.03
$\mathbf{11\ (V.High \backslash Mid)}$	12.62	0.00	1.06	0.02	0.061±0.000	10.08±0.01

Table 6.9: The TSM 125 Inlet 2, quadrants to anchors, RTD metrics. The curves were generated 5 times using the procedure outlined in materials and methods, this allowed a calculation of the standard error for τ and σ^2; and so subsequently the confidence intervals of the fill % and velocity, which were given as the Standard Error. The code refers to the TSM Screw Tip Speed and powder Feed Rate used in the DoE, which may be referenced in tables 3.1 and 3.4.

$\boldsymbol{Run\ (Code)}$	$\boldsymbol{\tau, s}$	$\boldsymbol{SE(\tau), s}$	$\boldsymbol{\sigma^2, s^2}$	$\boldsymbol{SE(\sigma^2), s^2}$	$\boldsymbol{V, m/s}$	$\boldsymbol{Fill, \%}$
$\mathbf{1\ (Mid\backslash Mid)}$	11.65	0.01	2.54	0.09	0.028±0.000	22.18±0.03
$\mathbf{2\ (Mid\backslash V.High)}$	13.51	0.01	4.97	0.26	0.024±0.000	44.98±0.08
$\mathbf{3\ (Mid\backslash Low)}$	5.76	0.03	1.06	0.14	0.056±0.000	6.59±0.07
$\mathbf{4\ (V.Low\backslash Mid)}$	25.70	0.03	11.93	0.29	0.013±0.000	48.94±0.12
$\mathbf{5\ (High\backslash High)}$	5.36	0.00	0.96	0.01	0.061±0.000	15.30±0.01
$\mathbf{6\ (Mid\backslash V.Low)}$	16.50	0.03	4.82	0.30	0.020±0.000	15.72±0.05
$\mathbf{7\ (Low\backslash Low)}$	13.50	0.01	4.40	0.26	0.024±0.000	15.45±0.03
$\mathbf{8\ (Mid\backslash Mid)}$	12.66	0.04	2.86	0.21	0.026±0.000	24.10±0.15
$\mathbf{9\ (Low\backslash High)}$	14.66	0.54	7.03	0.17	0.022±0.001	41.89±3.18
$\mathbf{10\ (Mid\backslash Mid)}$	13.78	0.02	5.58	0.34	0.024±0.000	26.25±0.09
$\mathbf{11\ (V.High\backslash Mid)}$	5.69	0.01	0.94	0.09	0.057±0.000	10.84±0.05

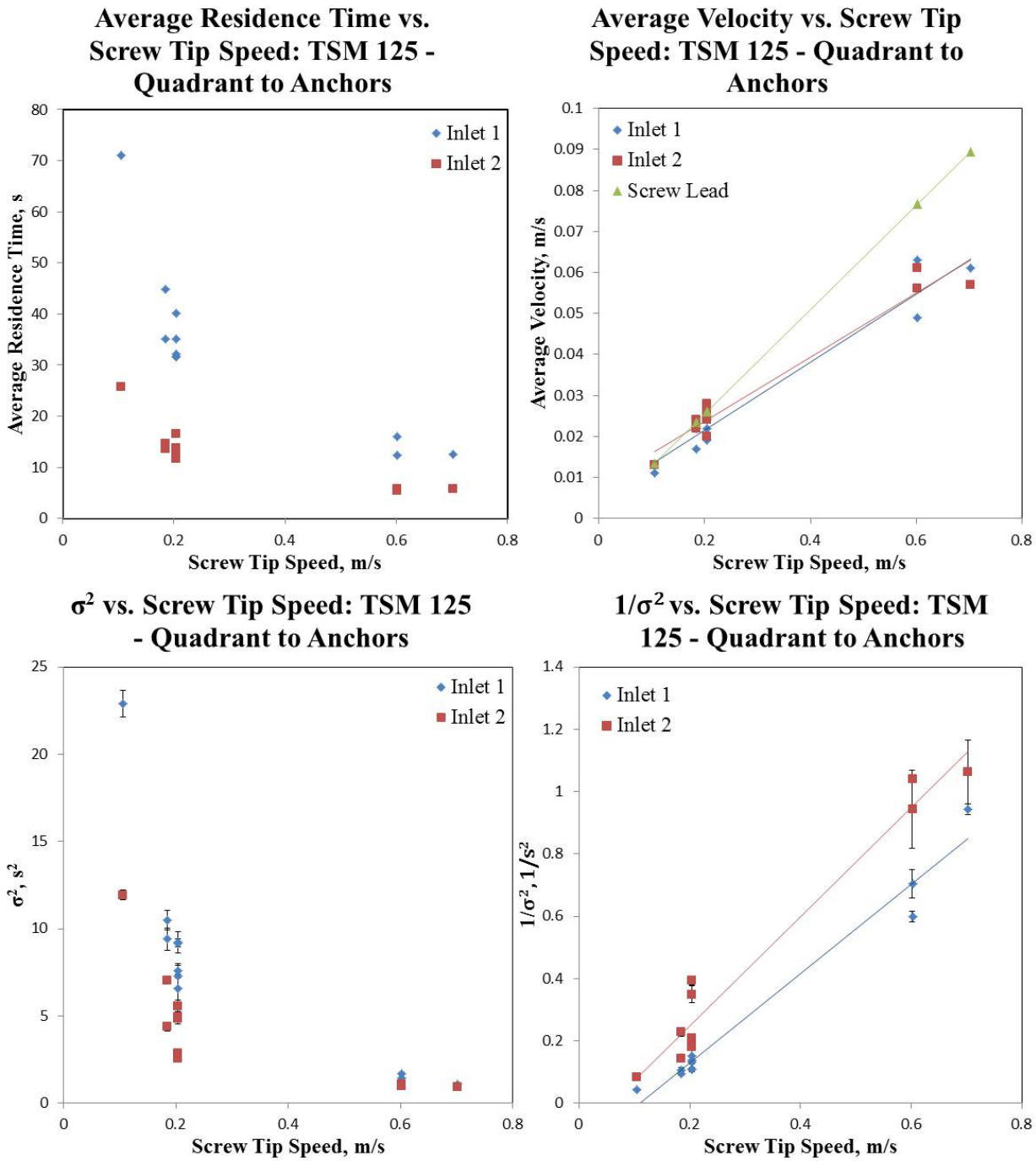

Figure 6.5: The RTD metrics for the TSM 125 - Quadrant to Anchors, plotted vs. Screw Tip Speed. The error bars denote the SE (error bars have been provided for all data points but some are too small to discern).

Table 6.10: TSM 125 - Quadrant to Anchors: Screw Speed vs. RTD metrics straight line equation parameters (as displayed in 6.5).

Dependent Variable	**Gradient**	**Constant**	R^2
$\boldsymbol{Screw\ Lead}, m/s$	0.13	0.00	N/A
$\boldsymbol{V(Inlet, 1)}, m/s$	0.08	0.01	0.95
$\boldsymbol{V(Inlet, 2)}, m/s$	0.08	0.01	0.95
$\boldsymbol{1/\sigma^2(Inlet, 1)}, 1/s^2$	1.44	-0.16	0.97
$\boldsymbol{1/\sigma^2(Inlet, 2)}, 1/s^2$	1.76	-0.10	0.96

In general the change in geometry has caused a slight decrease in the Average Powder Velocity, as indicated by the Gradient dropping to 0.08 for the TSM 125 Quandrants to Anchors from 0.09 for the TSM 125 All Quadrants (with the Constant values remaining relatively unchanged). The change in geometry has meant also a slight increase in σ^2 from Inlets 1 and 2 of the TSM 125.

Table 6.11 displays the RSM model for the Average Velocity model at Inlet 1 in its coded coefficient form and Equation 6.5 shows the same model in uncoded units. The model scores very highly on all the statistical metrics used to measure the Goodness-of-Fit and so should be highly accurate.

Table 6.11: Coded Coefficient Table for TSM 125 Inlet 1, quadrants to anchors, Velocity Model. The hierarchical model retained terms using 95% confidence, determined via the P-values. Metrics to determine the Goodness-of-Fit included: R^2 of 99.86%, Adjusted R^2 of 99.71%, a Predicted R^2 of 99.08% and a Lack-of-Fit P-value greater than 0.05.

Term	**Coefficient**	**P-Value**	**VIF**
$\boldsymbol{Constant}$	0.035842	0.000	
$\boldsymbol{Tip\ Speed}$	0.10276	0.000	7.22
$\boldsymbol{Feed\ Rate}$	0.00908	0.027	1.14
$\boldsymbol{(Tip\ Speed)}^2$	-0.0949	0.003	7.59
$\boldsymbol{(Feed\ Rate)}^2$	-0.1110	0.013	1.43
$\boldsymbol{(Tip\ Speed)} \times \boldsymbol{(Feed\ Rate)}$	0.1630	0.000	1.03

$$\begin{aligned} Velocity,\ m/s\ (Inlet\ 1) = -0.00234 + 0.1143 Tip\ Speed,\ m/s + 0.0229 Feed\ Rate,\ kg/s \\ -0.0949(Tip\ Speed,\ m/s)^2 - 0.1110(Feed\ Rate,\ kg/s)^2 \\ +0.1630(Tip\ Speed,\ m/s) \times (Feed\ Rate,\ kg/s) \end{aligned} \tag{6.5}$$

Table 6.12 displays the RSM model for $1/\sigma^2$ at Inlet 1 in its coded coefficient form and Equation 6.6 shows the same model in uncoded units. The model scores very highly on all the statistical metrics used to measure the Goodness-of-Fit and so should be highly accurate. Figure 6.6 shows the response surfaces of these models.

Table 6.12: Coded Coefficient Table for TSM 125 Inlet 1, quadrants to anchors, $(\sigma^2)^{-1}$. The hierarchical model retained terms using 90% confidence, determined via the P-values (the more usual 95% confidence was not used, as a visual inspection of the data indicated that the interaction term should be retained). Metrics to determine the Goodness-of-Fit included: R^2 of 99.35%, Adjusted R^2 of 98.91%, a Predicted R^2 of 89.67% and a Lack-of-Fit P-value greater than 0.05.

Term	**Coefficient**	**P-Value**	**VIF**
$\boldsymbol{Constant}$	0.2026	0.000	
$\boldsymbol{Tip\ Speed}$	1.030	0.000	6.12
$\boldsymbol{Feed\ Rate}$	0.0901	0.366	1.01
$\boldsymbol{(Tip\ Speed)^2}$	2.015	0.009	6.13
$\boldsymbol{(Tip\ Speed) \times (Feed\ Rate)}$	0.974	0.111	1.00

$$\begin{aligned} 1/\sigma^2,\ 1/s^2\ (Inlet\ 1) = 0.01378 - 0.497 Tip\ Speed,\ m/s - 0.211 Feed\ Rate,\ kg/s \\ +2.015(Tip\ Speed,\ m/s)^2 + 0.974(Tip\ Speed,\ m/s) \times (Feed\ Rate,\ kg/s) \end{aligned} \tag{6.6}$$

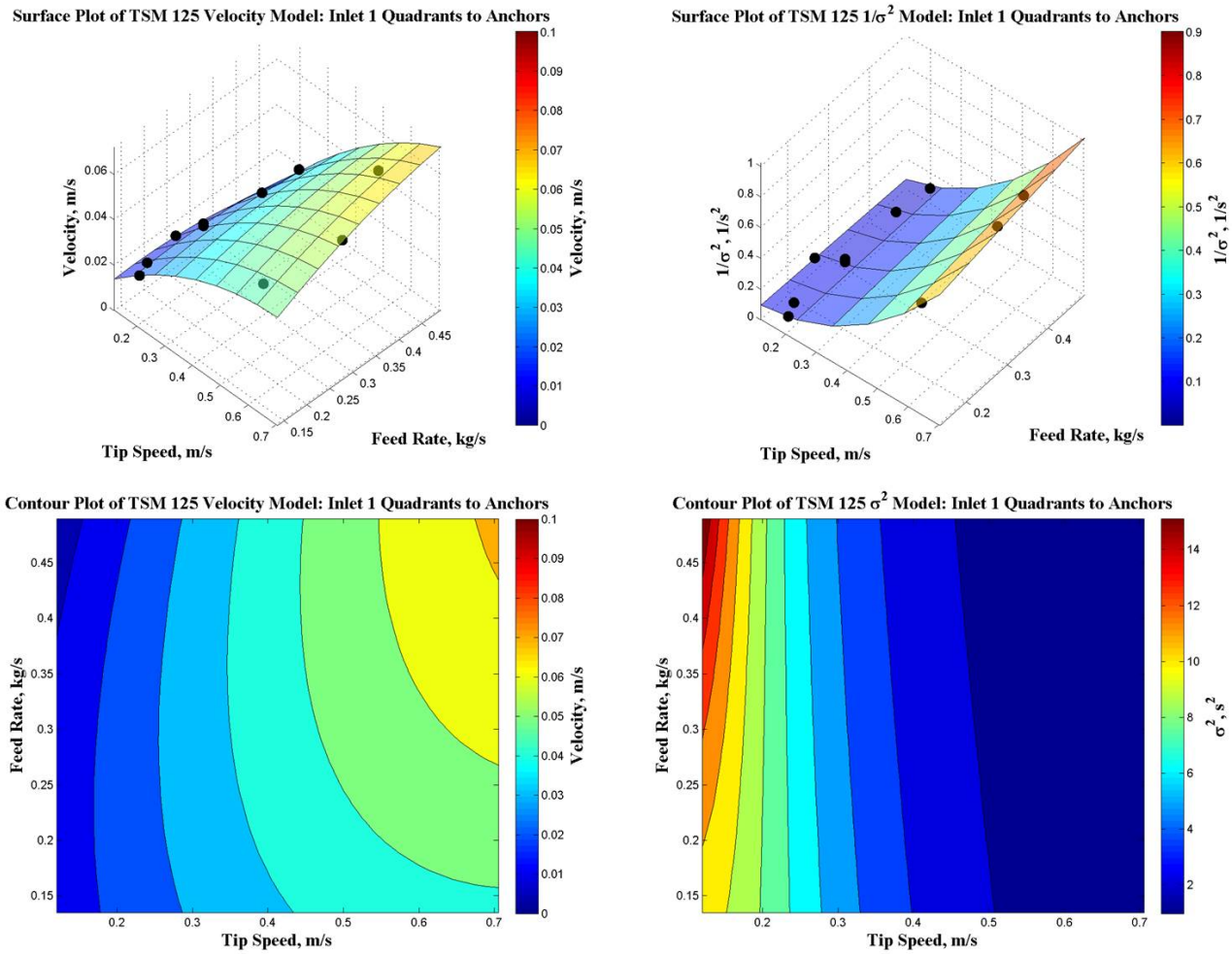

Figure 6.6: (Left) The TSM 125 Inlet 1, quadrants to anchors, Velocity Model, displayed as a 3D surface plot (top) and a 2D contour plot (bottom). (Right) The TSM 125 Inlet 1, quadrants to anchors, $1/sigma^2$ Model, displayed as a 3D surface plot (top), and displayed in non-reciprocal form as a 2D contour plot (bottom).

Table 6.13 and Table 6.14 displays the RSM models for Average Velocity and $1/\sigma^2$, at Inlet 2, in their coded coefficient form and Equations 6.7 and 6.8 shows the same models in uncoded units. The models score very highly on all the statistical metrics used to measure the Goodness-of-Fit and so should be highly accurate. Figure 6.7 shows the response surfaces of these models, and Figure 6.8 shows the Static Fill Level Models.

Table 6.13: Coded Coefficient Table for TSM 125 Inlet 2, quadrants to anchors, Velocity Model. The hierarchical model retained terms using 80% confidence, determined via the P-values (the more usual 95% confidence was not used, as a visual inspection of the data indicated that the feed rate and squared feed rate terms should be retained). Metrics to determine the Goodness-of-Fit included: R^2 of 98.53%, Adjusted R^2 of 97.56%, a Predicted R^2 of 93.72% and a Lack-of-Fit P-value greater than 0.05.

Term	**Coefficient**	**P-Value**	**VIF**
$\boldsymbol{Constant}$	0.03981	0.000	
$\boldsymbol{Tip\ Speed}$	0.1088	0.000	7.19
$\boldsymbol{Feed\ Rate}$	0.001137	0.207	1.14
$(\boldsymbol{Tip\ Speed})^2$	-0.1511	0.021	7.53
$(\boldsymbol{Feed\ Rate})^2$	-0.1152	0.194	1.39

$$Velocity,\ m/s\ (Inlet\ 2) = -0.0212 + 0.2022 Tip\ Speed,\ m/s + 0.0780 Feed\ Rate,\ kg/s \\ -0.1511(Tip\ Speed,\ m/s)^2 - 0.1152(Feed\ Rate,\ kg/s)^2 \tag{6.7}$$

Table 6.14: Coded Coefficient Table for TSM 125 Inlet 2, quadrants to anchors, $(\sigma^2)^{-1}$. The hierarchical model retained terms using 95% confidence, determined via the P-values. Metrics to determine the Goodness-of-Fit included: R^2 of 98.75%, Adjusted R^2 of 97.75%, a Predicted R^2 of 95.40% and a Lack-of-Fit P-value greater than 0.05.

Term	**Coefficient**	**P-Value**	**VIF**
$\boldsymbol{Constant}$	0.6672	0.000	
$\boldsymbol{Tip\ Speed}$	2.252	0.000	6.16
$\boldsymbol{Feed\ Rate}$	0.134	0.484	1.13
$(\boldsymbol{Tip\ Speed})^2$	-3.01	0.046	6.78
$(\boldsymbol{Feed\ Rate})^2$	-5.57	0.034	1.52

$$1/\sigma^2,\ 1/s^2\ (Inlet\ 2) = -0.870 + 4.17 Tip\ Speed,\ m/s + 3.37 Feed\ Rate,\ kg/s \\ -3.01(Tip\ Speed,\ m/s)^2 - 5.57(Feed\ Rate,\ kg/s)^2 \tag{6.8}$$

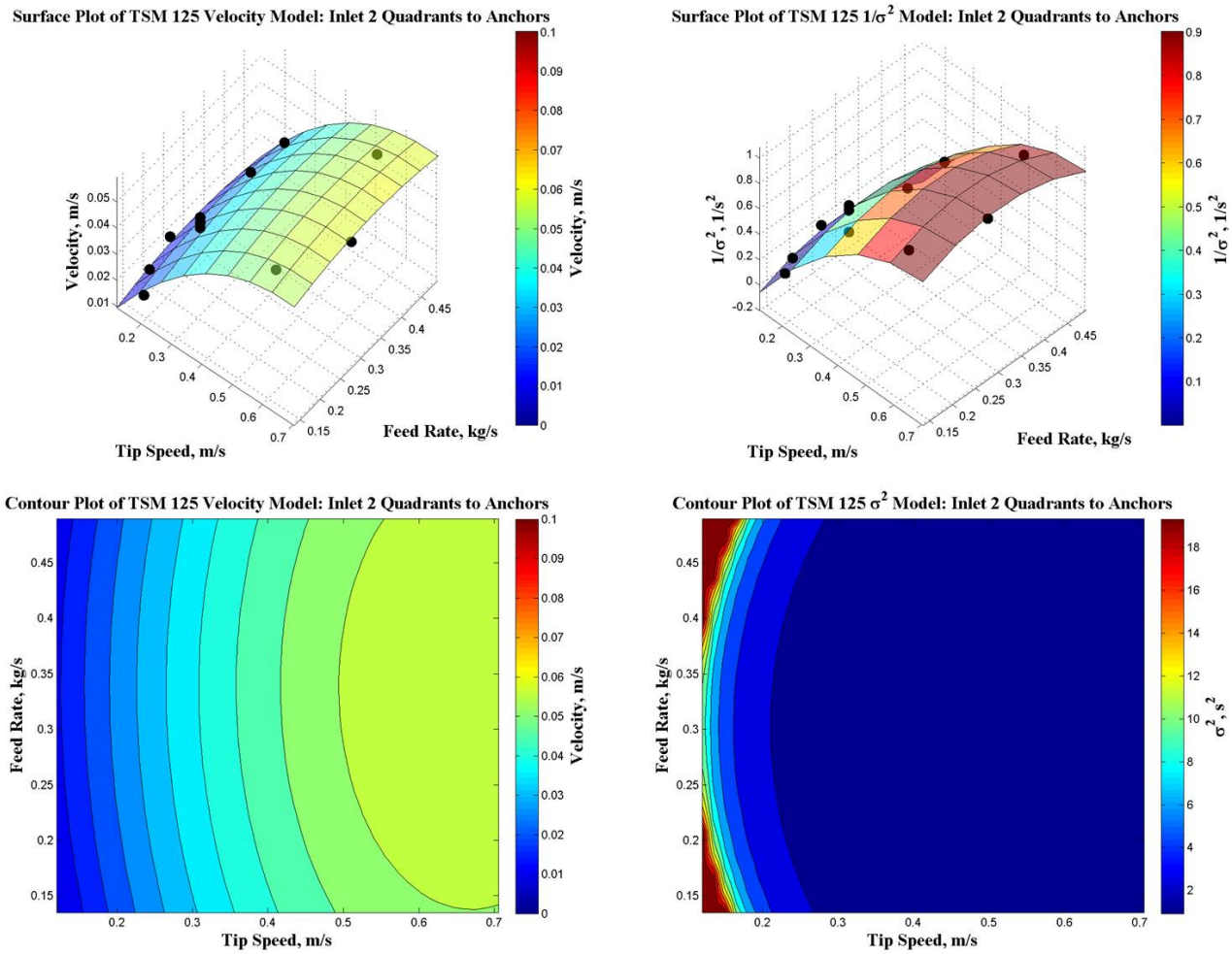

Figure 6.7: (Left) The TSM 125 Inlet 2, quadrants to anchors, Velocity Model, displayed as a 3D surface plot (top) and a 2D contour plot (bottom). (Right) The TSM 125 Inlet 2, all quadrant, $1/sigma^2$ Model, displayed as a 3D surface plot (top), and displayed in non-reciprocal form as a 2D contour plot (bottom).

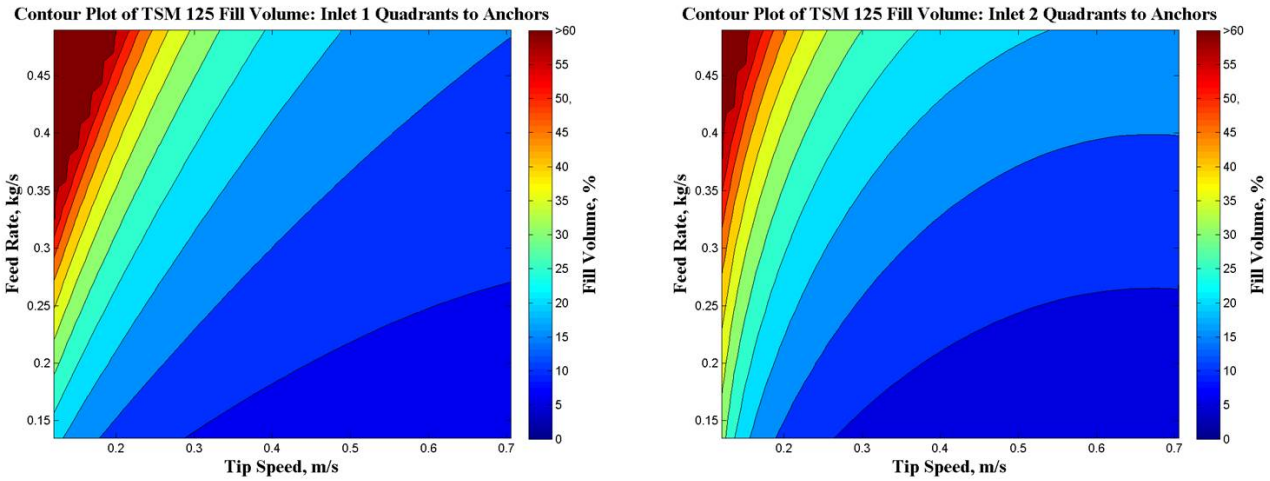

Figure 6.8: (Left) The TSM 125 Inlet 1, quadrants to anchors, Fill Level Model, calculated using the Inlet 1, quadrant to anchors, Velocity Model, displayed as a 2D contour plot. (Right) The TSM 125 Inlet 2, quadrants to anchors, Fill Level Model, calculated using the Inlet 2, quadrant to anchors, Velocity Model, displayed as a 2D contour plot.

The TSM 125 Quadrant to Anchor models are very similar to the TSM 125 All Quadrant models with some key differences. As the Anchor paddles have less surface area, the overall axial Velocity of the bulk has been slightly reduced. The decrease in paddle surface area created by switching to anchors has also led to a slight increase in curve variance as powder is able to axially disperse more easily. Finally, the increase in residence time in the TSM 125 Quadrants to Anchors configuration has led to higher static fill levels than within the TSM 125 All Quadrant set-up.

6.1.2 Tanks-in-Series (T-i-S) Models Investigation TSM 125.

A variability of the RTD measurement technique may be assessed to some extent by examining the three repeated values: Run 1, Run 8 and Run 10. This has been provided as figure 6.9. The RTDs all look remarkably similar which gives confidence the technique is adequate.

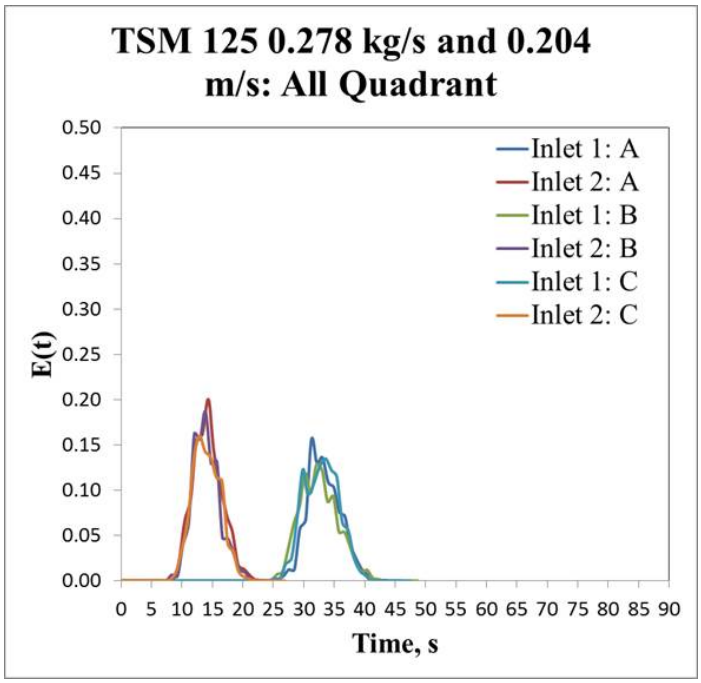

Figure 6.9: Comparison between TSM 125 All Quadrant repeats: Run 1 (A), Run 8 (B) and Run 10 (C).

The TSM 125 provided in Figures 6.10 and 6.12 show, as do their TSM 75 counterparts (see figure 4.8), Inlet 2 peaks generally being taller and less spread out than at Inlet 1. This is because the powder has spent less time in the system overall and so has had less opportunity to spread out. Again, as for the TSM 75, this is also the reason why curves positioned towards the left hand side of the time axis present thin tall sharper peaks.

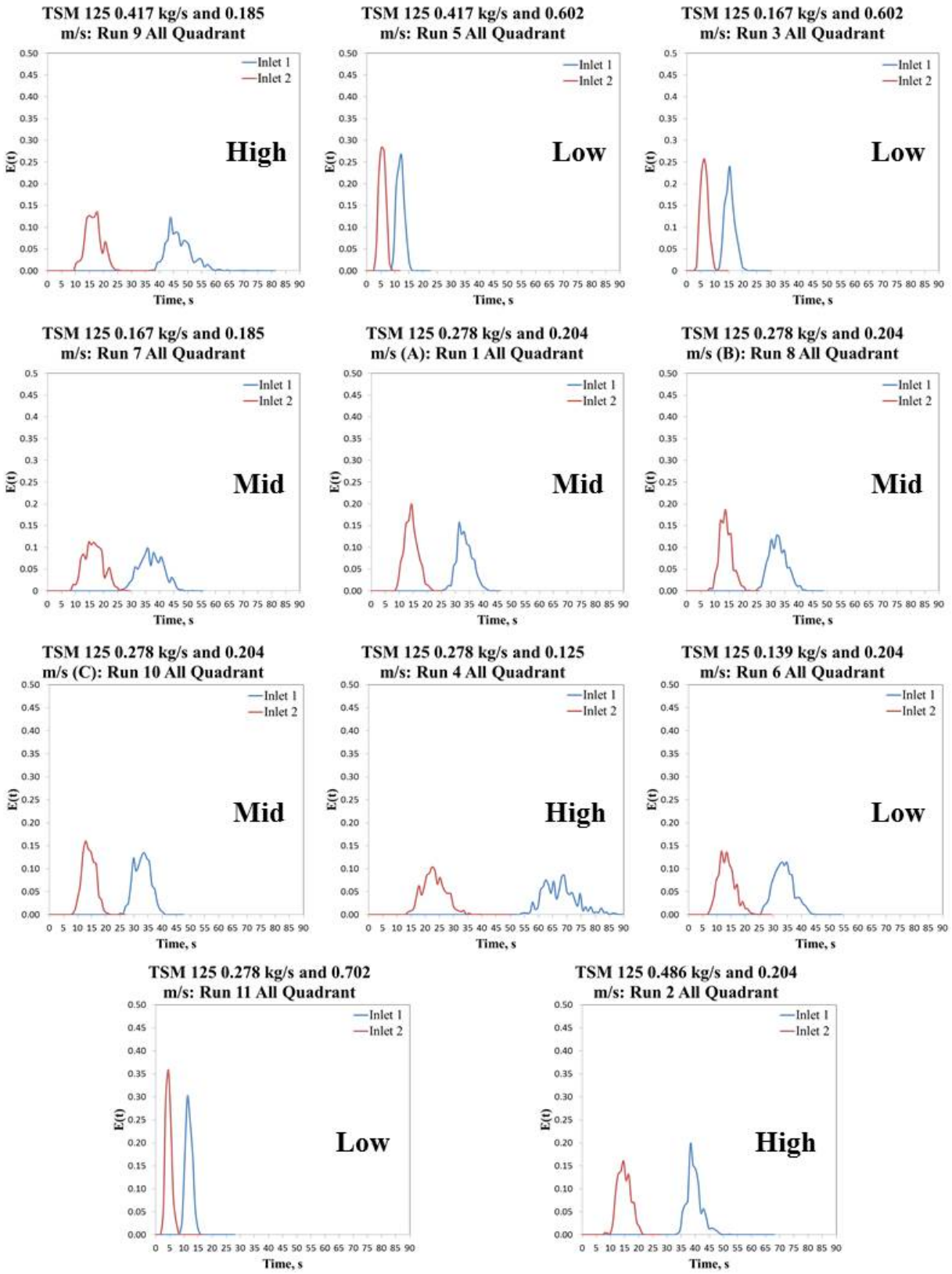

Figure 6.10: TSM 125, all quadrant, Residence Time Distributions. The terms: low, mid and high give a brief description of the visual fill level within the TSM, for a more in depth description refer to table 3.3.

Variability of the RTD measurement technique (during the TSM 125 quadrant to anchors measurement) may be assessed to some extent by examining the three repeated values: Run 1, Run 8 and Run 10. This has been provided as figure 6.11. Run 1 (A) appears to be slightly different at Inlet 1 than Runs 8 and 10 (B and C respectively). This could either be indicative of variability in how the RTD is calculated, or this difference could also be explained by extra variability in the axial flow, as a result of the introduction of anchors.

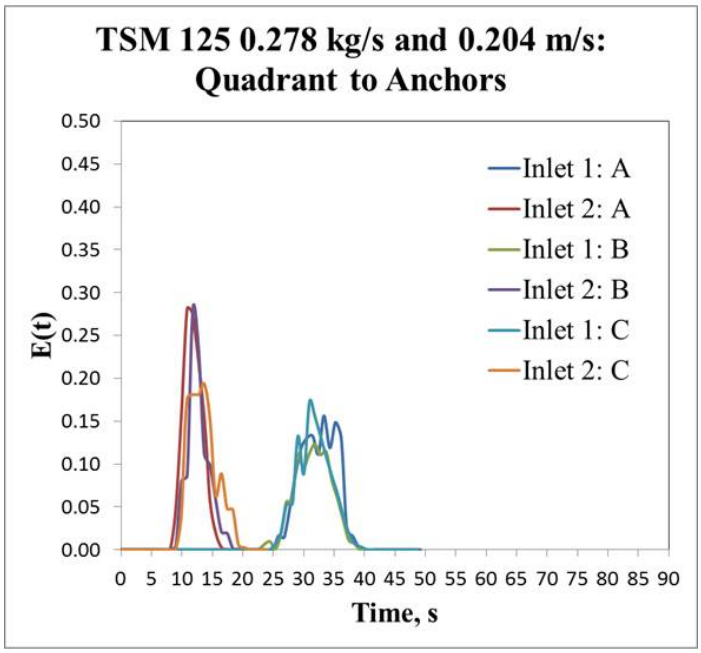

Figure 6.11: Comparison between TSM 125 Quadrant to Anchors repeats: Run 1 (A), Run 3 (B) and Run 10 (C).

The curves for all experiments appear more lumpy as a function of increasing the average residence time and/or the curve variance. This is to be expected, as the longer time and more spread out the tracer becomes within the system the more likely that different sub-sections of the tracer will go on slightly different journeys. The concentration will also be lower when the tracer is spread out more, which could introduce more noise into the measurement. However, as long as the noise is randomly distributed the measures of: residence time, curve variance and the T-i-S models should remain accurate (although in the T-i-S case this only holds true if the model chosen is suitable for the system).

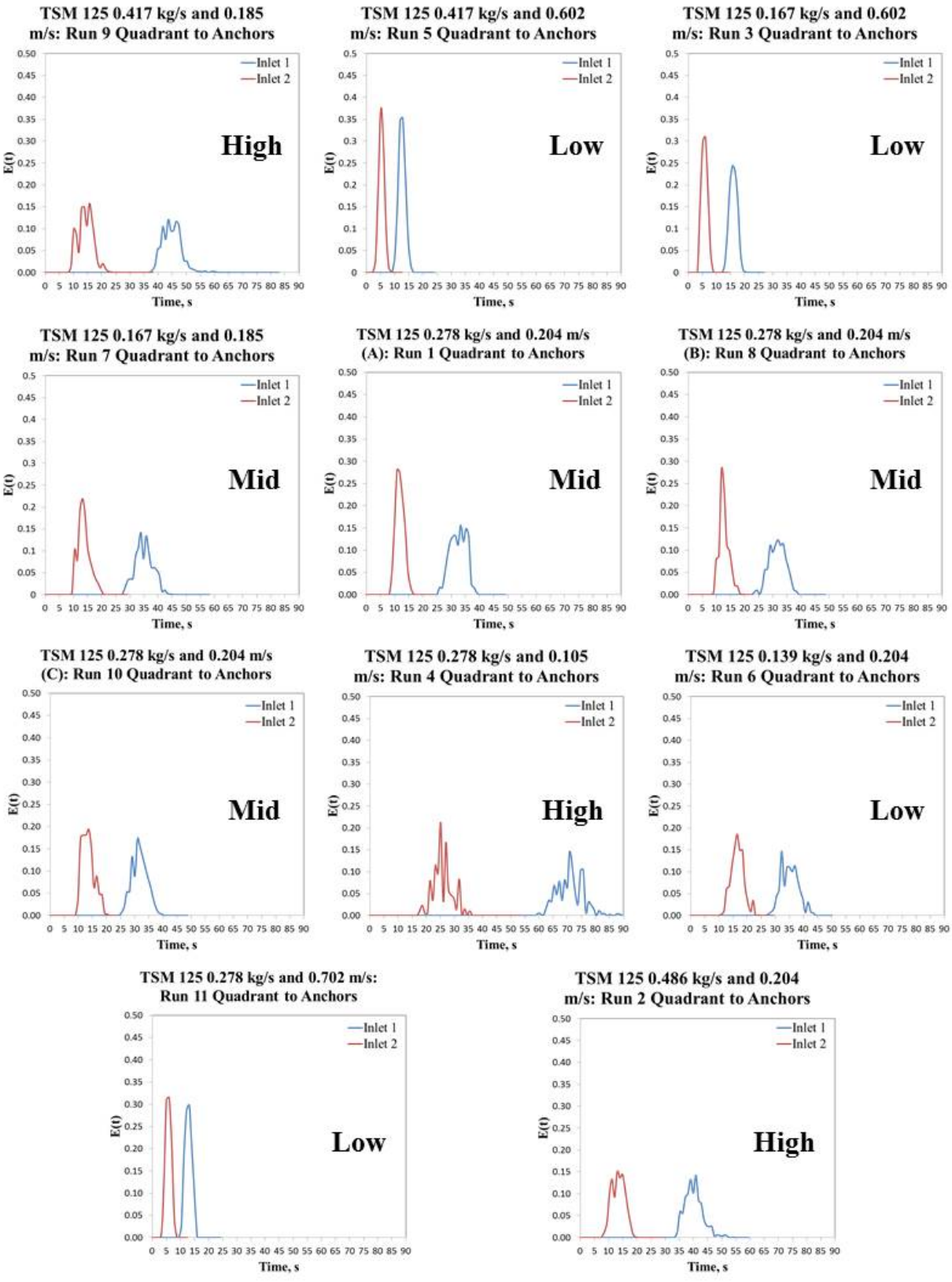

Figure 6.12: TSM 125, quadrants to anchors, Residence Time Distributions. The terms: low, mid and high give a brief description of the visual fill level within the TSM, for a more in depth description refer to table 3.4.

The normalised T-i-S with plug flow and dead time, for the TSM 125 All Quadrant, Inlet 1 and 2 RTDs have been provided in Tables 6.15 and 6.16. The curves have also been provided in Figures 6.13 and 6.14. As in Chapter 4.1.2 these shall be compared with the T-i-S and Pe number.

Table 6.15: TSM 125 Inlet 1 All Quadrant Tanks-in-Series Model Data. The code refers to the TSM Screw Tip Speed and powder Feed Rate used in the DoE, which may be referenced in tables 3.1 and 3.3.

$\boldsymbol{Run}$	$(\boldsymbol{Code})$	$\boldsymbol{n}$	$\boldsymbol{p}$	$\boldsymbol{d}$	$\boldsymbol{R^2}$
$\mathbf{1}$	$(\boldsymbol{Mid \backslash Mid})$	20	0.62	0.00	0.96
$\mathbf{2}$	$(\boldsymbol{Mid \backslash V.High})$	16	0.75	0.01	0.93
$\mathbf{3}$	$(\boldsymbol{Mid \backslash Low})$	50	0.17	0.00	0.99
$\mathbf{4}$	$(\boldsymbol{V.Low \backslash Mid})$	13	0.68	0.00	0.84
$\mathbf{5}$	$(\boldsymbol{High \backslash High})$	46	0.18	0.00	0.99
$\mathbf{6}$	$(\boldsymbol{Mid \backslash V.Low})$	30	0.41	0.01	0.98
$\mathbf{7}$	$(\boldsymbol{Low \backslash Low})$	50	0.11	0.00	0.94
$\mathbf{8}$	$(\boldsymbol{Mid \backslash Mid})$	50	0.29	0.00	0.97
$\mathbf{9}$	$(\boldsymbol{Low \backslash High})$	6	0.77	0.00	0.95
$\mathbf{10}$	$(\boldsymbol{Mid \backslash Mid})$	69	0.22	0.00	0.96
$\mathbf{11}$	$(\boldsymbol{V.High \backslash Mid})$	29	0.40	0.00	0.99

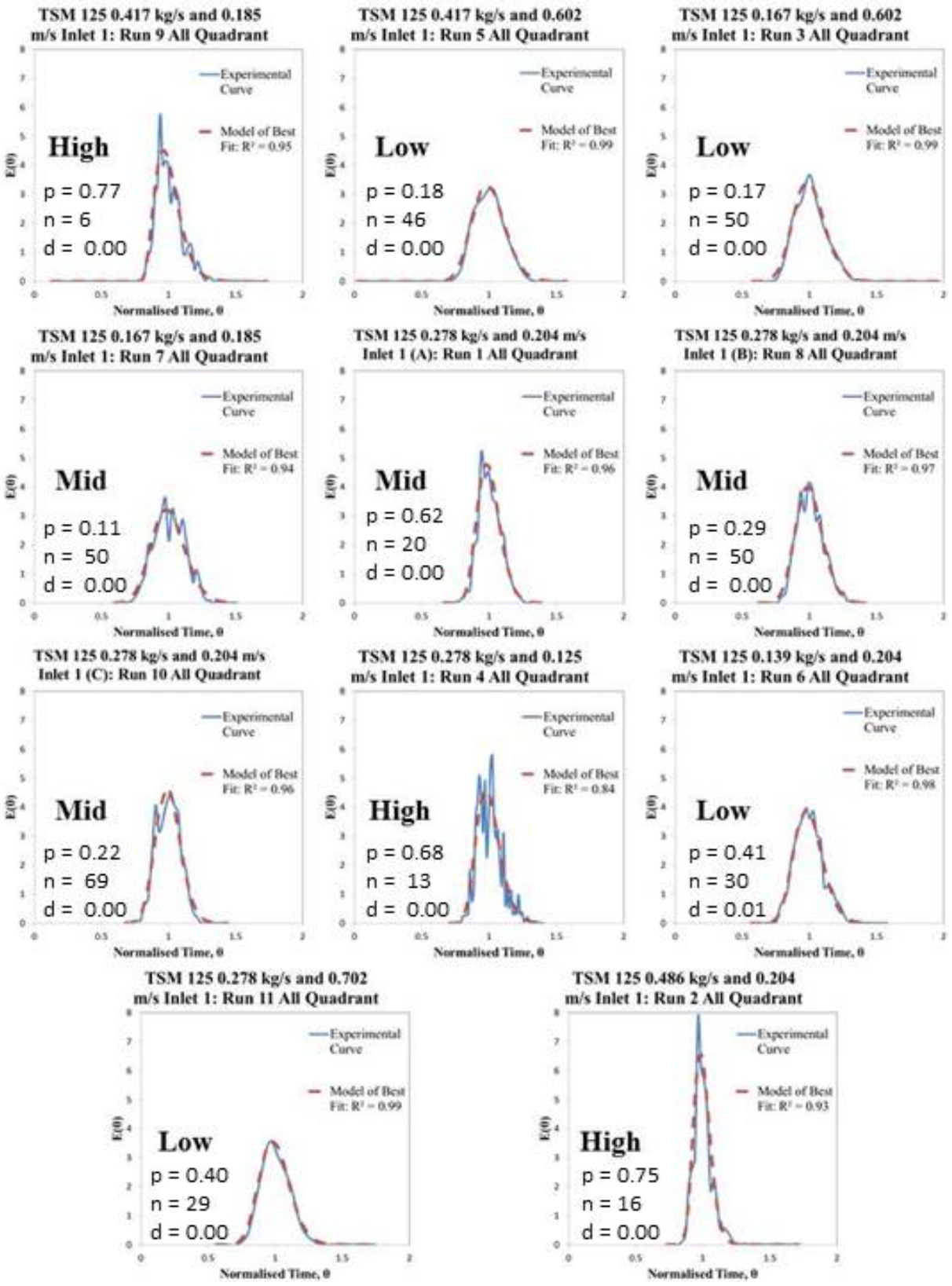

Figure 6.13: TSM 125 Normalised Residence Time Distributions with the best fitting Tanks-in-Series Models: Inlet 1 All Quadrant. The terms: low, mid and high give a brief description of the visual fill level within the TSM, for a more in depth description refer to table 3.3.

Table 6.16: TSM 125 Inlet 2 All Quadrant Tanks-in-Series Model Data. The code refers to the TSM Screw Tip Speed and powder Feed Rate used in the DoE, which may be referenced in tables 3.1 and 3.3.

$\boldsymbol{Run}$	$(\boldsymbol{Code})$	$\boldsymbol{n}$	$\boldsymbol{p}$	$\boldsymbol{d}$	$\boldsymbol{R^2}$
1	$(\boldsymbol{Mid \backslash Mid})$	35	0.00	0.00	0.97
2	$(\boldsymbol{Mid \backslash V.High})$	19	0.25	0.00	0.97
3	$(\boldsymbol{Mid \backslash Low})$	18	0.00	0.00	0.99
4	$(\boldsymbol{V.Low \backslash Mid})$	29	0.00	0.00	0.96
5	$(\boldsymbol{High \backslash High})$	19	0.00	0.00	0.98
6	$(\boldsymbol{Mid \backslash V.Low})$	12	0.21	0.00	0.97
7	$(\boldsymbol{Low \backslash Low})$	20	0.00	0.00	0.93
8	$(\boldsymbol{Mid \backslash Mid})$	16	0.36	0.00	0.97
9	$(\boldsymbol{Low \backslash High})$	13	0.35	0.00	0.96
10	$(\boldsymbol{Mid \backslash Mid})$	32	0.00	0.00	0.98
11	$(\boldsymbol{V.High \backslash Mid})$	17	0.04	0.00	0.99

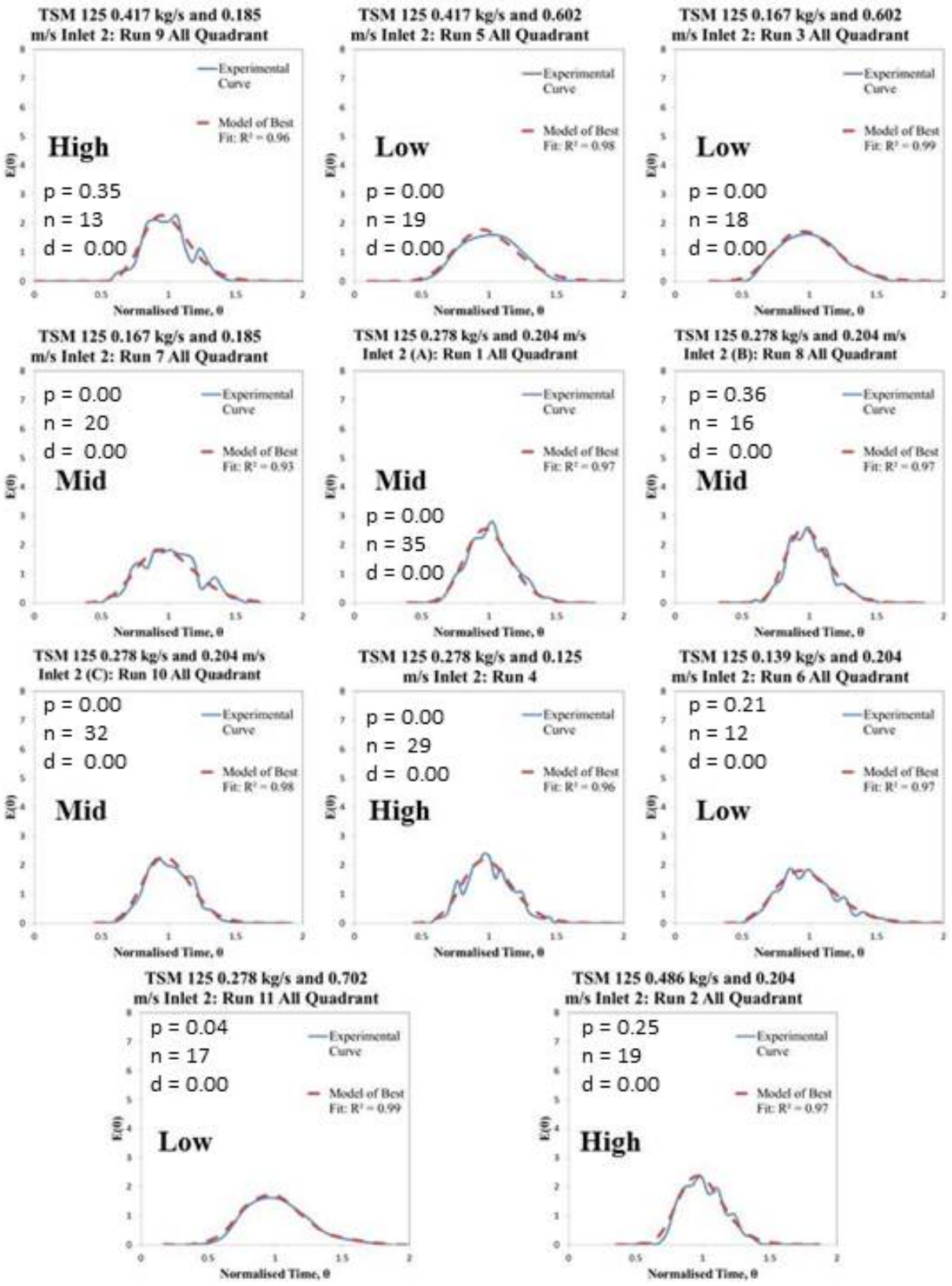

Figure 6.14: TSM 125 Normalised Residence Time Distributions with the best fitting Tanks-in-Series Models: Inlet 2 All Quadrant. The terms: low, mid and high give a brief description of the visual fill level within the TSM, for a more in depth description refer to table 3.3.

Figure 6.15 displays the T-i-S models with plug flow and dead time models that best fit the TSM 125 All Quadrant system over the entire design space. The Inlet 1 model shows that the system resembles a PFR for 35% of its axial length (p=0.35) followed by a series of 47 CSTRs in series (n=47). As the total length from Inlet 1 to the exit is 775 mm, this gives the PFR a length of 271.3 mm, followed by 47 CSTRs, each being 10.7 mm in diameter. The Inlet 2 model approximately corroborates this (barring a small discrepancy as p=0.01), as this part of the system is made up of 27 CSTRs in series. As the axial length from Inlet 2 to the exit is 325 mm this means each tank has a diameter of 12 mm.

The TSM 75 T-i-S with plug flow and dead time model on the other hand (discussed in Chapter 4) predicts a PFR value of 32% followed by 22 CSTRs in series. This validates the expectation that the extra mass overall has dampened axial dispersion within the system, due to less time being spent at the TSM wall.

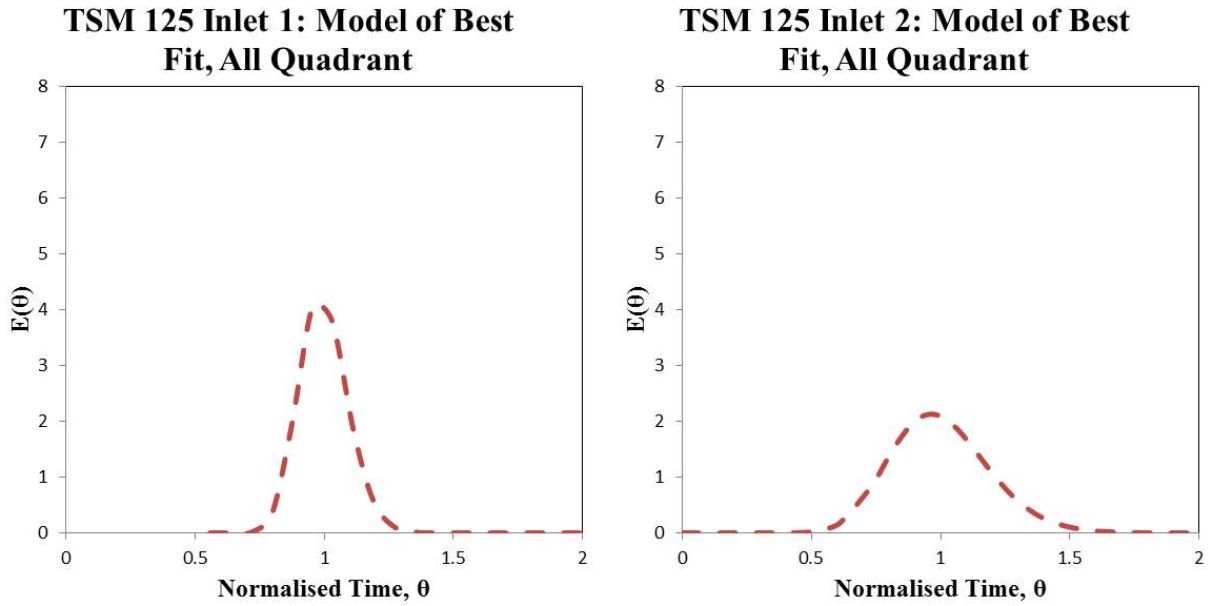

Figure 6.15: The Tanks-in-Series (T-i-S) Models that best describe flow in the TSM 125 - all quadrant. (Left) From Inlet 1 to exit model parameters are: n = 47, d = 0 and p = 0.35, the Residual Sum of Squares (RSS) = 87.56. (Right) From Inlet 2 to exit model parameters are: n = 27, d = 0 and p = 0.01, the Residual Sum of Squares (RSS) = 8.30.

The normalised T-i-S with plug flow and dead time data, for the TSM 125 Quadrant to Anchors, Inlet 1 and 2 RTDs have been provided in Tables 6.17 and 6.18. The curves have also been provided in Figures 6.16 and 6.17. The T-i-S models of best fit across the design space meanwhile has been provided as Figure 6.18.

Table 6.17: TSM 125 Inlet 1 Quadrant to Anchors Tanks-in-Series Model Data. The code refers to the TSM Screw Tip Speed and powder Feed Rate used in the DoE, which may be referenced in tables 3.1 and 3.4.

$\boldsymbol{Run}$	$(\boldsymbol{Code})$	$\boldsymbol{n}$	$\boldsymbol{p}$	$\boldsymbol{d}$	$\boldsymbol{R^2}$
1	$(\boldsymbol{Mid \backslash Mid})$	69	0.17	0.01	0.92
2	$(\boldsymbol{Mid \backslash V.High})$	46	0.46	0.01	0.96
3	$(\boldsymbol{Mid \backslash Low})$	100	0.05	0.00	0.99
4	$(\boldsymbol{V.Low \backslash Mid})$	69	0.44	0.00	0.76
5	$(\boldsymbol{High \backslash High})$	67	0.27	0.00	0.98
6	$(\boldsymbol{Mid \backslash V.Low})$	34	0.43	0.00	0.91
7	$(\boldsymbol{Low \backslash Low})$	47	0.35	0.00	0.94
8	$(\boldsymbol{Mid \backslash Mid})$	70	0.16	0.00	0.97
9	$(\boldsymbol{Low \backslash High})$	70	0.36	0.00	0.95
10	$(\boldsymbol{Mid \backslash Mid})$	69	0.26	0.00	0.95
11	$(\boldsymbol{V.High \backslash Mid})$	70	0.17	0.00	0.98

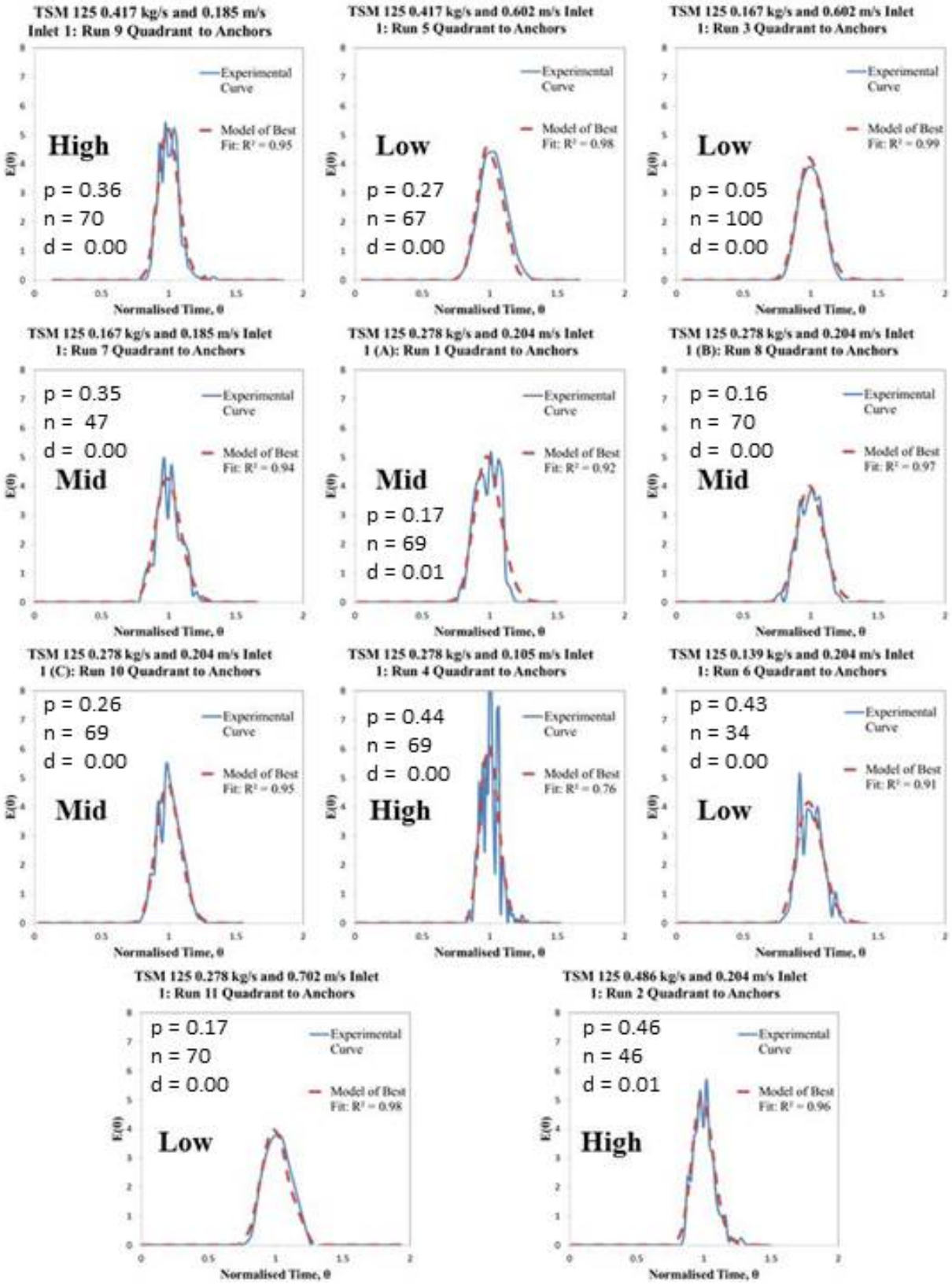

Figure 6.16: TSM 125 Normalised Residence Time Distributions with the best fitting Tanks-in-Series Models: Inlet 1 Quadrants to Anchors. The terms: low, mid and high give a brief description of the visual fill level within the TSM, for a more in depth description refer to table 3.4.

Table 6.18: TSM 125 Inlet 2 Quadrant to Anchors Tanks-in-Series Model Data. The code refers to the TSM Screw Tip Speed and powder Feed Rate used in the DoE, which may be referenced in tables 3.1 and 3.4.

$\boldsymbol{Run}$	$(\boldsymbol{Code})$	$\boldsymbol{n}$	$\boldsymbol{p}$	$\boldsymbol{d}$	$\boldsymbol{R^2}$
1	$(\boldsymbol{Mid \backslash Mid})$	56	0.00	0.00	0.98
2	$(\boldsymbol{Mid \backslash V.High})$	25	0.00	0.00	0.94
3	$(\boldsymbol{Mid \backslash Low})$	24	0.00	0.00	0.99
4	$(\boldsymbol{V.Low \backslash Mid})$	30	0.34	0.00	0.71
5	$(\boldsymbol{High \backslash High})$	27	0.00	0.00	1.00
6	$(\boldsymbol{Mid \backslash V.Low})$	52	0.00	0.00	0.96
7	$(\boldsymbol{Low \backslash Low})$	25	0.25	0.00	0.95
8	$(\boldsymbol{Mid \backslash Mid})$	1	0.85	0.00	0.93
9	$(\boldsymbol{Low \backslash High})$	24	0.00	0.00	0.86
10	$(\boldsymbol{Mid \backslash Mid})$	2	0.70	0.02	0.96
11	$(\boldsymbol{V.High \backslash Mid})$	25	0.00	0.00	0.99

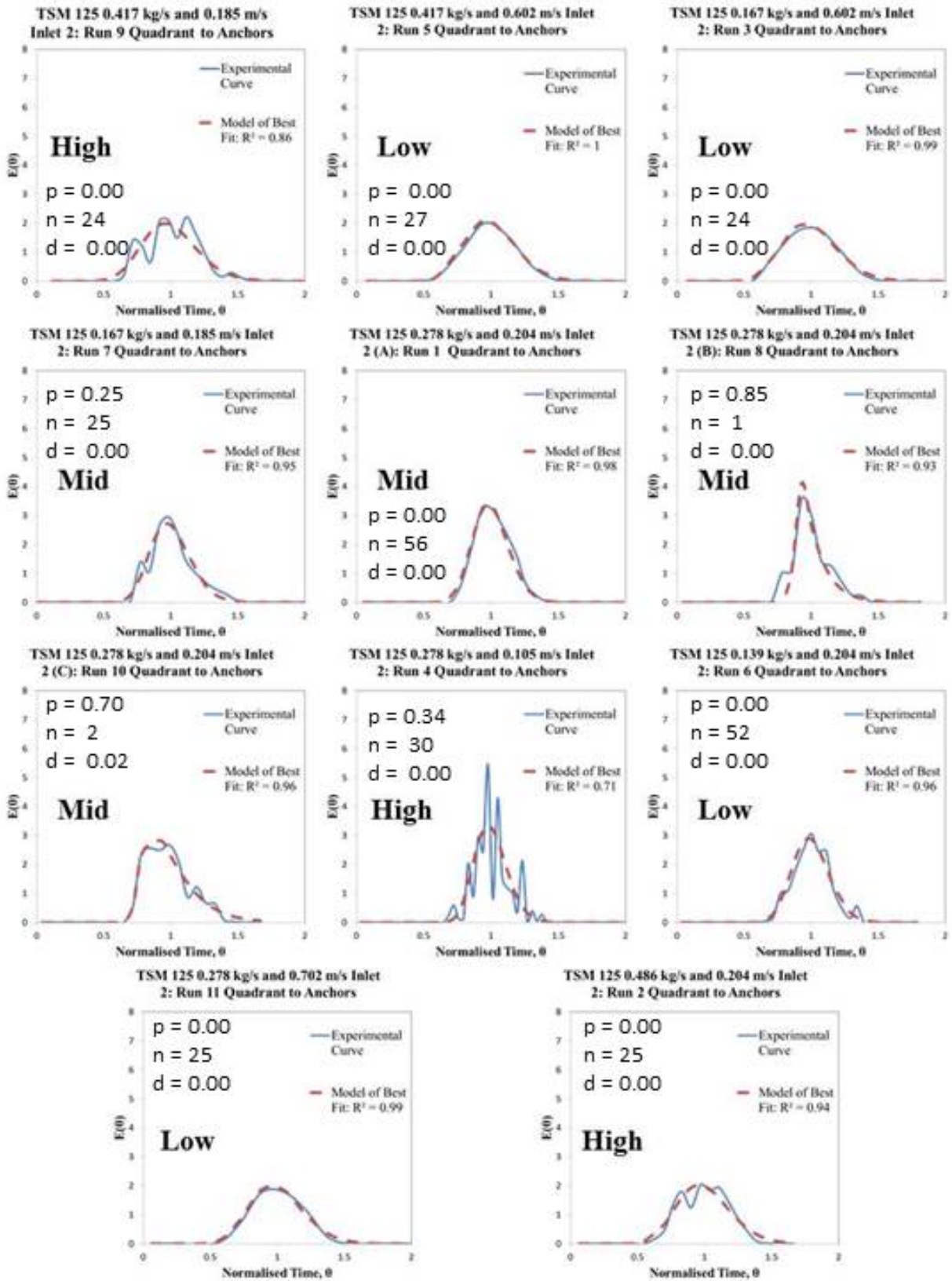

Figure 6.17: TSM 125 Normalised Residence Time Distributions with the best fitting Tanks-in-Series Models: Inlet 2 Quadrants to Anchors. The terms: low, mid and high give a brief description of the visual fill level within the TSM, for a more in depth description refer to table 3.4.

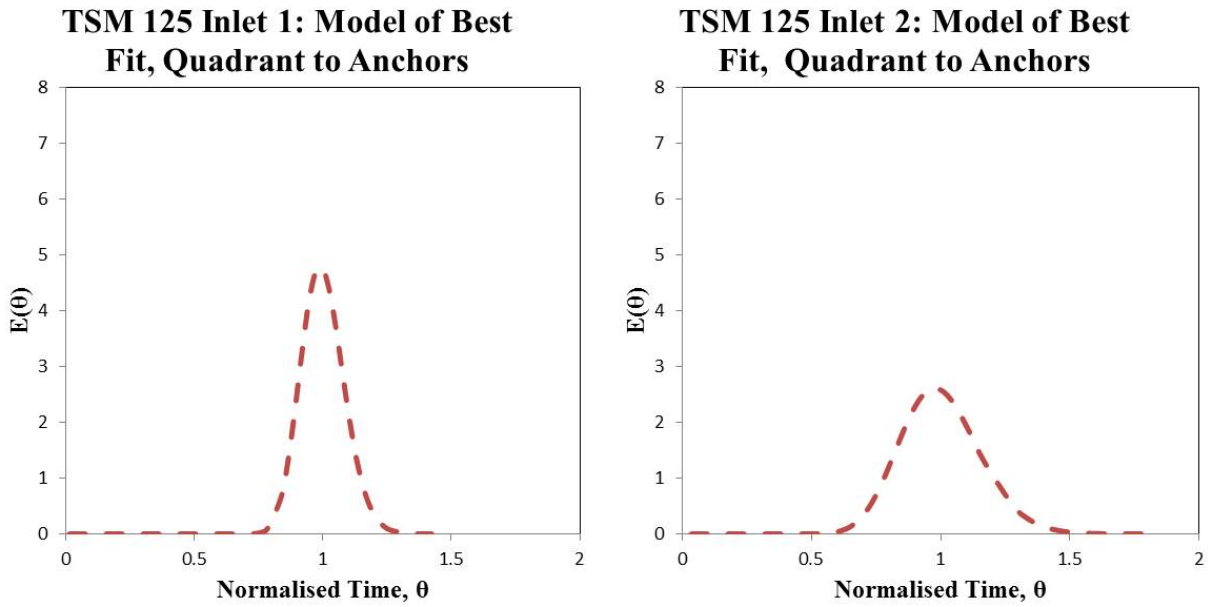

Figure 6.18: The Tanks-in-Series (T-i-S) Models that best describe flow in the TSM 125 - quadrants to anchors. (Left) From Inlet 1 to exit model parameters are: n = 56, d = 0 and p = 0.37, the Residual Sum of Squares (RSS) = 150.15. (Right) From Inlet 2 to exit model parameters are: n = 42, d = 0 and p = 0.00, the Residual Sum of Squares (RSS) = 38.34.

The Inlet 1 model shows that the system resembles a PFR for 37% of its axial length (p=0.37) followed by a series of 56 CSTRs in series (n=56). As the total length from Inlet 1 to the exit is 775 mm, this gives the PFR a length of 286.8 mm, followed by 56 CSTRs, each being 8.7 mm in diameter. The Inlet 2 model approximately corroborates this, as this part of the system is made up of 42 CSTRs in series. As the axial length from Inlet 2 to the exit is 325 mm this means each tank has a diameter of 7.7 mm.

As discussed in Chapter 4.1.2 it is difficult to compare systems whilst using the T-i-S with plug flow and dead time model (as many tanks in series may also approximate a plug flow fraction). Therefore, the same systems shall now be analysed using only the T-i-S models and the Pe number. The T-i-S model number of tanks, n, and Peclet number for each regime has been provided in tables 6.19 and 6.20, for the TSM 125 all quadrant geometry. The models and normalised curves have also been provided as figures 6.19 and 6.20.

Table 6.19: TSM 125 All Quadrant Normalised Residence Time Distributions with the best fitting, n only, Tanks-in-Series (T-i-S) Models and Peclet Numbers: Inlet 1.

$\boldsymbol{Run}$	$\boldsymbol{n}$	$\boldsymbol{R^2}$	Pe
1	135	0.95	320.82
2	140	0.84	428.51
3	74	0.99	172.79
4	126	0.83	277.81
5	68	0.99	197.17
6	89	0.98	161.40
7	64	0.94	163.22
8	98	0.97	253.81
9	106	0.92	208.04
10	123	0.96	250.71
11	79	0.99	189.82

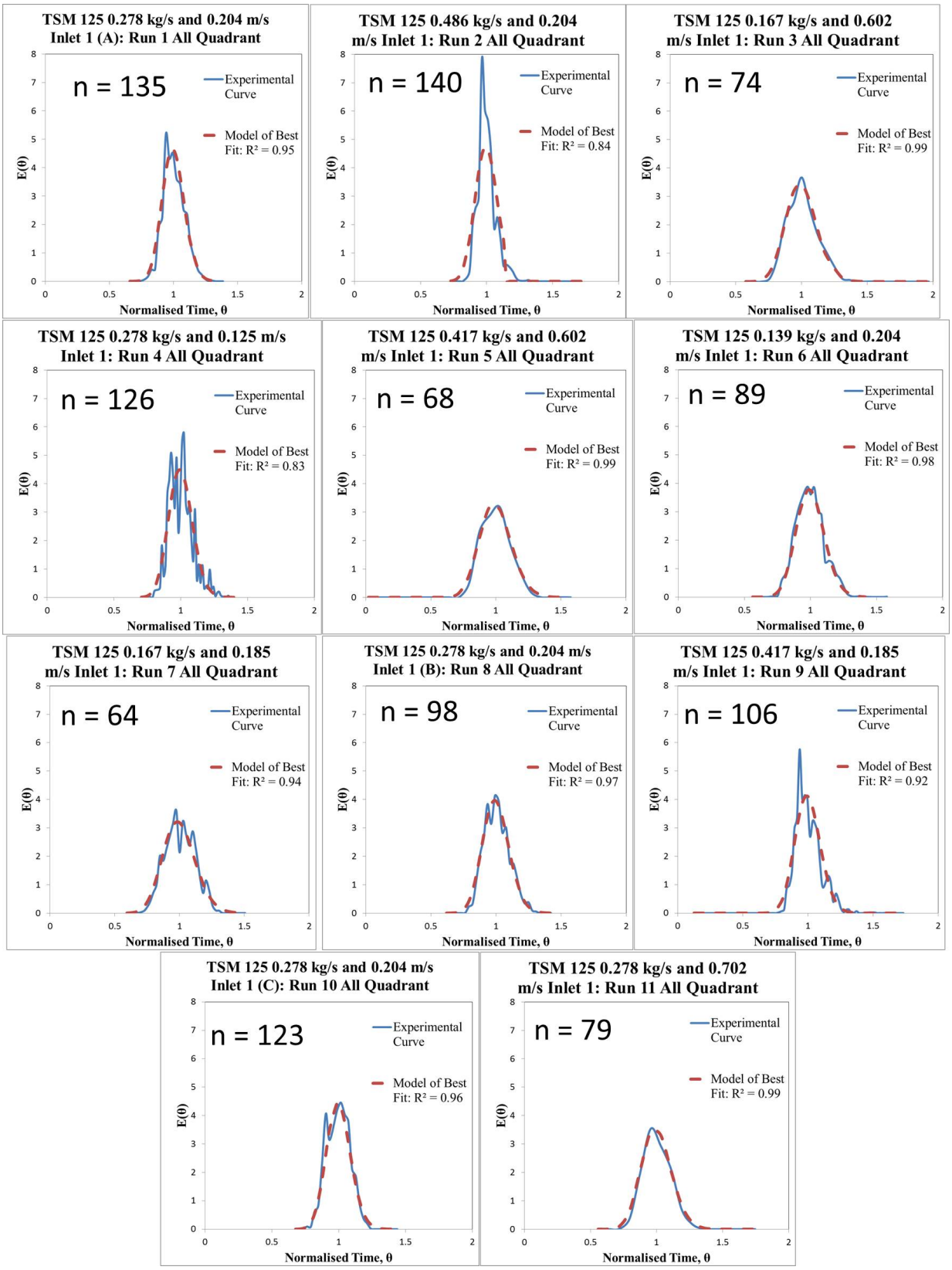

Figure 6.19: TSM 125, All Quadrant, Normalised Residence Time Distributions with the best fitting, n only, Tanks-in-Series (T-i-S) Models: Inlet 1.

Table 6.20: TSM 125 All Quadrant Normalised Residence Time Distributions with the best fitting, n only, Tanks-in-Series (T-i-S) Models and Peclet Numbers: Inlet 2.

$\boldsymbol{Run}$	$\boldsymbol{n}$	$\boldsymbol{R^2}$	Pe
1	35	0.97	66.47
2	33	0.97	80.28
3	18	0.99	49.83
4	29	0.96	66.74
5	19	0.98	45.34
6	21	0.97	46.59
7	20	0.93	40.23
8	36	0.96	81.09
9	30	0.96	69.60
10	32	0.98	79.37
11	19	1.00	38.91

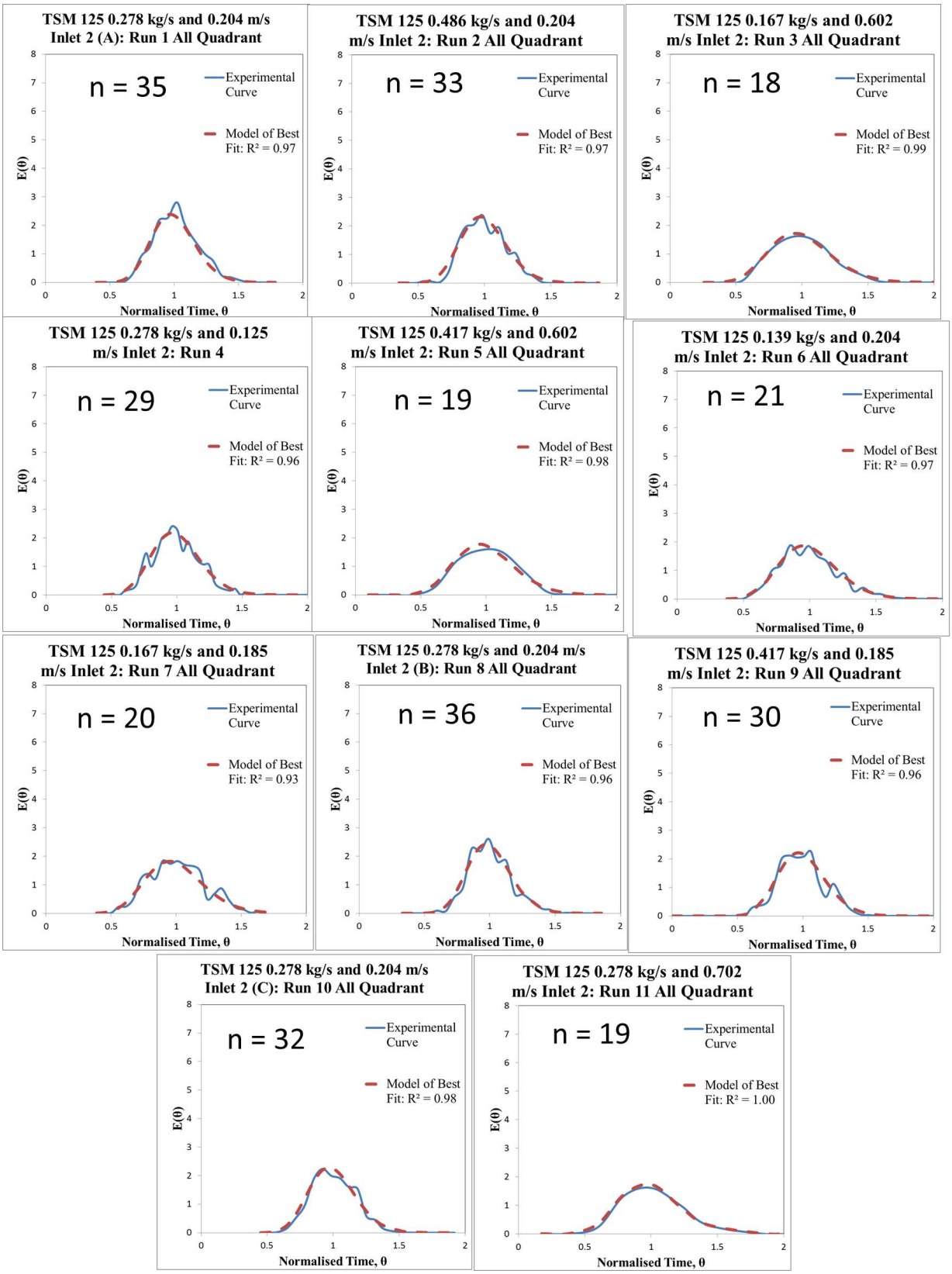

Figure 6.20: TSM 125, All Quadrant, Normalised Residence Time Distributions with the best fitting, n only, Tanks-in-Series (T-i-S) Models: Inlet 2.

As can been seen from figure 6.21 Pe and n correlate well for the TSM 75 and TSM 125 whilst both have all quadrant geometry. The average number of n that is needed to describe the TSM 75 for its 555 mm length (Inlet 1 to exit) is roughly half what is needed to described the TSM 125 for its 775 mm length (Inlet 1 to exit). The average number of n that is needed to describe the TSM 75 for its 195 mm length (Inlet 2 to exit) is roughly a third of what is needed to described the TSM 125 for its 325 mm length (Inlet 2 to exit).

This indicates that both scales of machine behave more like a plug flow reactor than a CSTR at the start of its axial length before transitioning to a series of CSTRs. This corroborates the T-i-S plus dead time models for each system. It also shows that the extra mass present in the TSM 125 cause it to behave more like a PFR than the TSM 75.

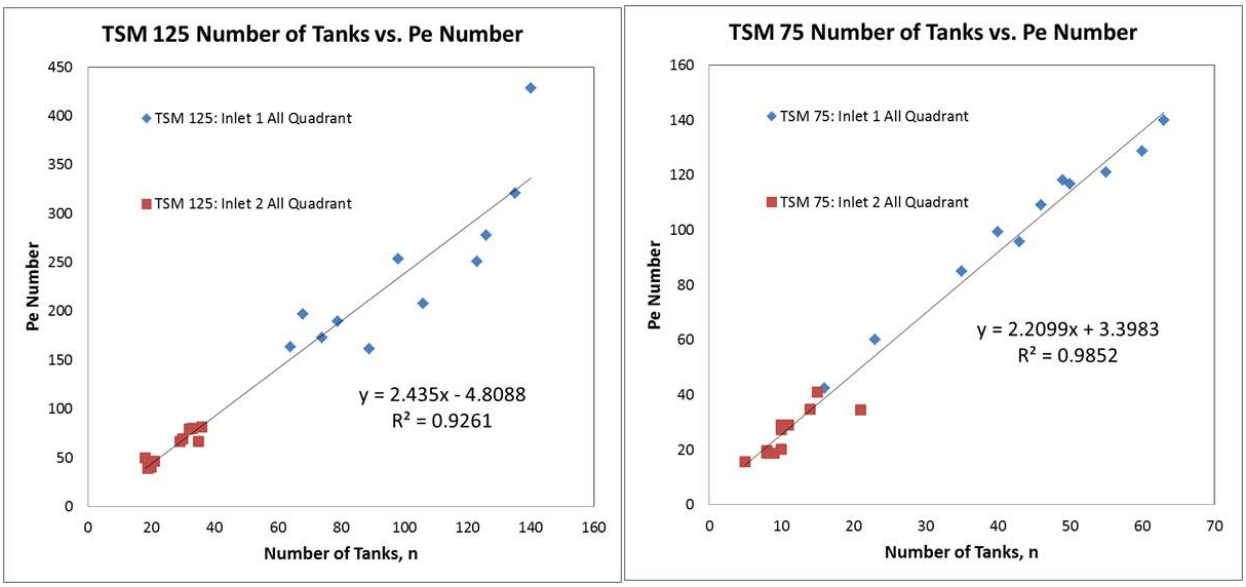

Figure 6.21: (Left) TSM 125, All Quadrant, Number of T-i-S, n, vs. Peclet number. (Right) TSM 75, All Quadrant, Number of T-i-S, n, vs. Peclet number.

The Peclet numbers show that intermediate dispersion tending towards plug flow is present in the TSM 125 from Inlet 1 (Pe range is 161.40 to 428.51). Whereas, in the TSM 75 this was a lot less (Pe range was 95.62 to 139.86). The Peclet numbers also show that intermediate dispersion is present in the TSM 125 from Inlet 2 (Pe range is 38.91 to 81.09). Whereas, in the TSM 75 this was a lot less (Pe range was 15.52 to 40.96). Also, unlike the TSM 75, there is no strong univariate relationship with Tip Speed (as well as: bulk velocity, curve variance, screw lead or fill level). This shows that the factors that influence the axial dispersion become more complex upon scale-up.

The T-i-S model number of tanks, n, and Peclet number for each regime has been provided in ta-

bles 6.21 and 6.22, for the TSM 125 quadrant to anchors geometry. The models and normalised curves have also been provided as figures 6.22 and 6.22.

Table 6.21: TSM 125 Quadrant to Anchors Normalised Residence Time Distributions with the best fitting, n only, Tanks-in-Series (T-i-S) Models and Peclet Numbers: Inlet 1.

$\boldsymbol{Run}$	$\boldsymbol{n}$	$\boldsymbol{R^2}$	Pe
1	140	0.90	313.19
2	139	0.95	349.74
3	113	0.99	304.71
4	140	0.74	439.78
5	133	0.98	211.30
6	107	0.91	268.60
7	112	0.94	262.18
8	101	0.97	356.50
9	138	0.94	382.56
10	137	0.95	261.51
11	101	0.98	300.54

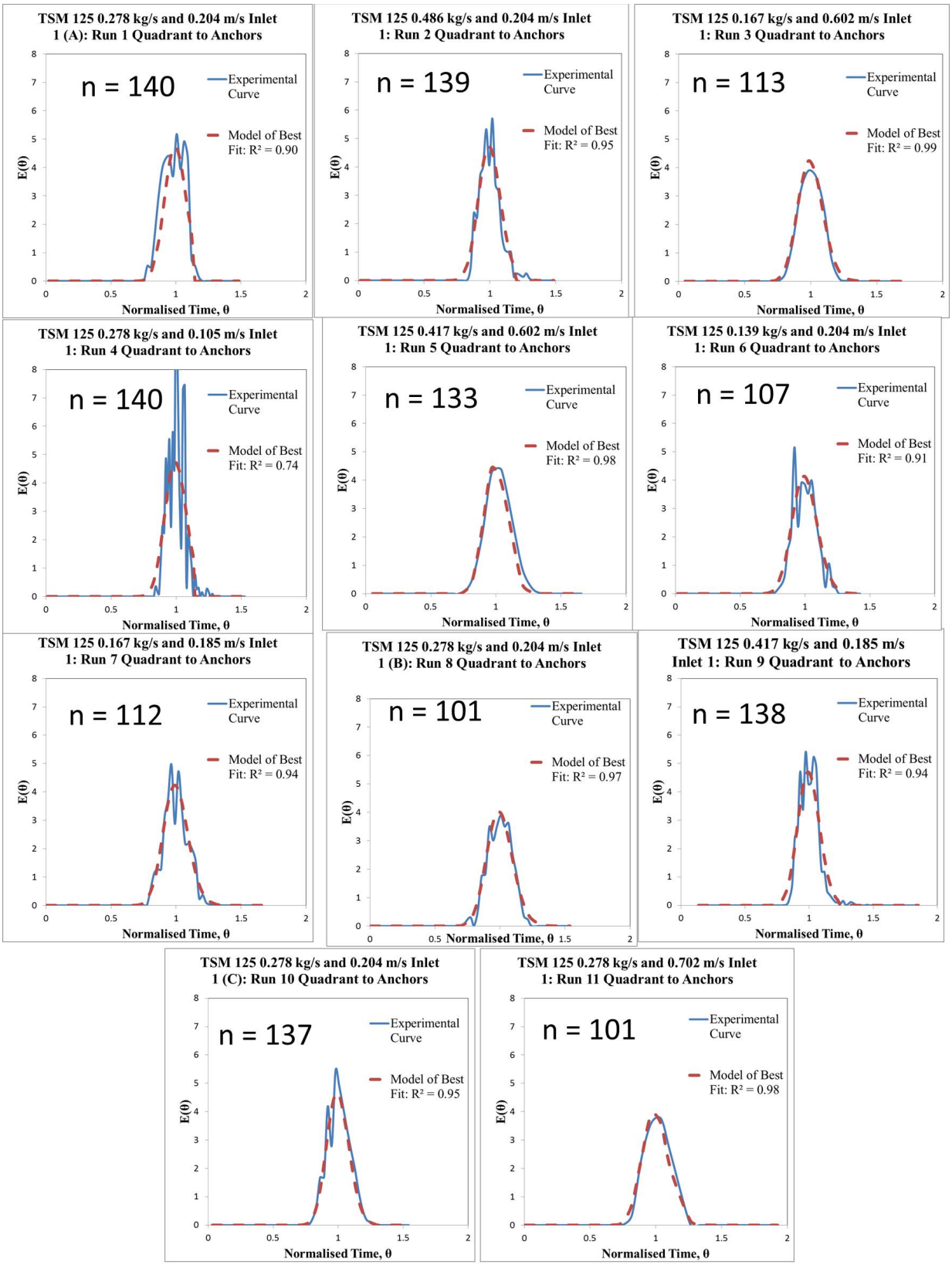

Figure 6.22: TSM 125, Quadrant to Anchors, Normalised Residence Time Distributions with the best fitting, n only, Tanks-in-Series (T-i-S) Models: Inlet 1.

Table 6.22: TSM 125 Quadrant to Anchors Normalised Residence Time Distributions with the best fitting, n only, Tanks-in-Series (T-i-S) Models and Peclet Numbers: Inlet 2.

$\boldsymbol{Run}$	$\boldsymbol{n}$	$\boldsymbol{R^2}$	Pe
1	56	0.98	105.91
2	25	0.94	78.23
3	24	0.99	61.39
4	69	0.71	109.72
5	27	1.00	59.00
6	52	0.96	112.11
7	43	0.95	81.90
8	58	0.90	110.84
9	24	0.86	60.18
10	33	0.88	67.13
11	25	0.99	67.77

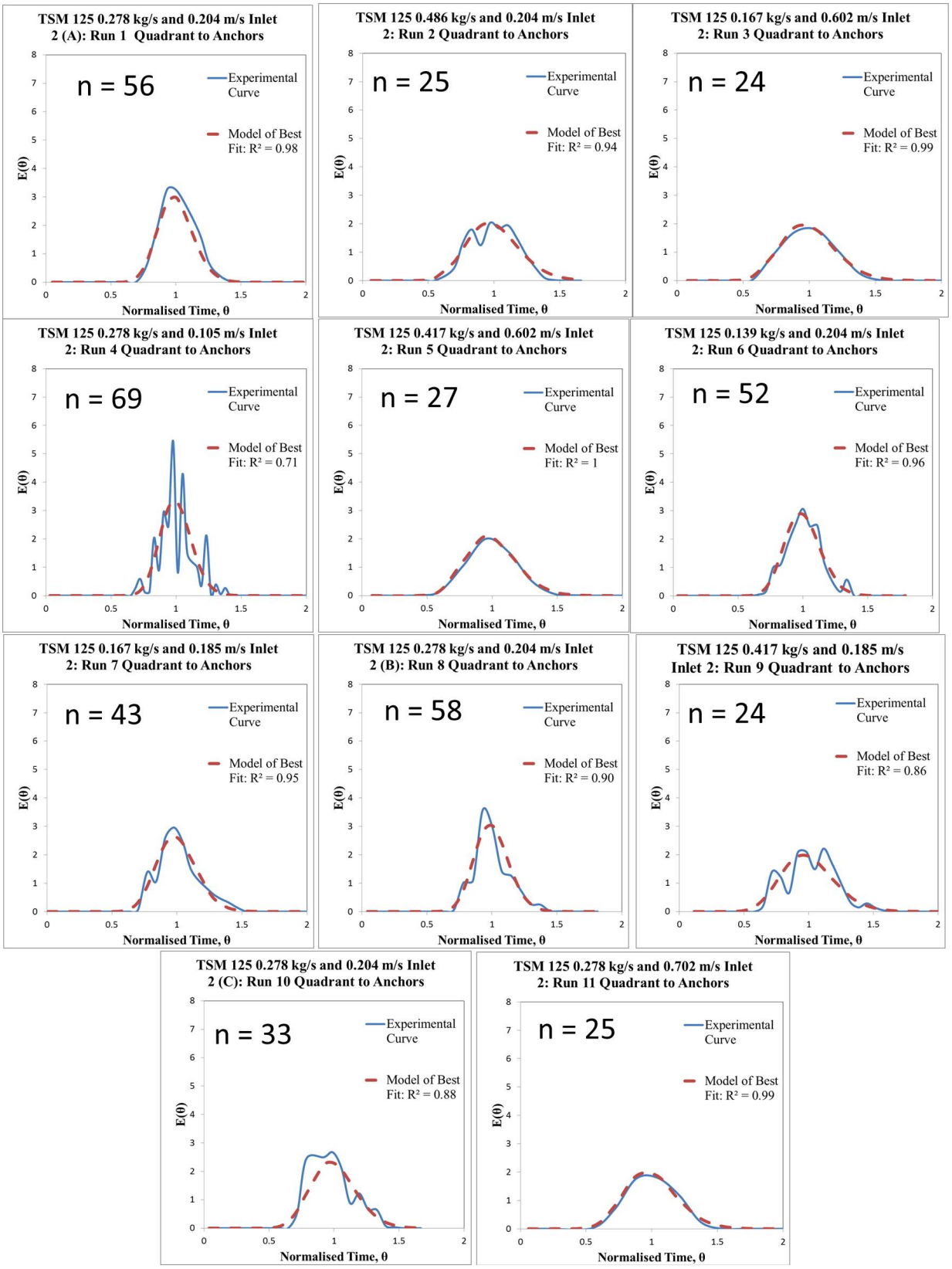

Figure 6.23: TSM 125, Quadrant to Anchors, Normalised Residence Time Distributions with the best fitting, n only, Tanks-in-Series (T-i-S) Models: Inlet 2.

The results from the quadrant to anchors T-i-S models and Peclet numbers are interesting. As while there is a strong relationship between n and Pe from Inlet 2, this is not the case for Inlet 1. This indicates that the T-i-S model may not be an accurate representation of Quadrant to Anchors this system.

Furthermore, the TSM 125 all quadrant Peclet numbers are similar to those in the TSM 125 all quadrant (including Peclet number not having a strong univariate relationship with: Tip Speed, bulk velocity, curve variance, screw lead or fill level). However, they tend to be slightly higher indicating axial dispersion actually decreases despite curve variance also slightly increasing. This is because according to equation 3.11 the Peclet number is a non-linear function of the ratio of variance and residence time. Therefore, this ratio seems to have shifted slightly with the new geometry to create less axial dispersion (when compared to the all quadrant regime). This may be a result of less reordering of the bulk by the paddles, due to a lower surface area.

6.2 Conclusions

The method that was developed for characterising the TSM 75 in Chapter 4 has proved to be extremely adept for characterising the TSM 125, and the two appear to be quite similar. This is a strong indication that the way these machines have been kept geometrically similar leads to similar results in terms of particle motion.

However, there are some differences in the way the powder behaves. The extra mass in the system means that higher fill levels are needed for powder to more closely track the Screw Lead Velocity. It is also possible to fit more powder in the system as a percentage of the TSMs static fill volume before flooding occurs, due to compression of the bulk under it's own weight (however, this phenomena would be expected to reach some limit as scales become even larger). Furthermore, by increasing the mass volume to TSM wall surface area less axial dispersion is generated within the system for two reasons: 1) powder spends less time at the wall and 2) the powder becoming more consolidated and spreading out less in an axial fashion.

Finally, the change in geometry has also had an effect on powder motion. Adding anchors of less surface area than paddles has led to less efficient axial transport, therefore slightly slowing the bulks axial velocity. Curve variance has also slightly increased. Despite this, the change in the normalised curve variance (from the TSM 125 all quadrant to the TSM 125 quadrant to anchors) has led to less axial dispersion in the system overall as discerned by the Peclet number.

Chapter 7

Summary

The DIP measurement strategy has been validated using the TSM 75 and the PEPT technique, as well as statistical methods and conceptual understanding. This should prove to be a very adaptable technique that could find use for a variety of different applications.

In general, bulk Velocity and the inverse of the RTD curve variance is positively affected by the Screw Speed and the Feed Rate. However, it is the Screw Speed that is the most important predictor.

Within the TSM 75, below Screw Tip speeds of 0.3 m/s the bulk tends to be pushed along in a piecemeal fashion. This leads to the curve variance, σ^2, becoming exponentially large as the Screw Tip speed drops below this value. Above 0.8 m/s the Feed Rate starts to become equally important to the Screw Speed to prevent extreme system starvation. This is because below a certain fill level axial transport becomes much less efficient.

The same phenomena are witnessed in the TSM 125 All Quadrant. Except the extra weight of the bulk has led to the powder being pushed along in a piecemeal fashion at 0.4 m/s Tip Speed. The fill level also starts to become equally important to bulk velocity at a lower Tip Speed, 0.6 m/s, indicating system starvation is an even more important consideration when considering axial flow in larger machines.

In the TSM 75 when the static fill volume is <18% the powder is not pushed over the shafts. When the static fill volume is between 18 - 22% the powder begins to be pushed over the shafts. Above 48% static fill volume the system becomes flooded.

However, in the TSM 125 All Quadrant the static fill volume when the powder is not pushed over the shafts raises to <22%. Furthermore, when the static fill volume is between 22 - 26% the powder begins to be pushed over the shafts, which is higher than the TSM 75 counterpart. Above 58% static fill volume the TSM 125 system becomes flooded, as opposed to 48% in the TSM 75. This shows that the extra weight of the bulk is causing the powder in the system to consolidate.

PEPT has shown that the bulk tends to be pushed together centrally between the shafts. When the

powder is located centrally between the shafts it tends to travel axially downstream and up to the top of the bulk. Once the powder has reached the top of the bulk it tends to fall down the bulk towards the radial extremes.

The study also discerned that at a medium fill level, when powder begins to start flowing over the shafts, circular flow patters emerge around the shafts. Furthermore, whilst powder is in the central region it tends to travel at the rate of the screw lead whereas at the radial extremes it tends to travel approximately 25% of this.

The T-i-S and Peclet analysis showed that their is intermediate axial dispersion within these machines. However, the consolidation created in the larger machine (TSM 125) has led to it tending more towards plug flow than the smaller machine (TSM 75).

Finally, when the TSM 125 is changed to the Quadrant to Anchors geometry the T-i-S model no longer tracks the Peclet number as closely indicting this is not a good fitting model for this system configuration. Furthermore, the Peclet number reveals that axial dispersion becomes less.

Chapter 8

Future Work & Industrial Impact

The sulphate powders motion, within TSMs of two different scales and with two different geometrical configurations, has been thoroughly investigated. A robust framework for characterising flow in these systems has also been established.

This has led to the construction of Response Surface and T-i-S models, which has made planning future experiments with the equipment a much easier procedure. This is because investigators are able to construct experiments based upon some desired: Fill Level, Average Velocity or σ^2 of the RTD curve; as well as discerning how a particular size and geometry will affect system flow properties overall. Whereas previously, Average Velocity and σ^2 were completely unknown, and Fill Level had to be approximated by eye whilst adjusting machine parameters. Figure 8.1 shows the TSM 125 within a laboratory in CPI, and Figure 8.2 shows the RSM models for Fill level, that have been left on a white board within the laboratory to aid in experimental planning.

Figure 8.1: The TSM 125 set-up within a laboratory in CPI.

Figure 8.2: A white board in CPI that contains the Fill Level RSM models for the TSM 75 and TSM 125.

The next step in investigating the TSMs should be to develop RSM models, for both the TSM 75 and TSM 125, that measure critical quality attributes. This may include:

- The PSD after undergoing a coating process.
- The uniformity of content during a mixing study.
- The PSD after undergoing a wet granulation procedure.

These RSM models could then be compared with the corresponding: T-i-S, Velocity, σ^2 and Fill Level models, to see how scaleable these parameters are. In this fashion it will be possible to discern the important flow parameters to establish within the system in order to produce a desired result. This will lead to more confidence before triggering an expensive capital investment decision, as the TSM P&G would need for commercial scale operations would need to be many times larger than those investigated here.

The consortium has also found these investigations invaluable for validating their DEM models of the system. These models can now be scaled in silico, in order to add another layer of confidence for a future capital investment.

Finally, as discussed with Section 1.3, TSMs have rarely been addressed within academia, and to the best of this author's knowledge never at the scales investigated here. Therefore, how these systems may behave whilst being subjected to changes such as: powder formulation, paddle shape, paddle angle and screw shaft rotational direction, is still largely unknown. This thesis offers a robust and efficient framework, for academics and industrialist alike, to begin investigating the many system alterations one could make whilst utilising a TSM.

References

[1] Simon M Iveson, James D Litster, Karen Hapgood, and Bryan J Ennis. Nucleation, growth and breakage phenomena in agitated wet granulation processes: a review. *Powder technology*, 117(1):3–39, 2001.

[2] John Bridgwater. Mixing of powders and granular materials by mechanical means—a perspective. *Particuology*, 10(4):397–427, 2012.

[3] AS El Hagrasy, JR Hennenkamp, MD Burke, JJ Cartwright, and JD Litster. Twin screw wet granulation: influence of formulation parameters on granule properties and growth behavior. *Powder technology*, 238:108–115, 2013.

[4] Charlie Martin. *Melt Extrusion: Materials, Technology and Drug Product Design. Twin Screw Extrusion for Pharmaceutical Processes*. AAPS Advances in the Pharmaceutical Sciences Series. Springer New York, 2013.

[5] M. R. Thompson. Twin screw granulation - review of current progress. *Drug Development and Industrial Pharmacy*, Early Online:1–9, 2014.

[6] Todd A. Kingston and Theodore J. Heindel. Granular mixing optimization and the influence of operating conditions in a double screw mixer. *Powder Technology*, 266:144–155, 2014.

[7] Sundaram Gunasekaran. Computer vision technology for food quality assurance. *Trends in Food Science & Technology*, 7(8):245 – 256, 1996.

[8] Cheng-Jin Du and Da-Wen Sun. Recent developments in the applications of image processing techniques for food quality evaluation. *Trends in Food Science & Technology*, 15(5):230 – 249, 2004.

[9] Baohua Zhang, Wenqian Huang, Jiangbo Li, Chunjiang Zhao, Shuxiang Fan, Jitao Wu, and Chengliang Liu. Principles, developments and applications of computer vision for external quality inspection of fruits and vegetables: A review. *Food Research International*, 62:326–343, 2014.

[10] Fernando Mendoza, Petr Dejmek, and José M. Aguilera. Calibrated color measurements of agricultural foods using image analysis. *Postharvest Biology and Technology*, 41(3):285 – 295, 2006.

[11] D.B. MacDougall. *3.7 Colour Description: Uniform Colour Space*. Woodhead Publishing, 2002.

[12] Unknown. The cie 1931 xyz color matching functions. `https://commons.wikimedia.org/wiki/File:CIE_1931_XYZ_Color_Matching_Functions.svg`, March 2009. Accessed December 2, 2016.

[13] Unknown. About color spaces. `http://developers-club.com/posts/181580/`, 2013. Accessed December 2, 2016.

[14] Unknown. Lab color space. `https://upload.wikimedia.org/wikipedia/commons/thumb/7/70/SRGB_gamut_within_CIELAB_color_space_isosurface.png/220px-SRGB_gamut_within_CIELAB_color_space_isosurface.png`, 2016. Accessed December 4, 2016.

[15] G. Sharma and R. Bala. *Digital Color Imaging Handbook*. Electrical Engineering & Applied Signal Processing Series. CRC Press, 2002.

[16] Yijie Gao, Fernando J. Muzzio, and Marianthi G. Ierapetritou. A review of the residence time distribution (rtd) applications in solid unit operations. *Powder Technology*, 228(2012):416–423, 2012.

[17] Gregory R. Ziegler and Carlos A. Aguilar. Residence time distribution in a co-rotating, twin-screw continuous mixer by the step change method. *Journal of Food Engineering*, 59(2):161 – 167, 2003.

[18] Ajay Kumar, Girish M. Ganjyal, David D. Jones, and Milford A. Hanna. Digital image processing for measurement of residence time distribution in a laboratory extruder. *Journal of Food Engineering*, 75(2):237 – 244, 2006.

[19] Chao Bi, Bo Jiang, and Ao Li. Digital image processing method for measuring the residence time distribution in a plasticating extruder. *Polymer Engineering & Science*, 2007:1108–1113, 2007.

[20] Siew Yoong Lee, Milford A. Hanna, and David D. Jones. Residence time distribution using on-line digital image processing. *Starch/Staerke*, 61(2009):146–153, 2009.

[21] Dejan Djuric and Peter Kleinebudde. Impact of screw elements on continuous granulation with a twin-screw extruder. *Journal of Pharmaceutical Sciences*, 97(11):4934 – 4942, 2008.

[22] Todd A Kingston and Theodore J Heindel. Optical visualization and composition analysis to quantify continuous granular mixing processes. *Powder Technology*, 262:257–264, 2014.

[23] Todd A Kingston, Taylor A Geick, Teshia R Robinson, and Theodore J Heindel. Characterizing 3d granular flow structures in a double screw mixer using x-ray particle tracking velocimetry. *Powder Technology*, 278:211–222, 2015.

[24] Breanna L Marmur and Theodore J Heindel. Effect of particle size, density, and concentration on granular mixing in a double screw pyrolyzer. *Powder Technology*, 302:222–235, 2016.

[25] Fenglei Qi, Theodore J Heindel, and Mark Mba Wright. Numerical study of particle mixing in a lab-scale screw mixer using the discrete element method. *Powder Technology*, 308:334–345, 2017.

[26] Sinnott Ray K. Towler, Gavin. *Chemical Engineering Design - Principles, Practice and Economics of Plant and Process Design (2nd Edition) Chapter 18*. Elsevier, 2013.

[27] Dana Barrasso, Samjit Walia, and Rohit Ramachandran. Multi-component population balance modeling of continuous granulation processes: a parametric study and comparison with experimental trends. *Powder technology*, 241:85–97, 2013.

[28] Rohit Ramachandran, Jonathan M-H Poon, Constantijn FW Sanders, Thomas Glaser, Charles D Immanuel, Francis J Doyle, James D Litster, Frantisek Stepanek, Fu-Yang Wang, and Ian T Cameron. Experimental studies on distributions of granule size, binder content and porosity in batch drum granulation: Inferences on process modelling requirements and process sensitivities. *Powder Technology*, 188(2):89–101, 2008.

[29] Jonathan M-H Poon, Charles D Immanuel, Francis J Doyle Iii, and James D Litster. A three-dimensional population balance model of granulation with a mechanistic representation of the nucleation and aggregation phenomena. *Chemical Engineering Science*, 63(5):1315–1329, 2008.

[30] Simon M. Iveson. Limitations of one-dimensional population balance models of wet granulation processes. *Powder Technology*, 124(3):219 – 229, 2002. Control of Particulate Processess {IV}.

[31] Charles David Immanuel and Francis Joseph Doyle III. Solution technique for a multi-dimensional population balance model describing granulation processes. *Powder Technology*, 156(2–3):213 – 225, 2005. Particle Technology Forum Special IssuePapers presented in the Particle Technology Forum sessions at the 2003 Annual {AIChE} meeting in San Francisco (November, 2003)Papers presented in the Particle Technology Forum sessions at the 2003 Annual {AIChE} meeting in San Francisco (November, 2003).

[32] Jonathan M.-H. Poon, Rohit Ramachandran, Constantijn F.W. Sanders, Thomas Glaser, Charles D. Immanuel, Francis J. Doyle III, James D. Litster, Frantisek Stepanek, Fu-Yang Wang, and Ian T. Cameron. Experimental validation studies on a multi-dimensional and multi-scale population balance model of batch granulation. *Chemical Engineering Science*, 64(4):775 – 786, 2009. 3rd International Conference on Population Balance Modelling.

[33] J Zhang, JD Litster, FY Wang, and IT Cameron. Evaluation of control strategies for fertiliser granulation circuits using dynamic simulation. *Powder Technology*, 108(2):122–129, 2000.

[34] Fu Yang Wang and Ian T Cameron. Review and future directions in the modelling and control of continuous drum granulation. *Powder Technology*, 124(3):238–253, 2002.

[35] Daniel A Pohlman and James D Litster. Coalescence model for induction growth behavior in high shear granulation. *Powder Technology*, 270:435–444, 2015.

[36] Rohit Ramachandran and Anwesha Chaudhury. Model-based design and control of a continuous drum granulation process. *Chemical Engineering Research and Design*, 90(8):1063–1073, 2012.

[37] I.T. Cameron and F.Y. Wang. Chapter 11 process systems engineering applied to granulation. In M.J. Hounslow A.D. Salman and J.P.K. Seville, editors, *Granulation*, volume 11 of *Handbook of Powder Technology*, pages 499 – 552. Elsevier Science B.V., 2007.

[38] Rohit Ramachandran and Paul I Barton. Effective parameter estimation within a multi-dimensional population balance model framework. *Chemical Engineering Science*, 65(16):4884–4893, 2010.

[39] Shivendra Singh Chauhan, Abhinandan Chiney, and Sanjeev Kumar. On the solution of bivariate population balance equations for aggregation: X–discretization of space for expansion and contraction of computational domain. *Chemical engineering science*, 70:135–145, 2012.

[40] EI Keleb, An Vermeire, Chris Vervaet, and Jean Paul Remon. Continuous twin screw extrusion for the wet granulation of lactose. *International journal of pharmaceutics*, 239(1):69–80, 2002.

[41] Kai T Lee, Andy Ingram, and Neil A Rowson. Comparison of granule properties produced using twin screw extruder and high shear mixer: A step towards understanding the mechanism of twin screw wet granulation. *Powder technology*, 238:91–98, 2013.

[42] ML Booy. Isothermal flow of viscous liquids in corotating twin screw devices. *Polymer Engineering & Science*, 20(18):1220–1228, 1980.

[43] Serafim Bakalis and Mukund V Karwe. Velocity distributions and volume flow rates in the nip and translational regions of a co-rotating, self-wiping, twin-screw extruder. *Journal of food engineering*, 51(4):273–282, 2002.

[44] OS Carneiro, G Caldeira, and JA Covas. Flow patterns in twin-screw extruders. *Journal of Materials Processing Technology*, 92:309–315, 1999.

[45] AKHILESH GAUTAM and GOUR S CHOUDHURY. Screw configuration effects on residence time distribution and mixing in twin-screw extruders during extrusion of rice flour. *Journal of food process engineering*, 22(4):263–285, 1999.

[46] O. Levenspiel. *Chemical reaction engineering*. Wiley series in chemical engineering. Wiley, 1972.

[47] DJ Van Zuilichem, E Kuiper, W Stolp, and T Jager. Mixing effects of constituting elements of mixing screws in single and twin screw extruders. *Powder technology*, 106(3):147–159, 1999.

[48] T Jager, DJ Van Zuilichem, JG De Swart, and K Van't Riet. Residence time distributions in extrusion-cooking: Part 7—modelling of a corotating, twin-screw extruder fed with maize grits. *Journal of food engineering*, 14(3):203–239, 1991.

[49] M. R. Thompson. Twin screw granulation – review of current progress. *Drug Development and Industrial Pharmacy*, 41(8):1223–1231, 2015. PMID: 25402966.

[50] Tim Chan Seem, Neil A. Rowson, Andy Ingram, Zhenyu Huang, Shen Yu, Marcel de Matas, Ian Gabbott, and Gavin K. Reynolds. Twin screw granulation - a literature review. *Powder Technology*, 276:89 – 102, 2015.

[51] MJ Gamlen and C Eardley. Continuous extrusion using a raker perkins mp50 (multipurpose) extruder. *Drug Development and Industrial Pharmacy*, 12(11-13):1701–1713, 1986.

[52] N.-O. Lindberg, C. Tufvesson, and L. Olbjer. Extrusion of an effervescent granulation with a twin screw extruder, baker perkins mpf 50 d. *Drug Development and Industrial Pharmacy*, 13(9-11):1891–1913, 1987.

[53] N.-O. Lindberg, M. Myrenas, C. Tufvesson, and L. Olbjer. Extrusion of an effervescent granulation with a twin screw extruder, baker perkins mpf 50d. determination of mean residence time. *Drug Development and Industrial Pharmacy*, 14(5):649–655, 1988.

[54] N. O. Lindberg, C. Tufvesson, P. Holm, and L. Olbjer. Extrusion of an effervescent granulation with a twin screw extruder, baker perkins mpf 50 d. influence on intragranular porosity and liquid saturation. *Drug Development and Industrial Pharmacy*, 14(13):1791–1798, 1988.

[55] EI Keleb, A Vermeire, Chris Vervaet, and Jean Paul Remon. Twin screw granulation as a simple and efficient tool for continuous wet granulation. *International journal of pharmaceutics*, 273(1):183–194, 2004.

[56] Peter J Fellows. *Food processing technology: principles and practice*. Elsevier, 2009.

[57] Ashish Kumar, Jurgen Vercruysse, Valérie Vanhoorne, Maunu Toiviainen, Pierre-Emmanuel Panouillot, Mikko Juuti, Chris Vervaet, Jean Paul Remon, Krist V Gernaey, Thomas De Beer, et al. Conceptual framework for model-based analysis of residence time distribution in twin-screw granulation. *European Journal of Pharmaceutical Sciences*, 71:25–34, 2015.

[58] A Shah and M Gupta. Comparison of the flow in co-rotating and counter-rotating twin-screw extruders. In *ANTEC-CONFERENCE PROCEEDINGS-.*, volume 1, pages 443–447. UNKNOWN, 2004.

[59] Werner Wiedmann and Maria Hölzel. Twin-screw extruders in ceramic extrusion. In *Extrusion in Ceramics*, pages 241–258. Springer, 2009.

[60] Barbara Van Melkebeke, Chris Vervaet, and Jean Paul Remon. Validation of a continuous granulation process using a twin-screw extruder. *International journal of pharmaceutics*, 356(1):224–230, 2008.

[61] D. Djuric, B. Van Melkebeke, P. Kleinebudde, J.P. Remon, and C. Vervaet. Comparison of two twin-screw extruders for continuous granulation. *European Journal of Pharmaceutics and Biopharmaceutics*, 71(1):155 – 160, 2009. Special Issue: Solid State and Solid Dosage Forms.

[62] Ranjit M Dhenge, Richard S Fyles, James J Cartwright, David G Doughty, Michael J Hounslow, and Agba D Salman. Twin screw wet granulation: granule properties. *Chemical Engineering Journal*, 164(2):322–329, 2010.

[63] Unknown. Mathworks: patch. `https://uk.mathworks.com/help/matlab/ref/patch.html`, 2006. Accessed January 20, 2016.

[64] Unknown. Mathworks: polyarea. `http://uk.mathworks.com/help/matlab/ref/polyarea.html`, 2006. Accessed January 21, 2016.

[65] Unknown. wstyler: Ro-tap sieve shakers. `http://wstyler.com/product/ro-tap-sieve-shakers/`, September 2017. Accessed September 25, 2017.

[66] Unknown. Sodium sulphate: Uses and applications. `http://www.crimidesa.es/_en/sulfato-usos-aplicaciones.html`, September 2017. Accessed September 25, 2017.

[67] Clifford Matthews. *Engineers' Guide to Rotating Equipment - The Pocket Reference*. John Wiley & Sons, 2001.

[68] Chris Rauwendaal. *8. Extruder Screw Design*. Hanser Publishers, 2014.

[69] Terence Allen. *Particle size measurement*. Springer, 2013.

[70] Unknown. Windows movie maker. `http://www.windows-movie-maker.org/`, 2016. Accessed March 25, 2016.

[71] Unknown. srgb. `https://techterms.com/definition/srgb`, November 2017. Accessed November 30, 2017.

[72] Image Analyst. Color segmentation by delta e color difference. `https://uk.mathworks.com/matlabcentral/fileexchange/31118-color-segmentation-by-delta-e-color-difference`, October 2011. Accessed December 1, 2017.

[73] G. N. Srinivasan and G. Shobha. Segmentation techniques for target recognition. *International Journal of Computers and Communications*, 1(3):75–81, 2007.

[74] Unknown. Mathworks: imfreehand. `https://uk.mathworks.com/help/images/ref/imfreehand.html`, 2007. Accessed September 1, 2016.

[75] Unknown. Image processing toolbox. `https://uk.mathworks.com/products/image.html`, 2014. Accessed December 1, 2017.

[76] J. Best. *Colour Design: Theories and Applications*. The Textile Institute Book Series. Elsevier Science, 2017.

[77] Unknown. Mathworks: whitepoint. `https://uk.mathworks.com/products/image.html`, 2014. Accessed December 1, 2017.

[78] P. Bodrogi, B. Sinka, Á. Borbély, N. Geiger, and J. Schanda. On the use of the srgb colour space: the 'gamma' problem. *Displays*, 23(4):165 – 170, 2002.

[79] H. Scott Fogler. *Elements of Chemical Reaction Engineering*, volume 5th Edition. Prentice Hall, 2016.

[80] FrontlineSolvers. Standard excel solver - limitations of nonlinear optimization. `https://www.solver.com/standard-excel-solver-limitations-nonlinear-optimization`, 2018. Accessed March 13, 2018.

[81] Douglas C. Montgomery. *Design and Analysis of Experiments*, volume 5th Edition. John Wiley & Sons, 2001.

[82] NIST. Engineering statistics handbook. `https://www.itl.nist.gov/div898/handbook/index.htm`, October 2013. Accessed February 1, 2018.

[83] Xavier Élie Dit-Cosaque, Chebbah Mohamed-saïd, Hakim Naceur, and A Gakwaya. Analysis and design of hydroformed thin-walled tubes using enhanced one-step method. 59, 03 2011.

[84] Minitab. Methods and formulas for stepwise in fit regression model. `https://support.minitab.com/en-us/minitab/18/help-and-how-to/modeling-statistics/regression/how-to/fit-regression-model/methods-and-formulas/stepwise/`, 2017. Accessed October 1, 2017.

[85] Minitab. Multiple regression analysis: Use adjusted r-squared and predicted r-squared to include the correct number of variables. `http://blog.minitab.com/blog/adventures-in-statistics-2/`, 2017. Accessed October 1, 2017.

[86] D. J. Parker and T W Leadbeater. New life in old pets - the work of the university of birmingham positron imaging centre. *6th International Symposium on Process Tomography*, pages 1–7, 2012.

[87] X Fan, DJ Parker, and MD Smith. Labelling a single particle for positron emission particle tracking using direct activation and ion-exchange techniques. *Nuclear Instruments and*

Methods in Physics Research Section A: Accelerators, Spectrometers, Detectors and Associated Equipment, 562(1):345–350, 2006.

[88] Unknown. Sigma-aldrich: Sodium sulfate. https://www.sigmaaldrich.com/catalog/product/vetec/v800401?lang=en&region=GB, June 2017. Accessed January 6, 2017.

[89] Thomas W Leadbeater, David J Parker, and Joseph Gargiuli. Positron imaging systems for studying particulate, granular and multiphase flows. *Particuology*, 10(2):146–153, 2012.

[90] MathWorks. quiver. https://uk.mathworks.com/help/matlab/ref/quiver.html, September 2017. Accessed September 25, 2017.